INFORMATION TO USERS

This manuscript has been reproduced from the microfilm master. UMI films the text directly from the original or copy submitted. Thus, some thesis and dissertation copies are in typewriter face, while others may be from any type of computer printer.

The quality of this reproduction is dependent upon the quality of the copy submitted. Broken or indistinct print, colored or poor quality illustrations and photographs, print bleedthrough, substandard margins, and improper alignment can adversely affect reproduction.

In the unlikely event that the author did not send UMI a complete manuscript and there are missing pages, these will be noted. Also, if unauthorized copyright material had to be removed, a note will indicate the deletion.

Oversize materials (e.g., maps, drawings, charts) are reproduced by sectioning the original, beginning at the upper left-hand corner and continuing from left to right in equal sections with small overlaps. Each original is also photographed in one exposure and is included in reduced form at the back of the book.

Photographs included in the original manuscript have been reproduced xerographically in this copy. Higher quality 6" x 9" black and white photographic prints are available for any photographs or illustrations appearing in this copy for an additional charge. Contact UMI directly to order.

UMI

A Bell & Howell Information Company
300 North Zeeb Road, Ann Arbor MI 48106-1346 USA
313/761-4700 800/521-0600

NEAR INFRARED OPTICAL IMAGING AND LIGHT PROPAGATION IN HIGHLY SCATTERING RANDOM MEDIA

by

MANUEL E. ZEVALLOS

A dissertation submitted to the Graduate Faculty in Engineering in partial fulfillment of the requirements of Doctor of Philosophy, The City University of New York

1999

This manuscript has been read and accepted for the Graduate Faculty in Engineering in satisfaction off the dissertation requirements for the degree of Doctor in Philosophy.

4/28/99
Date

Robert R. Alfano
Chair of Examining committee
Professor Robert R. Alfano

4-28/1999
Date

Mumtaz K. Kassir
Executive Officer
Dean Mumtaz K. Kassir

Professor P. P. Ho

Professor K. Shum

Professor M. Lax

Dr. S. Gayen

Dr. F. Liu

Dr. H. Savage
Supervisory committee

The City University of New York

Abstract

NEAR INFRARED OPTICAL IMAGING AND LIGHT PROPAGATION IN HIGHLY SCATTERING RANDOM MEDIA

By

MANUEL E. ZEVALLOS

Advisor: Professor Robert R. Alfano

This thesis presents a study of near-infrared optical Imaging and photon migration through highly scattering random media. Near-infrared (NIR) time-sliced and continuous-wave (CW) spectroscopic imaging techniques were developed and used to obtain in vitro images of excised human breast tissue specimens and to characterize inhomogeneities and locate objects inside highly scattering biological and model random media. Investigation of photon migration involved time-resolved studies of light propagating through various types of highly scattering biological and non-biological media.

NIR CW transillumination images of an object hidden inside biological media of different thickness were improved by preferentially selecting the image-bearing photons through the use of polarization gating and spatial filtering techniques. Through the use of

a time-gated imaging approach to sort out the early photons, e.g. ballistic and snake components, the transillumination images of objects embedded in highly scattering diffusive media were improved. Higher image contrast was obtained using time-resolved as compared to CW imaging techniques.

A tunable chromium-doped forsterite laser system was used to explore the wavelengths that enhance image contrast of excised human breast tissue samples. The contrast of the images was improved by selecting appropriate wavelengths of light for better penetration and enhancement of the intrinsic properties of tissue constituents. In particular, the image contrast of human breast tissue samples showed strong wavelength dependence in the absorption band of fat, one of its main constituents. In the two-dimensional time-sliced transillumination imaging approach, an ultrafast electronic gated imaging system was used to select and record the image-bearing photons. Images recorded with different temporal slices of the transmitted light are found to selectively highlight different types of tissues, such as, adipose and fibrous or normal and cancerous in excised breast tissue specimens.

Time-resolved and CW light propagation in tissues with tubular structures were studied. Results show that transmission of linearly polarized light through tissues with tubular structures depends on the orientation of the structure of the sample with respect to the incident light, proving the existence of different paths for photon propagation.

Intensity temporal profiles at a fixed point in space as a function of angle of detection (arrival angle of light) were measured for ultrashort pulses of light propagating through highly scattering random media. It was found that there is a strong angular dependence of light traveling in a highly scattering media even for distances as large as

20 transport mean free path. To describe the high degree of anisotropy in the medium. two new anisotropy parameters are introduced.

The accuracy of the Non-Euclidean Diffusion (NED) equation to predict photon transport in a highly forward scattering medium was tested against experimentally measured temporal intensity profiles and compared to theoretical predictions given by the Diffusion Approximation (DA) in the pre-diffusive and diffusive regimes. It was found that the NED is more accurate than the DA. specifically in the pre-diffusive regime.

I dedicate this thesis to my Grandfather

Dr. Manuel Eduardo Zevallos Jijon

Who passed away while in pursuit of my dreams

And my loving parents

Nollan and Ana

For their love and spoiling...

Patience, and understanding.

Also to my brothers Nollan and Pierre

And

My sweet sister Melody

IDEALS

As you think, you travel; and as you love, you attract.
You are today where your thoughts have brought you;
you will be tomorrow where your thoughts take you.

You can not escape the result of your thoughts,
but you can endure and learn, can accept and be glad.

You will realize the vision (not the idle wish), of your heart,
be it base or beautiful, or a mixture of both,
for you will always gravitate towards that which you,
secretly, most love.

Into your hands will be placed the exact result of your thoughts;
you will receive that which you earn: no more, no less.

Whatever your present environment may be,
you will fall, remain, or rise with your *thoughts*, your *vision*, your *ideal*.

You will become as small as your controlling desire;
as great as your dominant aspirations.

Unknown

Acknowledgements

I would like specially thanks my Mentor Professor Robert R. Alfano who I look up to with the utmost respect and admiration and who through his guidance, training, and motivation encouraged me to continue and successfully finish the doctoral degree.

I want to specially thank Drs. Swapan Gayen, Feng Liu, and Bidyut Das for their great help, ideas, and training provided to me during my graduate years and during the investigations performed for this thesis.

I thank Professors Pin Ho, Kai Shum, Melvin Lax, and Dr. Howard Savage for being part of my doctoral dissertation committee.

I want to thank the IUSL family for their support, and general advice during the course work of this thesis.

I would like to specially thanks the National Aeronautics and Space Administration-Institutional Research Awards (NASA-IRA) for supporting most of my graduates studies and giving me the opportunity to attend to several scientific conferences and visit some of their facilities.

I would also like to thanks The Center for Analysis of Structures and Interfaces (CASI) and their members, specially Dr. Ron Brown and Dr. Daniel Akins for their support and friendship.

I would also like to thanks the Program for the Retention of Engineering Students (PRES) and her Director Dean Ramona Brown, for their guidance and support during my undergraduate years.

Finally I want to thank all my relatives, friends, and professors at City College who helped me and encouraged me to continue and finish my studies.

The research work in this thesis was made possible with the financial support from National Aeronautics and Space Administration, Office of Naval Research, National Science Foundation, and Mediscience Technology Corp.

Table of Contents

List of Tables

List of Figures

Chapter 1

Introduction

1.1 Background

The beginning of the medical imaging of the interior of human body can be traced back to the 1895 discovery of x-rays by Wilhelm Conrad Roentgen.[1.1] The potential of x-rays to provide images for use in diagnosis was immediately recognized by the medical community. The first x-radiograph taken with clinical intent was made the following year, 1896 by two English doctors to show a needle in a woman's hand. Seven years later, the first mammogram ever was reported by Salomon.[1.1] Through out the next century, several imaging techniques have been presented but only the most efficient ones have survived. At the present time, one of the newest and most appealing imaging techniques in the medical field is **Optical Imaging**. Optical Imaging through highly scattering media such as biological tissues has received renewed interest in recent years because of its non-ionizing and diagnostic potential in the medical field. The wide variety of colors of light that could be used in optical imaging presents a significant advantage over all other imaging methods.

M. Cutler, in 1929 in New York, was the first person to report measurements of transmitted light through tissues as an aid in the diagnosis of breast lesions.[1.2] This transillumination technique became known as Diaphanography and produced shadowgrams. Although first medical-related imaging work using light began shortly

after Cutler's discovery, there was no commercially available equipment until the late 1970's. The fifty-year delay of optical imaging had could be attributed to several factors, the major ones being: poor spatial resolution and lack of suitable light sources, as well as of adequate imaging photo-detectors. Likewise, the enormous success of x-rays and the emergence of several competing imaging technologies during this period also overshadowed the optical technique and contributed to its slow start. The imaging techniques that appeared prior to the late 1970's, and which remain active up to this day (to list a few) are x-rays, x-ray computed tomography (CT), single-photon emission tomography (SPET), nuclear magnetic resonance (NMR), ultrasound, and radioisotope imaging. Unfortunately, some of these currently available non-optical imaging modalities are costly, have a poor spatial resolution, and present potential hazards to the human body.[1,3]

With the advent of new light sources, such as lasers with different wavelengths, and the general availability of charged-coupled device (CCD) cameras, fibers, and fast photo-detectors in the ultra-violet (UV), visible, and near infra-red (NIR) spectrum, optical imaging has reappeared in the 80's as a compliment or rather as a promising alternative to the current imaging modalities. New excitation and detection schemes facilitated by the growth of photonic technology have greatly enhanced the capability and potential of optical imaging in the medical field. The main reasons why optical imaging technology is highly attractive to the medical community are that it may offer safer, non-ionizing, non-invasive, and in-expensive diagnostic methods for the detection and

characterization of diseases. ***Light has the potential to provide spectroscopic information of the sample constituents and monitor physiological changes of the body's key molecular components in real time, offering unmatched diagnostic capabilities*** when compared to current non-light based imaging modalities. Better-developed optical tomography can complement MRI and ultrasound imaging.

The goal of every imaging technology is to be able to detect defects, objects or diseases buried or hidden inside highly scattering opaque media, which can not be observed or diagnosed by simple eye inspection. Examples are abnormal growths such as cancer inside a human breast, or airplanes inside clouds. In particular, the physical basis of transillumination imaging (also known as Shadowgrams or Diaphanography) is based on the light transmission difference between a normal tissue and a foreign object or growth inside it.[1,4] This difference in transmitted light, in principle, should lead to the formation of the "shadow" of the hidden object, or a tumor in the case of breast cancer.

In general, light traveling through a highly scattering medium will be attenuated mainly due to the scattering and absorption properties of the medium. Alfano and co-workers introduced the concept of the *light breakup* into three main signal components called *ballistic, snake, and diffusive* photons.[1,5,16]

The original characteristics of the incident light —such as its original direction of propagation, intensity, coherence, and polarization— are scrambled, and in many cases

lost. This, in fact, can easily be observed that the ballistic component disappears as light travels long distances through dense, turbid medium. The Ballistic component is coherent photons that do not scatter and travel a straight line following its original direction of propagation arriving at time $t_{ballistic} = x_o / (c/n_g)$, where x_o is the thickness of the medium, c is the speed of light in vacuum and n_g the group index of refraction of the medium. The snake photons travel in a snake like-manner around the initial direction of propagation and arrive at a later time, $t_{snake} > t_{ballistic}$. The ballistic and snake photons contain the least distorted image information.

The diffusive component are photons undergoing multiple scattering, and are completely randomized. These photons arrive at a much later time, $t_{diffusive} >> t_{ballistic}$, and lose their direct image information. In order to extract information from the diffuse component, one must employ mathematical algorithms to reconstruct the image.

To obtain shadowgram information about the medium in transillumination imaging, sorting of the image-bearing photons from the higher intensity diffusive ones is imperative. Light detection approaches can use either steady state or ultrafast techniques depending on the light source use to illuminate the sample. Steady state techniques are used when the sample is under continuous wave (CW) illumination. In this case, spatial and polarization filtering techniques can be used to reduce the highly diffuse light, and improve the image quality. Ultrafast time-resolved technology is required when the

sample is illuminated with ultrashort pulses of light to further improve the image of quality. In these cases, a Streak Camera and Kerr gate technology are often used to select the early arriving light and get rid of the late arriving diffusive light. In this way optimal time windows for imaging are obtained.[1.7—1.10] In spite of the great achievements accomplished by optical technology in the last decade, there are still problems associated with the speed and recovery of the signal. A combination of filtering techniques with a clever manipulation of procedures is likely to be more successful in providing useful information for optical imaging. In addition, a clear understanding of light transport through a highly scattering medium, and light-tissue interaction are, in fact, key requirements for the successful development and introduction of optical imaging in the medical field.[1.11—1.13]

Much research has been devoted to solve the radiative transfer Boltzmann equation which describes photon migration in random medium. Due to the difficulty in solving this equation, various approximations have been proposed for different geometrical considerations, in both time and frequency domains.[1.14—1.17] So far, a general solution for this equation, in particular for the time-dependent case, has not yet been obtained. In addition to higher order approximations of the Boltzmann equation,[1.19,1.20] approximations such as the telegrapher's equation[1.18] and the diffusion approximation (DA) are commonly used models to predict the phenomenon of photon migration which is used in sophisticated computer algorithms to inverse reconstruct information about the medium. The imaging results obtained using these models are rather modest and lack the

high resolution needed for biomedical imaging. More accurate light transport models are needed and are crucial to better describe light scattering through highly turbid media.

One of the advantages of using light for the development of an imaging technique is the property of **"color"**. In the optical mammography arena, as Prof. Alfano states, "the **'Holy Grail'** is the proper selection of color (or wavelength of light) which can separate cancer from normal tissue". Spectroscopic information is a special property of optical imaging to examine tissue interior. The wavelength of choice for optical imaging resides in the NIR spectral band (e.g. 700-1500 nm) where these wavelengths are less scattered, and allow deeper penetration of light into the sample.[1.21—1.23] Identification of the **"fingerprint wavelengths"** that can characterize breast tissue constituents and provide a good signal to noise ratio still remains a challenge to the optical medical imaging community.

The main challenges in optical imaging are: 1) availability of adequate light transport models that could describe photon migration in random media with a higher degree of accuracy, 2) development of new imaging techniques and electronic devices that could resolve problems associated with the recovery of the signal, and 3) the identification of key wavelengths of light that harness good penetration depth and are less scattered which could provide adequate spectroscopic information about the sample under study and produce good imaging contrast.

1.2 Thesis Statement and Organization

This thesis will focus on light propagation in highly scattering media, improving optical imaging approaches for the production of shadowgrams based on space, time, and polarization gating techniques, and techniques used to discriminate the image-bearing photons from the highly diffusive ones. Moreover, to demonstrate the effectiveness of proper selection of wavelengths, a two-dimensional (2-D) NIR spectroscopy imaging approach will be used to identify the main breast tissue constituents, blood, fat, fibrous, and tumors. Time resolved and CW near-infrared shadowgram and spectroscopic imaging via experimental and theoretical modeling will be used in this thesis, in the steps towards an optical mammographic system.

The research part of this thesis presented in Chapters 3 through 8 is divided in two parts. The first part—Chapters 3 through 5—will theoretically and experimentally investigate the propagation of light through various types of highly scattering anisotropic media. This will be achieved using steady state and ultrafast detection schemes to better understand photon migration and light-tissue interaction. The second part of the research—Chapters 6 through 8—will further build on the concept of near-infrared transillumination imaging, by implementing detection schemes based on spatial, polarization, and time gating light sorting techniques, whilst paying special attention to the spectroscopic information obtained through the selection of optimum wavelengths. This will be achieved using state of the art two-dimensional CW and time-resolved light detection imaging systems, with the aim to improve image quality.

In the first part, time-resolved studies of light propagation through various highly scattering biological and non-biological (with and without an axis of symmetry) media will be performed. Temporal intensity profile-measurements of photons scattered in a highly turbid medium, moving through a fixed point in space with different angular directions, will be obtained. Analysis of these profiles will show that angular-detection dependence of the scattered light is preserved through large source-detector distances as big as 20 transport mean free paths. Experiments similar to those mentioned above will be carried out, and the results obtained will be compared to predictions obtained by the Non-Euclidean Diffusion (NED) and the conventional DA models. This will prove the efficacy of the NED equation in predicting light propagation in both the highly diffusive and the pre-diffusive regime, the latter one being where the diffusion approximation fails. The studies performed on biological media will investigate different scattering behaviors (if any) of polarized light traveling through tissues of well defined cellular structures. The results obtained will show the feasibility of applying different polarization schemes for imaging samples with defined internal cellular structures.

The second part of this thesis concentrates on CW, time-resolved, and spectroscopic near-infrared optical imaging of tissues.

Two-dimensional NIR shadowgrams of hidden objects inside different biological media will be obtained via CW techniques. The efficacy of, both, Fourier and polarization gates to sort out the image-bearing photons and discriminate against multiply scattered image-blurring photons will be examined using a Nd:YAG and Cr^{4+}: Forsterite

laser systems. Optimum wavelengths for deeper penetration and less scattering that could provide better image qualities will be investigated.

In the time-resolved section, two-dimensional time-sliced NIR transillumination images of hidden objects will be obtained by applying ultrashort pulses of light to the samples and using a time gated image intensifier coupled to a charged-coupled device (CCD) for its detection. The time-resolved CCD camera will take advantage of the time domain and improve the image quality by selecting early-light components. Direct information from the samples that otherwise would have been impossible to obtain by using only steady state measurements, will be obtained through time-sliced imaging. Time-sliced imaging shows the 2-D spatial intensity distribution of light transmitted through the different tissue constituents for different time windows.

NIR spectroscopic imaging studies on different excised human breast tissues will be performed in an effort to exploit the spectral signatures of the different tissue constituents. Such information will prove valuable in the detection of cancer. Certainly, the wide spectrum of light offers vast possibilities for the detection and monitoring of diseases which are being and will be discovered to the pace of the emerging technology.

In short, the contents of the different chapters are as follows:

Chapter 2 presents a brief review of Light Transport Theory, and the Radiative Transfer Equation. In addition, the Diffusion Approximation as well as the Non-Euclidean Diffusion Equation will be described in this chapter.

Chapter 3 shows the angular dependence of scattered pulses in highly scattering media in the pre-diffusive and diffusive regime. Two new equations are introduced in order to describe the degree of anisotropy in photon distribution in the medium.

Chapter 4 compares the accuracy of the DA and the NED equations in predicting light propagation in a highly forward-scattering medium against measured scattered light temporal profiles acquired for the pre-diffusive and diffusive regime.

Chapter 5 shows that tissues with definite internal structure could offer different pathways for photon propagation, and that the sample structure orientation with respect to the incident beam polarization direction influences on the transmitted scattered light.

Chapter 6 presents two-dimensional NIR transillumination images of an object hidden inside different biological media. A Fourier gate in tandem with a polarization gate is used to improve the image quality. Images obtained using light from a Cr^{4+}:Forsterite and a Nd:YAG laser systems are compared.

Chapter 7 presents the results of a time-gated imaging approach to select the early arriving photons to improve the image quality. Two-dimensional time-sliced NIR transillumination images of thick biological media are presented.

Chapter 8 NIR laser spectroscopic and time-sliced transillumination optical imaging approaches are used in an attempt to characterize breast tissue constituents.

Chapter 9 summarizes the results of this thesis.

Chapter 10 introduces some future research directions and presents a list of publications and presentations by the author of this thesis related to this work.

1.3 References

1.1 S. Webb. The Physics of Medical Imaging: Medical Science Series. (Institute of Physics (IOP) Publishing Ltd., 1988).

1.2 M. Cutler, "Transillumination as an aid in the diagnosis of breast lesions: with special reference to its value in cases of bleeding nipples." Surg. Gyncol. Obstet., 48, 721-729, 1929.

1.3 Z. H. Cho, J. P. Jones and M. Singh, Foundations of Medical Imaging (Wiley, New York, 1993).

1.4 R. R. Alfano, S. G. Demos, and S. K. Gayen, "Advances of Optical Imaging of Biomedical Media." Annals of the New York Academy of sciences, 820, 248-271 1997.

1.5 L. Wang, P. P. Ho, C. Liu, G. Zhang, and R. R. Alfano, "Ballistic 2-D imaging through scattering walls using an Ultrafast Optical Kerr Gate," Science 253, 769-771, 1991.

1.6 K. M. Yoo, and R. R. Alfano, "Time resolved coherent and incoherent components of forward light scattering in random media," Opt. Lett., 15, 320-322, 1990.

1.7 Koichi Furutsu, and Yukio Yamada, "Diffusion approximation for a dissipative random medium and the applications," Phys. Review E, 50, 3634-3641, 1994.

1.8 B. B. Das, J. Dolne, R. L. Barbour, H. L. Grabber, J. Chang, M. E. Zevallos, F. Liu, and R. R. Alfano, "Analysis of Time-Resolved Data For Tomographical Image Reconstruction Of Opaque Phantoms And Finite Absorbers In Diffusive Media," Proc. SPIE, 2389, 16-28, 1995.

1.9 L. Wang, P. P. Ho, X. Liang, H. Dai, and R. R. Alfano, "Fourier-Kerr imaging in thick turbid media," Opt. Lett., 18, 241-243, 1993.

1.10 L. Wang, P. P. Ho, C. Liu, G. Zhang, and R. R. Alfano, "Ballistic 2-D imaging through scattering wall using an ultrafast Kerr gate," Science 253, 769-771, 1991.

1.11 D. Huang, J. Wang, C. P. Lin, C. A. Puliafito, and J. G. Fujimoto, "Micro-resolution ranging of cornea anterior chamber by optical reflectometry," Las. Sur. Med., 11 419-425, 1991.

1.12 K. M. Yoo, Y. Takiguchi and R. R. Alfano, "Dynamic Effect of Weak Localization on the Light Scattering from Random Media Using Ultrafast Laser Technology," Appl. Opt., 28, 2343-2349, 1989.

1.13 S. L. Jacques, "Time Resolved Propagation of Ultrashort Laser Pulses within Turbid Tissues." Appl. Opt., 28, 2223-2229, 1989.

1.14 J. Fishkin, E. Gratton, M. J. vande Ven, and W. W. Mantulin, "Diffusion of Intensity Modulated Near-Infrared Light in Turbid Media," Time-Resolved Spectroscopy and Imaging of Tissues, B. Chance, Editor, Proc., SPIE, 1431, 122-135,1991.

1.15 M. S. Paterson, B. C. Chance, and B. C. Wilson, "Time resolved reflectance and transmittance for the non-invasive measurements of tissue optical properties." App. Optics, 28, 2331-2336, 1989.

1.16 S. J. Madsen, M. S. Patterson, B. C. Wilson, Y. D. Park, J. D. Moulton, S. L. Jacques, M. D. Anderson, and Y. Hefetz. "Time-resolved diffuse reflectance and transmittance studies in tissue simulating phantoms: a comparison between theory and experiment," Time-Resolved Spectroscopy and Imaging of Tissues, B. C. Chance, Editor, Proc. SPIE, 1431, 42-52, 1991.

1.17 S. R. Arridge, P. van der Zee, M. Cope, and D. T. Delpy, "Reconstruction methods for infrared absorption imaging," Time-Resolved Spectroscopy and Imaging of Tissues, B. C. Chance, Editor, Proc. SPIE, 1431, 204-217, 1991.

1.18 P. M. Morse and H. Feshback, Methods of theoretical Physics, McGraw-Hill, New York, Part 1, p. 865, 1993.

1.19 A. Ya. Polishchuk, S. Gutman, M. Lax, and R. R. Alfano, "Photon-density modes beyond the diffusion approximation: scalar wave-diffusion equation," J. Opt. Soc. Am. A., 14, 230-234, 1997.

1.20 J. Kaltenbach, M. Kashke, and C. Zeiss, "Frequency and Time Domain Modelling of Light Transport in Random Media," Medical Optical Tomography, 64-86, 1996.

1.21 V. G. Peters, D. R. Wyman, M. S. Patterson, and G. L. Frank, "Optical properties of normal and diseased human breast tissues in the visible and near infrared," Phys. Med. Biol. 35, 1317-1334, 1990.

1.22 H. Key, E. R. Davics, P. C. Jackson, and P.N. T. Wells, "Optical attenuation characteristics of breast tissues at visible and near-infrared wavelengths," Phys. Med. Biol. 6, 579-590, 1991.

1.23 1.23 P. French, "The light fantastic," New Scientist magazine, 25-29, 11 march, 1995.

1.4 Figures

Figure 1.1 Light propagation through highly scattering media showing the ballistic. snake and diffusive components.

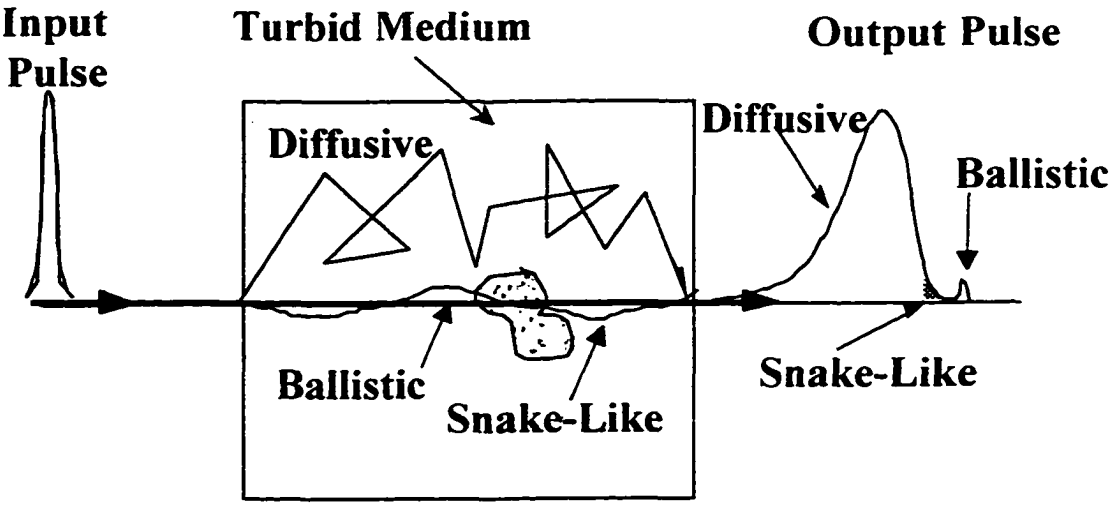

- **Ballistic Photons:** Coherently forward scattered
- **Snake Photons:** Paraxially forward scattered
- **Diffusive photons:** Multiple scattered

Image Bearing

Chapter 2

Photon Migration in Random Media: Light transport theory

2.1 Introduction

Photon migration in highly scattering media has been studied for many years.[2.1,2.2] Most recently, work on light scattering has been conducted in biological tissues. Experimental investigations into the nature and behavior of light interaction in this type of media are required to understand the propagation phenomena. The evolution of new ideas and approaches in this field depends on the understanding of the interaction of light and matter. The work conducted in this thesis will experimentally tap on the behavior of light propagation in different biological and model random media.

Light propagation in a random scattering media is best described by the radiative transfer theory, also known as the transport theory. Radiative transfer means the transport of light energy through matter. A medium such as vacuum has no influence on light propagation; that is, its initial energy and direction of propagation are maintained. In such a case, photons are neither absorbed, nor scattered. On the other hand, scattering and absorption of light occur if photons interact with particles of the medium. The way particles are arranged in the medium is important since it will influence how the light is scattered. If a medium has particles that are arranged in a very regular way, the light scattered by the particles interfere in such way that causes no scattering at all, such as in a crystal. If they are not arranged in a regular way and are closely pack, the cooperative scattering effect of all the particles should be taken into account.

The problem of light scattering is more than a hundred years old. It was first studied by Lord Rayleigh[2.1] [1847] and then by Gustav Mie[2.2] [1908]. Lord Rayleigh's theory applied to small dust particles requires the following assumptions: (1) there must be an assembly of small spheres in the medium. (2) The scattering must be coherent implying that addition of the scattered light amplitude at each scattering angle for all these speheres is allowed. For this to occur, a plane wave must be incident on all these spheres. (3) All the spheres must have the same size and must be small compared to the wavelength of the incident light.[2.3] (4) The scattering spheres should not be closely packed.[2.4, 2.5] If they are closely packed then multiple scattering is bound to occur. Mie extended Lord Rayleigh's theory by studying light propagating through a medium of gold spheres of different sizes, comparable to the wavelength of the light and by considering absorption in addition to scattering. The phenomena studied by Rayleigh and Mie is applied to loosely packed scatters and is known as single scattering. Schuster [1905] and Schwarzchild [1914] were the first ones to considered multiple scattering.[2.6, 2.7, and 2.8.] Schuster's theory considers a medium with closely packed absorbing and scattering particles of various sizes and shapes. The differences in sizes and shape are not as important as in the Rayleigh and Mie cases because of the closer packing of the particles. Therefore, the values obtained by Schuster are statistical averages over the range of sizes and shapes. In his theory, Schuster assumed light travels only in two directions, one forward (initial direction of propagation), and one backward (opposite to initial direction). Shwarzschild, on the other hand, modified the forward and backward differential Schuster's equations by integrating over all directions the scatter light in the forward and backward hemisphere respectively. Shwarzschild's formulation is the first

example of radiative transfer proper. See Ref. 2.7 and 2.8. Schuster-Shwarzschild's formulation has been perfected by subsequent authors. In its actual form, It is no longer a differential equation (or two differential equations, as with Schuster) but an integro-differential equation. Analytical solutions to the transport equation are difficult to obtain and numerical calculations require large amount of computational work. Most solutions to the transport equation, so far, are for defined geometries and have been obtained via approximations. The Diffusion Approximation and the Non-Euclidean Diffusion (NED) equation will be compared to experimental data in Chapter 4.

2.2 Radiative Transfer Equation (Boltzmann Equation)

The basic differential Radiative Transfer Equation is similar to the Boltzmann Equation in Kinetic theory of gases and in neutron transport theory.[2.9—2.11] It treats the flow of particles, e.g. photons, —per unit area, per unit time, per unit solid angle— incident with direction $\vec{s}$ on a given volume element (with unit cross section and length dl, with particle density ρ) and scattering in the $\vec{s}'$ direction due to collisions, i.e. scattering and absorption. See Fig. 2.1.

The equation of transfer can be written as follows:[2.12—2.14]

$$\left(\frac{\partial}{c\,\partial t} + s\cdot\nabla\right) I(r,s,t) = -\mu_T I(r,s,t) + \frac{\mu_T}{4\pi}\int p(s,s')I(r,s',t)d\Omega' + S(r,s,t), \qquad (2.1)$$

where $I(\vec{r},\vec{s},t)$ is the specific intensity or radiance and represents the number of photons at position $\vec{r}$, traveling in the direction $\vec{s}$, at time t, with units Wm^{-2}/sr (sr = steradian =

unit solid angle). $\mu_T = \mu_s + \mu_a$ is the total attenuation factor, where μ_s is the scattering coefficient and μ_a is the absorption coefficient.

The $p(\bar{s},\bar{s}')$ function inside the second term is a normalized phase function, and represents the probability of scattering into a direction $\bar{s}'$ from direction $\bar{s}$. This phase function is normalized by the condition $\frac{1}{4\pi}\int_{\bar{\Omega}'} p(\bar{s},\bar{s}')d\bar{\Omega}' = \frac{1}{4\pi}\int_{\bar{\Omega}} p(\bar{s},\bar{s}')d\bar{\Omega} = 1$, integrating over the solid angle $\bar{\Omega}$, where $d\bar{\Omega} = \sin\theta\, d\theta\, d\phi$. The term $S(\bar{r},\bar{s},t)$ represents a light source within the volume. The $\bar{r}$ and $\bar{s}$ dependence in this term indicates the spatial and angular distribution of the source, respectively, at time t.

The first term on the left-hand side $\frac{\partial I(\bar{r},\bar{s},t)}{c\partial t}$ is the time derivative of the radiance and accounts for the rate of change of photons entering minus photons leaving the volume element. The second term $s\cdot\nabla I(r,s,t)$ accounts for the photon flux along the direction $\bar{s}$.

On the right hand side the first term accounts for the attenuation (absorption + scattering) of photons within the volume. The second term takes into account the intensity gain due to secondary scattering from all surrounding angles,[2.8] always under the provision that the re-emitted or scattered energy has the same frequency as the incident energy. The term $S(\bar{r},\bar{s},t)$ represents a light source within the volume.

The photon number density is obtained by integrating the specific intensity over all directions as follows:

$$n(\bar{r},t) = \frac{1}{c}\int_{4\pi} I(\bar{r},\bar{s},t)\, d\bar{\Omega} \qquad (2.2)$$

The photon fluence is given by $\Phi(\vec{r},t) = c\, n(\vec{r},t)$.

The number of photons reaching the surface per unit area per unit time is known as the photon flux. The photon flux represents the amount and the direction of the net flow of power and is given by:

$$\vec{j}(\vec{r},t) = \int_{4\pi} \vec{s} I(\vec{r},\vec{s},t)\, d\vec{\Omega} \tag{2.3}$$

Both the photon fluence and the photon flux have units Wm^{-2}.

A general solution to the transport equation 2.1, in particular for the time dependent case has not been obtained, basically, due to the difficulty and the number of variables inherent in the equation. Solutions obtained to describe the transport of light have been achieved by cutting down the level of difficulty of the transport equation by using specific information and assumptions related to the propagating medium under study, such as geometry of the medium and scattering/absorption properties of the scattering particles.[2.15—2.19] By expanding the transport equation, using spherical harmonics, different approximations could be obtained depending on the number of terms used in the expansion. The expansion method is also known as the P_N approximation and is better described in Ref. [2.20, 2.21, 2.9, 2.10]. Several solutions obtained through approximations have been reported for define geometries such as for infinite media,[2.15, 2.16] slab,[2.16, 2.17] cylindrical,[2.17, 2.18] and spherical[2.19]. In this thesis experimental results of a pulse of light propagating in a highly anisotropic turbid media will be compared to

the Diffusion Approximation and the recently introduced Non-Euclidean Diffusion Equation.

2.3 Diffusion Approximation (DA) and Non-Euclidean Diffusion (NED) Equations

The DA and NED equations are described in sections 2.3.1 and 2.3.2. respectively. Solutions to these equations are presented and compared against experimental data in Chapter 4.

2.3.1 Diffusion Approximation equation

The most common approximation used to predict the transport of photons in turbid media is the diffusion approximation. This approximation is obtained by the spherical harmonic method.[2.20, 2.22] The essential idea of this method, as proposed by Eddington,[2.23] lies in seeking the solution of the equation of transfer in the form of an expansion of the intensity in a series of Legendre polynomials in traveling direction s. The diffusion approximation assumes that the specific intensity is described by the first two terms of the expansion, and that $j(\vec{r},t) = -(D/c)\nabla n(\vec{r},t)$. The time-dependent diffusion approximation equation is:

$$\frac{\partial n(\vec{r},t)}{\partial t} = D\nabla^2 n(\vec{r},t) - c\mu_a n(\vec{r},t) + S(\vec{r},t) \tag{2.4}$$

where $D = \frac{c}{3\,(\mu_a + \mu_s'(1-g))}$ is the diffusion coefficient. c is the speed of light in the medium, g is the anisotropic factor, defined as the mean cosine of the scattering angle[2.24].

μ_a is the absorption coefficient. $n(\vec{r},t)$ is the photon density, and $S(\vec{r},t)$ is the photon source.

The Diffusion Approximation or P1 approximation is valid when the albedo is close to unity, e.g. $\mu_s / (\mu_s + \mu_a) \approx 1$, which is the zero order function of the phase function, and the scattering is quite isotropic (highly diffusive). Solutions to the DA have been used extensively by atomic physicist and most currently have been applied to the optical medical imaging field. Yoo, *et. al.*, have shown that the diffusion approximation is an excellent approach to study photon transport in the highly diffusive regime,[2.25] such as for thick biological samples, to determine their key optical parameters. However, the DA approximation has been found to be inadequate for predicting the photon distribution in the *pre-diffusive regime* by Alfano's group and others as well.[2.26, 2.27] This inaccuracy has led to the introduction of the NED equation[2.28] whose solution predicts photon propagation better in both the *diffusive* and *pre-diffusive regime* as well. The NED equation will be discussed in the following section.

2.3.2 The Non-Euclidean Diffusion (NED) Equation

The NED equation was recently introduced by A. Polishchuk, *et. al.*,[2.28, 2.29] and its efficacy was addressed in Ref. [2.30, 2.31]. Some important aspects of the NED equation are presented in this section.

The Non-Euclidean Diffusion Equation is derived from the general Boltzmann equation. It describes photon migration in turbid media as a random walk on a spherical surface of radius c, non-Euclidean velocity space. This equation was developed

specifically for highly forward scattering medium, such as human tissues. Ref. 2.29 presents the mathematical background to the physical ideas behind photon diffusion on the velocity sphere. Under the small angle approximation (i.e. highly forward scattering phase function), the non-Euclidean diffusion equation is written as:

$$\frac{\partial n}{\partial t} + \bar{s}\bar{\nabla}_r n - \frac{c^3}{2l_t}\Delta_s n + v_a n = \delta(t)\delta(\bar{r})\delta(\bar{s} - \bar{s}_o). \tag{2.5}$$

where $n(\bar{r},\bar{s},\bar{s}_o,t)$ is the *specific* photon number density at the time-space-velocity point $(\bar{r},\bar{s},t)$, which satisfies the above non-Euclidean diffusion equation. $\bar{s}_o$ is the initial velocity orientation for photons in a point-like ultrashort pulse. v_a is the absorption collision frequency an is given by c/l_a. Δ_s is the non-Euclidean Laplace spherical operator acting on the photon velocity sphere. It is obtained by going from the Cartesian to the spherical domain, replacing the Euclidean Laplace operators $\Delta_2 = \frac{\partial^2}{\partial x^2} + \frac{\partial^2}{\partial y^2}$. The right hand side of the NED eq. implies initial condition $n(t = 0) = \delta(\bar{r})\delta(\bar{s} - \bar{s}_o)$. which means that initially all photons are concentrated at the origin and possess the same propagation direction $\bar{s}_o$.

Although the NED equation is also an approximation to the transport equation, there are important differences between the NED and DA equations. The main differences between the NED and the DA equations are that: (1) the diffusion process in the NED case occurs on the velocity sphere rather than in real coordinate space. (2) The NED equation describes ballistic, transient, and diffusive motion of photons, which can

not be accomplished by the standard diffusion model. e.g. DA could only predict accurately photon propagation in the diffusive regime.

Solutions for both the NED and DA equations are presented and compared against experimental data in Chapter 4.

2.4 Background to Optical Imaging: Experimental Techniques

The basic idea of optical biomedical imaging is that of extracting information from a medium, such as for detection of hidden objects, without loss of information. The ability to image internal structures using transillumination techniques is limited by several factors, such as the thickness of the sample, as well as on the sensitivity of detector, and the color of light used. It is the overwhelming scattering that light suffers —while travelling through tissue— which limits this technique. In this thesis, near infrared light and various filtering techniques have been combined and used to improve the image resolution. The techniques implemented in this research to eliminate the undesirable highly scattering photons are: Polarization, Fourier, and time gate filtering techniques, as well as careful selection of the wavelength of the light source.

2.4.1 Photon Sorting Methods

The different photon sorting techniques used in optical imaging are briefly described below. These techniques have been implemented and their performance analyzed in subsequent chapters in this thesis.

a) Polarization Gating

The polarization gate makes use of the fact that scattering events depolarize an incident beam of polarized light, so that ballistic and snake photons retain their

polarization memory while the multiple-scattered photons are depolarized.[2.32-2.35] In order to implement a polarization gate, two polarizers are commonly used. The first polarizer is placed in front of the sample and is used to ensure the polarization state of the probing beam when entering the medium. The second polarizer is the actual gate and is used to select the photons that keep the same polarization state as the probing beam.

b) Spatial filtering: Fourier Gating

Spatial filtering is one of the simplest methods for the suppression of scattered light. The main idea is that of applying a spatial aperture that allows the undeviated ballistic light to pass through while blocking the highly scattered light (or high frequency components). The spatial gate implemented in our laboratory is a Fourier gate. In this system, a collimated beam is used to illuminate the sample. The sample is located at a distance equal to the focal length (f) of the collecting lens. The scatter light from the sample, after being collected by the lens, is focused at the Fourier plane where a small aperture is placed to eliminate the high diffusive component. A second lens is placed at a distance equal to its focal length from the Fourier plane to detect the scattered photons in a collimated fashion. The detector is placed at the image plane at a focal distance f. It has been demonstrated that by varying the aperture diameter, the Fourier gate may be used as a temporal gate for selecting out the early arriving less scattering photons. This system, unfortunately, cannot discriminate against highly scattered photons exiting the medium with a propagation direction equal to the input beam.

c) Time Gating

A pulse of light traveling through a medium other than vacuum will suffer a temporal spreading or pulse broadening. In principle, the early arriving photons would have travelled shortest distance and therefore have encountered fewer scattering events. In time gate imaging, the main idea resides in the detection of these early arriving photons. The time gating technique is exclusively used when the light source is a pulse of light. It has been broadly classified into incoherent and coherent techniques. In the incoherent techniques, selection of the early arriving photons is achieved by opening a time gate for a short period of time.[2.36, 2.37] On the other hand, the coherent gating technique requires that the light transmitted through the medium is combined spatially and temporally with a reference beam.[2.38, 2.39]

d) Wavelength selection

The critical factors that need to be considered for wavelength selection have been nicely described by Alfano, *et. al.*, in Ref. 2.32 and are quoted here: "*The color of light selection is probably the most important consideration in optical imaging of tissues. ... Several factors must be considered to choose the optical wavelength. First, to form a sharp image one needs light that is scattered the least. Second, the chosen wavelength should provide high spatial resolution, but should not be strongly absorbed by the tissue. Finally the Wavelength range need to be suitable to detect the key chemicals that can indicate how the body is functioning. Unlike ultrasound and X-rays, only light offers this capability of spectroscopic monitoring of body chemistry.*"

2.5 References

2.1 Lord Rayleigh,; Scientific Papers I. (Cambridge University Press. 1899). Phil. Mag. 41. 107; p. 96. 1871.

2.2 G. Mie. (Ann. Physik). 25. 377. 1908.

2.3 Lord Rayleigh was able to deduce the blue color of the sky. The blue color of the sky arises since the scattering occurs due dust particles or atmospheric molecules which are small (order of 10^{-10} m.) compared to the wavelength of the light (order 10^{-7} m.). The scattered intensity is proportional to $1/\lambda^4$, so that short wavelength (such as blue light) are scattered more than long wavelengths (such as red light).

2.4 H. C. Van de Hulst, Light Scattering by Small Particles, (Dover Publications Inc., New York, 1981)

2.5 Distances between sphere to ensure independent scattering is estimated to be bigger than 3 times the radio of the sphere. See Ref. 2.4 p. 5.

2.6 A. Schuster, Astrophys. J. 21, 1, 1905.

2.7 K. Schwarzchild, Sitz.ber. Preuss. Akad. Wiss. Berlin, 1183, 1914.

2.8 Frederich Kottler, The elements of radiative transfer, Progress in Optics Vol. III, part I, edited by E. Wolf, University of Rochester, NY, USA. 1964.

2.9 B. Davison and J. B. Sykes, Neutron Transport Theory, (Oxford University Press, London, 1957).

2.10 S. Glasstone and M. C. Edlund, The Elements of Nuclear Reactor Theory, (D. van Nostrand Co., Princeton NJ, 1952).

2.11 K. M. Case and P. F. Zweifel, in Linear Transport Theory, (Addison-Wesley, MA, 1967)

2.12 A. Ishimaru, Wave propagation and scattering random media, (Academic Press, New York, 1978).

2.13 B. B. Das, Feng Liu, and R. R. Alfano, "Time-resolved fluorescence and photon migration studies in biomedical and model random media", Rep. Prog. Phys. 60, p. 227-292, 1997.

2.14 S. Chandrasekhar, Radiative Transfer, (Dover Publications Inc., New York, 1960).

2.15 J. Fishkin, E. Gratton, M. J. vande Ven, and W. W. Mantulin, "Diffusion of Intensity Modulated Near-Infrared Light in Turbid Media", Time Resolved Spectroscopy and Imaging of Tissues, B. Chance, Editor, Proc. SPIE, 1431, p. 122-135, 1991.

2.16 M. S. Patterson, B. Chance, and B. C. Wilson, "Time resolved reflectance and transmittance for the non-invasive measurement of tissue optical properties", Appl. Optics, 28, p. 2331-2336, 1989.

2.17 S. J. Madsen, M. S. Patterson, B. C. Wilson, Y. D. Park, J. D Moulton, S. L. Jaques, M. D. Anderson, and Y. Hefez, "Time-resolved diffusive reflectance and transillumination and transmittance studies in tissue simulating phantons: a comparison between theory and experiment". Time Resolved Spectroscopy and Imaging of Tissues, B. Chance, Editor, Proc. SPIE, 1431, p. 42-51, 1991.

2.18 S. R. Arridge, P. van der Zee, M. Cope, and D. T. Delpy, "Reconstruction methods for infrared absorption imaging". Time Resolved Spectroscopy and Imaging of Tissues, B. Chance, Editor, Proc. SPIE, 1431, p. 204-217, 1991.

2.19 R. Aronson, "Subcritical problems in spherical geometry", Nuclear Science and Engineering 86, 436 (1984).

2.20 J. Kaltenback, and M. Kashke, "Frequency and time-domain modeling of light transport in random media", Medical Optical Tomography, p. 65-86, 1994.

2.21 K. M. Case and P. F. Zweifel, in Linear Transport Theory, (Addison-Wesley, MA, 1967).

2.22 V. Kourganoff, Basic methods in transfer problems, radiative equilibrium and neutron diffusion, (Dover Publications Inc., New York, 1963)

2.23 A. Eddington, The Internal Constitutions of the Stars, (Dover Publications Inc., New York, 1926)

2.24 The scattering cross-sections are defined in terms of the scattering amplitude. $f(\vec{s},\vec{s}')$ represents the amplitude, the phase and the polarization of the scatter wave at a large distance from a scatterer in the direction $\vec{s}$ when the particle is illuminated by a plane wave in the $\vec{s}'$ direction. The differential scattering cross-section $\sigma(\vec{s},\vec{s}')$ and the phase function $p(\vec{s},\vec{s}')$ are related by

$$\sigma(\vec{s},\vec{s}') \equiv \left|f(\vec{s},\vec{s}')\right|^2 \equiv \frac{\sigma_T}{4\pi} p(\vec{s},\vec{s}'),$$

where the total cross section is defined as $\sigma_T = \sigma_s + \sigma_a$. σ_s and σ_a are the scattering and absorption cross section. The scattering cross section σ_s is related to the differential cross section $\sigma(\theta,\varphi)$ as:

$$\sigma_s = \int \sigma(\theta,\varphi)\, d\Omega = \int \sigma(\theta,\varphi)\, \sin\theta\, d\theta\, d\varphi,$$

where the integration is performed over the whole 4π solid angle.

The transport scattering cross section or momentum transfer scattering cross section which gives a measure of the photons scattered away from the initial direction of propagation is defined as:

$\sigma_t = \int \sigma(\theta,\varphi)\ (1-\cos\theta) d\Omega$.

The anisotropic factor is defined as:

$$g=\langle\cos\theta\rangle=\frac{\int \sigma(\theta,\varphi)\ \cos\theta\ d\Omega}{\int \sigma(\theta,\varphi)\ d\Omega}.$$

Thus we have $\sigma_t = \sigma_s(1-g)$. The transport scattering cross section is related to the transport mean free path (l_t) by $l_t = 1/n\sigma_t = 1/n\sigma_s(1-g) = l_s/(1-g)$, where n is the scatter density.

For a more complete description see Ref. 2.13, and Leming Wang. Ph.D. Thesis. The City University of NY. 1995.

2.25 K. M. Yoo, F. Liu, and R. R. Alfano, Phys. Rev. Lett., 64, 2647, 1990.

2.26 Feng Liu, K. M. Yoo, and R. R. Alfano, "Early arriving transmitted photon intensity through tissues," edited by R. Alfano, OSA Proc. on Advances in Optical Imaging and Photon Migration, OSA, 21, p. 170, 1994.

2.27 E. P. Zege, A. P. Ivanov, and I. L. Katsev, Image Transfer through a Scattering Medium, (Springer-Verlag, Heidelberg, 1991).

2.28 A. Ya Polishchuk, and R. R. Alfano, "Non-Euclidean diffusion and "Fermat" photons in turbid media", SPIE Proc. in Optical tomography, Photon Migration, and spectroscopy of Tissue and Model Media: Theory, Human Studies, and Intrumentations, SPIE, 2389, 1995.

2.29 A. Ya Polishchuk, and R. R. Alfano, "Photon diffusion on the velocity sphere", Opt. Lett., 21, 916-918, 1996.

2.30 A. Ya Polishchuk, M. E. Zevallos, F. Liu, and R. R. Alfano, "Generalization of Fermat's principle for photons in random media: The least mean square curvature of paths and photon diffusion on the velocity sphere," Phys. Rev. E, 53, 5523, 1996.

2.31 M. E. Zevallos, A. Ya Polishchuk, F. Liu, B. B. Das, and R. R. Alfano, "Time-resolved scattering measurements from scattering media fitted to Non-Euclidean and Conventional Diffusion model," Phys. Rev. E, 56, No 6, 1998.

2.32 R. R. Alfano, S. G. Demos, and S. K. Gayen, Advances, "Optical imaging of Biomedical Media, on Imaging Brain Structure and Function,"Annals of the New York Academy of Sciences, 248-271, 1997.

2.33 S. G. Demos and R. R. Alfano, "Temporal gating in highly scattering media by the degree of optical polarization." Opt. Lett., 21, 161-163, 1996.

2.34 H. Horinaka, K. Hashimoto, K. Wada, and Y. Cho, "Extraction of quasi-straightforward-propagating photons from diffused light transmitting through a scattering medium by polarization modulation," Opt. Lett., 20, 1501-1503, 1995.

2.35 J. C. Hebden, S. R. Arridge, D. T. Delpy, "Optical imaging in medicine: I. Experimental Techniques," Phys. Med. Biol., 42, 825-840, 1997.

2.36 B. B. Das, K. M. Yoo, and R. R. Alfano, "Ultrafast time-gated imaging in thick tissues: A step toward optical mammography." Opt. Lett., 18, 1002-1004, 1993.

2.37 J. C. Hebden, R. A. Kruger, and K. S. Wong, "Time resolved imaging through a highly scattering medium." Appl. Opt., 30, 788-794, 1991.

2.38 K. M. Yoo, Q. Xing, and R. R. Alfano, "Imaging objects hidden in highly scattering media using femtosecond second-harmonic generation cross-correlation time gating," Opt. Lett., 16, 1019-1021, 1991.

2.39 M. R. Hee, J. A. Izzat, J. M. Jacobson, J. G. Fujimoto, and E. A. Swanson, "Femtosecond transillumination optical coherence tomography," Opt. Lett., 18, 950-952, 1993.

2.6 Figures

Figure 2.1 Flow of particles, e.g. photons, —per unit area, per unit time, per unit solid angle—incident with direction s on a given volume element (with unit cross section and length dl, with particle density ρ) and scattering in the s' direction due to collision, i. e. scattering and absorption.

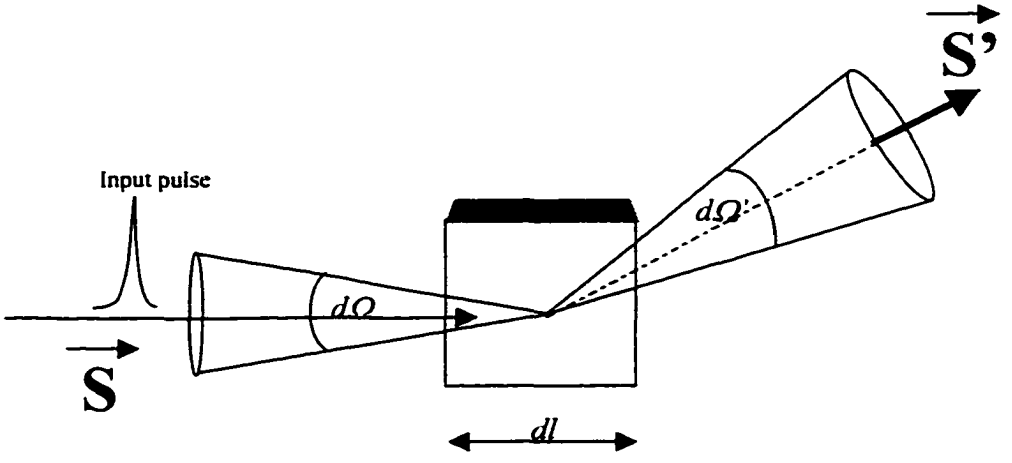

Part I

LIGHT PROPAGATION

IN HIGHLY SCATTERING RANDOM MEDIA

Chapter 3

Angular Dependence of the Temporal Intensity Profiles of Scattered Light Pulses in Highly Scattering Media

3.1 Introduction

It is commonly believed that the direction of light in a highly scattering turbid medium is randomized after photons travel many transport lengths. No angular dependence should be present. Prior research conducted by this group and others has been done by taking the detected intensity profile in either time or frequency domain as a function of source detector distance *(r)* while neglecting the dependence of angle of detection.[3.1—3.4] In this chapter, I focus on the angle of detection dependence on light traveling through a fixed spatial point in highly scattering random media. The influence of the media scatter size on this dependence will also be analized for three different media.

Intensity temporal profiles $I(r, \theta, t)$, of scattered light traveling in various directions (angles) at a fixed spatial point, were measured using optical fiber probes; where r is vector (x,y,z) which indicates the source-detector (S-D) distances; and θ is the detector angular position of collection of photons travelling through a fixed point in space with various directions. The detection angle at a fixed point is varied. Similar detection points in each medium have been chosen along two directions: forward –along the light source launching direction, x-axis; and lateral or perpendicular direction, y-axis, for comparison. Figure 3.1 shows the S-D configuration arrangement used for this work. In order to relate the angle of detection dependence to the scattering size property, three

different sizes of polystyrene spheres comparable to the size of cells found in a human breast were chosen.

The anisotropy of light propagation was detected by comparing temporal profiles with different angles of collection at: a) a fixed point, and b) two equidistant points from the source. For this purpose, an equation to describe the degree of anisotropy has been introduced.

The degrees of anisotropy in photon distribution in the medium due to the source directionality are defined as:

a) Angular anisotropy at a point

$$A_{xx}(r,\theta_x,\theta'_x,t) \equiv \frac{I(r,\theta_x,t) - I(r,\theta'_x,t)}{I(r,\theta_x,t) + I(r,\theta'_x,t)} \tag{3.1}$$

b) Angular-spatial anisotropy between two points

$$A_{xy}(|r|,\theta_x,\theta_y,t) \equiv \frac{I(r,\theta_x,t) - I(r,\theta_y,t)}{I(r,\theta_x,t) + I(r,\theta_y,t)} \tag{3.2}$$

Equation (3.1), A_{xx} describes the degree of angular anisotropy at the same spatial point between two propagation directions, θ_x and θ'_x. The subscript xx in the first equation indicates that two profiles, of a fixed point on the x-axis, have been chosen. The subscript yy indicates that a point on the y-axis has been chosen. The second equation A_{xy}

describes the degree of angular-spatial anisotropy between two profiles taken at two different equidistant spatial points from the source in the forward and lateral directions and considers angular dependence.

3.2 Experimental Methods and Materials

A schematic of the experimental set up is shown in Fig. 3.2. Ultrashort laser pulses of 100-fs duration at 625-nm wavelength, 82-MHz pulse repetition rate, and 10-mW power were generated from a colliding-pulse mode- locked (CPM) dye-laser system. The laser beam was split into a reference and signal beam by a glass slide. The reference beam was used to mark the zero time of the signal beam and monitor the intensity fluctuations of the laser pulse. The signal light was guided into and out of the medium using two 200-μm core diameter optical fibers with a numerical aperture (N.A.) in the medium of 0.287. Scattering samples suspended in water were placed in a transparent cylindrical tank of 100-mm diameter and 90-mm height. The input fiber was fixed at one of the walls of the tank; while, the detection fiber was mounted on a x-y-z translation stage and a rotational stage θ. The output of the detection fiber (scattered signal) as well as the reference beam were imaged into the input slit of a 10-ps resolution streak camera.

Polystyrene micro-spheres of three different diameters, (i) small d= 0.091-μm, (ii) medium d= 0.304-μm, (iii) large d= 1.11 -μm, were used individually in each scattering medium. The scattering concentrations used to obtain a 2-mm transport mean free path (l_t) for each sample are given in Ref. 3.5. The absorption length (l_a) of each medium was set to 300-mm by adding a small amount of absorbing dye (Malachite Green). The scattering mean free path (l_s) and scattering mean cosine factor (g) were 1.88-mm and

0.06. 0.62-mm and 0.69. 0.14-nm and 0.93 for small. medium. and large scatters sample. respectively.

The source-detector distance was varied from 1 l_t (2-mm) to 20 l_t (40-mm) in the launching direction (x- axis) and lateral direction (y-axis). At each distance. scattered pulse profiles of various angular orientations were measured for the forward and lateral direction. The detection angles around a fixed point were varied. Similar detection points in each media have been chosen along two directions: forward - along the light source launching direction, x-axis; and lateral or perpendicular direction. y-axis. for comparison. For 15 l_t (30-mm) the angular range on the forward direction (x-direction) was from 0_x° to 135° clockwise[3.6], and in the lateral direction (y-direction), it was from 0_y° to 40° clockwise and from 0_y° to 135° counter-clockwise for the three different media.

3.3 Results and Discussions

Figure 3.3 shows intensity temporal profiles for a source-detector separation of 15 l_t (30-mm) for small, medium and large scatterer size respectively. The inset in Fig. 3.3(a) shows the source-detector positions for the three different media (one in the forward direction and one in the lateral direction); in the forward direction. the fiber angular orientations were 0_x° and 90_x° (clockwise); for the lateral direction, the angular orientations were 0_y° and 90_y° (counter-clockwise). The common features of the data for the three media are: (a) Highest intensity temporal profile -for a fixed point- along the launching direction is localized at 0_x° detector angular orientation. (Profiles at 0_x° were

higher in intensity than any profile in the lateral direction). (b) In the lateral direction, the highest intensity temporal profile is at $0_y^{\circ} + \Delta\theta$ detector angular orientation.[3.7] (c) Intensity temporal profiles detected in the lateral direction randomized faster than the one in the forward or launching direction, for the three media. This can be better observed in Fig. 3.3(c) by comparing the two profiles in the y-direction vs. the two profiles in the x-direction. (d) Intensity peak time detection at 0_x° occurs at an earlier time than any other intensity peak with a different angular detector orientation for either the forward or lateral direction. See Figs. 3.3(a)—(c). (e) As the angle of rotation is increased away from maximum angles of detection (0_x° in the forward direction and $0_y^{\circ} + \Delta\theta$ in the lateral direction), the following features are observed: (1) the intensity temporal profile decreases, (2) the intensity peak time (τ_p) is delayed; and (3) there is an increase in time the full width at half-maximum (FWHM).

Observations mentioned above are enhanced when one compares profile 0_x^{o} versus that of 90_x^{o} or profile 0_x^{o} versus 90_y^{o} in Fig. 3.3 (c).

In addition to these observations, certain differences were encountered in the three scattering media: (a) The emergence of a strong ballistic light for the medium with smaller diameter particles was observed, see Fig. 3.3(a). This ballistic light appears on the forward direction on and about 0_x^{o}-degree detector angular orientation. Ballistic light was still visible at a distance of 20 l_t (40-mm) away from the source. No ballistic light was detected in the experiment for larger particles. (b) The intensity angular distribution is more uniform for the larger scatterers. In other words, peak intensity values at a fixed point in the forward and lateral direction become closer to each other in the medium of

larger scatters size than for the medium of a smaller scatters size. This is even more evident when we observed the two profiles at *(0,30,0)* vs. the two profiles at *(30,0,0)* in Fig. 3.3(c).

The degree of anisotropy is plotted in Figs. 3.4 (a). and (b) using the profiles shown in Fig. 3.3 (c), which correspond to the medium of larger scatters diameter (1.11-μm).

Curve A_{xx} in Fig. 3.4(a) shows the angular anisotropy between 0_x^o and 90_x^o in the forward direction as indicated by the inset *xx*, while curve A_{yy} shows the anisotropy between 0_y^o and 90_y^o in the lateral direction as indicated by the inset *yy*. The two profiles in Fig. 3.4(a) show a higher degree of anisotropy mainly in the first 500 ps. Curve A_{xx} becomes negative around 800 ps. This is because the intensity of the profile detected at 90_x^o is higher than the one detected at 0_x^o for 800 ps and later times. See Fig. 3.3(c). This flipping in intensity values occurring after 800 ps can be attributed to the isotropic behavior of light for late times that is when a higher amount of diffusive photons exist.

Profile A_{yy} becomes more uniform after the first 500 ps. This uniformity at an earlier time was expected since randomization occurs faster in the lateral direction than in the launching detection. See Fig. 3.3(c).

Fig. 3.4(b) shows the degree of spatial anisotropy A_{xy} between two equidistant spatial points from the source as indicated by the inset labeled *xy*. It was observed that the degree of anisotropy in profile A_{xy} is four times larger in the early portion (0.8) than in the tail (0.2). This can be explained since photons experience less scattering events in the early time.

3.4 Conclusion

Randomization of light going through a highly scattering medium after traveling 7 or more transport lengths was expected. However, we have observed that light retains a strong angular dependence for large r/l_t distances. In the three media under study, temporal profiles maintained a non-diffusive behavior even for distances as far as 15 l_t to 20 l_t. This is an indication that well-defined photon paths are preserved in the launching direction and that photon direction (momentum) is maintained even after light has traveled 20 l_t away from the source. It was also observed that key profile characteristics such as intensity, τ_p, snake light and FWHM are affected by the strong angular dependence on the scattered light. To describe the degree of anisotropy in photon distribution due to the source directionality, two new parameters were introduced: A_{xx} and A_{xy}. It was found that there is a higher degree of anisotropy in the early time where photons experience less scattering events. The anisotropy of photon migration provides additional data and may need to be taken into consideration in image reconstruction in optical tomography.

Establishing at which distance from the source total randomization of a pulse of light occurs is a key pre-requirement for the scientist to be able to accurately apply the diffusion approximation model. Measuring photon migration at a fixed point under various collection angles could help to determine where total randomization starts. The angular information of photons travelling through a fixed spatial position may help scientist in the future to predict photon transport with higher accuracy.

3.5 References

3.1 M. A. O'Leary, D. A. Boas, B. Chance, and A. G. Yodh, "Experimental images of heterogeneous turbid media by frequency-domain diffusing-photon tomography", Opt. Lett., 20,426-428, 1995

3.2 B. Chance, K. Kang, L. He, J. Weng, and E. Sevick, "Highly sensitive object location in tissue model with linear in-phase and anti-phase multi-element optical arrays in one and two dimensions", Proc. Natl. Acad. Sci., USA., 90, 3423-3427, 1993.

3.3 M. Miwa, Y. Ueda and B. Chance, "Development of time resolved spectroscopy system for quantitative non-invasive tissue measurement", SPIE, 2389, 142-149, 1995.

3.4 F. Liu, K. M. Yoo, and R. R. Alfano, "Should the photon flux or the photon density be used to described the temporal profiles of scattered ultrashort laser pulses in ransom media?", Opt. Lett., 18, 432-434, 1993.

3.5 The scattering concentrations used to obtained l_t= 2-mm and l_a= 300-mm in the three samples are:

i. For the small diameter scatters (d= 0.091-μm), we used 653.46 mL of water, 43.87 mL of the 10% concentration polystyrene micro-spheres emulsion, and 2.641 mL dye.

ii. For the medium diameter scatters (d= 0.304-μm), we used 680.162 mL of water, 18.41 mL of the 10% concentration polystyrene micro-spheres emulsion, and 1.428 mL dye.

iii. For the large diameter scatters (d= 1.11 -μm), we used 686.679 mL of water, 11.893 mL of the 10% concentration polystyrene micro-spheres emulsion, and 2.641 mL dye.

3.6 Counter-clockwise measurements were not recorded in the forward direction since there is symmetry along the launching direction.

3.7 $\Delta\theta$ (clockwise) is a small angle, which increased as S-D distance (r) increases. At large distances, It fades away.

3.6 Figures

Figure 3.1 S-D configuration arrangement for detecting photons passing through a fixed point in space, with different directions. The figure shows detection of photons arriving with different directions at a distance **r** away from the source, for two different spatial positions, one in the forward direction (r,0,0) and one in the lateral direction (0,r,0). The light intensity detected becomes a function of position, time, an angle of photon arrival or detection, that is $I(\mathbf{r},t,\theta)$. The diameter size of the polystyrene micro-spheres used in each medium was: (i) 0.091-μm, (ii) 0.304-μm, and (iii) 1.11 -μm.

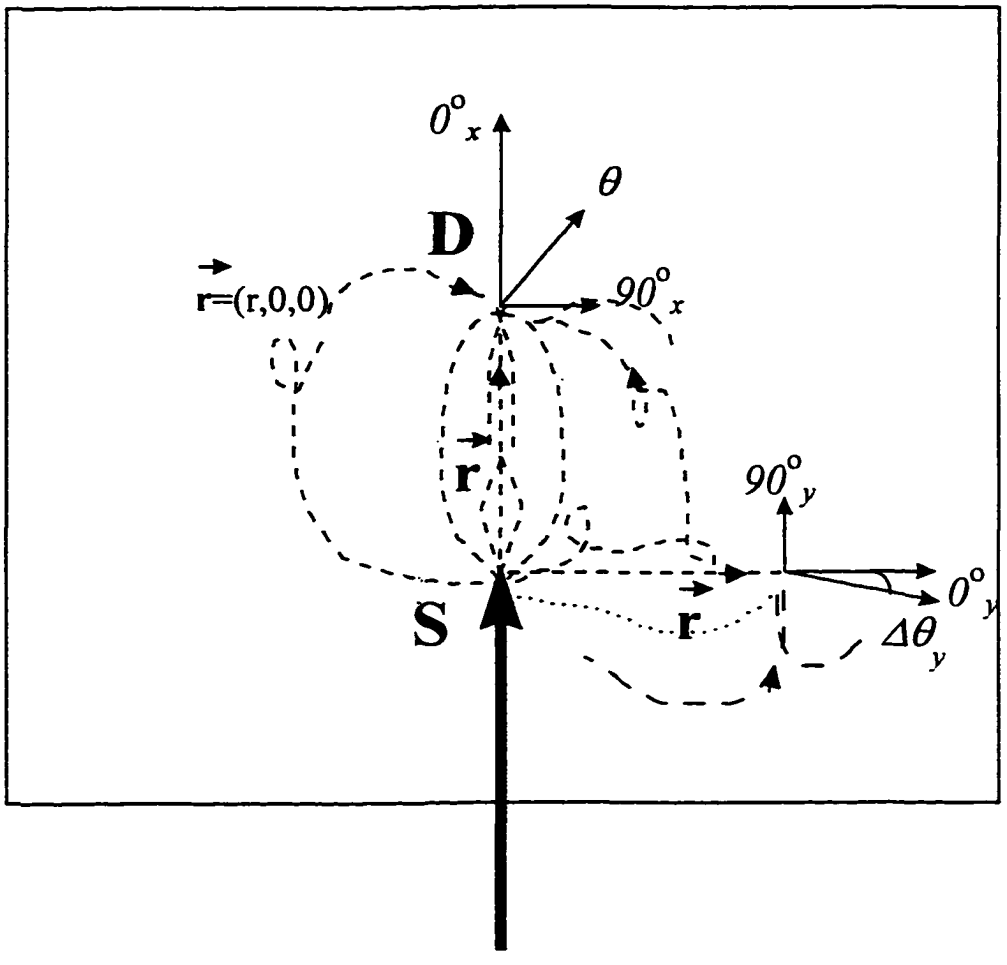

Fig. 3.2 Experimental setup. Ultrashort laser pulses of 100-fs duration at 625-nm wavelength, 82-MHz pulse repetition rate, and 10-mW power were generated from a colliding-pulse mode- locked (CPM) dye-laser system. The laser beam was split into a reference and signal beam by a glass slide. The signal light was guided into and out of the medium using two 200-μm core diameter optical fibers with a numerical aperture (N.A.) in the medium of 0.287. Scattering samples suspended in water were placed in a transparent cylindrical tank of 100-mm diameter and 90-mm height. The input fiber was fixed at one of the walls of the tank; while, the detection fiber was mounted on a x-y-z translation stage and a rotational stage θ. The output of the detection fiber (scattered signal) as well as the reference beam were imaged into the input slit of a 10-ps resolution streak camera.

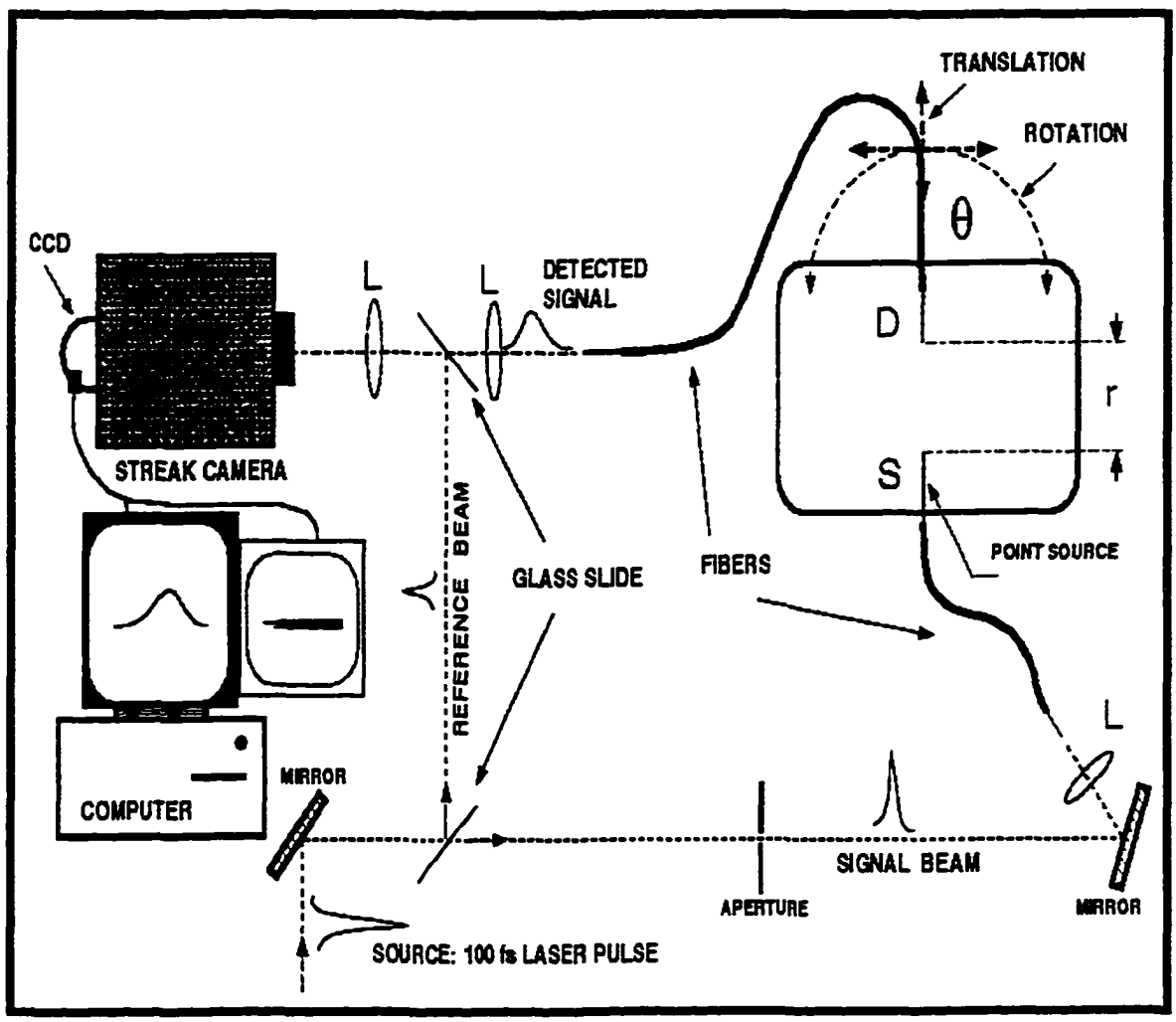

Fig. 3.3 Temporal intensity profiles for different collection angles obtained for a 30-mm S-D separation for three different media. In each medium, l_t and l_a was fixed to 2-mm and 300-mm, respectively. Profiles in 3.3(a) correspond to the small size scatters of diameter=0.091 μm; profiles in 3.3(b) correspond to the medium size scatters of diameter =0.304 μm; while profiles in 3.3(c) correspond to large size scatters of diameter=1.11 μm. The recorded intensity profiles has been labeled 0^o when the detector is facing the source. The subscripts x and y are to indicate measurements taken along the direction of propagation and in the lateral direction, respectively. Intensity temporal profiles labeled 90^o has been obtained by rotating the detector at a fixed spatial point 90^o. Each figure has four temporal profiles detected at 0_x^o, 90_x^o in the forward direction and 0_y^o and 90_y^o in the lateral direction. Inset in 3.3(a) shows the S-D positions and angles of detection of the plotted profiles for the three different media.

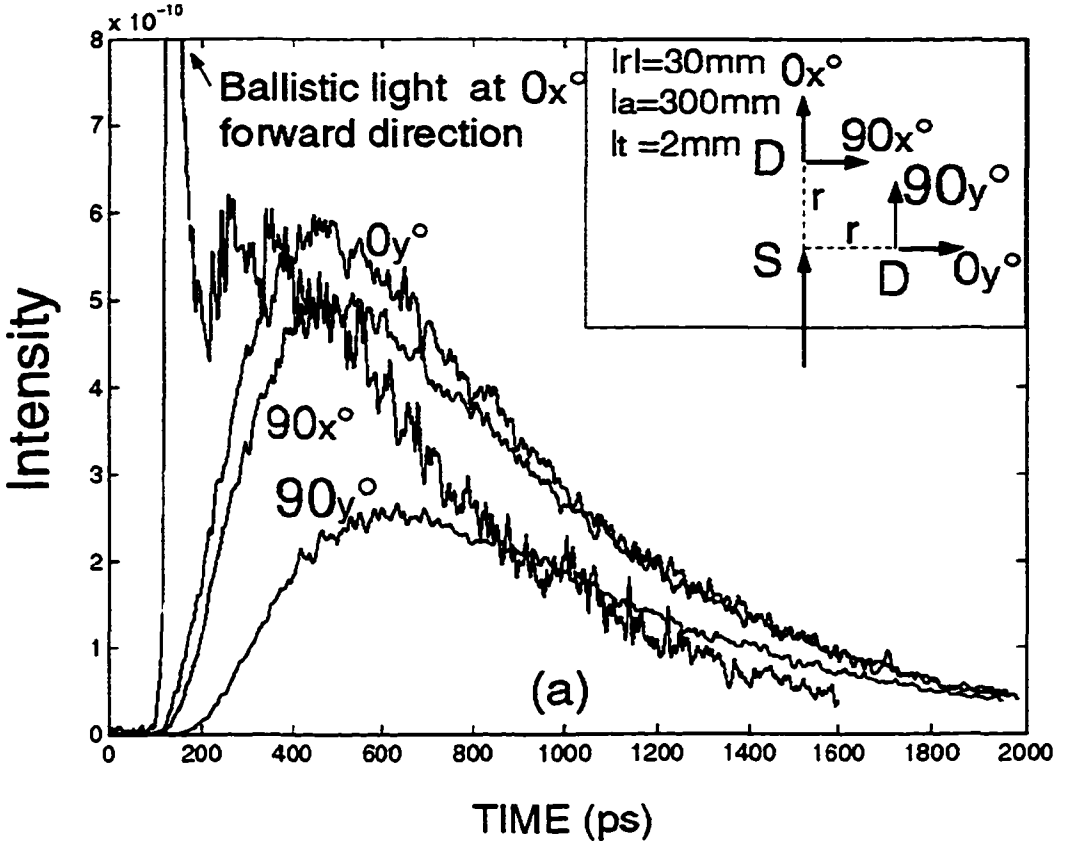

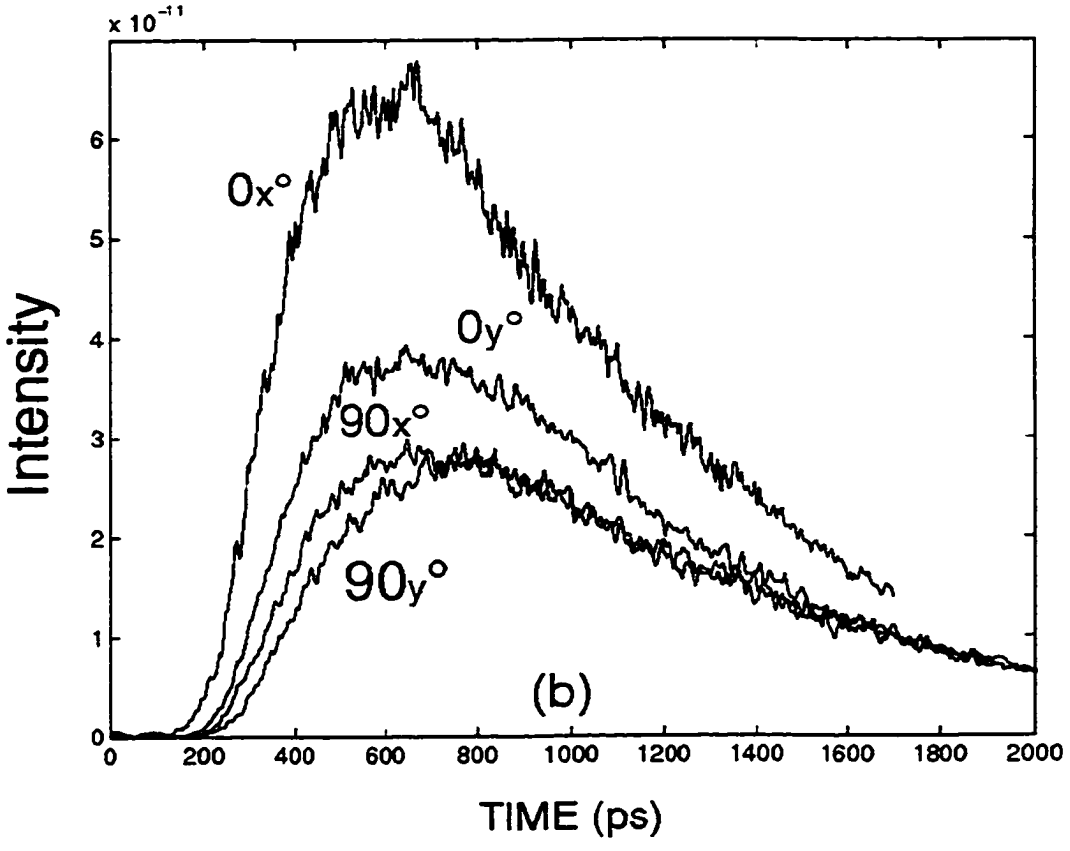

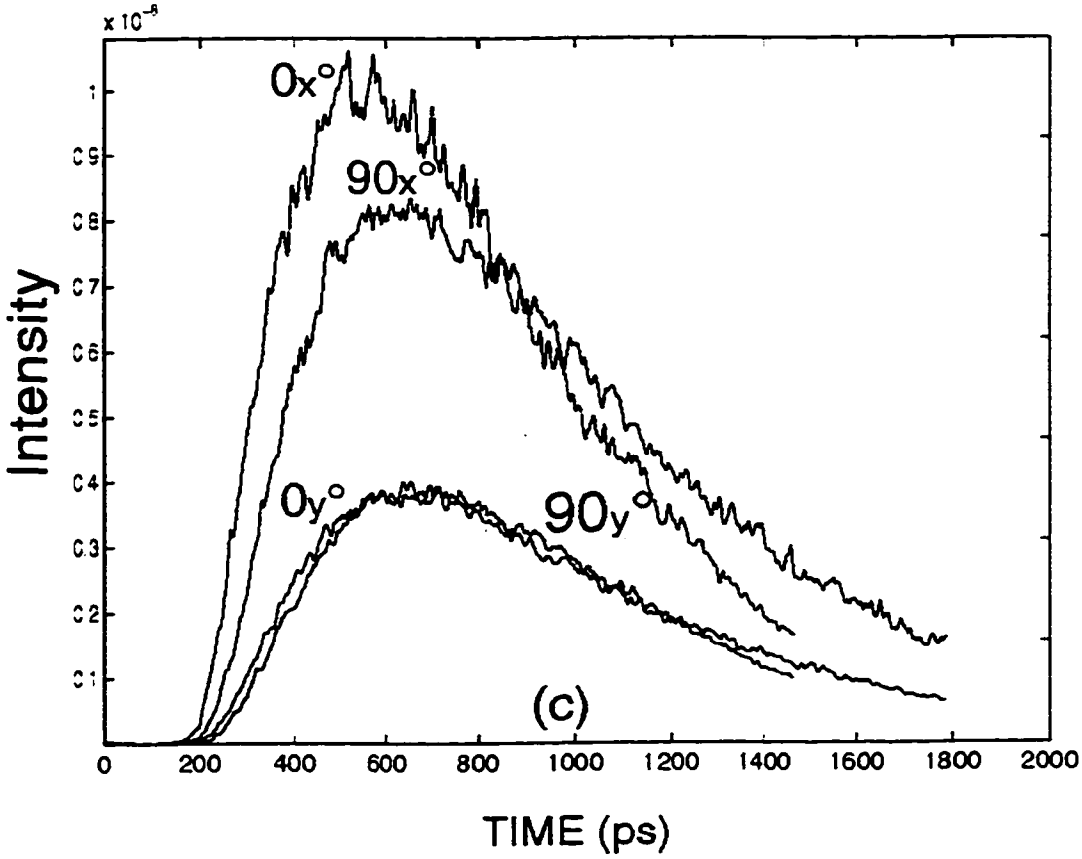

Figs. 3.4 Degree of anisotropy for profiles in figure 3.3(c). In Fig. 3.4(a), the degree of angular anisotropy at a point is plotted for a point along the launching direction A_{xx} and for a point in the lateral direction A_{yy}. The inset *xx* and the inset *yy* show the source-detector distance and angular orientations. Fig. 3.4(b) shows the degree of anisotropy A_{xy} in the medium. Inset *xy* shows the locations and angle of detection of the two chosen points.

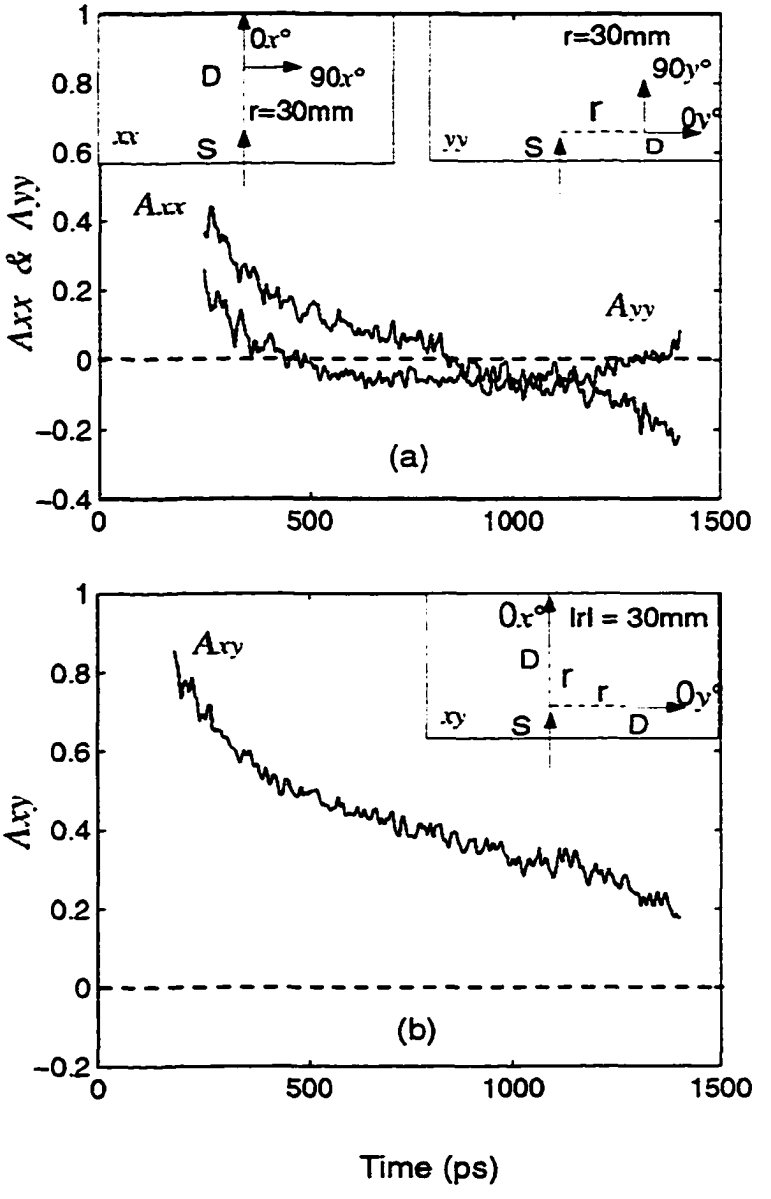

Chapter 4

Time-Resolved Photon Scattering Measurements from Scattering Media Fitted to Non-Euclidean and Conventional Diffusion Models

4.1 Introduction

As it was stated in Chapter 2, the radiative transfer Boltzmann equation can describe photon migration in a random medium; however, because of its complexity several approximations have been developed, such as the diffusion approximation (DA), the telegrapher's equation, and higher order approximations to Boltzmann equation.[4.1,4.2] These approximations with the help of fitting techniques have been used to determine the values of some key optical parameters that describe the scattering medium such as the transport mean free path (l_t) and the absorption length (l_a). Determination of these key optical parameters is important for predicting the photon temporal distribution at a fixed point inside a scattering medium or the photon spatial evolution between two or more different points. The limitations of the DA are its inaccuracy in predicting the intensity of early arriving light and the location of the maxima intensity peak position. This inaccuracy leads to a failure in fitting experimental intensity temporal profiles obtained in the *pre-diffusive regime* (distances $\leq 5 - 7\, l_t$ —transport mean free path— that is, 10 to 15 mm for human breast tissue in the near-infrared (NIR) region). The DA deficiency in predicting the nature of photon migration in a close spatial region has been shown in refs.

[4.3.4.4]. Further improvements in this onset regime should prove useful in the detection of hidden abnormalities in medical imaging and optical tomography. It is not the distance between source (S) and detector (D) that determines the applicability of DA in optical tomography, but the distance between hidden objects (tumour) and the source (or detector). In this context, Polishchuk, *et. al.*, recently introduced the non-Euclidean (NED) model[4.5,4.6] and in contrast to the DA offers an improvement in predicting photon transport in the pre-diffusive regime. Based on past experiments performed on different animal tissues, the transport mean free path (l_t) is about 2.5 mm at 625 nm, and ~5 mm in the NIR region.[4.7,4.8] The transport mean free path in human breast tissues is $l_t \sim 1$ mm in the visible region and, is expected to be more than twice that value by selecting the appropriate NIR wavelength. The S-D distances of 5 l_t and 15 l_t used for the measurements of this experiment correspond to typical distances between source/detectors and hidden inhomogeneities—such as tumours—located in the middle of a typical compressed human breast size of $\approx$ 60 mm or $30l_t$ under NIR light. Interesting tissue components of a human breast include adipose (fat), glandular, ducts, blood vessels, calcifications, and growths—each with different scattering properties.

In this chapter, theoretical predictions from the NED and the DA equations obtained for the pre-diffusive and diffusive regions are compared with the measured scattered light temporal profiles. The NED equation represents a bridge between the ballistic regime at small l_t distances and the diffusive regime at large l_t distances. At large times, for a fixed distance, the NED equation describes the diffusive regime and NED and DA approach each other.

4.2 DA and NED Models

DA Model

The photon number density function $N(t,\vec{r})$ is used to describe the temporal and spatial evolution of scattered photons originating instantaneously from a point-like collimated source and travelling in a highly forward-scattering medium. The photon number density profiles obtained from the NED and the DA equations for an infinite medium are compared in this paper with experimental profiles in time and space.

For the DA model the photon number density for an infinite medium is given by:[4.9,4.10]

$$N(t,\vec{r}) = \frac{1}{(4\pi)^{1/2}(Dt)^{1/2}} e^{\frac{-1}{4Dt}(\vec{r})^2} e^{-\nu_a t} \qquad (4.1)$$

where the source is assumed at the origin and ; $D \approx \frac{c}{3[(1-g)\mu_s]} = \frac{c\, l_t}{3}$. The term $(1\text{-}g)\mu_S = \mu'_S$ is the reduced scattering coefficient; c is the speed of light, and l_t is the transport mean free path. The last exponential decay term ($e^{-\nu_a t}$) is the absorption term that affects the pulse profiles, more strongly, at large times when $t > t_a = (\nu_a)^{-1}$. ν_a is defined as c/l_a. For this study, the absorption length in the media was fixed at $l_a = 300$ *mm* and the transport mean free path to $l_t = 2$ *mm*. The absorption dependence of D has been neglected since l_a is much larger than l_t. A problem of the absorption dependence of D was recently reconsidered in Ref. [4.2] and references therein.

NED Model

For the NED model, the photon number density is given by Polischuck as:[4,5,6,11]

$$N(t,\vec{r},\vec{s}_u)=\frac{1}{(4\pi)^{\frac{3}{2}}}\frac{1}{\sqrt{\det\Delta}}e^{\frac{-1}{4}\Delta^{-1}_{\alpha\beta}(r-r_c)_\alpha(r-r_c)_\beta}\quad e^{-\nu a t}. \tag{4.2}$$

where Δ is a 3 by 3 matrix and Δ^{-1} is its inverse. The exponential term, $\Delta^{-1}_{\alpha\beta}(r-r_c)_\alpha(r-r_c)_\beta$, indicates the summation of the multiplication of the components of the inverse matrix with the components of the vector difference $(\vec{r}-\vec{r}_c)$. The components of the Δ matrix as well as the components of the vector difference are indicated by the subscripts α and β which can take the numbers 1, 2, or 3. The components of the Δ matrix are given by

$$\Delta_{\alpha\beta}(t)=\frac{l_t^2}{2}\delta_{\alpha\beta}(\frac{2}{3}\tau-f_1+\frac{1}{9}f_3)+\frac{l_t^2}{2c^2}(s_u)_\alpha(s_u)_\beta(f_1-\frac{1}{3}f_3-f_1^2), \tag{4.3}$$

where $f_1=1-e^{-1\tau}$, $f_3=1-e^{-3\tau}$, $\tau=\frac{c\,t}{l_t}$, and $(s_u)_\alpha(s_u)_\beta$ is the multiplication of the components of the initial velocity propagation direction vector $\vec{s}_u$, which for our system is defined as (0,0,c). Notice that the multiplication $(s_u)_\alpha(s_u)_\beta$ will only survive for α and β equal to 3 for our particular experimental system, i. e. light propagation in the z-direction. On the other hand, $(r-r_c)_\alpha(r-r_c)_\beta$ indicates the multiplication of components of

the vector difference $(\vec{r}-\vec{r}_c)$. Here, $\vec{r}$ is the detector location or final photon trajectory detection position; $\vec{r}_c(t)$ is the position of the center of mass of the photon cloud and it is equal to $\vec{r}_c(t)=<\vec{r}(t)> = \vec{s}_o(\frac{l_t}{c})(1-e^{-\frac{ct}{l_t}})$. The symbol < > stands for the averaging over all trajectories with the same initial velocity propagation $\vec{s}_o$.

From Eq. (4.2), for small times $t<<(l_t / c)$ one has $\Delta_{\alpha\beta}\to 0$ and $N(t,\vec{r},\vec{s}_o)\to \delta(\vec{r}-\vec{s}_o t)$; the ballistic regime is recovered. On the other hand, for larger times $t>>(l_t / c)$, $\Delta_{\alpha\beta}\to \delta_{\alpha\beta}\frac{cl_t t}{3}=Dt$; the diffusion regime is attained and the solution for the NED equation $N(t,\vec{r},\vec{s}_o)$ approaches to the solution of the conventional DA. Note that the photon number density in Eqs. (4.1) and (4.2) are normalized to the initial number of photons in the pulse.

The time-resolved intensity profile from red scattered light was measured in the range 10—30 mm (5 to 15 l_t) for a calculated l_t = 2 mm value to check on the predictions of the NED-based Eq. (4.2) and the conventional DA Eq. (4.1). It should be noted that even at distances as large as 15 transport mean free paths (l_t) the photon number density predicted by the NED and by the conventional DA differ appreciably; see Ref. [4.5].

4.3 Experimental Method

The schematic diagram of the experimental setup is shown in Fig. 4.1. A laser of ultrashort pulses of 100 *fs* duration at 82 *MHz* pulse repetition rate and 10 *mW* with average power generated from a colliding-pulse mode-locked (CPM) dye-laser system was used to simulate an instantaneous point source. The wavelength of laser pulses was centered at 625 *nm*. The laser beam was split into a reference and signal beam by a glass slide. The reference beam was used to mark the arrival time of the signal beam and to normalize the intensity fluctuations of the laser. The signal beam was coupled into the medium using a 100 *mm* focal length lens and an optical fiber. A 10 *ps* resolution streak camera was used to measure the collected scattered pulse travelling inside the highly scattering medium.

The scattering media consisted of polystyrene micro-spheres and absorbing dye suspended in de-ionized water. The diameter of the polystyrene spheres was 1.11 μm. A scattering concentration (of polystyrene sphere) of 0.169% of the total volume was selected to ensure $l_t = 2.00 \pm 0.04$ *mm*. The absorption length was set to l_a = 300 *mm* by adding a calculated small amount of absorbing dye (Malachite Green) to the scattering medium. The scattering mean free path (l_s) and scattering mean cosine factor (g) were 0.144 and 0.926, respectively. The value of l_t was calculated on the basis of the Mie theory. For such a concentration of scattering particles l_t was experimentally shown to be proportional to the number density of scatters.[4.12] The scattering medium was placed in a transparent cylindrical tank of 100 *mm* in diameter and 100 *mm* in altitude.

To simulate a point source and a point detection, the signal light was guided into and out of the medium by means of two 200 μm core diameter optical fibers with a numerical aperture (N.A.) inside the medium of 0.287. These fibers represented the source (S) and detector (D). The input fiber (S) was fixed at one of the walls of the tank. The detector (D) was mounted on a *x-y-z* translational and angular (θ) rotational stage and positioned on the optical axis right across the source direction ($\bar{s}_o$). The translational stage was used to vary the source-detector distance r while the angular rotational stage was used to rotate the detector and collect the light arriving from different directions at a fixed point. The output of the detection fiber (scattered signal) was focused into the input slit of the streak camera.

Intensity temporal profiles $I(t,r,\bar{m},\bar{s}_o)$ were measured at various distances r and various angular orientations $\bar{m}$, where $\bar{m}$ is the orientation of the detecting fiber with respect to the propagation direction $\bar{s}_o$ [see inset in Fig. 4.2(a)].

The measured intensities are related to the photon specific number density $n(t,\bar{r},\bar{s},\bar{s}_o)$ by

$$I(t,r,\bar{m},\bar{s}_o) = \int d\bar{s}\ A(\bar{m},\bar{s})\ n(t,\bar{r},\bar{s},\bar{s}_o), \tag{4.4}$$

where $A(\bar{m},\bar{s})\ d\bar{s}$ is the ratio of the number of photons in a solid angle $d\bar{s}$ collected by the detector per unit time to the photon flux in the $\bar{s}$ direction. For additional information on the receiving cross sectional area for the receiver see Refs. [4.13—4.16].

The *angular-integrated intensity temporal profile* $I(t,\bar{r},\bar{s}_o)$ is represented as :

$$I(t,r,\bar{s}_o) = \int d\bar{m}\ I(t,r,\bar{m},\bar{s}_o) = \mathbf{W}\ N(t,\bar{r},\bar{s}_u) \tag{4.5}$$

where $\mathbf{W} = \tilde{A}\, c\, N_o$; N_o is the number of photons in the incident pulse and $\tilde{A} = \int d\bar{m}\ A(\bar{m},\bar{s})$ is a constant characterizing the effective fiber system receiving area.

The corresponding experimental temporal profiles detected with different angles of collection $\bar{m}$ at a fixed spatial point r were combined to obtain ***an angular-integrated intensity temporal profile,*** $I(t,\bar{r},\bar{s}_u)$. The procedure described above makes possible the comparison of the experimental angular-integrated intensity temporal profiles for a fixed distance r (presented in Fig. 4.2) with the theoretical result *predicted* by the NED and DA equations.

4.4 Experimental Results and Discussion

In this experiment, the source-detector distance was varied from 5 l_t to 15 l_t ; at each distance r, scattered pulse profiles $I(t,r,\bar{m},\bar{s}_o)$ of various angular orientations were measured. Figs. 4.2(a)—4.2(c) show intensity temporal profiles obtained for r = 5, 7.5, and 15 l_t respectively. Each temporal profile in Fig. 4.2 has been labelled with its respective angle of detection ($\bar{m}$). The inset in Fig. 4.2(a) shows a schematic of the source and detector position and angular orientations for a fixed distance r. These profiles were averaged to obtain $I(t,\bar{r},\bar{s}_u)$.

The salient features of profiles shown on Fig. 4.2(a) for 5 l_t are the following: (a) the highest-intensity temporal profiles for a point in space are localized along the launching direction and around the 0° detector angular orientation. (b) as the angle of rotation is increased away from the 0° collinear direction, the temporal profiles are affected and the following features are observed: (i) the intensity temporal profile decreases; (ii) the early light (snake light) and the time to reach the intensity peak (T_p) is delayed in time; (iii) there is an increased in the full width at half-maximum (FWHM) and the scattered pulse becomes broadened. These features were consistent for all distances in the range chosen for this study (5 l_t to 15 l_t) and can also be observed in Figs. 4.2(b) and 4.2(c). The strong angular and spatial dependence of photons travelling in a highly scattering medium in the forward direction (source launching direction) and lateral direction (perpendicular to source launching direction) have previously been mentioned in Ref. 4.17. In this work only light propagation in the forward direction was considered. In the near zone at a fixed distance r, the local scattered light intensity is strongly angular dependent. This local angular dependence (anisotropy) gradually decreases with *time* as a result of multiple scattering. For a *fixed point*, photon distribution in time becomes more isotropic as time passes; in addition, the intensity detected at a fixed point decays as we move away from the source. When comparing profile groups obtained at different distances, another important feature can also be observed: mainly, the striking difference due to the angle of detection dependence starts fading away as the source-detector distance is increased. It is clear that even at the distance 15 l_t the angular distribution of

light is still appreciably anisotropic. Note that almost isotropic angular distribution of photons is a necessary condition for the diffusion model to be valid.

The curves in Figs. 4.3(a) and 4.3(b) show the experimental angular-integrated intensity temporal profiles $I(t,\vec{r},\vec{s}_n)$ for $r=5\ l_t$ *and* $r=15\ l_t$ together with the ***normalized*** photon number density temporal profiles calculated using the NED and the ordinary diffusion approximation DA. The theoretical curves calculated for different distances r were normalized to the experimental peak intensity values obtained at each distance respectively. The *a priori* known optical parameters l_t and l_a used in the prediction of these theoretical curves were 2 *mm* and 300 *mm*, respectively. The curves predicted by the DA have been plotted using dashed lines, while the NED predictions use a smooth solid line. The difference in *shape accuracy* of the theoretical curves with respect to the experimental data is presented in Fig. 4.4(a). Although theoretical curves were normalized to experimental data, NED and DA predictions (profiles) still showed considerable differences for different distances, as is shown in Figs. 4.3(a) and 4.3(b). The experimental data favour more the curves predicted by the NED theory than the ones predicted by the DA. It should be emphasized once again that the theoretical curves plotted in Figs. 4.3(a) and 4.3(b) *do not use the best fitting parameter* approach; instead, we make use of the *a priori* known actual parameters (e.g., l_t =2 *mm* and l_a =300 *mm*) of the scattering medium to plot both theoretical curves.

Since the theoretical results were obtained for an infinite medium while the experiment was performed in a finite medium (e.g., a tank 100 mm in diameter), an estimated time (T_m) where the walls of the tank commence to affect the experimental

measurements was found to start at around 600 ps. We attribute the intensity mismatch of the experimental temporal profile with respect to the theoretical curves shown at the falling wing in Fig. 4.3b to the *boundary effects* (for $t > T_m$) since photons escaping through walls are equivalent to surface absorption. Therefore the region between 0 and 600 ps should be considered for the match with theory.

The fitting of the key parameters l_t and l_a of the experimental data obtained by both theories for different distances is displayed in Table I. The values in Table I correspond to the best fitting predicted by both theories while using the *least square curve fitting* technique.

Distance	NED best fitting parameters		DA best fitting parameters	
r (mm)	l_t (mm)	l_a (mm)	l_t (mm)	l_a (mm)
10	1.69	101.6	1.75	62.24
14	1.64	104.0	1.73	82.4
17	1.66	102.1	1.74	85.4
25	1.68	125.0	1.77	115.3
30	1.81	145.3	1.91	137.4

Table I. Best fitting values (l_t, l_a) to the measured temporal profiles for NED and DA for different distances r.

The best fitting parameter values from Table I are used to plot the theoretical intensity temporal profiles for the NED and the DA models for distances *r=10 mm and r=30 mm* and are compared to the experimental data in Figs. 4.3(c) and 4.3(d), respectively. The average value found through the best fitting approach for l_t and l_a is 1.7 and 115.6 for the NED and for the DA, 1.78 and 96.54, respectively.

Although the values obtained through fitting differ from the *a priori* known fixed values l_t =2 *mm* and l_a =300 *mm*, both theories could provide a good fit. Notice that, although fitted, l_a shows a strong dependence on distance especially for the DA. Table I

indicates that the simple two parameter fitting procedure may not be a correct way to obtain the l_t and l_a parameters since the values obtained differ significantly, given errors over 13% and 100% for l_t and l_a, respectively.

The relative error, deviation δ of normalized predicted theoretical curves $I_T(t)$ from experimental intensity temporal profiles $I_{expt}(t)$ was calculated for different distances r in order to have a feeling of the *shape accuracy* for both theories. The relative deviation was characterized by a parameter $\delta = 100\ ||I_T(t)-I_{expt}(t)||/||I_{expt}(t)||$ where $||I(t)|| = \sqrt{\int_0^{T_m} I^2(t)\,dt}$ is the L_2 norm of the Intensity function $I(t)$ defined on a segment $[0, T_m]$. Figure 4.4(a) shows a histogram plot of the relative deviation δ of both models using l_t =2 *mm* and l_a =300 *mm*. To avoid the boundary effects, the parameter δ was calculated using the first 600 ps of the experimental and theoretical profiles for distances r / l_t of 5, 7, 8.5, 12 and 15. It can be observed in this histogram that the relative deviation δ is bigger for the DA than for the NED mainly in the close region 5, 7, and 8.5 l_t. These results demonstrate that the NED describes the shape of the intensity temporal profiles of scattered light better than the DA does at different spatial positions.

The plot of the full width at half maximum (FWHM) of the experimental and theoretical temporal profiles for each distance (r / l_t) is shown in Fig. 4.4b. A large deviation arising from the boundary effects is observed in the FWHM for distances r / l_t =12.5 and 15. The theoretical FWHM values predicted by the NED model were found to be closer to the experimental results than those predicted by the DA.

The plot in Fig. 4.4(c) shows the time peak (T_p) corresponding to the maxima intensity temporal position for different distances r for both models NED and DA, and for the experimental results. It could be observed that the T_p values for the DA model are further apart from the experimental values than the ones obtained by the NED model. This time peak shift in the DA profiles has been observed before and addressed in Refs. [4.3,4.4]. *The main advantage of the NED versus the DA model is that the NED model can describe with greater accuracy the transition between ballistic and developed diffusion regimes, e.g., that it is where the DA starts to fail.*

To determine the accuracy of both models when only one parameter l_a or l_t is known in advance, the standard best fitting approach has been used to calculate one of these optical parameters while the other one has been kept fixed. The results are given in Table II-a. The parameters l_t' obtained as a result of fitting the NED and DA to the experimental data taken at different distances from the source (r) holding the *a priori* known value of l_a fixed (e.g., equal to 300 *mm*) are plotted in Fig. 4.5(a). This figure shows the variation of the fitted value l_t' with respect to *a priori* calculated l_t value (e.g., equal to 2 *mm*) given by the NED and the DA theory for different distances. The fitted l_t' values predicted by the NED and DA are plotted using stars (*) and circles (o), respectively, and are connected with solid lines, while the *a priori* l_t constant known value has been plotted using plus signs (+) and are connected by dashed lines. The mean transport length values predicted by the DA show a higher deviation than those predicted by the NED. The variation of error (e) to the fitted parameter l_t' with respect to l_t = 2mm

has also been tabulated in Table II-a and ranges from 0.5% to 4.5% for the NED model and from 4.0% to 24.5% for the DA model.

Distance	NED best l_t' fitting parameter			DA best l_t' fitting parameter		
r (mm)	l_t' *(mm)*	l_a *(mm)*	$e = \frac{\lvert 2 - l_t' \rvert}{2} * 100$	l_t' *(mm)*	l_a *(mm)*	$e = \frac{\lvert 2 - l_t' \rvert}{2} * 100$
10	1.96	300	2.0 %	2.49	300	**24.5 %**
14	1.93	300	3.5 %	2.25	300	12.5 %
17	1.99	300	**0.5 %**	2.26	300	13.0 %
25	1.91	300	**4.5 %**	2.08	300	**4.0 %**
30	1.98	300	1.0 %	2.12	300	6.0 %

Table IIa. Best fitting values (l_t') and respective errors (e) for NED and DA obtained by keeping fixed the *a priori* known parameter l_a =300 *mm* fixed for different distances *r*.

In a similar manner, Table II-b shows the best fit for l_a' obtained by both models for different distances while keeping fixed the *a priori* calculated l_t value equal to 2 *mm*.

Distance	NED best l_a' fitting parameter			DA best l_a' fitting parameter		
r (mm)	fixed l_t *(mm)*	l_a' *(mm)*	$e = \frac{\lvert 300 - l_a' \rvert}{300} * 100$	fixed l_t *(mm)*	l_a' *(mm)*	$e = \frac{\lvert 300 - l_a' \rvert}{300} * 100$
10	2.0	223.8	25.4 %	2.0	80.0	**73.3 %**
14	2.0	252.5	15.8 %	2.0	119.0	60.3 %
17	2.0	223.0	25.6 %	2.0	122.0	59.3 %
25	2.0	392.0	**30.6 %**	2.0	190.2	**36.6 %**
30	2.0	281.8	**6.0 %**	2.0	167.7	44.1 %

Table II-b. Best fitting values (l_a') and respective errors (e) for NED and DA obtained by keeping fixed the *a priori* known parameter l_t = 2 *mm* fixed for different distances *r*.

The error given by fitting the absorption length l_a' with respect to l_a =300 *mm* has been tabulated in Table II-b. Figure 4.5(b) depicts the results of Table II-b. Once again the

predicted l_a values obtained by the NED and DA are plotted using stars (*) and circles (o), respectively, and are connected with solid lines, while the *a priori* l_a constant known value has been plotted using plus signs (+) and are connected by dash lines. Notice that the *margin of error* for l_a is *below 30.6 %* for the NED and *above 36.6 %* for the DA model with respect to the *a priori fixed and constant known value* l_a =300 *mm*.

Figures 4.5(a), 4.5(b) show that, when a parameter l_t or l_a is *a priori* known, the NED model will predict with a considerably higher accuracy the unknown parameter values (l_a or l_t) than the DA at any distance in the pre-diffuse regime.

In Figs. 4.3 and 4.4, we have compared to the experimental data only the *shape* of the *normalized theoretical curves* predicted by both models which correspond to the *photon temporal distribution at fixed distances*. To make a fair comparison between the two theories and the experiment, one needs to observe not only the prediction of *the temporal evolution of local photons (i.e., distribution of photons in time at a fixed distance r)* but also the consistency in predicting *the spatial-temporal distribution of scattered light at different distances*. On the other hand, an absolute direct comparison of the intensities calculated and measured at different spatial locations is difficult since the effective receiving cross section $\bar{A}$ and the number N_o of the initially launched photons have not been measured in the experiment (see also the respective discussion below). A relative comparison at different distances r does provide critical information regarding the capabilities of the NED and DA in describing *the scattered light distribution in space and time*. Intensity peak ratios $I_{peak}(r, T_P) / I_{peak}(15l_t, T_P)$ obtained from the experimental

profiles and both theories have been plotted in Fig. 4.6 for different distances r. The experimental values in Fig. 4.6 are connected with a solid line while the ones obtained by both theories are connected with dashed and smooth solid lines. The intensity ratios in Fig. 4.6 provide insight into the consistency and accuracy of both theories in predicting intensity values at different spatial locations. Looking at the intensity ratios predicted by both theories, one could observe a larger deviation for the DA with respect to the experimental values in the close region (below $10\ l_t$) as expected. This figure mainly demonstrates that the spatial distribution of scattered light intensity is better described by the NED than by the DA.

A similar comparison could be done by using the absolute intensity values predicted by each theory. In order to do this, one needs to use directly the experimental intensity values $I_{expt}(t,\vec{r},\vec{s}_0)$ and compare them independently to the intensity values predicted by both theories ($I_{NED}(t,\vec{r},\vec{s}_0), I_{DA}(t,\vec{r})$), ***in time and space***. Although the parameters $\tilde{A}$ and N_o are *a priori* unknown, we may use fitting of either theories to the experimental data to determine an intensity normalization factor $\mathbf{W} = \tilde{A}\ \mathrm{c}\ N_o$. Since the photon number density values of both theories differ from each other the factor $\mathbf{W}$ will be individual for each theory; however, for a consistent theory $\mathbf{W}$ should be the same when comparing theoretical and experimental intensities at different times and distances. Since the NED and DA models approach each other at large l_t distances and at large times, we have picked $\mathbf{W}$ from the experimental intensity temporal profile at $r = 15\ l_t$ (the furthest distance in our experiment) and at $t = 600\ ps$ (later times are strongly subject to

our boundaries constraints). We calculate W for each theory as follows: for the NED theory $W_{NED} = \frac{I_{expt}(t=600,\vec{r}=30,\vec{s}_0)}{N_{NED}(t=600,\vec{r}=30,\vec{s}_0)}$, and for the DA theory $W_{DA} = \frac{I_{expt}(t=600,\vec{r}=30,\vec{s}_0)}{N_{DA}(t=600,\vec{r}=30)}$.

The values found for W_{NED} and W_{DA} were 0.0405 and 0.0545, respectively.

The plots in Figs. 4.7(a) and 4.7(b) show the experimental profiles obtained at r = 10 mm and r = 30 mm (*e.g., 5 l_t and 15 l_t*) compared with two theoretical curves—$I_{NED}(t,\vec{r},\vec{s}_0) = W_{NED}\ N_{NED}(t,\vec{r},\vec{s}_0)$ and $I_{DA}(t,\vec{r}) = W_{DA}\ N_{DA}(t,\vec{r})$—obtained after the introduction of the intensity weight factors W_{NED} and W_{DA} at t=*600 ps* and r = 30 mm. In these figures, the *a priori* known values l_t =2*mm* and l_a =300 *mm* have been used. At t=*600 ps*, an exact matching in intensities for both theories and experiment is observed in Fig. 4.7(b). This matching is a result of the individual intensity factors (W_{NED} and W_{DA}) introduced by each theory. In the same plot [Fig. 4.7(b)] for t<*600*, the intensity values at different times for the NED model are in better agreement with the experimental intensity values than those for the DA model. This asymptotic intensity matching should be consistent at shorter distances. Indeed, the NED is shown to be in better agreement to the experimental intensity values than the DA at these distances—see Fig. 4.7a. The agreement of the intensities predicted in the pre-diffusive regime by the NED at different time and at different spatial positions is shown to be more consistent than intensity values predicted by the DA. In fact, intensity peak values predicted by DA at short distances ($r \leq$ *10 l_t*) are underestimated by about 40% with respect to the experimental values. It should also be mentioned that choosing a bigger W_{DA} value (in order to have a better intensity match at 5 l_t) will overestimate the intensity values obtained at 15 l_t and beyond.

The factor obtained by W_{NED} is considered to be a more reliable value since it is shown to be more consistent with the experimental results at different times and distances as shown in Figs. 4.7(a) and 4.7(b). In order to have a direct comparison of both theories and experimental results, we have plotted in Figs. 4.8(a) and 4.8(b) the intensity predicted by each theory using a common factor ($W = W_{NED}$) as well as the profiles obtained experimentally for distances *5 lt and 15 lt* , respectively. Performing a direct comparison of the two theories under a common factor W clearly shows appreciable intensity differences between them. These differences are observed in the peak intensity values as well as in time peak positions (T_{peak}). Fig. 4.8(a) shows a 46.4% peak intensity difference between the two theories plus a delay in time of *18 ps* for the DA. Fig. 4.8(b) shows a 22.88% peak intensity difference between the two theories and a delay in time of *60 ps* for the DA. The intensity difference of the two theories decreased for large *lt* distances as expected since the NED model takes the form of the DA. Also in Fig. 4.8, the DA model can be compared to the experimental results. Here it could be observed a complete intensity mismatch of the DA with respect to the experimental results at different times and distances. Asymptotic comparison of intensities in time of the two theories for different distances (spatial locations) with respect to experimental values is essential and provides a better description of the capabilities of both theories. *The NED model in contrast to the DA showed a satisfactory and consistent description of scattered light intensity at most distances and times.*

4.5 Conclusion

In conclusion. I have demonstrated by a comparative study that the NED model provides a better description of the temporal and spatial evolution of scattered light than the DA does without taking boundary conditions into account. Appreciable differences between the NED and DA were observed for photon number density for distances as large as 10 to 15 l_t. Even larger differences are expected for specific number density. The NED approach may be considered as a possible alternative to the DA in future optical imaging algorithms. It is worth mentioning here that the good agreement with the experimental data reported in this paper by the NED in the pre-diffusive regime (short range) makes it a good candidate to become a mathematical basis for the non-stationary LIDAR equation.

4.6 References.

4.1 P. M. Morse. and H. Feshbach. Methods of Theoretical Physics. (McGraw-Hill Book Co., Part 1, 865. 1953).

4.2 A. Ya. Polishchuk. S. Gutman. M. Lax, and R. R. Alfano. J. Opt. Soc. Am. A. 14. 230. 1997.

4.3 K. M. Yoo, Feng Liu, and R. R. Alfano. Phys. Rev. Lett.. 64. 2647. 1990.

4.4 K. M. Yoo, Feng Liu, and R. R. Alfano, SPIE Proceedings on Time-Resolved Laser Spectroscopy in Biochemistry II, 1204. 492, 1990.

4.5 A. Ya Polishchuk and R.R. Alfano, Optics Letters, 21. 916. 1996.

4.6 A. Ya. Polishchuk, M. E. Zevallos, F. Liu. and R. R. Alfano, Phys. Rev. E. 53. 5523. 1996.

4.7 K. M. Yoo, B. B. Das. F. Liu, and R. R. Alfano. Medical Optical Tomography. SPIE. IS11, G. Muller (ed.), 425, 1993.

4.8 F. Liu, K. M. Yoo, and R. R. Alfano, OSA Proceedings on Advances in Optical Imaging and Photon Migration, R. R. Alfano (ed.). 21, 170, 1994.

4.9 Samuel Glasstone and Milton C. Edlund, The Elements of Nuclear Reactor Theory. (D. Van Nostrand Company, Inc., New York, 174-180, 1952).

4.10 Enrico Fermi, Nuclear Physics, Course Notes Compiled by Jay Orear, A. H. Rosenfeld, and R. A. Schluter, (The University of Chicago Press, Chicago, 187-189, 1950.

4.11 A. Ya Polishchuk, "A solution to the non-Euclidean diffusion equation for photon migration in random media," unpublished, records on IUSL Department at CCNY.

4.12 G.H. Watson, S. L. McCall, P. A. Fleury, and K. B. Lyons, Phys. Rev. B, 41, 10947, 1990.

4.13 A. Ishimaru, Wave Propagation and Scattering in Random Media, (Academic Press, New York, 1978).

4.14 John Gowar, Optical Communication Systems, (Second Edition, Prentice Hall, New York, 34-36 and 337-338, 1994).

4.15 Leo Levi, Applied Optics, (John Wiley & Sons, Inc., New York, 2, 231-233, 1996).

4.16 John R. Taylor, Scattering Theory: the quantum theory of nonrelativistic collisions, (John Wiley & Sons, Inc., New York, 44-51, 1972)

4.17 M. E. Zevallos, F. Liu, B. B. Das, A. Ya Polischuck, and R. R. Alfano, OSA Trends in Optics and Photonics on Advances in Optical Imaging and Photon Migration, R. R. Alfano and James G. Fujimoto, eds., Vol. II, 21-24, 1996.

4.7 Figures

Fig. 4.1 Schematic diagram of the experimental setup.

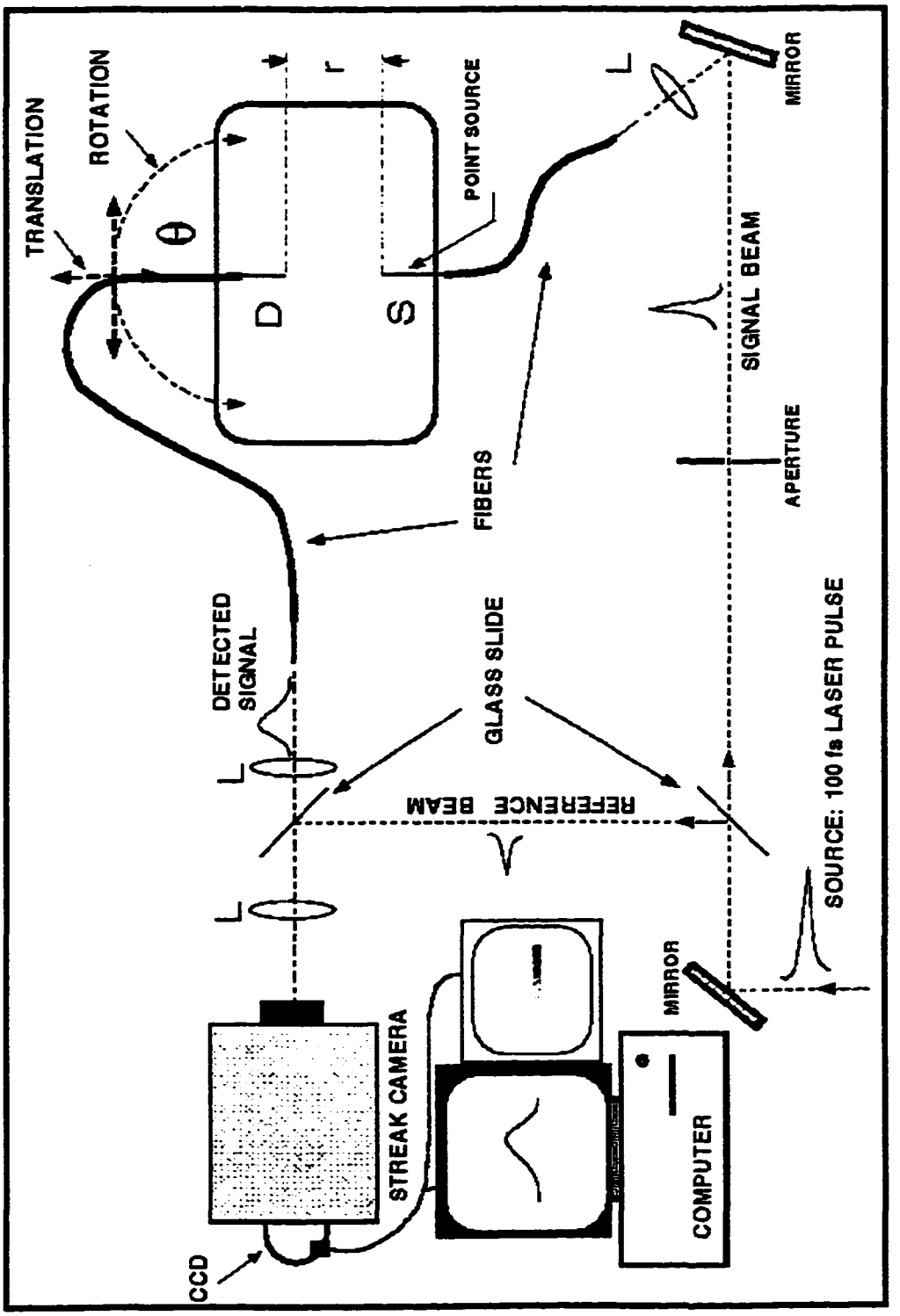

Fig. 4.2 Scattered light intensity temporal profiles measured at various distances for different detection angles. The medium optical parameters are: l_t = 2.00 ± 0.04 *mm* and l_a = 300 *mm*. The inset shows a schematic of the source and detector angular positions. The point of detection was situated along the pulse launching direction. The plots in (a)—(c) show the measurements obtained at distances $r=5l_t$, $7l_t$, and $15l_t$, respectively, for various detection angles.

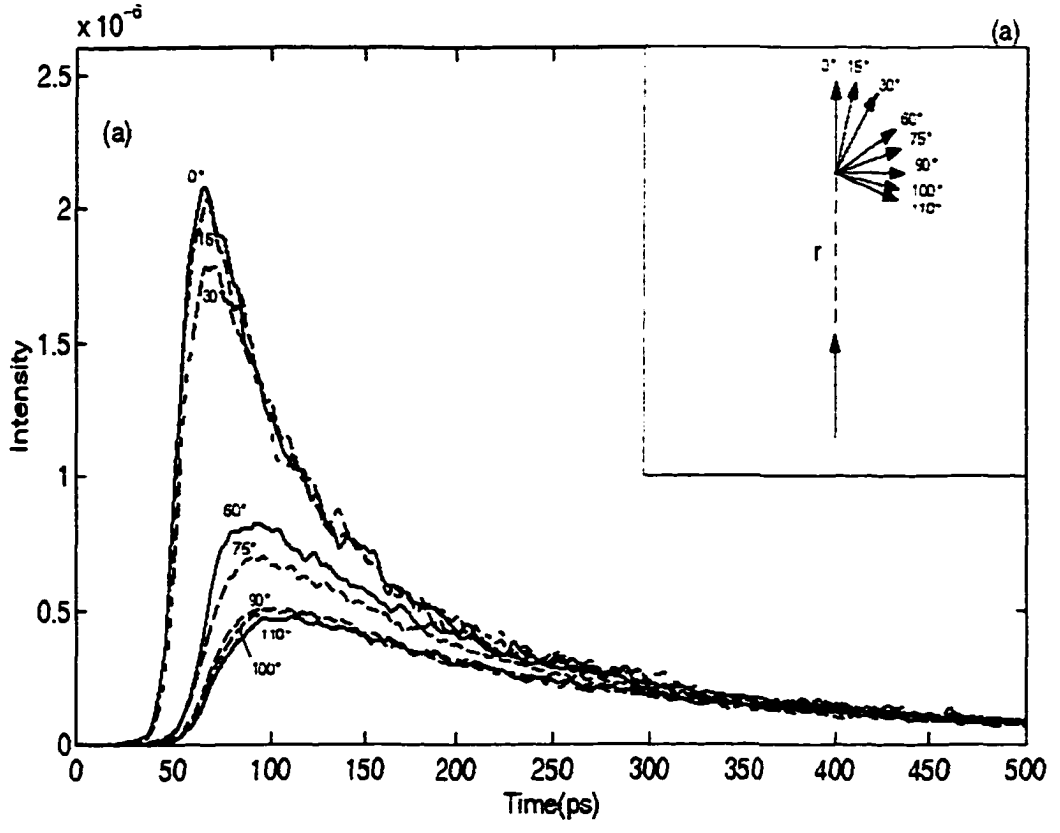

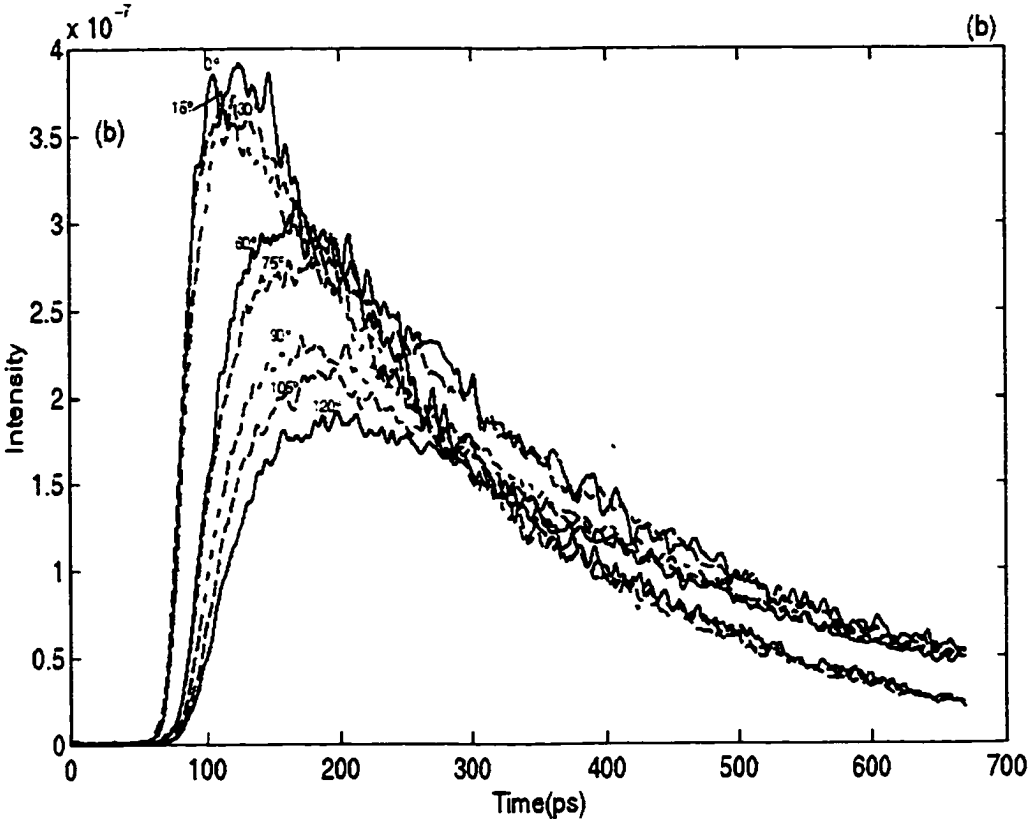

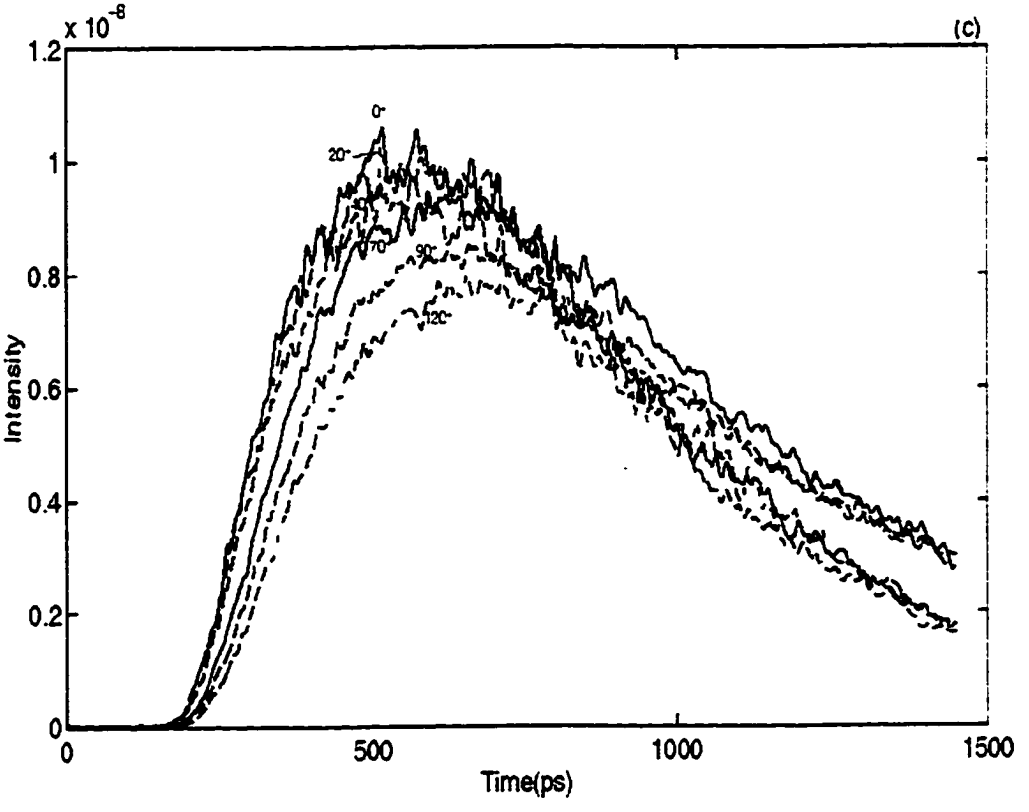

Fig. 4.3 Angle averaged scattered light intensity temporal profiles measured and calculated using the NED and DA at r=5l_t and r=15l_t. In (a) and (b). the theoretical intensity temporal profiles for both models are calculated using the *a priori* known optical parameters l_t = 2.00 *mm* and l_a = 300 *mm*. in (c) and (d) the theoretical profiles use the best fit optical parameters calculated in Table I using the best fit approach.

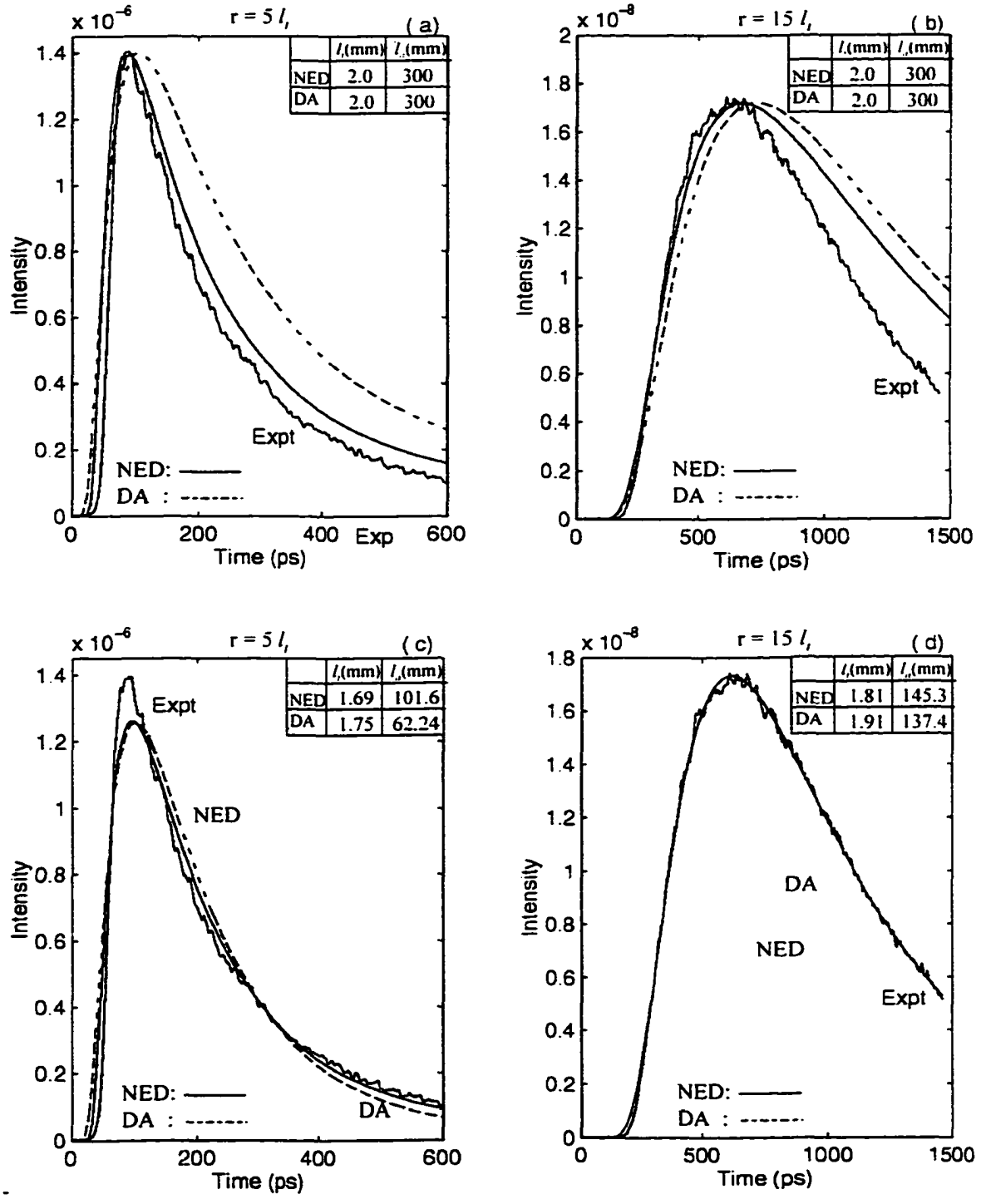

Fig. 4.4 General properties of scattered intensity temporal profiles predictions. (a) relative deviation δ (see text) of theoretical curves from an experimental intensity temporal profiles for the NED (open rectangles) and DA (filled rectangles) at various distances from the source: (b) FWHM for the calculated and measured temporal profiles: and (c) Temporal position of the peak of the scattered light intensity vs. source-detector distance.

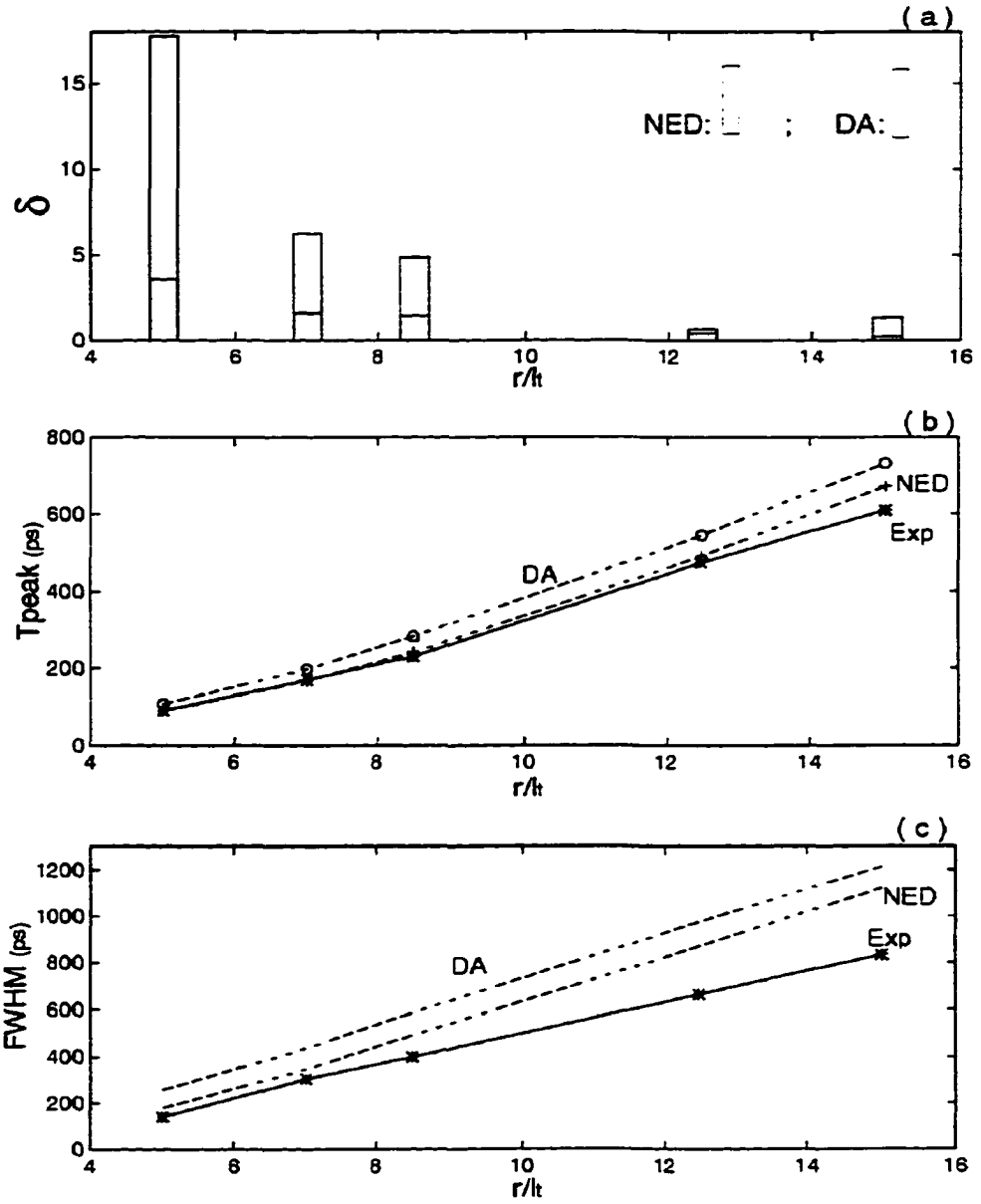

Fig. 4.5 Best fit optical parameters retrieved from the scattered light intensity measurements at different distances using the NED and DA theories. The dashed line represents *a priori* known values l_t = 2.00 *mm* and l_a = 300 *mm*. See text for more details. In figure (a), *a priori* known value l_a is kept fixed to 300mm while obtaining l_t best fits; In figure (b) *a priori* known value l_t is kept fixed at 2 mm while obtaining l_a best fits.

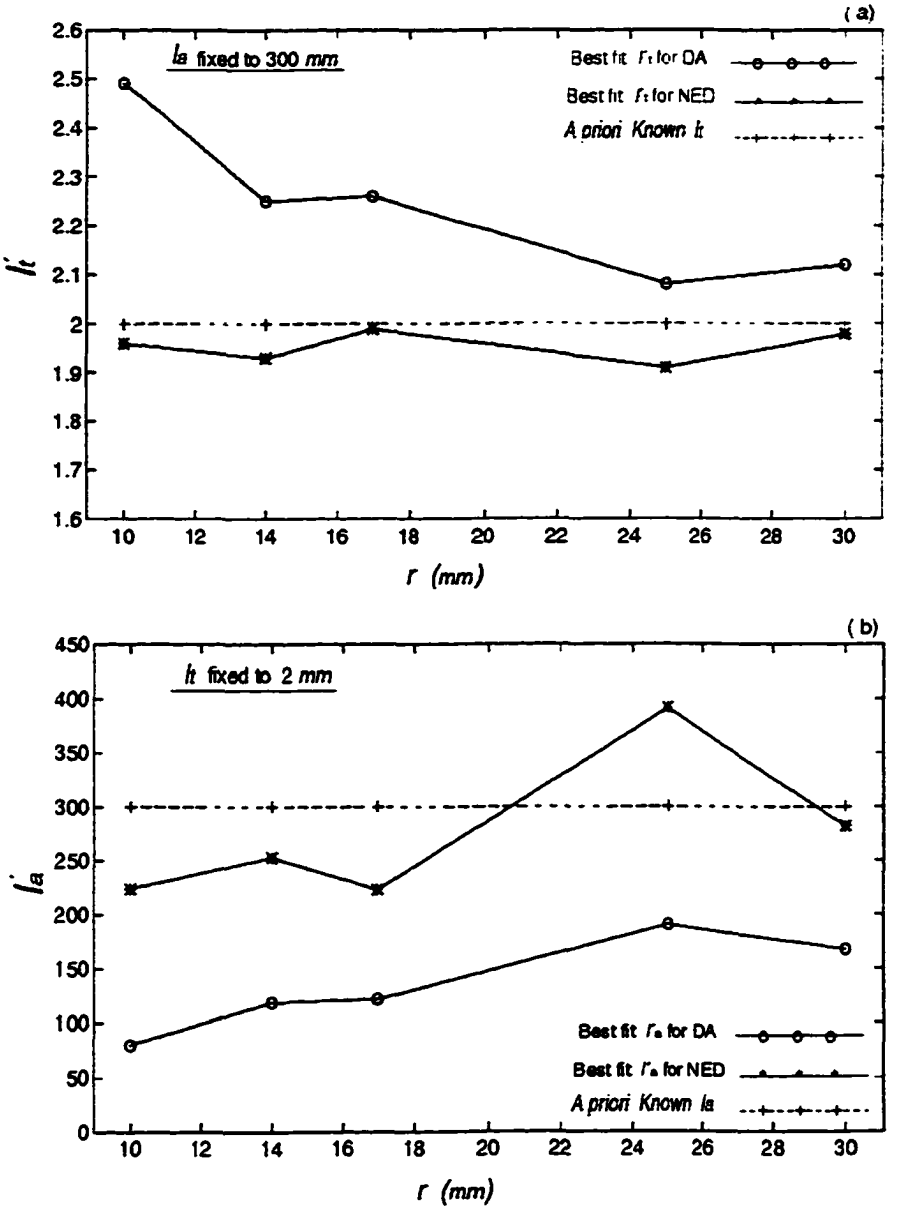

Fig. 4.6 Relative peak intensity ratios vs. source-detector distance. Peak intensity values were obtained from experimental and theoretical profiles at the peak time (T_p). The peak intensity ratio was taken for different distances r with respect to the individual peak intensity values obtained experimentally and theoretically at $r=15\ l_t$ as follows: $I'_{expt} = I_{expt}(r, T_p) / I_{expt}(15l_t, T_p)$. $I'_{DA} = I_{DA}(r, T_p) / I_{DA}(15l_t, T_p)$. and $I'_{NED} = I_{NED}(r, T_p) / I_{NED}(15l_t, T_p)$.

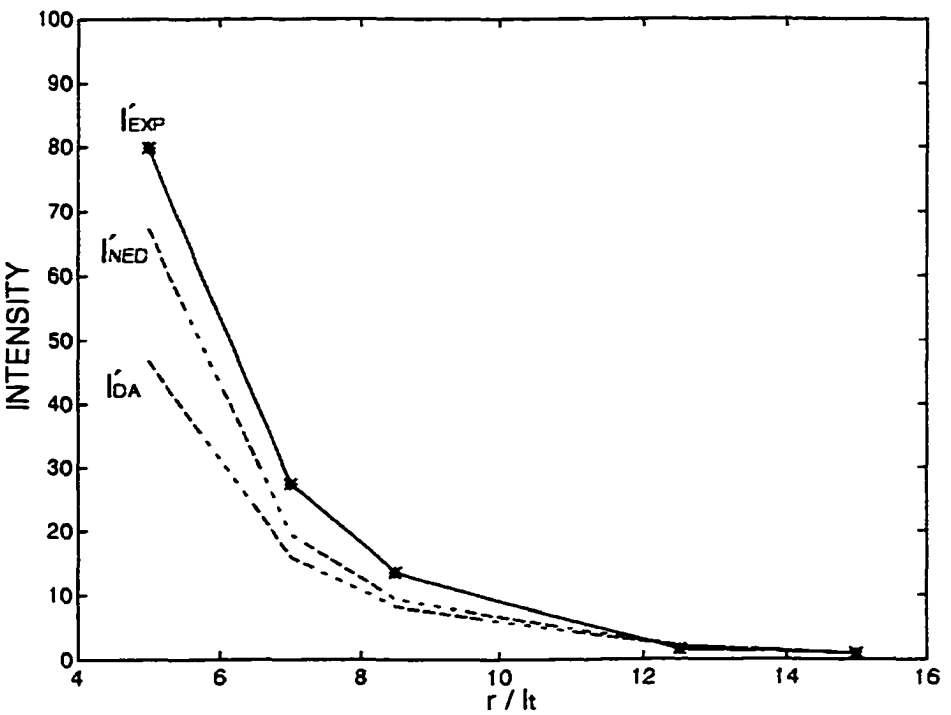

Fig. 4.7 Experimental scattered light intensity temporal profiles and theoretical profiles calculated using the NED and DA after the introduction of individual normalization factors W_{NED} and W_{DA} obtained at $r=15\ l_t$ and at $t=600\ ps$. See text for more details. The medium parameters are $l_t = 2.00 \pm 0.04\ mm$ and $l_a = 300\ mm$. Plots in figures (a) and (b) were measured and calculated at $r=5\ l_t$ and at $r=15\ l_t$, respectively.

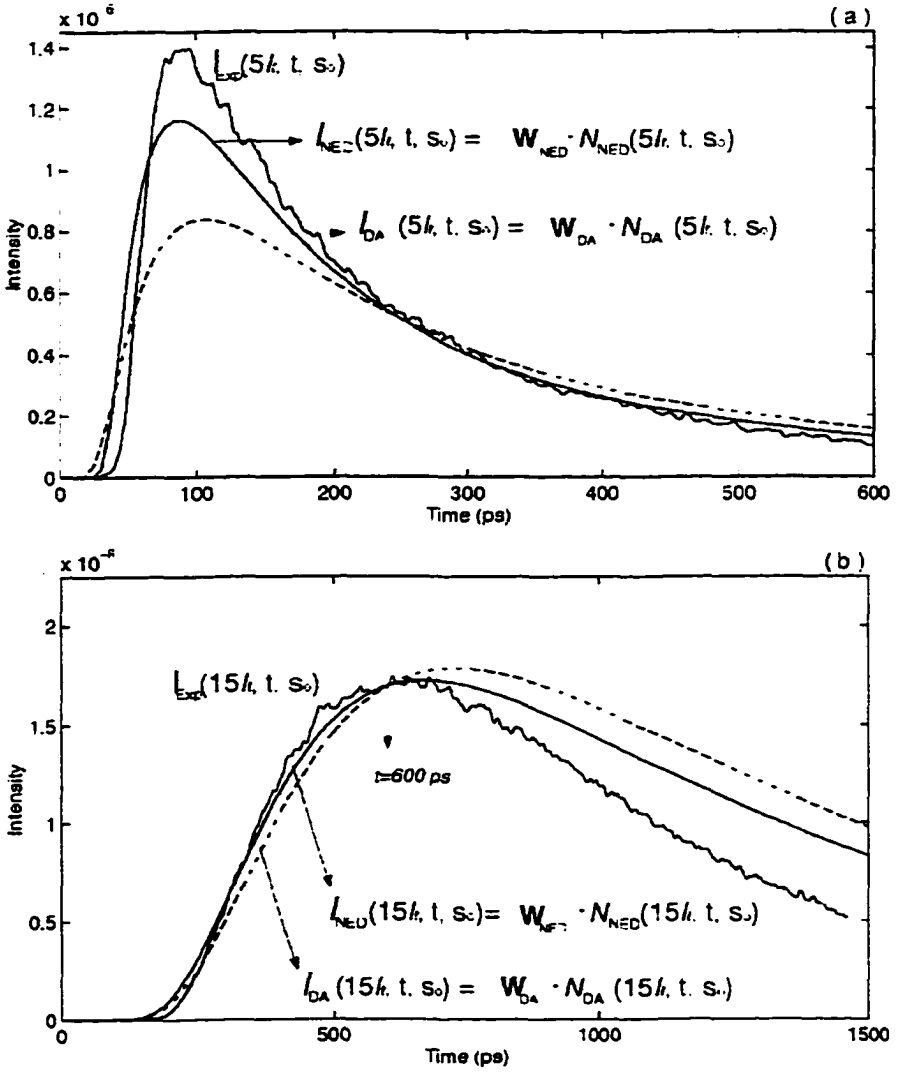

Fig. 4.8 Direct comparison of both models using a common weight factor $W=0.0405$. The medium parameters are $l_t = 2.00 \pm 0.04$ *mm* and $l_a = 300$ *mm*. Plots in figures (a) and (b) were measured and calculated at $r= 5\ l_t$ and at $r=15\ l_t$, respectively.

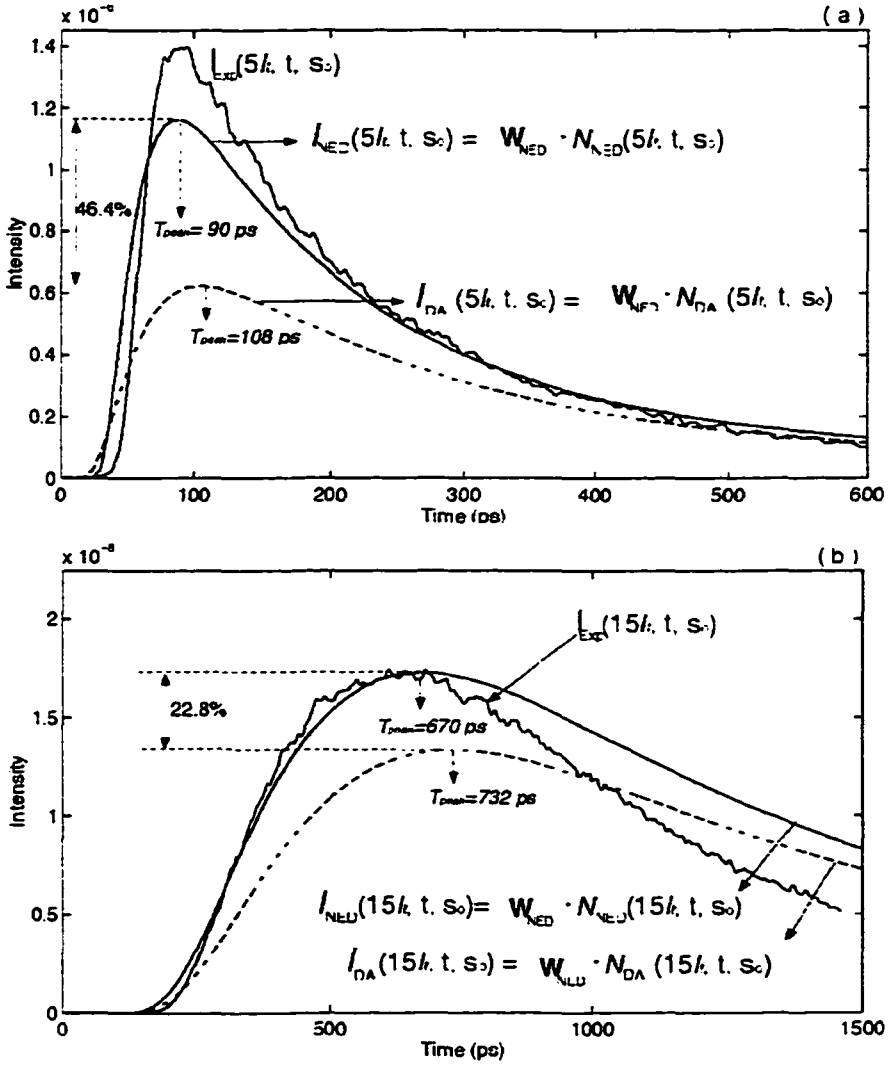

Chapter 5

Light Propagation in Biological Media With Definite Internal Structure

5.1 Introduction

In this section, tissue structure is shown to affect the transmission of linearly polarized light. Light propagating in a quasi-orderly, highly scattering/absorbing tissue media is investigated. Understanding how light propagates in media with definite internal structure such as in tubular structures is important to improve the use of light in medical applications. Light propagation through biological media formed by elongated fibers (fibrous tissue structure) has not been investigated extensively and is not well understood yet. This type of structure is found in muscle tissues and in some type of leaves.

In this chapter, I focus on the effect of parallel-fibrous structures on the transmission of linearly polarized light. I examine: (a) how the interior structures in tissues could offer different pathways for photon propagation, and (b) how *the sample structure orientation* with respect to the incident beam polarization direction influences the transmitted scattered light components (parallel and perpendicular components), specifically, when the sample under study possesses a defined axial structure.

Transmission—time-resolved and CW—measurements of scattered light have been performed on several biological samples of different thickness for different structure orientations. ***In addition, light transmission through a leaf with fibrous-like structure***

has also been investigated. The experiments were performed using 630-nm laser light. The detected transmitted scattered signal components (parallel and perpendicular to the incident polarization) have been analyzed via polarization gate for different structure orientations.

Experimental results indicate that the orientation of the fibers with respect to the polarization direction of the incident light play an important role on the polarization components of the light transmitted through a tissue sample. The scattering characteristics such as intensity and full width at half maximum were found to be dependant on the tissue structure and thickness of the samples.

Samples used

The samples used for this study are bovine muscular tissue of different thickness. The tissues were positioned at different orientations with respect to the incident linearly polarized beam orientation.

5.2 Time-Resolved and CW Studies on Bovine Muscular Tissues

In order to study the dependence of the transmitted light on tissue structure, time-resolved and CW experiments were performed on bovine brisket tissue samples. Section 5.2.1 presents the time-resolved studies. Section 5.2.2 presents the results and discussion. In the same way, sections 5.2.3 presents the CW studies, and 5.2.4 the results and discussion.

5.2.1 Time-resolved Studies: Experimental Methods and Media

A schematic of experimental setup is shown in Fig. 5.1. Ultrashort laser pulses of 100-fs duration at 625-nm wavelength, 82-MHz pulse repetition rate and 10-mW power were generated from a colliding-pulse mode- locked (CPM) dye-laser system. The laser beam was split into a reference and signal beam by a glass slide. The reference beam was used to mark the zero time of the signal beam and monitor the intensity fluctuations of the laser pulse. The signal light was loosely focused into the tissue, (e.g., bovine muscular tissue samples) using a lens (L). The focal length (F) of the lens was 50 mm. The diameter of the beam was approximately 1 mm, after focusing. A bifurcated optical fiber, with a 200-μm core diameter, was used to collect and detect the scattered signal and the reference beam, as seen in figure 5.1. The output of the bifurcated fiber (carrying the scattered signal and the reference beam) was coupled to the input slit of a 10-ps resolution streak camera.

Tissue samples (slab shape) with two different internal structures were tested: A and B. For structure A, the samples were cut such that the fibrous muscular tissue (FMT) structure was perpendicular to the incident beam. For structure B, the cross-sectional (CS) area of the tubular structure was facing the incident beam. Thickness of the samples range from 3.1 to 13 mm. Their rectangular dimensions were about 25 by 35 mm. Figure 5.2(a) and 5.2(b) are photographs of a bovine muscular tissue sample, showing the elongated tubular fibers and its cross-section.

In order to study tissue structure effect on the transmission of linearly polarized light, the sample was mounted on a x-y translational and angular (θ) rotational stage and

placed on the optical axis of the incident signal beam. The angular rotational stage was used to rotate the sample structure orientation with respect to the incident beam polarization direction, while the translational stage was used to probe different points in the sample. Intensity temporal profiles were detected for the FMT and CS structures oriented at different angles with respect to the incident beam linear polarization direction. *In the same fashion, in the second part of this study, scattered light intensity temporal profiles for samples of different thickness were analyzed using a removable polarizer* (analyzer).

5.2.2 Experimental Results and Discussion

In the first part of this study, the scattered light from the sample was collected with an optical fiber placed behind the sample and positioned across the incident signal beam optical axis of propagation. No polarizer was placed between the sample and the collection fiber. The incident signal beam polarization direction was parallel to the optical table; this angular direction was used as reference. For convenience this direction has been labelled: **E**(0°). In order to study the influence of the structure on light propagation, the fibrous muscular tissue (FMT) and the cross-section (CS) of the FMT structure were rotated to different angles while maintaining fixed the incident polarization.

Figures 5.3(a)—(d) show results obtained for a FMT sample 3.1 mm thick. Figure 5.3(a) shows the schematic orientation arrangement for the FMT sample. The sample was oriented at different angles with respect to **E**(0°). Figure 5.3(b) shows the intensity

temporal profiles collected for the FMT structure oriented at 0° and 90°. Notice that when the FMT is oriented at 0° and 90°, the fibrous structure is parallel and perpendicular to the polarization direction of the incident beam, respectively. Figs. 5.3(c) and (d) shows the peak intensity value and the full width at half maxima (FWHM), respectively, obtained at different FMT structure angular orientations.

The salient feature of profiles shown on Fig. 5.3(b) is that the highest peak intensity was obtained for the FMT structure oriented perpendicular to the incident beam polarization direction. It has been labelled $\mathbf{I}_{FMT}(90°)$. The peak intensity difference (ΔI) between profiles obtained with cross orientations [$\mathbf{I}_{FMT}(0°)$ and $\mathbf{I}_{FMT}(90°)$] is about 11%. For samples above 11mm in thickness the alignment of the fibers in the tissue samples was distorted, and the difference in peak intensity faded away since the sample is many transport length thick (>10). Figure 5.3(c) shows the peak intensity of temporal profiles obtained for orientations: 0°, 30°, 45°, 60°, and 90° degrees; once again, this figure shows that higher intensity transmission is attained by positioning the elongated tubular structure perpendicular to the polarization of the incident beam. Little variation in the FWHM of the collected intensity temporal profiles was observed, as shown in Figure 5.3(d).

In similar fashion, Figures 5.4(a)—(d) shows the result obtained for a CS sample of similar thickness, e.g., 3.1 mm. Figure 5.4(a) shows the schematic arrangement for the CS structure cut oriented at different angles with respect to **E**(0°). Figure 5.4(b) shows

the intensity temporal profiles collected for the CS structure oriented at 0° and 90°. Similarly Figs.5.4(c) and (d) shows the peak intensity and the FWHM. respectively. versus the CS structure angular orientation.

The profiles shown on Fig. 5.4(b) shows a very small peak intensity difference of about 1% between profiles obtained with cross orientations [$\mathbf{I}_{CS}(0°)$ and $\mathbf{I}_{CS}(90°)$]. Similarly, Peak intensity and FWHM for temporal profiles obtained for 0°, 30°, 45°, and 90° degrees have been plotted in Figure 5.4(c) and (d), and show that there is no difference in peak intensity nor in FWHM for this kind of tissue structure. As expected, little (~1%) or not difference was found in the detected intensity temporal profiles for the CS structure oriented at various angles, since the fibrous structure are aligned along the propagation direction of the incident beam.

The main differences found between figures 5.3 and 5.4 are: in (a) intensity and (b) FWHM. The CS structure allowed about 20 % more intensity transmission than the FMT sample. In addition the temporal profiles show a smaller FWHM value than the ones obtained for the FMT structure. This could be better observed in Fig. 5.7 (a).

Figures 5.5(a), (b), and (c) show normalized intensity temporal profiles obtained for FMT structure oriented at $\mathbf{I}_{FMT}(0°)$ and $\mathbf{I}_{FMT}(90°)$ for 3.1, 6.6, and 12.7 mm, respectively. In this figure, one can observe for the three different thicknesses that the transmitted light arrives faster and has a smaller FWHM value by placing FMT structure perpendicular to the incident polarization. Also, as expected, the intensity temporal profiles are spread and delayed in time as the thickness of the sample increase.

In the same fashion Figs. 5.6 (a)—(c) show the normalized intensity temporal profiles for CS of the FMT structure obtained for 0° and 90° orientation for similar thickness as in Fig. 5.5. No major difference was observed in the profiles for the two orientations. As before the profiles are spread and delayed in time as the thickness increase.

Figure 5.7 shows Figs. 5.5 and 5.6 together for better comparison. The salient feature of profiles shown in Fig. 5.7 (a) is that the FWHM of the CS is smaller than the FMT structure. Its intensity peak value higher (compare Fig. 5.4 and 5.3). Figs. 5.7 (b) and (c) show that as the thickness of the samples is increased, the temporal profiles obtained for the CS structure are delayed and start spreading more than the temporal profiles obtained for the FMT structure. This could be observed more clearly in Figure 5.6 (c). It should be mentioned that the intensity peak value for the 12.7-mm thick samples was smaller for CS structure than for the FMT structure—not shown in figure.

The first part of this study shows us that the orientation of fibrous or tubular structures with respect to the polarization of the incident beam plays an important role in the light transmission. In addition it also indicates that a higher transmission of light could be obtained when light is sent along the fibers (e.g., CS structure), mainly for thin samples. For very thick samples, less transmission was obtained for the CS structure orientation. The high transmission in thin samples along the CS could be due to the good alignment or connection of the tubular cells. Conversely, in thick samples this alignment is lost and less transmission is obtained.

In the second part of this study, the components of the transmitted scattered light for a FMT 3.1-mm thick sample are obtained using a removable polarizer (analyzer). For this study the analyzer was positioned parallel and perpendicular to the polarization direction of the incident beam while the sample was oriented at 0°, 45°, and 90° degrees. (The sample positioned 0° degrees implies that tubular structure alignment is parallel to the incident polarization).

Figures 5.8, 5.9, and 5.10 shows intensity temporal profiles for the FMT sample oriented at 0°, 45°, and 90°, respectively; the schematic arrangement for the different orientations are also shown at the top of the figure. The intensity temporal profiles shown in each figure were obtained by rotating the analyser to 0° and 90° degrees. Profiles obtained with the analyser at 0°and 90° were labelled $I_{\parallel}$ and $I_{\perp}$, respectively. The $I_{\parallel}$ profiles polarization direction are identical to the incident beam, and the $I_{\perp}$ profiles are perpendicular. The inset in each figure shows the intensity temporal profile difference $I_{\parallel} - I_{\perp}$, for the sample at its respective orientation. The salient features of the intensity temporal profiles shown in Figs. 5.8 and 5.10 are that in both figures the $I_{\parallel}$ profiles show a higher transmission than the $I_{\perp}$ profiles. The highest peak intensity difference was obtained for the sample oriented at 90°. This intensity difference was about 26% and 7% for the sample oriented at 90° and 0°, respectively. In addition, the intensity temporal profile difference ($I_{\parallel} - I_{\perp}$) in the insets in Figs. 5.8 and 5.10 show that when the sample is oriented at 90° , the difference in intensity occurs earlier in time than when its oriented at 0°. Figure 5.9 show profiles $I_{\parallel}$ and $I_{\perp}$ for the sample oriented at 45°. The salient feature of this figure is that a higher peak intensity was obtained for

profile $I_{\perp}$ than for profile $I_{\parallel}$. This result was totally unexpected. It is believed that this swapping in peak intensity has to do with the influence that the macro vs. microstructure has on light transmission.

Figure 5.11 shows the plot of the intensity values obtained in Figs. 5.8—5.10 for profiles $I_{\parallel}$ and $I_{\perp}$ for three different sample orientations. The peak values obtained for $I_{\parallel}$ have been plotted using circles (o), while $I_{\perp}$ uses plus signs (+). The results obtained have been connected using dashed thick lines. The thin dash line shows the average intensity $[(I_{\parallel} + I_{\perp})/2]$ expected for different orientations.

The results obtained for the parallel and perpendicular components of the scattered transmitted light clearly indicates that, in a transmission arrangement, more photons keep their original polarization when the fibers of the sample are oriented perpendicular to the incident beam polarization direction.

In the third part of this study, a pulse of light is sent through a piece of FMT sample with the tubular structures oriented parallel to the polarization of the incident beam. The transmitted light was collected by moving the collection fiber to different positions 1/20 th of an inch apart along the x and y-axis. The orientation of the fibers of the sample were aligned parallel to the polarization direction of the incident beam, e.g. 0°. See Figure 12 (a). No analyzer was used for this part of the study.

Figure 5.12 (b) shows the intensity temporal profiles obtained at different distances away from the center of the incident beam.. The profiles were taken 1/20 of an inch apart from each other. From left to right, the first row of profiles corresponds to

positions 0, 1/20, and 2/20 inch apart from the center; the second row corresponds to positions 3/20, 4/20, and 5/20; the third row corresponds to positions 6/20, 7/20, and 8/20. Profiles measured along the orientation of the fiber (x-direction) were plotted using a solid line, while profiles measured perpendicular to the orientation of the fiber (y-direction) were plotted using dashed lines. The profile at left top corner was obtained at the center of the sample, i.e., the collecting fiber was positioned directly across the incident beam. The transmitted pulse through the center of the sample has been plotted using a dotted line to be used as reference, for better comparison.

The salient feature of curves in Figure 5.12 (b) is that as we move away from the center of the sample, the intensity transmitted across the muscular fibers of the sample (y-axis) decreases faster that the light transmitted along the fibers (x-direction). This high transmission along the fibers of the sample could be attributed to photons that are trapped and channelled by the muscular fibers, indicating a waveguide feature of fiber due to the tubular structure.

Peak intensity values and FWHM vs. detector position—corresponding to profiles in Fig. 5.12 (b)—have been plotted in Fig. 5.12 (c) and Fig.5.12 (d), respectively. Values obtained along the fibers in the sample (x-axis) has been plotted using plus signs (+), while values obtained across it (y-direction) has been plotted using circles (o). The peak intensity plot was done using a logarithmic scale. The main results that can be appreciated in this figure is that higher peak intensity and less FWHM values (less temporal spreading) are obtained along the direction of the fibers in the sample (x-axis).

These results clearly indicate that there must be different diffusion coefficients in samples with tubular structures, i.e., FMT structures, one along the direction of the fibers and another across this direction. In addition, light t transmission along the fibers (CS of the FMT) must have a different diffusion coefficient. These different diffusion coefficients should be better appreciated on well-aligned tubular structures in the pre-diffuse regime.

5.2.3 CW Studies: Experimental Methods and Media

The dependence of the transmitted light polarization on tissue structure, using CW NIR light was investigated. A linearly polarized laser beam, 2.5 mm in diameter, was incident normal to the sample. The incident beam was chopped for better monitoring of the intensity values. The scattered signal light was collected using a Fourier and polarization gate. The diameter of the spatial filter was set to 2.5 mm. The analyzer was positioned behind the sample and was oriented at 0° and 90° to separate the parallel and perpendicular intensity components of the transmitted light. The photons were detected using a Germanium-Silicon photo detector placed at the image plane. The intensity readings were done using a Tektronix digital oscilloscope (model TDS 744 A), which was connected to the photo detector. The wavelength used for this experiment was 1250 nm obtained from a Forsterite laser system. A schematic of the experimental setup is shown in Fig. 5.13.

The sample used was a 6.3 mm thick bovine brisket tissue. The sample was cut such that the fibrous muscular tissue (FMT) structure was perpendicular to the incident beam.

In the same way as in section 5.2.1, in order to study tissue structure effect on the transmission of linearly polarized light, the sample was mounted on an angular (θ) rotational stage and placed on the optical axis of the incident signal beam. The angular rotational stage was used to rotate the orientation of the sample structure with respect to the incident beam polarization direction. The intensity of the transmitted light was measured as the angle, θ, between polarization direction of the incident light and the orientation of the fibers in the tissue sample was changed by rotating the sample about the axial direction. For every angular orientation of the sample, the intensity of transmitted light was measured for the axis of the polarizer (e.g., analyzer) oriented (a) parallel, and (b) perpendicular to the incident polarization direction. Its intensity values were labeled $I_{\parallel}$ and $I_{\perp}$, respectively.

5.2.4 Experimental Results and Discussion

Overall, the 'parallel' component ($I_{\parallel}$) of the transmitted intensity was either greater than or equal to the 'perpendicular' component ($I_{\perp}$). This is expected; since in the absence of scattering, $I_{\parallel}$ will be equal to the total incident intensity except for losses due to absorption in the sample and reflection at the interfaces. And $I_{\parallel}$ will be equal to $I_{\perp}$ when a large number of scattering events completely randomize the polarization of the transmitted beam such as in highly scattering and sufficiently thick samples.

The transmission polarization intensity dependence $I_{\parallel}$ and $I_{\perp}$ as a function of the fibrous structure orientation is displayed in Fig. 5.14. The intensity values obtained for $I_{\parallel}$ and $I_{\perp}$ has been plotted using squares (□) and circles (o), respectively. The salient feature of the two curves formed by the parallel and perpendicular intensity components is that both are symmetrically opposite to each other. In addition, there are some preferred orientations of the fibers in the tissue with respect to the polarization direction of the incident light for which $I_{\parallel}$ is optimal. Maxima of $I_{\parallel}$ were observed at 0°, 90°, 180° and 270°, and minima at 45°, 135°, and 225°. Maxima (minima) positions of $I_{\perp}$ coincided with those of minima (maxima) of $I_{\parallel}$. What is even more noteworthy is that the magnitude of maxima of $I_{\parallel}$ at 0° and 180° is not the same as that at 90° and 270°, the latter being approximately 7% higher. The orientation dependence of $I_{\parallel,\perp}$ may be expressed as

$$I_{\parallel}(\theta) = a + b\cos^2(2\theta) + c\sin^2(\theta), \qquad (5.1\text{-a})$$

$$I_{\perp}(\theta) = a' + b'\sin^2(2\theta) + c'\cos^2(\theta), \qquad (5.1\text{-b})$$

where θ is the angle between the incident polarization direction and the direction of fibers in the tissue, and *a*, *b* and *c* are presumed to be functions of tissue characteristics and sample thickness. The fitting values for the coefficients a, b, c, and K obtained for the parallel intensity values ($I_{\parallel}$) as a function of θ were 4.8, 3.19, 0.5, and 0°, respectively. In the same fashion, the fitting values for the coefficients a, b, c, and K obtained for the perpendicular intensity values ($I_{\perp}$) as a function of θ were 1.47, 3.57, 0.5, and 90°, respectively. In addition we also defined here, the maximum values of anisotropy caused by the structure orientation on the intensity components as:

$$A = \{I_{\|}(\theta) - I_{\|}^{min}\}/\{I_{\|}(\theta) + I_{\|}^{min}\}. \quad (5.2)$$

where the subscript || indicates the parallel component. $I_{\|}^{min}$ is the minimum value of $I_{\|}$. are 0.25 for 0° and 180°, and 0.28 for 90° and 270°. This difference in maximum values of A (and/or, the maximum values of $I_{\|}$) is small but consistent and was observed in repeated experiments with different bovine brisket tissue samples.

In addition, the depolarization values found for the parallel and perpendicular components (e.g., $I_{\|}$ and $I_{\perp}$) became a function of the angular position of the structure and has been defined here as

$$D(\theta_i) = 1 - |\{I_{\|}(\theta_i) - I_{\perp}(\theta_i)\}/\{I_{\|}(\theta_i) + I_{\perp}(\theta_i)\}| \quad (5.3)$$

θ_i indicates the angular orientation of the structure. When the sample was oriented at 45° and 135°, maximum depolarization values of about 0.96 were obtained. When the sample was oriented at 90° and 270°, minimum depolarization values of about 0.2 were obtained. At 0° and 180° the depolarization values were around 0.4. *It should be also mentioned that the difference found between the maximum intensity values at 0° and 180° and the maximum values found at 90° and 270° vanishes as the spatial aperture in the Fourier plane is increased. This clearly indicated that more information on the tissue structure is found by using spatial filters with small apertures.*

5.3 Conclusion

It was found that the structures of the samples play an important role in light propagation. In particular, a higher intensity transmission was obtained when the fibers

of the FMT structure were aligned perpendicular to the polarization of the incident beam. The difference on the transmitted intensity temporal profiles along and across the fibers of a tissue sample indicates the existence of different diffusion coefficients for tubular tissue structures. Moreover, the observed dependence of $I_{\parallel}$ and $I_{\perp}$ on structure orientation is significant, since the parallel component of light could form a sharper transillumination image of an object inside a turbid medium than the perpendicular component, and ways to optimize the magnitude of the parallel component are always sought. In this case, It was found that light is less depolarized when the structure orientations of the fibers are oriented perpendicular to the polarization of the incident beam.

5.4 References

5.1 S. L. Jacques, "Origins of tissue optical properties in the UVA, visible, and NIR regions," in *Advances in Optical Imaging and Photon Migration*, R. R. Alfano and J. G. Fujimoto, eds., Vol. 2, OSA Trend in Optics and Photonics (Optical Society of America, Washington D. C., 1996), pp. 364-371.

5.2 Y. C. Fung, Biomechanics: Mechanical Properties of Living Tissues, Second Edition, (Springer-Verlag, New York, 1993).

5.3 The organizational hierarchy of skeletal muscle, From Gray's Anatomy, 35th British ed. (1973), edited by Warwick and Williams

5.4 J. F. de Boer, T. E. Milner, M. J. C. van Gemert, J. S. Nelson, "Two-dimensional birefringence imaging in biological tissue by polarization-sensitive optical coherence tomography," Opt. Lett., 22, 934-936, 1997.

5.5 Figures

Figure 5.1 Experimental setup

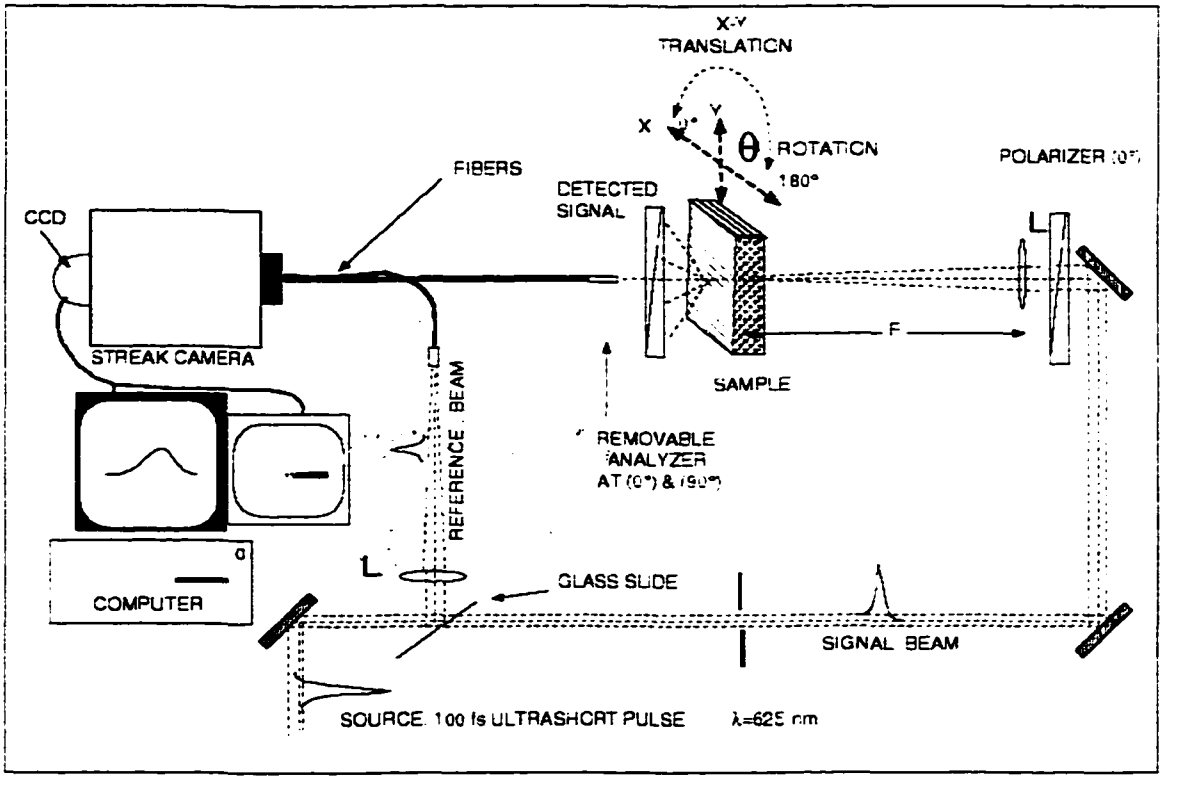

Figure 5.2 Photograph of a bovine muscular tissue samples. Pictures (a1) and (a2) correspond to dried and freshly cut muscular fibers. respectively. Picture (b) correspond to the cross section of the elongated muscular fibers.

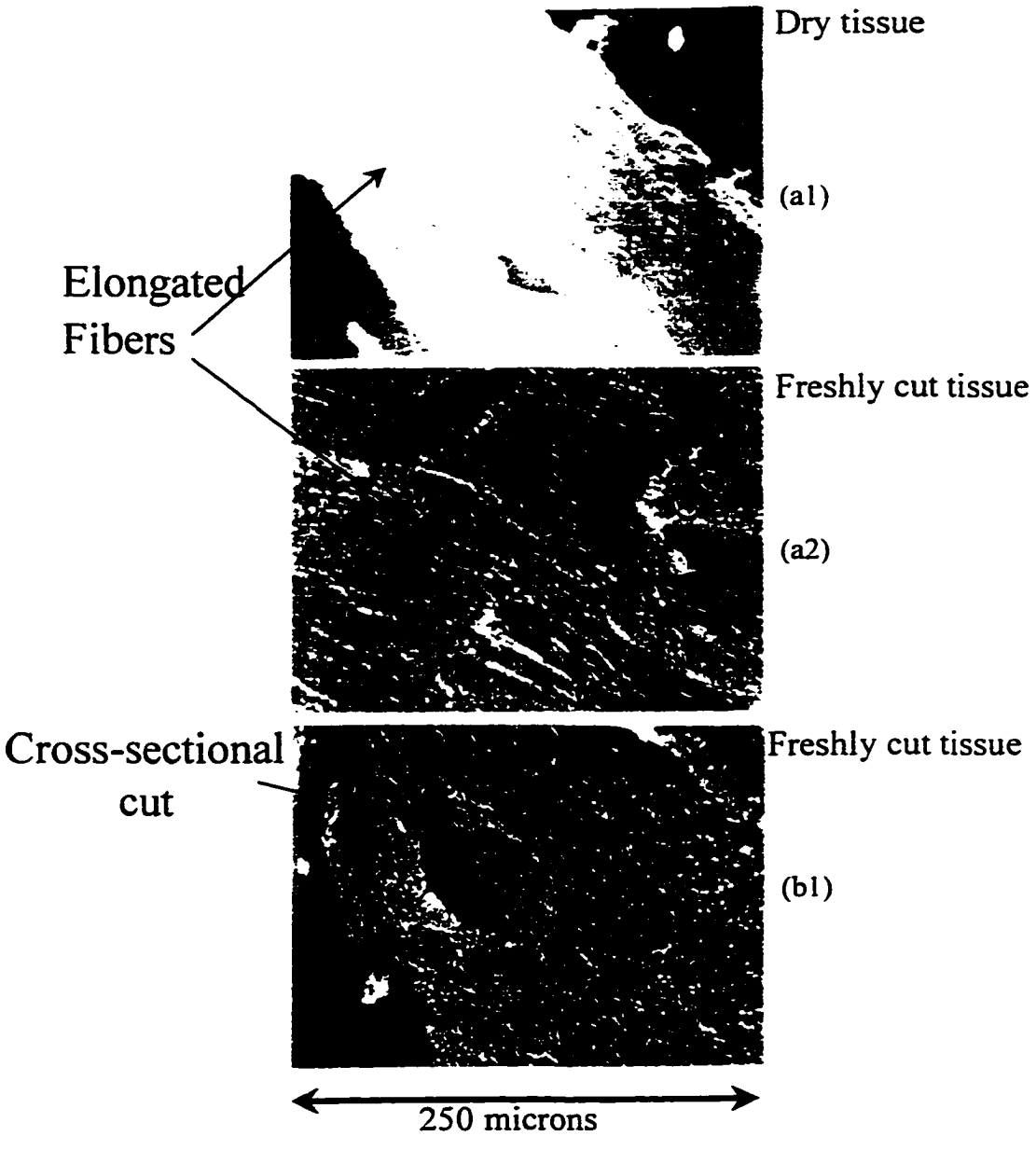

Figure 5.3 Results obtained for a fibrous muscular tissue (FMT) sample 3.1-mm thick. Figure 5.3(a) shows the schematic orientation arrangement. The sample was oriented at different angles with respect to E(0°). Figure 5.3(b) shows the intensity temporal profiles collected for the FMT structure oriented at 0° and 90°.

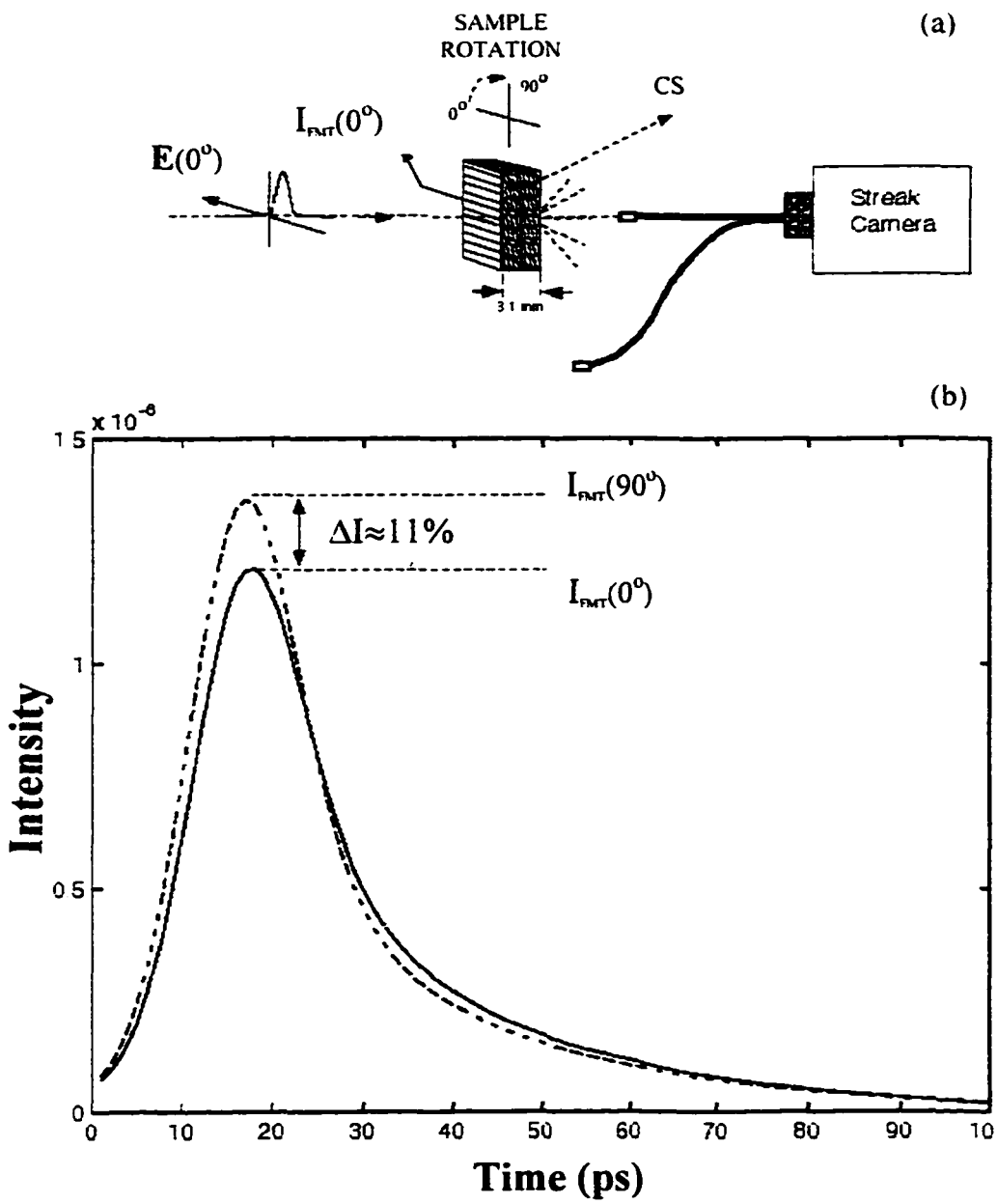

Figs. 5.3(c) and (d) shows the peak intensity values and the full width at half maxima (FWHM) , respectively, as a function of structure orientation, θ.

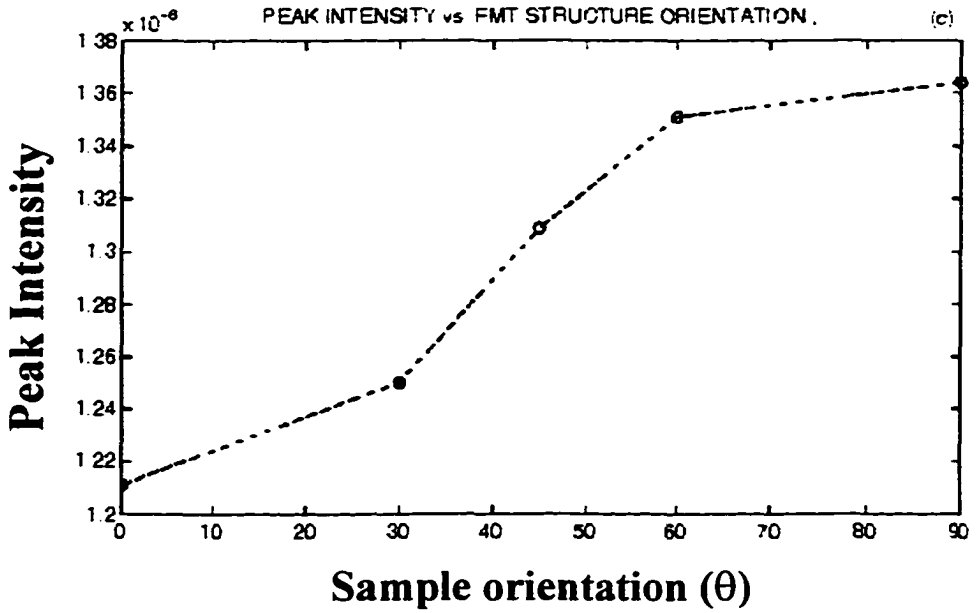

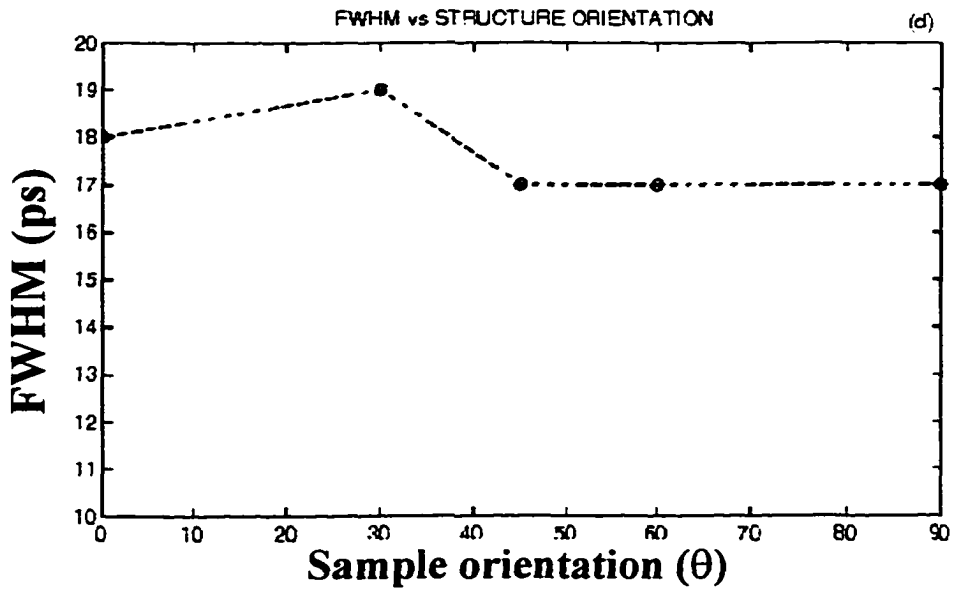

Figure 5.4 Results obtained using the cross section (CS) of a fibrous muscular tissue (FMT). The CS sample was 3.1 mm thick. Figure 5.4(a) shows the schematic orientation arrangement for the cross sectional slab. The sample was oriented at different angles with respect to **E**(0°). Figure 5.4(b) shows the intensity temporal profiles collected for the FMT structure oriented at 0° and 90°.

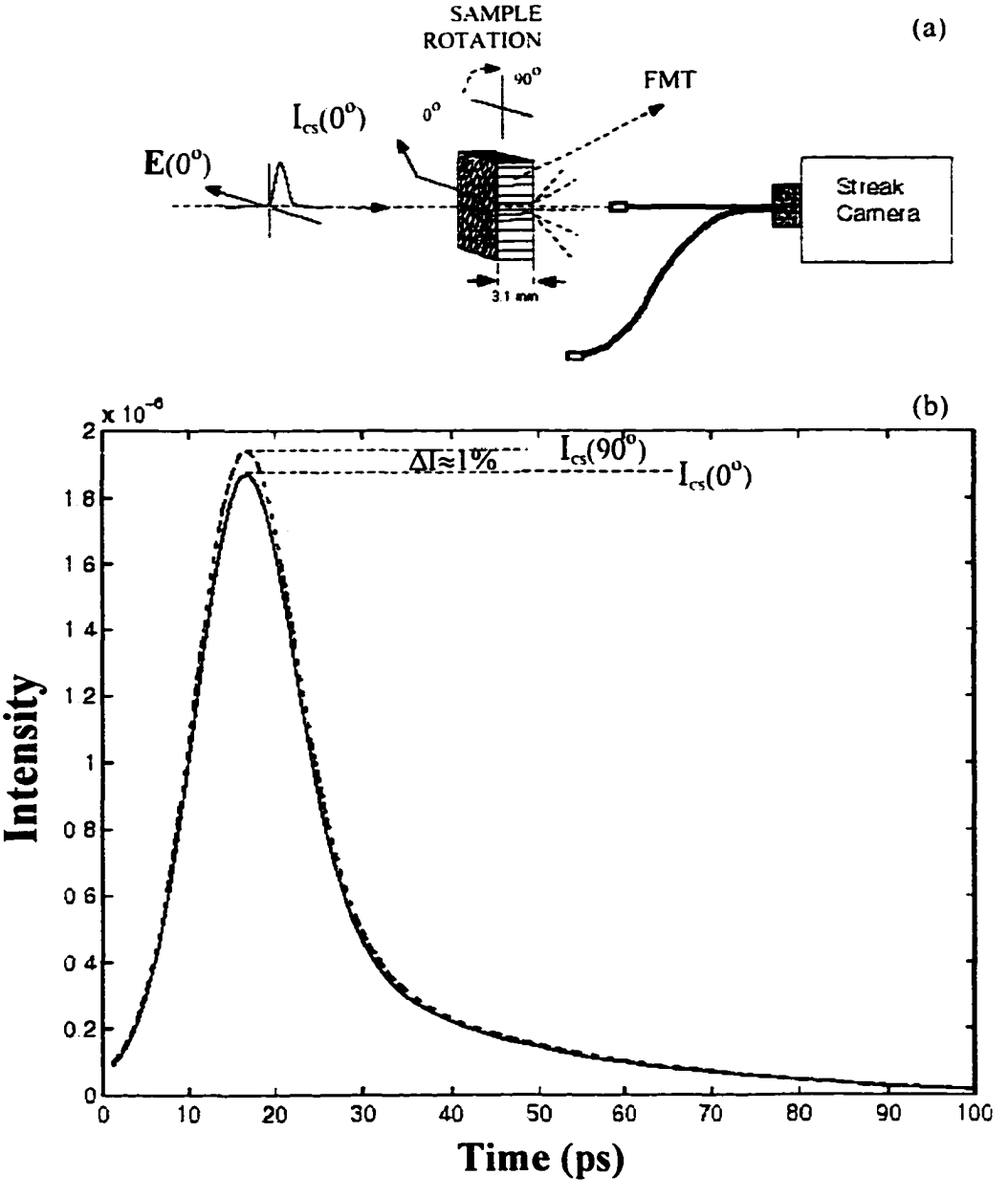

Figs. 5.4(c) and (d) shows the peak intensity values and the full width at half maxima (FWHM) , respectively, as a function of structure orientation θ.

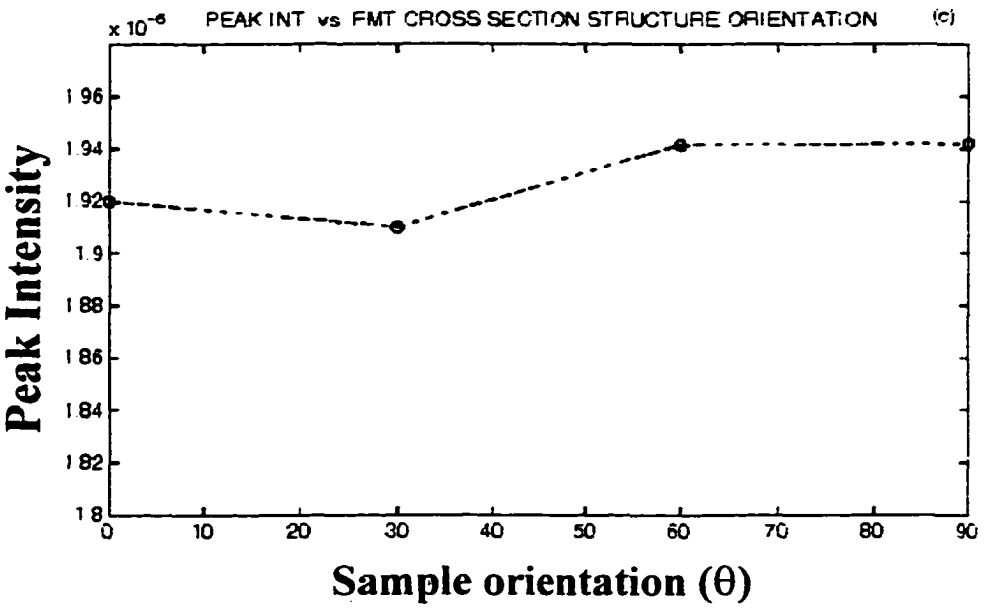

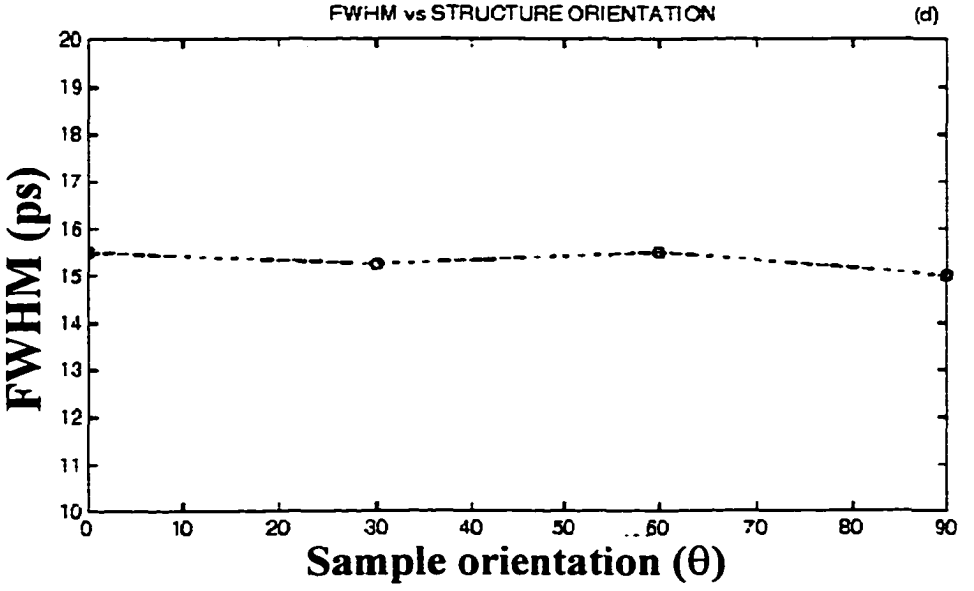

Figures 5.5 Normalized intensity temporal profiles obtained for different thickness for FMT sample oriented at $I_{FMT}(0°)$ and $I_{FMT}(90°)$. Figures (a), (b), and (c) correspond to samples 3.1, 6.6, and 12.7 mm thick, respectively.

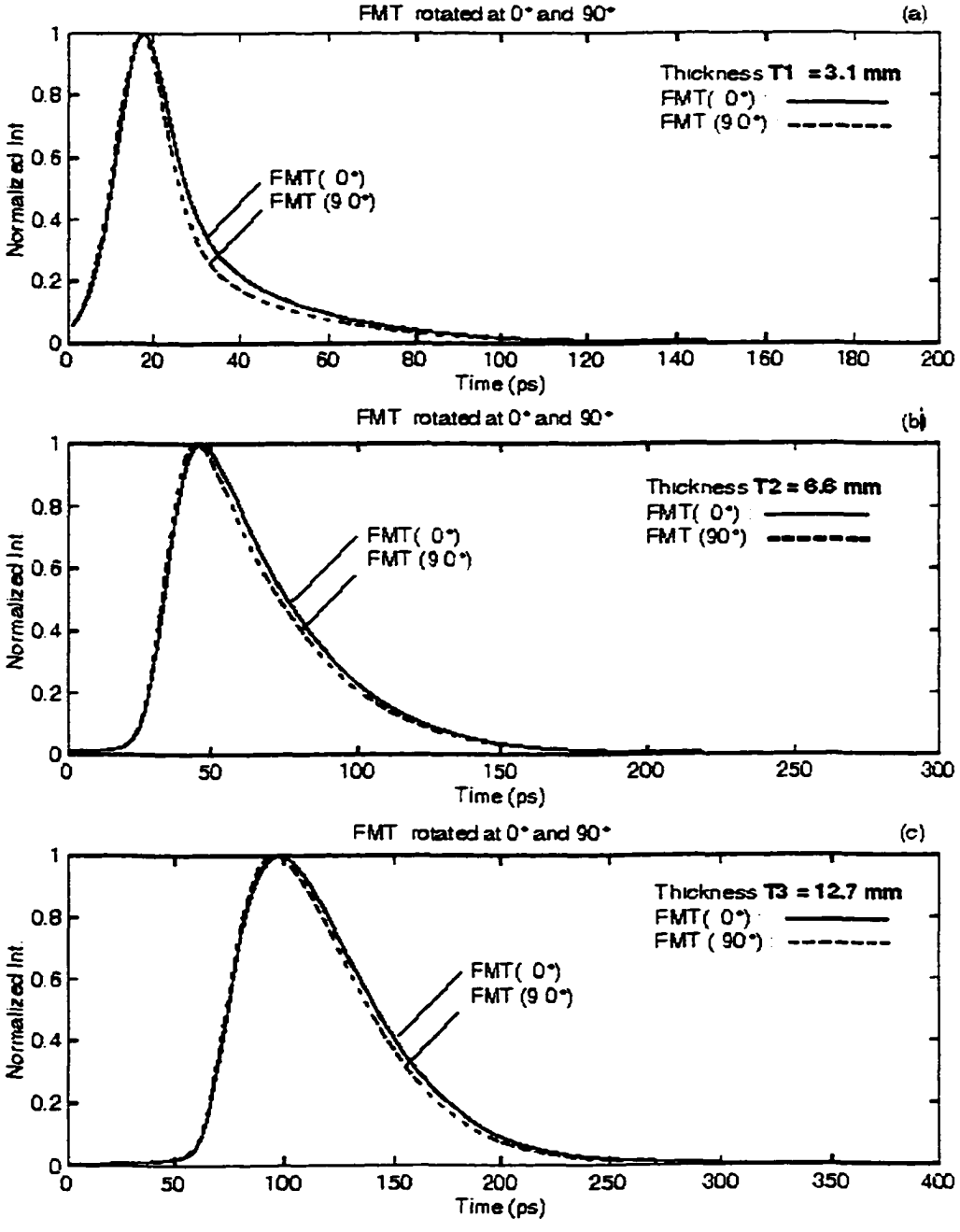

Figures 5.6 Normalized intensity temporal profiles obtained for different thickness for the CS of a FMT sample oriented at $I_{FMT}(0°)$ and $I_{FMT}(90°)$. Figures (a). (b). and (c) correspond to cross sections 3.1, 6.6, and 12.7 mm thick, respectively.

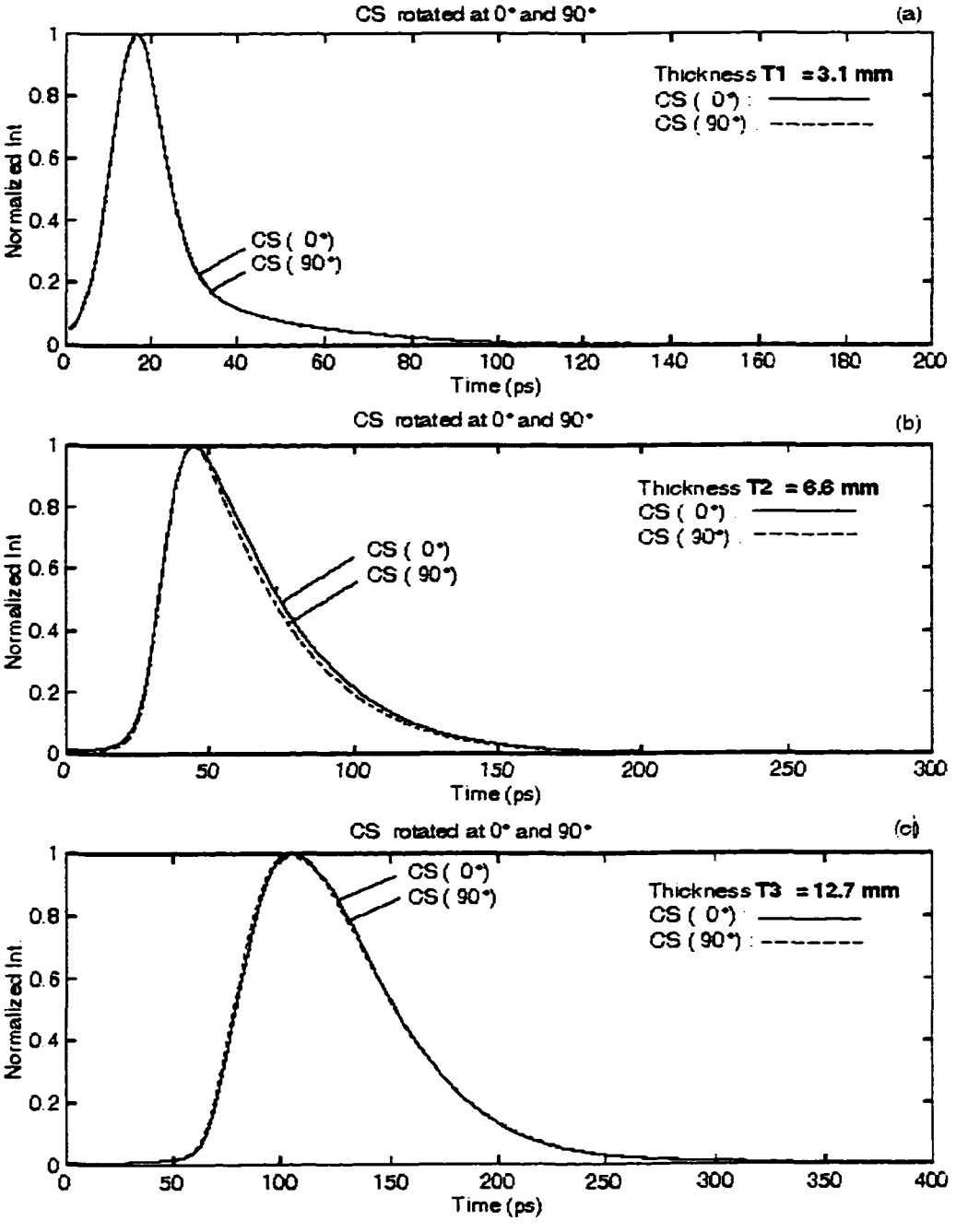

Figures 5.7 Intensity temporal profiles obtained in figures 5.5 and 5.6 together for the three different thicknesses for better comparison. Figures (a), (b), and (c) correspond to samples 3.1, 6.6, and 12.7 mm thick, respectively.

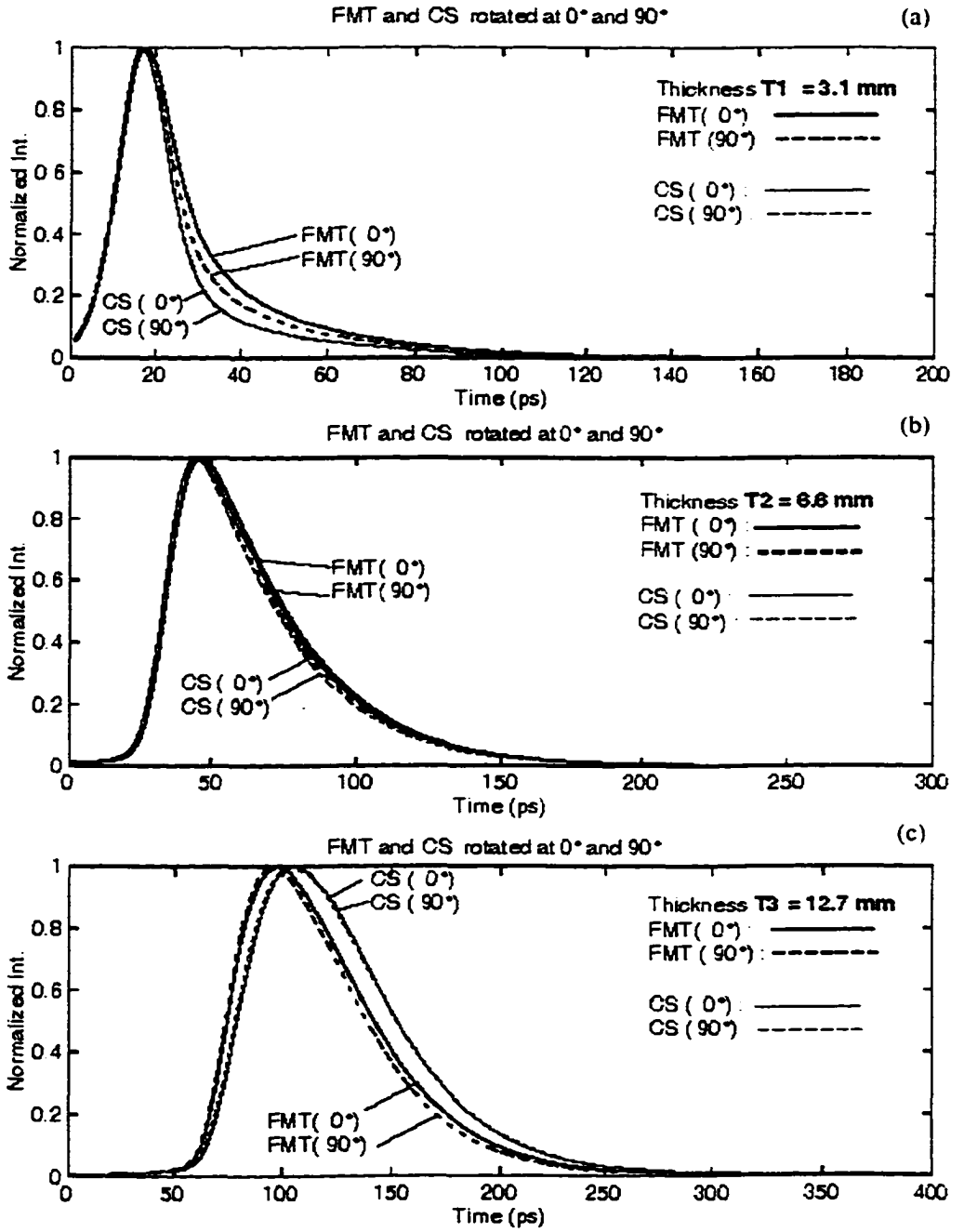

Figure 5.8 Parallel and perpendicular components of light traveling through the fibrous muscular tissue (FMT) sample oriented at 0°. The schematic arrangement is shown at the top. The intensity temporal profiles shown were obtained by rotating the analyzer to 0° and 90° degrees, and have been labeled $I_{\parallel}$ and $I_{\perp}$, respectively. The inset shows the intensity temporal profile difference ($I_{\parallel} - I_{\perp}$).

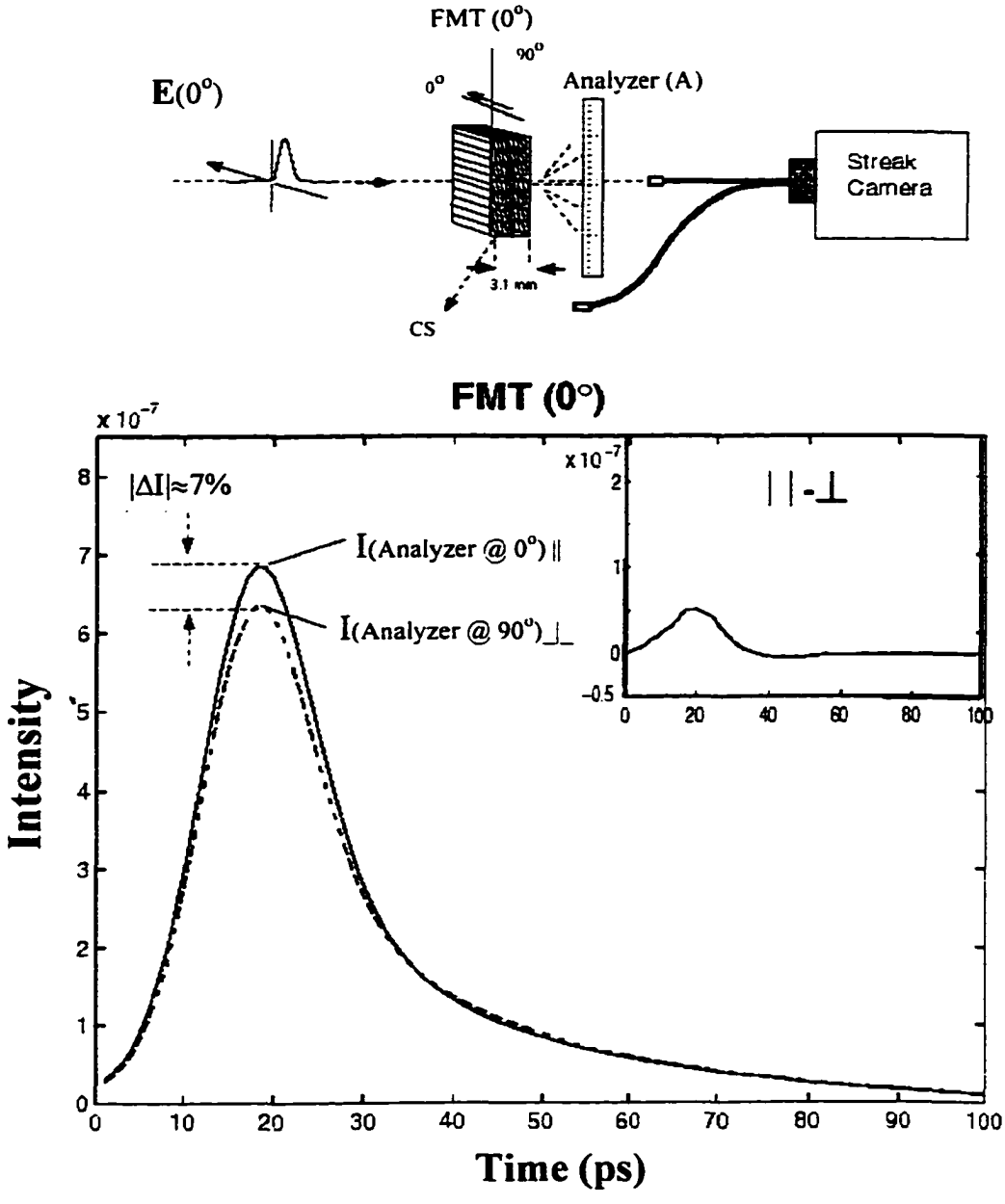

Figure 5.9 Parallel and perpendicular components of light traveling through the fibrous muscular tissue (FMT) sample oriented at 45°. The schematic arrangement is shown at the top. The intensity temporal profiles shown were obtained by rotating the analyzer to 0° and 90° degrees, and have been labeled I∥ and I⊥, respectively. The inset shows the intensity temporal profile difference (I∥ - I⊥).

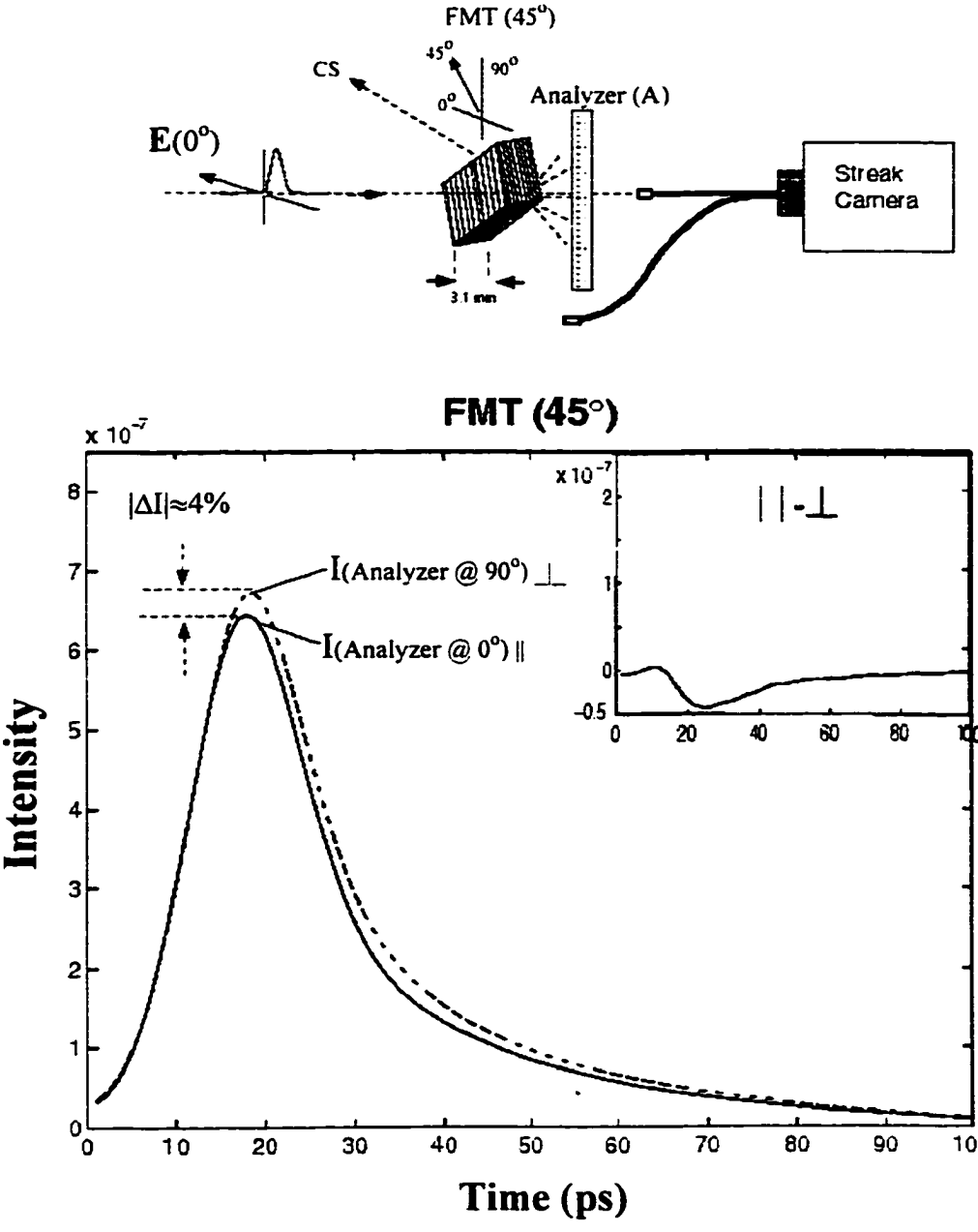

Figure 5.10 Parallel and perpendicular components of light traveling through the fibrous muscular tissue (FMT) sample oriented at 90°. The schematic arrangement is shown at the top. The intensity temporal profiles shown were obtained by rotating the analyzer to 0° and 90° degrees, and have been labeled I and I , respectively. The inset shows the intensity temporal profile difference (I - I).

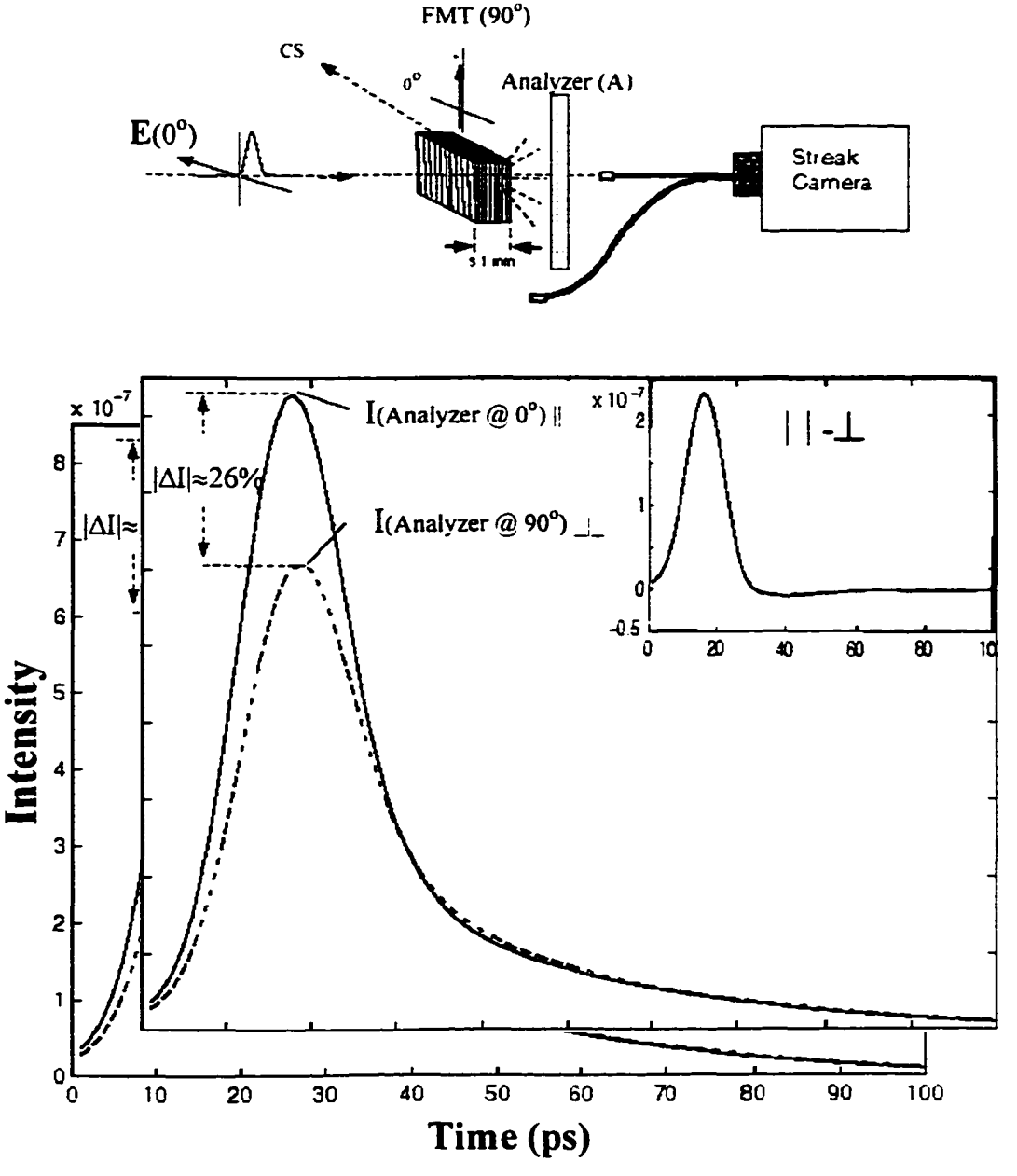

Figure 5.11 Plot of the peak intensity values obtained in Figs. 5.8—5.10 for profiles I and I__ for three different sample orientations.

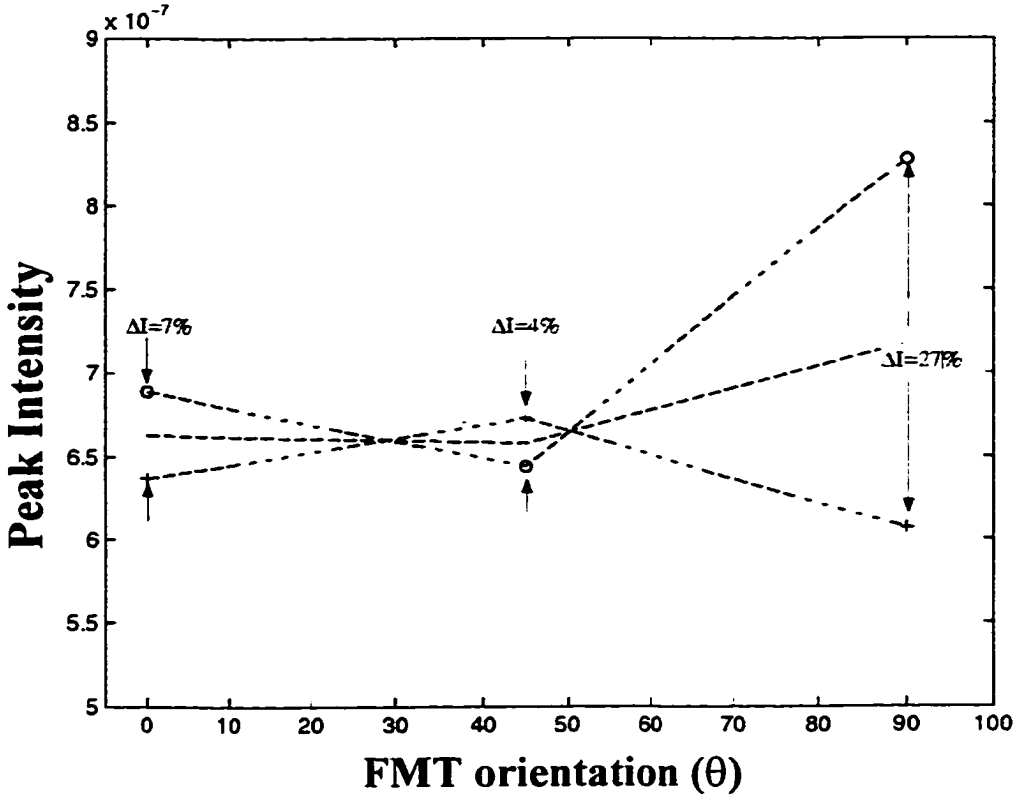

Figure 5.12 (a) Schematic of sample orientation with respect to the incident beam polarization direction, showing detector positions along the orientation of the fibers (x-direction) and perpendicular to it (y-direction). Eight positions 1/20 of an inch apart were recorded in the x and y direction.

(a)

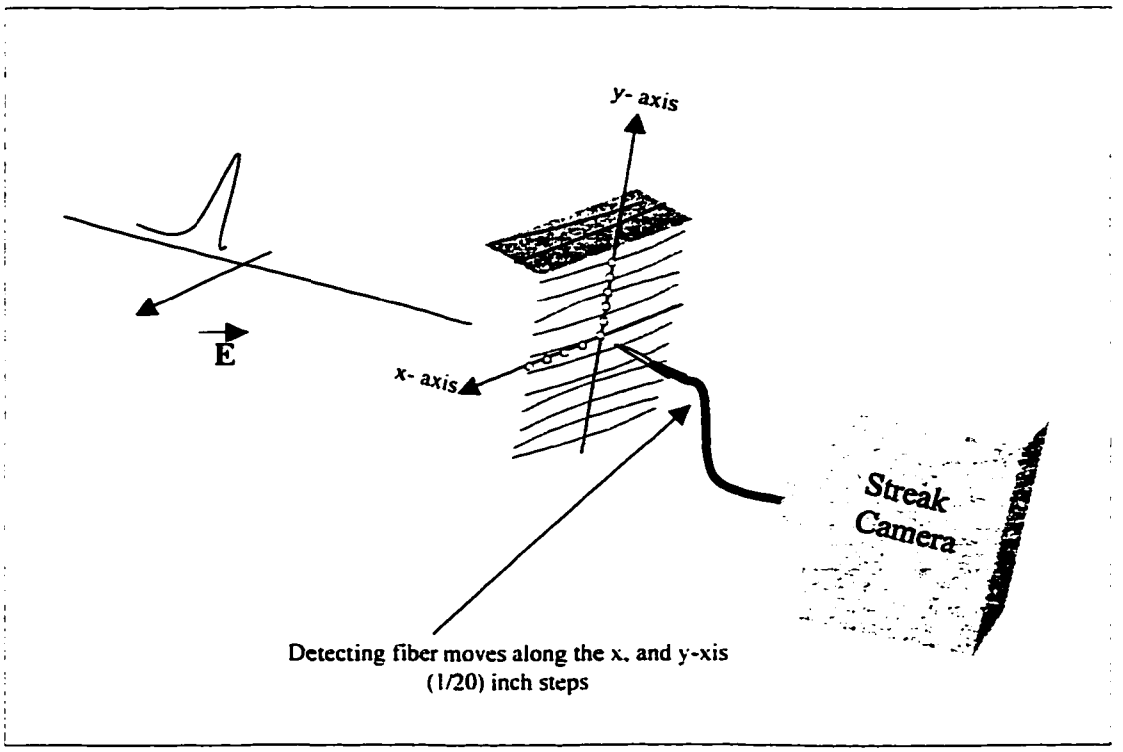

Figure 5.12 (b) Intensity temporal profiles obtained at different distances away from the center of the incident beam. Starting at the center (axis of propagation), nine positions 1/20 of an inch apart were recorded in the x and y direction. Profiles obtained along the x-axis have been plotted using a solid line, while profiles along the y-direction have been plotted using a dashed line.

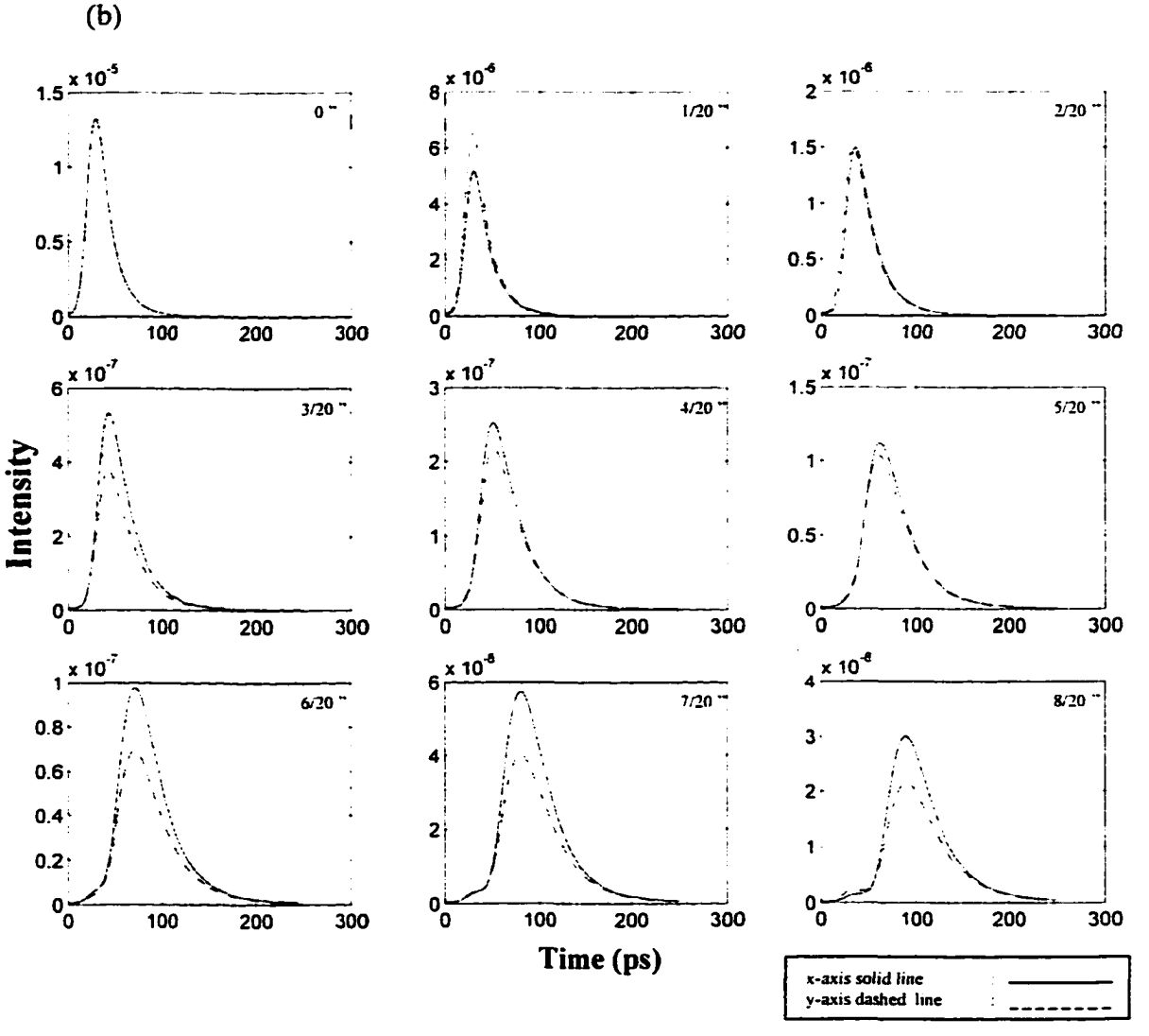

Figure 5.12 (c) Peak intensity values vs. detector position. (d) FWHM vs. values vs. detector position. See text for more details.

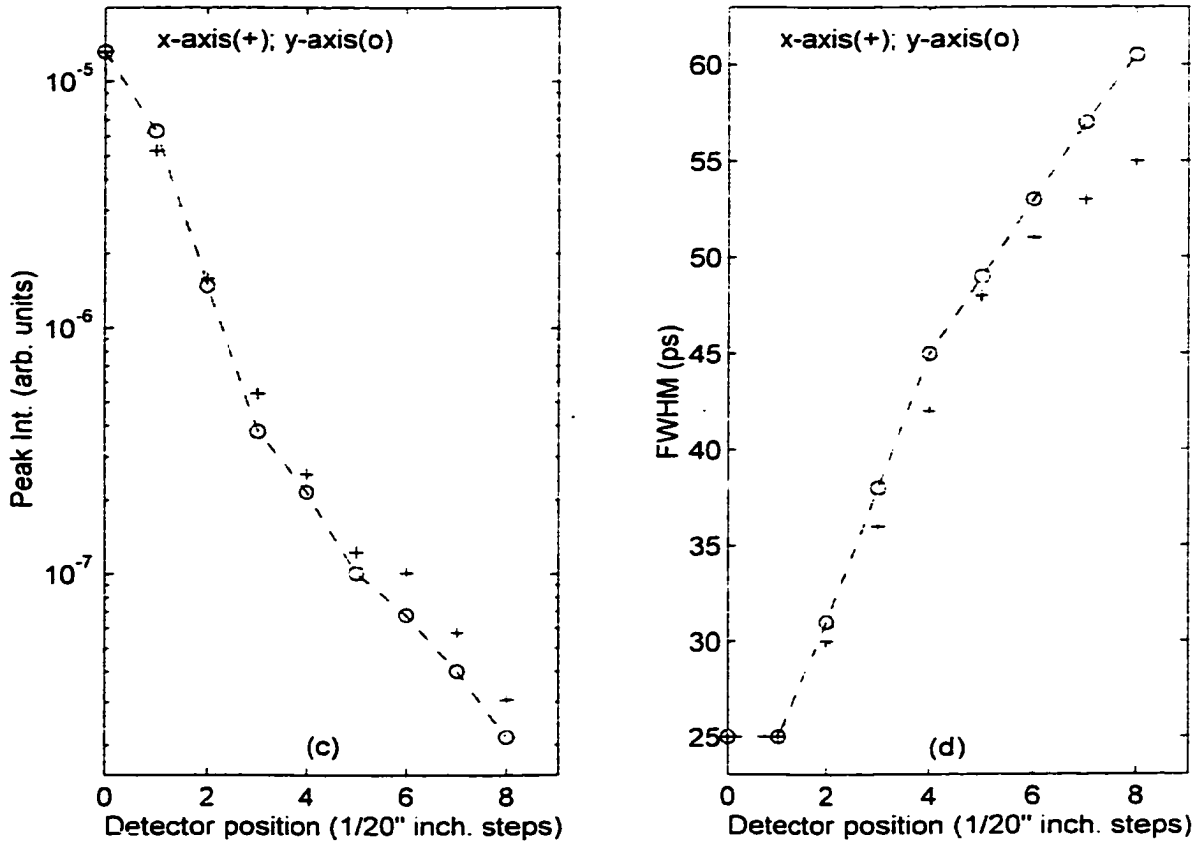

Fig. 5.13 CW: experimental setup.

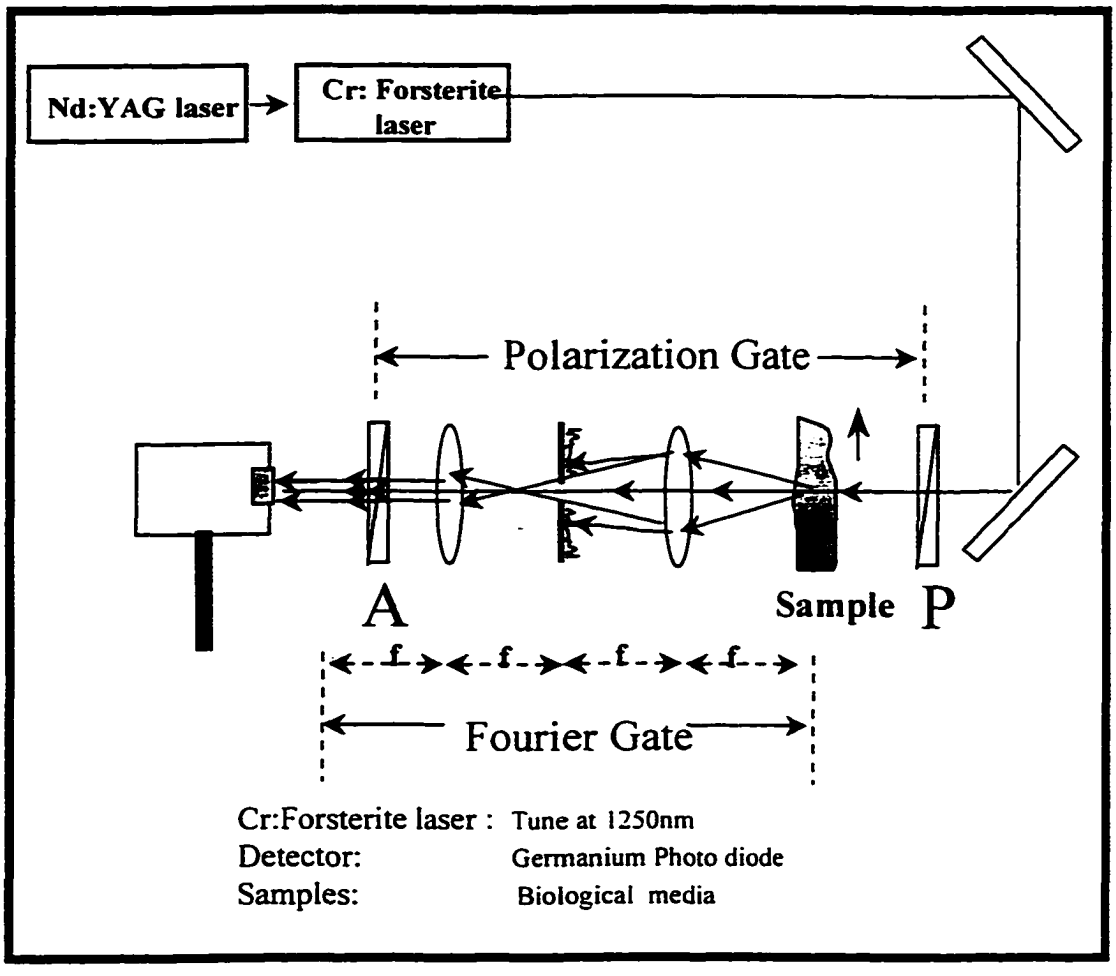

Fig. 5.14 Transmission intensity components $I_{\parallel}$ and $I_{\perp}$ (i.e., parallel and perpendicular) dependence as a function of the fibrous structure orientation. The $I_{\parallel}$ and $I_{\perp}$ were obtained by rotating the orientation of the sample around the axis of propagation and using a analyzer to separate the parallel and perpendicular components as indicated by schematic arrangement is shown at the top. The $I_{\parallel}$ and $I_{\perp}$ intensity data obtained for different sample orientations has been plotted in the graph beneath using squares (□) and circles (o), respectively. The orientation dependence for the parallel and perpendicular components can be expressed by $\mathbf{I}_{\parallel}(\theta) = \mathbf{a} + \mathbf{b}\cos^2(2\theta) + \mathbf{c}\sin^2(\theta)$, and $\mathbf{I}_{\perp}(\theta) = \mathbf{a'} + \mathbf{b'}\sin^2(2\theta) + \mathbf{c'}\cos^2(\theta+90^\circ)$, respectively, and it has also been plotted using a smooth solid line.

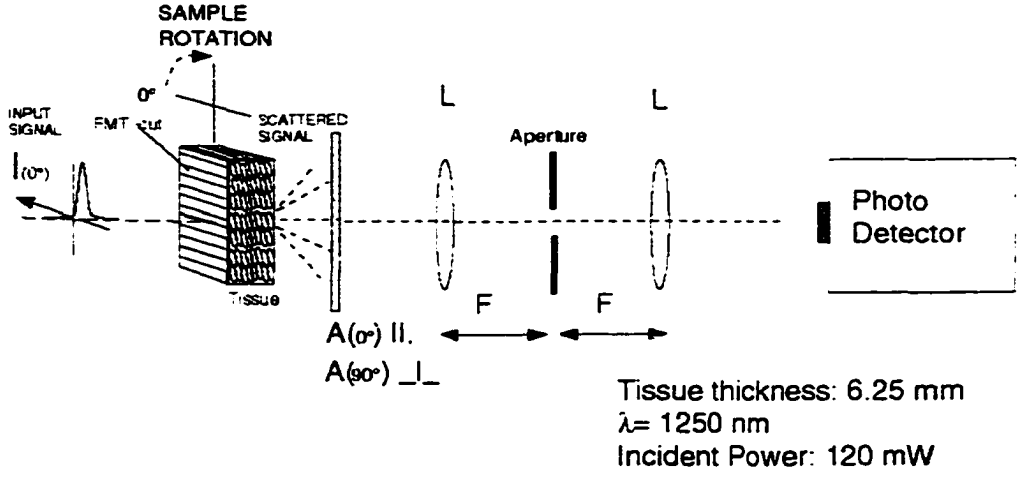

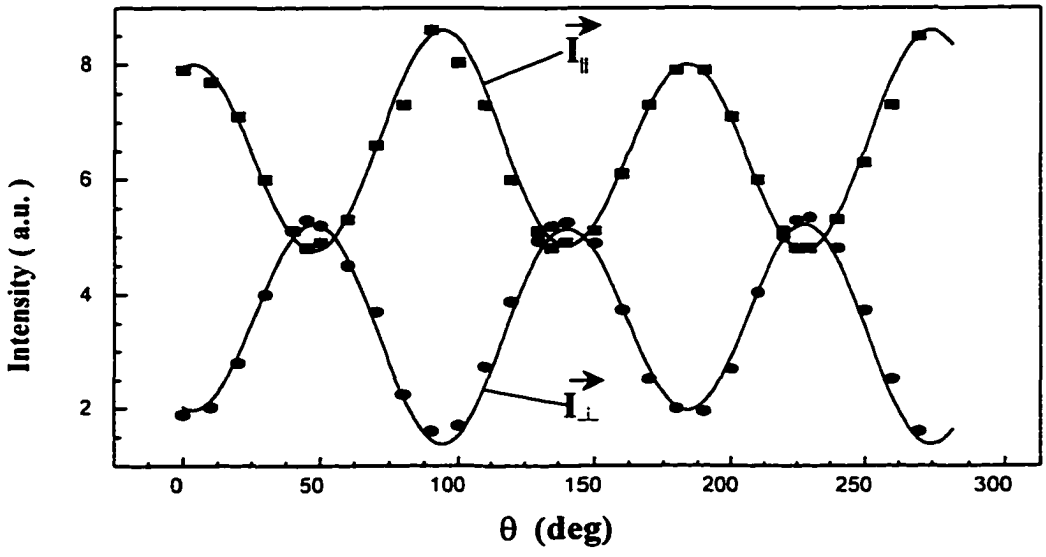

for $I_{\parallel}$: a=4.8 ; b=3.19 ; c=0.5; for $I_{\perp}$: a'=1.47; b'=3.57 ; c'=0.5

Part II

NEAR-INFRARED OPTICAL IMAGING OF BIOLOGICAL MEDIA

Chapter 6

Two-dimensional *CW* NIR Transillumination Imaging of Biological Media Using a Chromium-doped Forsterite Laser

6.1 Introduction

In this Chapter, the research is focused on imaging objects hidden inside normal and cancerous human breast tissues, as well as bovine, porcine, and gallinaceous (chicken) tissues, using *CW* NIR light. The imaging performance of 1250 nm light from a Cr^{4+}:Forsterite laser was compared with that of 1064-nm light from a Neodimium-doped yttrium aluminum garnet (Nd:YAG) laser. A Fourier space gate[6.2,6.3] in tandem with a polarization gate[6.4,6.5] was used to select out a fraction of the image-bearing photons. *No time-gating was performed in this section.*

The type of cancerous human breast sample examined here was found to be more scattering than the normal breast tissue. Both the Fourier spatial filtering and the polarization gate were observed to enhance image quality. The scattering characteristics of tissues and *image quality* were found to depend substantially on the orientation of polarization of the incident light beam with respect to fibers in the tissue, corroborating the findings in chapter 5. Using two different wavelengths of light to image a human breast tissue sample (comprised of fatty and glandular components), we observed that light which is moderately absorbed by the fat generates images of a higher contrast as compared to images obtained using the wavelength of light which is less absorbed.

This chapter is organized as follows. Section 6.2 presents the experimental arrangement, method and parameters. The results presented in Section 6.3 illustrate the importance of wavelength selection, efficacy of Fourier space gate and polarization gate in sorting out image-bearing photons, the image characteristics as a function of sample thickness, the dependence of transmitted light polarization and intensity on the alignment of fibers in the tissue, wavelength-dependent enhancement of contrast between fatty and fibrous tissues in the images of human breast tissues, and most importantly, the impact of the difference in scattering properties of normal and cancerous tissues on image quality. Finally, the implications of these results are discussed in Section 6.4.

6.2 Materials and Methods

6.2.1 Experimental Arrangement

The experimental arrangement used for NIR imaging is displayed schematically in Fig. 6.1. The 1250 nm continuous-wave (CW) mode-locked output of a Cr^{4+}:Forsterite laser pumped by a Nd:YAG laser was expanded and collimated to an approximately 8-mm-diameter beam and used to illuminate the sample. A fraction of the 1064 nm Nd:YAG laser output was picked up using a beamsplitter and was collimated and attenuated to have similar beam diameter and average power as the Cr^{4+}:forsterite laser beam. The optical power was maintained at approximately 100 mW for both the beams. Both the beams were linearly polarized along the horizontal direction.

A $4f$ Fourier space gate was realized by placing the sample at the back focal plane of a 20 cm focal-length lens and a variable-diameter aperture at the front focal plane with

the center of the aperture at the focus. Another 20 cm focal-length lens placed on the optical axis at a distance of 20 cm from the aperture collected and collimated the low-spatial-frequency light filtered by the aperture, and directed it to an InGaAs NIR area camera (Sensors Unlimited SU 128-1.7RT) placed at its front focal plane. The camera had a 128x128 pixels sensing element with a pixel size of 25 μm.

Since the incident light was linearly polarized, the polarization gate was implemented simply by using a linear polarizer before the camera to measure the components of the transmitted light polarized parallel (||) and perpendicular (⊥) to that of the incident light.

In order to measure the quality of the images, the contrast of the image was monitored, and it has been defined here as

$$C = (I_{max} - I_{min})/(I_{max} + I_{min}), \tag{6.1}$$

where I_{min} is the minimum value of the transmitted intensity on the shadow image, and I_{max} is the maximum value of transmitted intensity in the immediate vicinity of the shadow image. Figure 6.2 shows a schematic diagram of a shadow image casted by an object after being illuminated by a light source. The dashed rectangular box in the shadow image indicates the integrated intensity area (pixels) used to plot the spreading of the shadow image. I_{max} and I_{min} values are obtained from the intensity plot, as shown.

6.2.2 Sample Characteristics

The object used for imaging was a 1.5-mm-diameter aluminum rod painted black. Scattering media included samples of excised human breast and animal tissues, as detailed below.

(a) The normal and cancerous human breast tissue samples used included two normal and one cancerous each of which had a nominal thickness of 5 mm and lateral dimensions between 10 to 14 mm. The tissues were from the left breast of a 61 year old female patient, and were made available to us by National Disease Research Interchange (NDRI). An accompanying biopsy report interpreted the malignancy as infiltrating lobular carcinoma with focal intraductal carcinoma and noted that the specimen showed very severe cytologic atypia. The cancerous tissue sample had cancer throughout the entire specimen and the available literature value[6.6] of transport length l_t for such a specimen at 789 nm is approximately 1 mm, while that for the normal sample is approximately 1.7 mm.

(b) A normal human breast tissue sample obtained from the left breast of a 28 year old female patient following reduction mammoplasty was made available to us by NDRI. The specimen was composed of fat tissue with broad strands of firm fibrous tissue. The dimension of the specimen was approximately 70 mm x 50 mm x 5 mm. A 35 mm x 14 mm x 5 mm section of it comprising fat tissue in the middle and fibrous tissue on the two sides was used in the experiment reported. Available literature values[6.6] of transport length l_t for normal fatty and fibrous breast tissues at 789 nm are approximately 1.3 mm and 0.7 mm, respectively.

(c) Bovine brisket tissues, porcine leg-muscle tissues, and gallinaceous (chicken) breast tissues were obtained from a local butcher. Values l_t for all three types (bovine, gallinaceous, and porcine) of muscle tissues were available[6.7] only for 633 nm and are 2.27 mm, 3.03 mm, and 8.33 mm, respectively.

The biological tissue samples were placed in a container with two movable parallel glass plates that slightly compressed them in an attempt to maintain an overall uniform thickness. The tissue samples were frozen for storage and thawed before making measurements.

6.3. Results

6.3.1 Wavelength Dependence

Wavelength dependence studies on transillumination imaging using intralipid suspensions in water have been discussed in Ref. 6.8. This reference shows that the image contrast is much higher for 1250-nm illumination than for 1064-nm light, for the same levels of intralipic concentration. Since ¾ of the human body contains water, similar results were expected to take place on transillumination images of human and animal tissues. The observed dependence of image quality on the wavelength of the light source will be discussed in Sections 6.3.5 and 6.3.6 of this chapter.

6.3.2 Fourier Space Gate Enhances Image

The role of Fourier spatial filtering in discriminating against multiple scattered light and enhancing the image quality was investigated by recording the transillumination

images of the 1.5 mm-diameter black metal rod embedded horizontally in the middle of bovine tissue samples as a function of the diameter of the aperture in the Fourier spectral plane (focal plane of the first lens). The variation in the aperture diameter controlled the relative magnitude of lower-spatial-frequency light (ballistic and snake) and the higher-spatial-frequency light (multiple-scattered) that reached the image plane. The efficacy of Fourier spatial filtering is demonstrated in Figs. 6.3(a) and 6.3(b) that display the images of the 1.5 mm diameter rod embedded horizontally in the middle of a 12 mm thick bovine brisket tissue for aperture diameters of 0.9 mm and 6 mm, respectively. The shadow of the rod is apparent in Fig. 6.3(a) but is not observed in Fig. 6.3(b). The normalized spatial intensity distribution integrated along the same vertical region (marked by dashed lines) of both the images are shown in the curves of Fig. 6.3(c). The thin and thick lines show the spatial profiles of the images recorded with 6-mm diameter aperture and 0.9-mm-diameter apertures, respectively. The dip in the intensity profile (thick line) shows the position of the rod. No such dip is observed in the other profile (thin line) since the 6 mm-diameter aperture lets enough multiple-scattered light through to completely masks the image formed by much weaker image-bearing light.

The extent to which a Fourier gate would be effective in improving image quality, however, depends on the scattering characteristics of the sample, for example, the value of z/l_t, where z is the thickness of the scattering medium and l_t is the transport mean free path. We observed the image quality to depend more strongly on the aperture diameter for thicker samples. As an illustration, the variation of image contrast as a function of the aperture diameter when the rod was placed in the middle of a 9 mm and a 12 mm thick bovine tissue samples and imaged using 1250 nm light is shown in Fig. 6.3(d). It is

evident that the contrast decreased with the increase of the aperture diameter for both the sample thicknesses, since the larger-diameter apertures transmit more of the image-blurring light. However, the rate of contrast loss with the increase in aperture diameter is higher for the thicker sample.

The results clearly indicate that a better image contrast is obtained by closing the aperture; however, as the thickness of the sample increases the amount of light transmitted decreases, for this case the diameter of the aperture should be increased in order to be able to gather some signal. This incurs in a trade off between the image contrast and the amount of signal detected.

6.3.3 Polarization Gate Improves Image of Tissues

The polarization gate sorts out image-bearing light by using the polarization memory of the transmitted light. Scattering events depolarize a beam of linearly polarized light. Image-bearing photons are less scattered and retain more of the initial polarization compared to the multiple-scattered light. In implementing a polarization gate, images of the object inside the scattering medium are recorded with a linear polarizer oriented parallel ('parallel image') and perpendicular ('perpendicular image') to the polarization direction of the incident light. The parallel image is generally expected to have a better contrast than the perpendicular image. The 'difference image' obtained by subtracting the perpendicular image from the parallel image is even more free from the noise due to scattered light.

Quantitatively, the extent of depolarization of incident polarized light due to scattering in the intervening medium may be described in terms of the degree of polarization, D of the transmitted light, defined as

$$D = (I_{||} - I_{\perp}) / (I_{||} + I_{\perp}), \tag{6.2}$$

where $I_{||}$ and $I_{\perp}$ are transmitted intensities of light with the same polarization and orthogonal polarization with respect to the incident light, respectively. The degree of polarization is ideally expected to be unity for ballistic light, zero for completely depolarized light, and between 1 and 0 for the snake light. The snake light with higher values of D will form sharper shadowgrams than that formed by lower D-value snake light.

Figures 6.4 (a), (c), and (e) show the parallel, perpendicular, and difference transillumination images, respectively, of the metal bar placed horizontally in the middle of a 9 mm-thick bovine tissue sample. Corresponding spatial intensity profiles along the same vertical region of all three images are shown in Figs. 6.4(b), (d), and (f), respectively. The values of contrast for the parallel, perpendicular, and difference images are 0.31, 0.18, and 0.65, respectively. The remarkably higher value of contrast in the difference image demonstrates that the polarization difference imaging is a useful technique in enhancing the images of an object inside a scattering medium.

Enhancement of image quality using a polarization gate does not continue indefinitely. As the value of z/l_t, where z is the thickness of the scattering medium and l_t is the transport mean free path, increases the difference between $I_{||}$ and $I_{\perp}$ and the

magnitude of D decreases and image quality becomes poorer. The variation of contrast C and the degree of polarization, D as a function of bovine brisket tissue thickness is presented in Fig. 6.5. In this figure, the ellipses present values of D, while the triangles and the rectangles present the values of contrast for parallel and perpendicular images, respectively. It is evident that the contrasts for both the polarizations decrease with tissue thickness as does the degree of polarization. What is more important is that the difference between the contrasts for the two polarizations also decreases and is not appreciable for a bovine brisket tissue sample thickness of 16 mm. The maximum thickness of a sample over which the polarization gate would be effective depends on the photon transport characteristics of the sample. By the same token, polarization difference schemes usually used in imaging techniques would fail to improve the image or withdraw any information since, in very thick samples, the parallel and perpendicular intensity components are identical.

6.3.4 Imaging Dependence on Tissue Structure

The experimental results on photon transport dependence on tissue structure obtained in chapter 5 were tested by using bovine muscular fibrous tissues *in transillumination imaging* experiments performed in this section.

In order to examine the effect of the sample orientation—with respect to the polarization direction of the incident beam—on the image quality, we examined the images of the 1.5 mm diameter black metal rod embedded in a bovine brisket tissue sample, 10-mm thick. The incident beam fell perpendicularly to the fibers in the sample.

The orientation of the fibers in the tissue with respect to the polarization of the incident beam was changed by rotating the sample. The image contrast using the 'parallel' component ($I_{||}$) of the transmitted intensity were either better than or equal to the contrast using the 'perpendicular' component ($I_{\perp}$). Figure 6.6 (a), (b), and (c) are the images of the rod obtained using the parallel component of the light transmitted ($I_{||}$) for the fibers oriented at $\theta = 0^0$, 45^0, and 90^0, respectively. When the fibers were perpendicular (orientation 90^0) to the polarization of the incident beam there was a significant improvement in the image contrast. The spatial intensity profiles of the images integrated along the same vertical area (dashed box) are shown in Fig. 6.7(d). The value of the image contrast for the orientations 0^0, 45^0, and 90^0 are 0.12, 0.097, and 0.18, respectively. Notice that when the sample was oriented at 45^0, the image contrast using the parallel component decayed to 0.097, almost half the maximum contrast value obtained when the sample was oriented at 90^0.

In the same fas , Figure 6.7 (a), (b), and (c) are images of the rod obtained using the perpendicular component of the light transmitted ($I_{\perp}$) for the fibers oriented at $\theta = 0^0$, 45^0, and 90^0, respectively. The spatial intensity profiles are shown in Fig. 6.7(d). The value of the image contrast for the orientations 0^0, 45^0, and 90^0 are 0.08, 0.096, and 0.08, respectively. Notice this time that when the sample was oriented at 45^0, the image contrast (0.096) was better than for the other two orientations (0.08). In general, images obtained using the parallel component were better than the images obtained using the perpendicular component. This was expected since unscattered photons will preserve and keep the same polarization as the incident beam.

Plot in Figure 6.7 (e) corresponds to the image contrast value found in figure 6.6 (d) and in figure 6.7 (d) as a function of structure orientation. The contrast value obtained using the parallel component was plotted using open circles (o), while the ones obtained using the perpendicular value have been plotted using dark squares ( ). It is interesting to note that the image contrast plot follow the plot obtained for light transmission vs. structure orientation shown in Fig 5.14.

6.3.5 Imaging Through Biological Tissues

Imaging measurements were next extended to bovine, porcine and gallinaceous tissues of different thicknesses. The objectives were: (a) to test the feasibility and efficacy of optical imaging through different types of tissues; (b) to compare the imaging performance of 1250 nm and 1064 nm lights; and (c) to estimate the optimal thickness of tissues of different types that one can image through with a reasonable image quality. For these measurements the 1.5 mm diameter black metal rod was embedded in the middle of tissues of different thicknesses. One of the objectives was to image through as thick a tissue as possible with the same experimental arrangement, and to make optimal use of the weak transmitted light was an important consideration in signal collection. Within the sensitivity limit of our experimental arrangement, it was found that the polarization gate did not appreciably improve the image quality for samples beyond certain thickness. This thickness depends on the photon transport characteristics of the sample used (for the bovine sample this thickness is around 16mm). Since the sheet polarizer absorbs a fraction of the light that traverses it, the polarizer sheet was removed to avoid transmission loss and ensure higher incident fluence for imaging through thick samples.

As demonstrated in Section 6.3.3, polarization gate helps improve image for thinner samples. But we did not use it in these measurements in order to maintain identical experimental conditions for both thick and thin samples so that the results could be compared. The diameter of the aperture in the Fourier gate was maintained at 1.5 mm. For every sample thickness, a composite image of the object was constructed from a sum of 3 grabbed frames by the frame grabber. The same sample and experimental arrangements were used for imaging with both 1250 nm and 1064 nm.

In addition to the image contrast (e.g., C), we also monitored the relative lateral size, W of each of the images for tissue samples. (See Fig. 6.2) The relative lateral size was defined as

$$W = W_S / W_W, \tag{6.3}$$

where W_S and W_W are the full widths at half maximum (FWHM) of the spatial intensity profile of the shadow image of the object measured through the scattering medium and through clear water, respectively. The spreading provides a way to measure the spatial resolution of the image. The spreading $W = W_S / W_W = 1$ is obtained when $W_S = W_W$ which would imply that there is no scattering taking place in the medium and therefore no shadow-image spreading. A shadow image spreading will occur in a scattering medium, for which case $W_S > W_W$.

The contrast, C and relative lateral size, W of images recorded using 1250 nm and 1064 nm lights for sample located inside gallinaceous (chicken), bovine, and porcine tissues of different thicknesses are presented in Figs. 6.8(a), 6.8(b), and 6.8(c),

respectively. Contrast, C is represented by triangles and relative lateral size, W by circles. Filled circles and triangles pertain to measurements made using 1250 nm light, while open circles and open inverted triangles denote measurements carried out at 1064 nm.

The salient features of the data are as follows. First, the contrast decreased with the sample thickness for all three types of tissues. The loss of contrast was accompanied by a corresponding loss in the spatial resolution of the image as manifested by increase in the value of W. Since the point spread function of an imaging arrangement changes with the thickness and scattering characteristics of the sample,[6.10] this result is expected. Second, for the same type of tissue of a given thickness, 1250 nm light provided better contrast and significantly higher spatial resolution compared to 1064 nm light. An implication of this result is that the 1064 nm light is scattered more strongly by tissues than the 1250 nm light. Third, for the same tissue thickness both the contrast and the spatial resolution of the images were the highest when the object was located inside the gallinaceous tissue, next highest were for bovine and then porcine tissues. The result implies that among these three types of tissues, the porcine tissue is the most scattering, followed by the bovine and the gallinaceous tissues. We do not have values of optical transport coefficients for the bovine, gallinaceous, and porcine tissues for the two wavelengths used in the study, so a correlation of the observed behavior with transport properties is not feasible. The available values[6.7] of transport length of 2.27 mm and 3.03 mm at 633 nm for bovine and gallinaceous tissues are consistent with these measurements. However, l_t =8.33 mm for porcine tissue does not follow the observed behavior. Precise data at appropriate wavelengths are necessary to find a meaningful

correlation. Finally, we have demonstrated the ability to image a 1.5 mm diameter rod with reasonable contrast and resolution through 26 mm gallinaceous, 22 mm bovine, and 20 mm porcine tissue samples using 100 mW average power. Transillumination images through thicker samples may be obtained by: (a) increasing the fluence of the incident beam of light; (b) using a camera with higher sensitivity, resolution and lower noise than the 128x128 pixels camera used in the present work; and (c) improving the optical system for signal acquisition.

6.3.6 Imaging Through Human Breast Tissues

6.3.6.1 Cancer and Normal Tissue Samples

The utility of an optical imaging method would ultimately be determined by its ability to image through human tissues, and more so by its ability to distinguish between normal and malignant tissues. We used the near-infrared imaging arrangement described in Section 6.2 to obtain images of the 1.5 mm diameter rod placed inside human breast tissues. The objective was to explore if the characteristics of the image change when the object is placed inside a cancerous tissue as compared to the normal tissue. Appreciable differences in image characteristics may in turn provide useful information that help distinguish between normal and cancerous tissues.

For these measurements we used the normal and cancerous human breast tissue samples described in Section 6.2.2(a) in two configurations. First, the rod was sandwiched between the two normal breast tissues, each of which had a nominal thickness of 5 mm. Next the rod was placed between the 5 mm thick cancerous breast

tissue and a 5 mm thick normal breast tissue. The overall sample thickness in both the configurations was 10 mm. Figure 6.9(a) presents an image of the rod sandwiched between the normal tissues. Figure 6.9(b) shows the corresponding image when the rod was placed between a normal and a cancerous tissue. Both the images were recorded using 1250 nm light and a 1.5-mm aperture in the Fourier gate. Polarization gate was not used since at this thickness of human breast tissues, the polarization gate did not improve the image significantly. The normalized spatial intensity distribution integrated over the same horizontal area of both the images as highlighted by the dashed boxes in Figs. 6.9(a) and 6.9(b) are displayed in Fig. 6.9(c). The contrast of the image of the rod in Figs. 6.9(a) and 6.9(b) is 0.081, and 0.075, respectively. The relative lateral size of 2.7 for the normal-cancerous sample is almost a factor of 2 larger than that of 1.4 for the normal-normal sample. This dramatic change in the spatial resolution indicates that this kind of cancerous tissue is much more highly scattering than the normal human breast tissue. Although we do not have data for 1250 nm, the above observation is consistent with values obtained at at 789 nm where the transport length of cancerous and normal human breast tissues are of 1.0 mm and 1.7 mm, respectively.

6.3.6.2 Fatty and Fibrous Human Breast Tissue Samples

Transmission spectrum for a human breast tissue sample exhibit a local minima around 1203 nm that has been attributed to absorption by fat.[6.11] In order to explore the possibility that wavelength-dependent difference may provide a fingerprint for identification of tissues in the transillumination image, we compared images of the

normal human breast tissue sample that was comprised of fatty and fibrous tissues described in Section 6.2.2(b) using 1225 nm and 1250 nm wavelengths from the Cr^{4+}:Forsterite laser. While 1225 nm falls on the absorption band attributed to fatty tissues, 1250 nm is completely nonresonant with it. Optical transmission through a 3 mm thick slab of breast tissue is reported to be approximately 0.26 at 1225 nm and 0.32 at 1250 nm.[6.11] Two-dimensional transillumination images of the 5 mm thick sample recorded using 1225 nm and 1250 nm wavelengths are shown in Figs. 6.10(a) and 6.10(b), respectively. The fatty region in the middle of the specimen appears darker and distinct from the fibrous regions on the two sides in the 1225 nm image. No appreciable difference between the regions is observed in the 1250 nm image. The corresponding spatial intensity profiles integrated over the areas highlighted by white dashes are displayed in Fig. 6.10(c). The fatty region shows up as a distinct dip in the 1225 nm image profile, while no such dip is observed in the 1250 nm profile. This result clearly demonstrates that even a small spectroscopic difference may act as a fingerprint and enhance contrast between the images of different types of tissues.

6.4. Discussion

A salient observation of this work is that the near-infrared light around 1250 nm enables deeper penetration and provides higher image contrast than that obtained using 1064 nm or shorter-wavelength light. The absorption coefficient of water was measured and found to be 0.07 cm^{-1} at 1064 nm and 0.42 cm^{-1} at 1250 nm, respectively. Consequently 1250 nm light would be more strongly attenuated due to absorption by water (found in tissues) when compared to the 1064 nm light. Similar wavelength

dependence of optical transport properties was observed in various biological tissues as shown in Figs.6.8 and 6.10. The experimentally observed deeper penetration using 1250 nm light and the results displayed in Fig. 6.8 thus imply that the scattering cross section of the scatters in the tissue are much larger at 1064 nm than that at 1250 nm. The overall reduced scattering coefficient is thus higher at 1064 nm than that at 1250 nm. The somewhat higher overall absorption at 1250 nm also helps to enhance contrast by attenuating multiple-scattered light more than the image-bearing ballistic and snake light.[6.12] The higher attenuation of multiple-scattered light occurs because it traverses a longer path inside the medium than the image-bearing light, and the light intensity attenuates exponentially with distance due to absorption. A combination of lower scattering and higher absorption accounts for the better image quality obtained using 1250-nm light.

The Cr^{4+}:Forsterite laser, with its output centered on 1250 nm and continuously tunable[6.13] from 1150 nm to 1350 nm, is now well-developed and has already been used in optical coherence tomography.[6.14] This laser is expected to be even more useful in transillumination imaging through thicker tissues and in microscopic or backreflection imaging of structures deeper in tissues than other lasers operating at shorter wavelengths. Since its output tunes through an optical absorption band of human fatty tissues, it promises to be useful in diagnostic spectroscopic imaging involving these tissues. This will be treated in more detail in Chapter 8.

The polarization gate and the Fourier gate were both found to be effective in sorting out some of the image-bearing photons. The polarization gate is simple and easy to implement. Its efficacy for transillumination imaging is limited by sample thicknesses

for which the polarization of the transmitted light is completely randomized by scattering events within the tissue. In our experimental arrangement, this limit was 10 mm for human breast tissues, and 16 mm for bovine brisket tissues. However, the polarization gate promises to be more effective in subsurface imaging using backscattering geometry.[6.15] In that arrangement it can greatly reduce the reflected light from the surface which is dominantly polarized parallel to the incident light and contributes a strong noise to weaker signal from subsurface structures.

The Fourier gate, in principle, may be effective in discriminating against multiple-scattered photons for samples of any thickness. However, its effectiveness is more pronounced for sampleswith thickness in intermediate scattering regime. It cannot discriminate against on-line scattered photons. As the thickness of the turbid sample increases, the relative magnitude of image-bearing photons decreases and that of the on-line scattered photon increases, making the signal-to-noise ratio poorer. When combined with a time gate both the polarization gate and the Fourier gate may provide much stronger discrimination of multiple-scattered light.

A major observation of this work is that cancerous human breast tissue scatters light much more strongly than the normal tissues. Measurements on more specimens are required to establish if this observation holds in general for all types of carcinoma. A large difference in the scattering characteristics between the normal and cancerous tissues is expected to provide an opportunity for distinguishing them by using time-resolved imaging techniques. (Time-sliced transillumination images will be covered in chapters 7 and 8). Proper time gating may take advantage of this temporal behavior of transmitted light to accentuate the difference between the normal and cancerous regions.

By tuning the Cr:forsterite laser output into an absorption band of fatty human breast tissue. we obtained images that had marked contrast between the fat and fibrous tissues. The result is significant since it demonstrates that spectroscopic differences can enhance image contrast and may provide diagnostic ability. It also highlights the usefulness of the wavelength agility afforded by a Cr^{4+}:Forsterite laser for biomedical imaging applications. A more detailed spectroscopy imaging study using transillumination technique will be covered in Chapter 8.

Another interesting finding of this study is the polarization-orientation dependence of the transmitted image-bearing light. The observed existence of preferred orientation of muscle tissue fibers for higher transmission of image-bearing light is an useful information for optimizing the performance of a transillumination imaging system. The obvious question is: what is the origin of this dependence? Bovine muscle tissues are known to exhibit birefringence[6,16] that may have an effect on the polarization characteristics of the transmitted light. Detailed information about tissue fiber ultrastructure, molecular constituents, and their distribution along fiber are necessary to develop an understanding of the observed anisotropy. We have observed similar polarization anisotropy of light transmission through the leaves of palm trees as well. Elucidation of the origin of this polarization anisotropy in biological systems remains an interesting problem.

6.5 References

6.1 For a brief review of optical imaging techniques, see S. K. Gayen and R. R. Alfano, Emerging optical biomedical imaging techniques, Opt. Phot. News 7 (3), 17-22,1996.

6.2 B. E. A. Saleh and M. C. Teich, *Fundamentals of Photonics*, John Wiley and Sons, Inc., New York, 136-139, 1991.

6.3 J. J. Dolne, K. M. Yoo, F. Liu, and R. R. Alfano, "IR Fourier space gate and absorption imaging through random media," Lasers Life Sci., 6, 131-141, 1994.

6.4 H. Horinaka, K. Hashimoto, K. Wada, and Y. Cho, "Extraction of quasi-straightforward-propagating photons from diffused light transmitting through a scattering medium by polarization modulation," Opt. Lett. 20, 1501-1503, 1995.

6.5 S. G. Demos and R. R. Alfano "Temporal gating in highly scattering media by the degree of optical polarization," Opt. Lett. 2, 161-163 (1996).

6.6 T. Troy, D. Page, and E. Sevick-Muraca, "Optical properties of normal and diseased breast tissues: prognosis for mammography," J. Biomed. Opt., 1, 342-355, 1996. Tabulated values of optical transport properties vary widely. We chose values corresponding to those specimens in the table that closely matched the characteristics of our sample, such as, nature and extent of cancer in the cancerous specimen, relative distribution of constituents such as normal, fibrous and fat tissues in the normal specimens, and age of the patient.

6.7 W. Cheong, S. A. Prahl, and A. J. Welch, "A review of the optical properties of biological tissues," IEEE J. Quantum Electron., 26, 2166-2185, 1990.

6.8 S. Gayen, M. E. Zevallos, M. Alrubaiee, J. M. Evans, and R. R. Alfano, "Two-dimensional near-infrared transillumination imaging of biomedical media with a chromium-doped forsterite laser" Appl. Opt. Vol., 37, No. 32, 1998.

6.9 S. L. Jacques, "Origins of tissue optical properties in the UVA, visible, and NIR regions," in OSA TOPS on *Advances in Optical Imaging and Photon Migration 1996*, Vol. 2, R. R. Alfano and J. G. Fujimoto (eds.), Optical Society of America, Washington D. C., 364-371, 1996.

6.10 J. A. Moon, P. R. Battle, M. Bashkansky, R. Mahon, M. D. Duncan, and J. Reintjes, "Achievable spatial resolution of time-resolved transillumination imaging systems which use multiply scattered light," Phys. Rev. E ., 53, 1142-1155, 1996.

6.11 F. A. Marks, "Optical determination of the hemoglobin oxygenation state of breast biopsies and human breast cancer xenografts in nude mice," SPIE, 1641, 227-237, 1992.

6.12 K. M. Yoo, Z. W. Zang, S. A. Ahmed, and R. R. Alfano, "Imaging objects hidden in scattering media using fluorescence-absorption techniques," Opt. Lett., 16, 1252-1254, 1991.

6.13 V. Petricevic, S. K. Gayen, and R. R. Alfano, "Near infrared tunable operation of chromium-doped Forsterite Laser", Appl. Opt., 28, 1609-1611, 1989.

6.14 E. Bouma, G. J. Tearney, I. P. Bilinsky, B. Golubovic, and J. Fujimoto, "Self-phase-modulated Kerr-lens-modelocked Cr:forsterite laser source for optical coherence tomography," Opt. Lett., 21, 1839-1841, 1996.

6.15 S. G. Demos and R. R. Alfano, "Optical polarization imaging," Appl. Opt., 36,150-155, 1997.

6.16 J. F. de Boer, T. E. Milner, M. J. C. van Gemert, J. S. Nelson, "Two-dimensional birefringence imaging in biological tissue by polarization-sensitive optical coherence tomography," Opt. Lett., 22, 934-936,1997.

6.6 Figures

Figure 6.1 Schematic diagram of the experimental arrangement for NIR imaging of objects embedded in biological tissues and model turbid media. (A. aperture; P. linear polarizer; S. sample.)

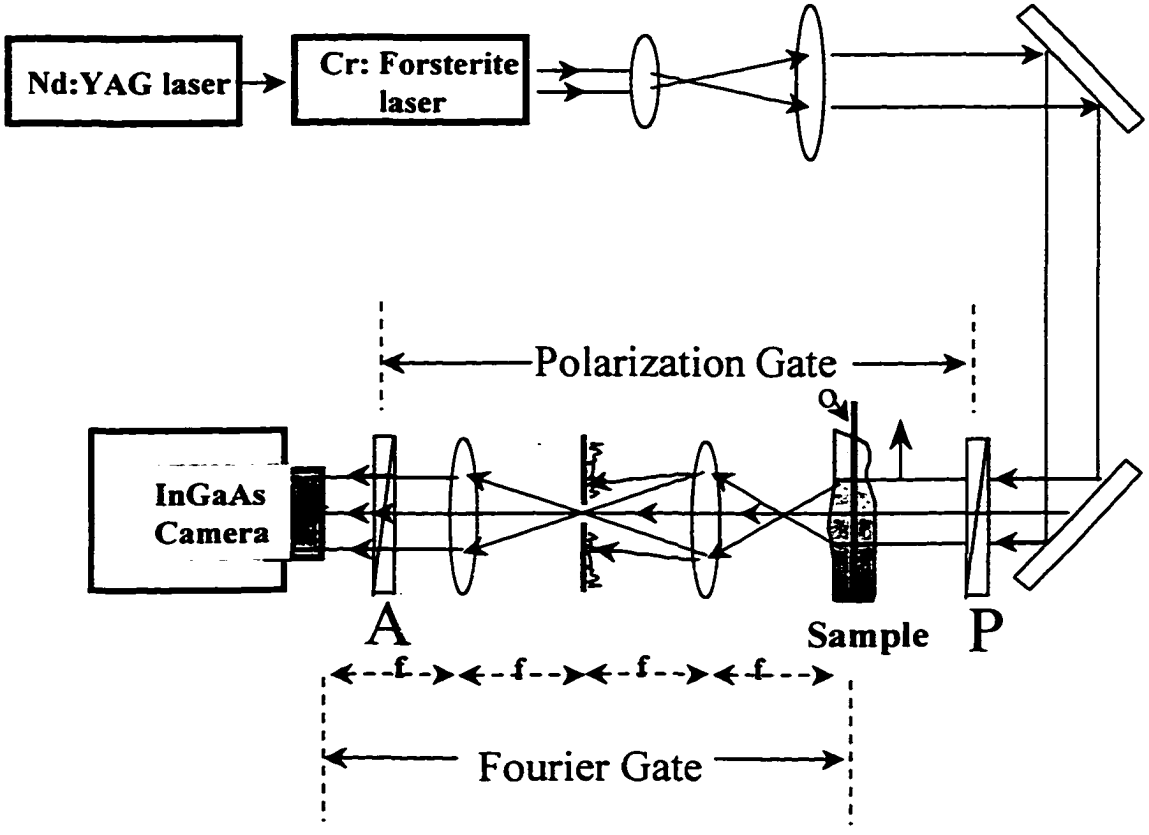

Cr:Forsterite laser :	Tuning range 1150-1350 nm, used 1250 and 1225nm
InGaAs Camera:	Area, 8 bit, 128x128 pixels
Scattering Media:	Human, Chicken, Bovine and Porcine tissues
Object (O) :	Metal rod
A:	Analyzer
P:	Polarizer

Figure 6.2 Schematic diagram of a shadow image casted by an object after been illuminated by a light source. The dashed rectangular box in the cartoon indicates the integrated intensity area (pixels) used to plot the spreading of the shadow image. I_{max} and I_{min} values are obtained from the intensity plot. as shown.

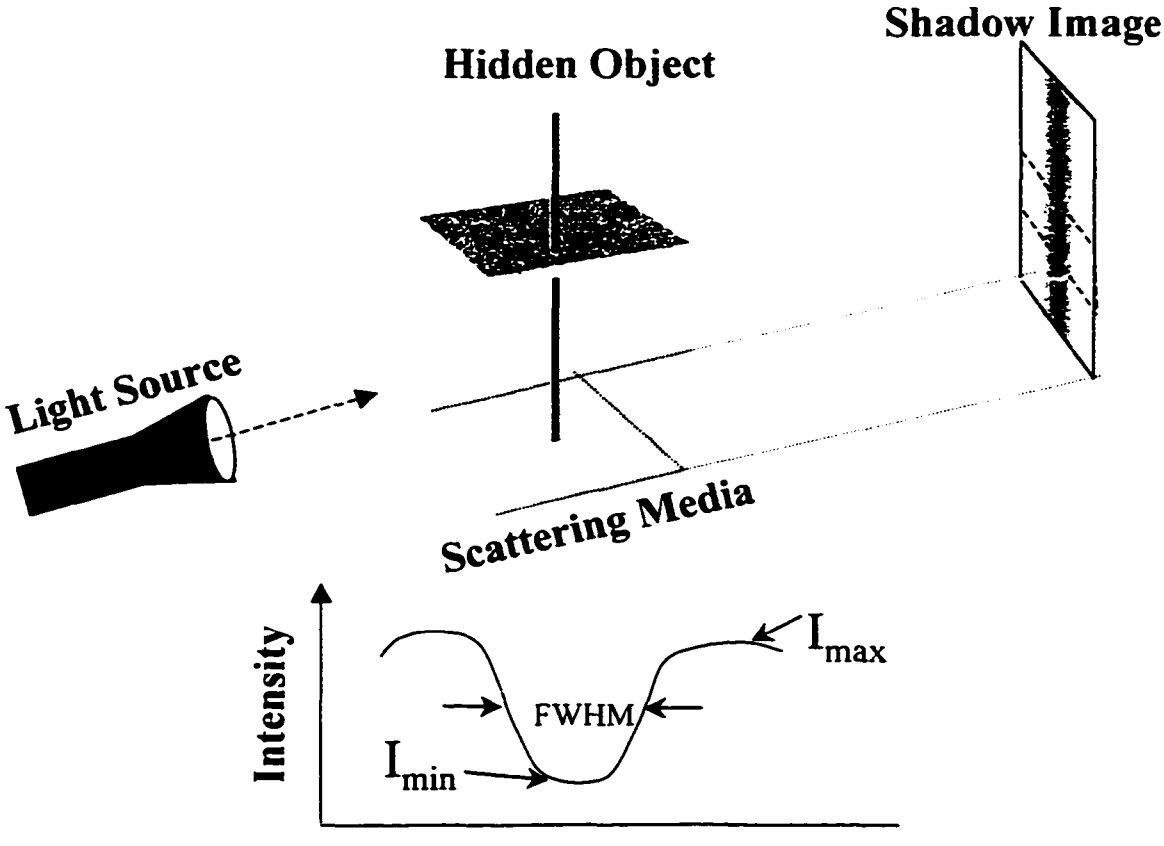

Contrast

$$C = (I_{max} - I_{min}) / (I_{max} + I_{min})$$

Relative Lateral Spreading W

$$W = W_s / W_w$$

W_s : FWHM of the Shadow image through the sample
W_w: FWHM of the Shadow image through clear water

Figure 6.3. Transillumination image of the 1.5 mm-diameter metal rod placed in the middle of a 12 mm thick bovine brisket tissue sample for aperture diameter of (a) 0.9 mm and (b) 6 mm. (c) Spatial intensity distribution of the transillumination image of Figs. 6.3(a) and 6.3(b) integrated over the area highlighted by dashed lines in respective images. (d) Contrast of the image as a function of the Fourier aperture diameter when the rod was placed in the middle of a bovine brisket tissue of thickness 12 mm (ellipses) and 9 mm (squares).

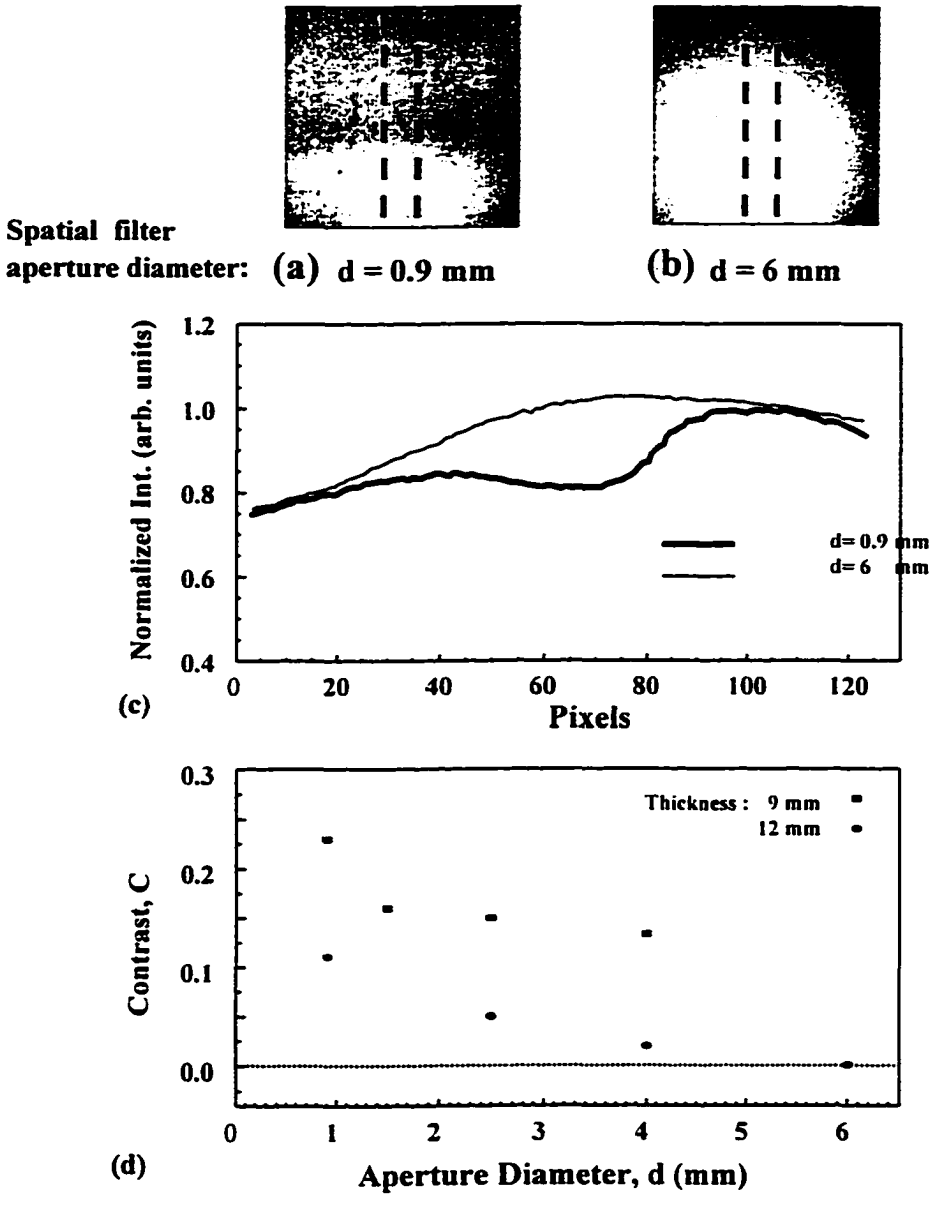

Figure 6.4. Transillumination image of a 1.5 mm black metal bar embedded in the middle of a 9 mm -thick bovine brisket tissue using a polarization gate with the polarizer before the NIR area camera oriented (a) parallel. (c) perpendicular to the incident polarization. Fig. 6.4(e) is the difference image obtained by subtracting the image in 6.4(c) from that in 6.4 (a). Figs. 6.4 (b). (d). and (f) show the normalized intensity distribution. integrated over the same vertical region highlighted by white dashed lines. in the images (a), (c). and (e), respectively.

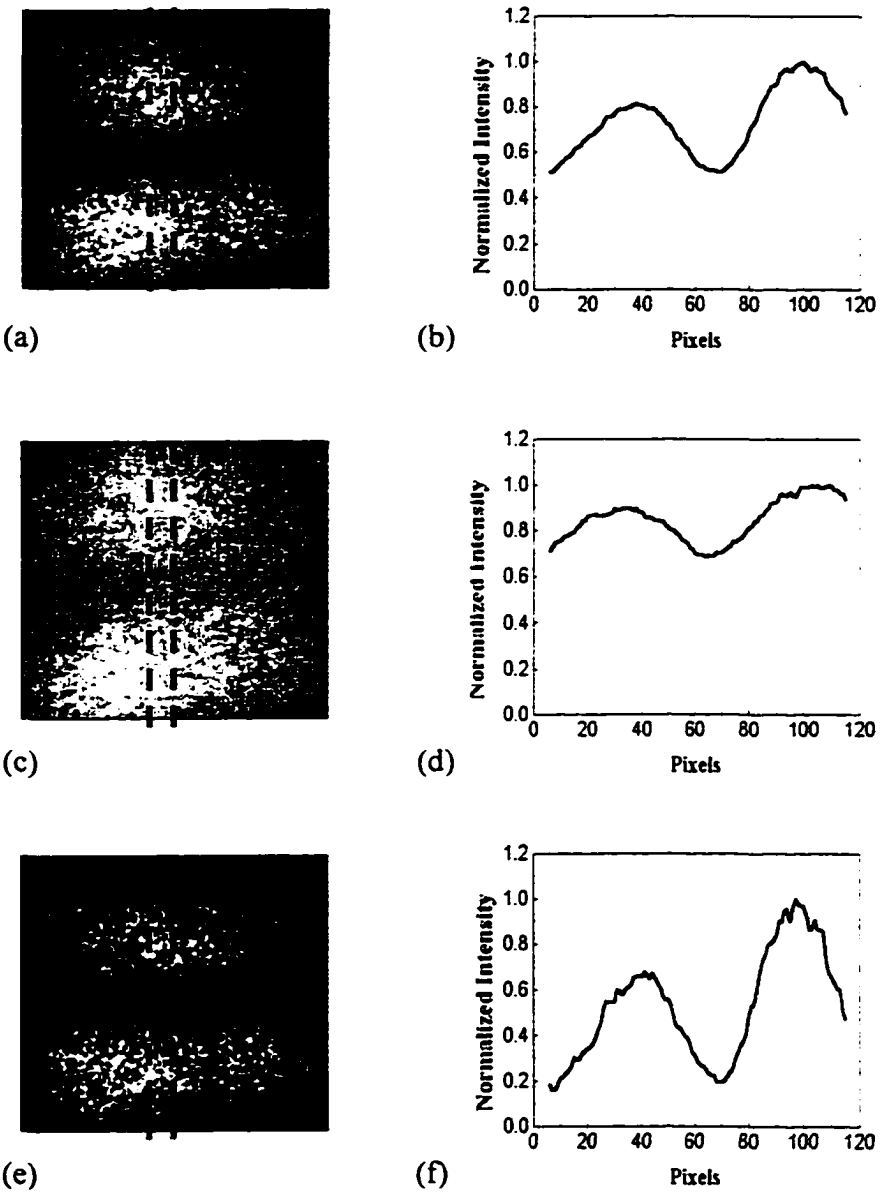

Figure 6.5 Degree of polarization D and the contrast C as a function of the thickness of the bovine brisket tissue sample. Ellipses represent the values of D, while the triangles and squares represent the values of contrast for parallel and perpendicular polarizations, respectively.

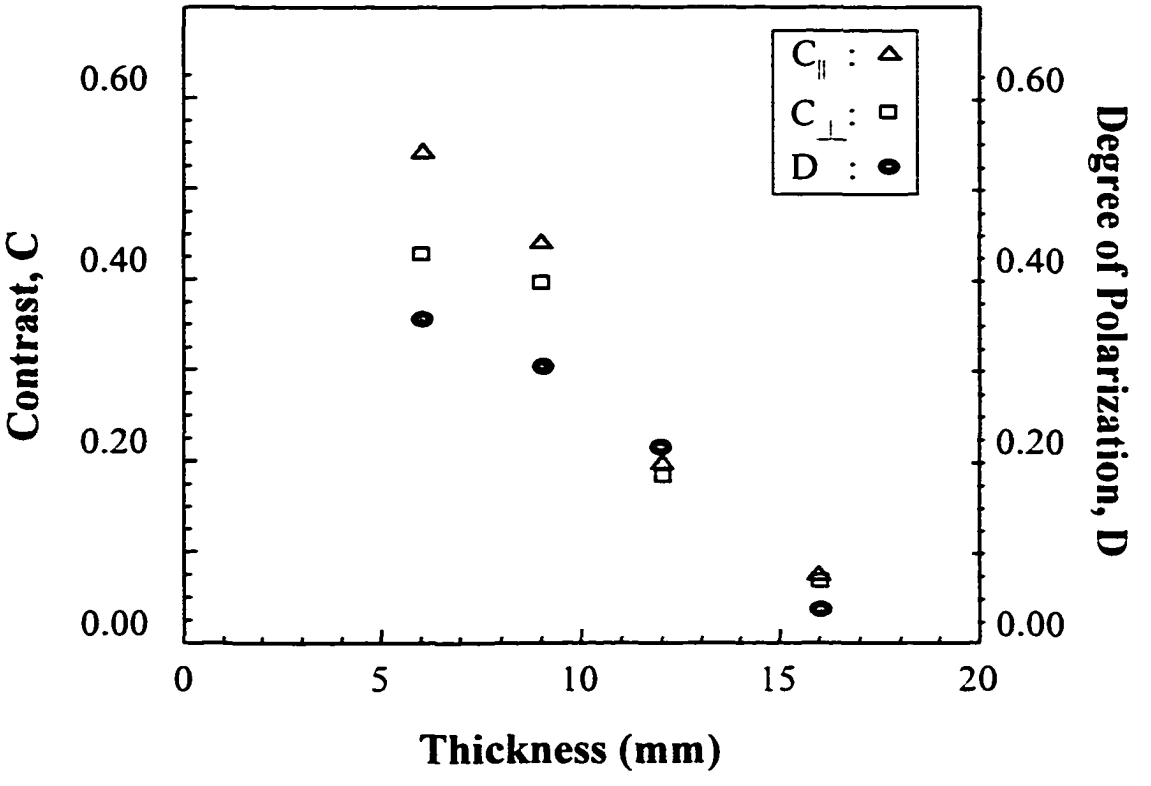

Figure 6.6 (a), (b), and (c) Transillumination images of the 1.5 mm diameter black metal rod placed in the middle of a 10 mm thick bovine brisket tissue sample for the fibers oriented at 0^0, 45^0, and 90^0. The images were obtained using the parallel component (I). Figure (d) shows the integrated intensity (marked by the square dashed boxes) for the three orientations.

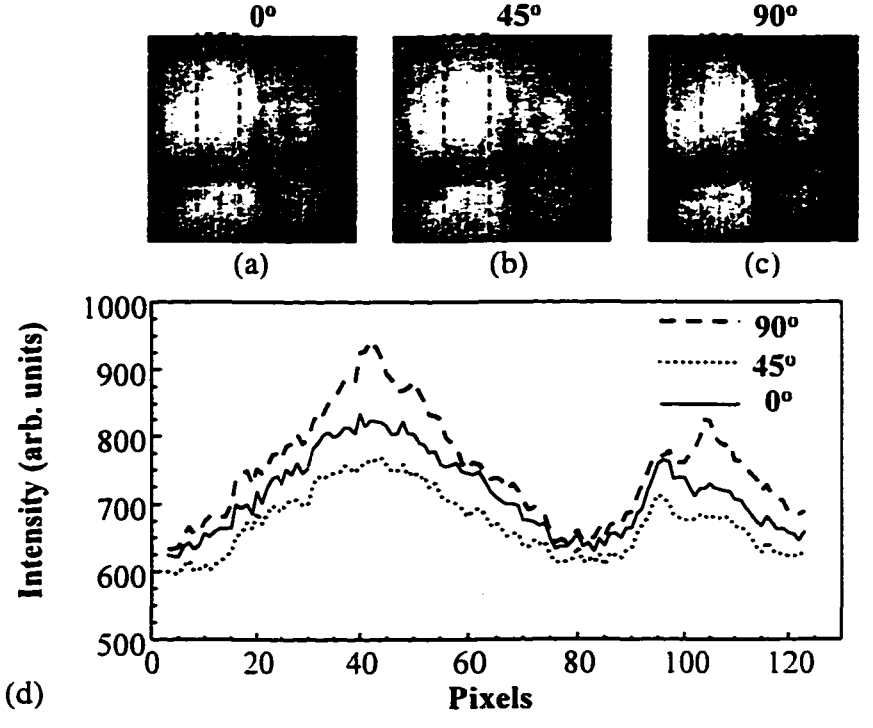

Figure 6.7 (a). (b). and (c) Transillumination images of the 1.5 mm diameter black metal rod placed in the middle of a 10 mm thick bovine brisket tissue sample for the fibers oriented at 0^0, 45^0, and 90^0. The images were obtained using the perpendicular component ($I_{\perp}$). Figure (d) shows the integrated intensity (marked by the square dashed boxes) for the three orientations.

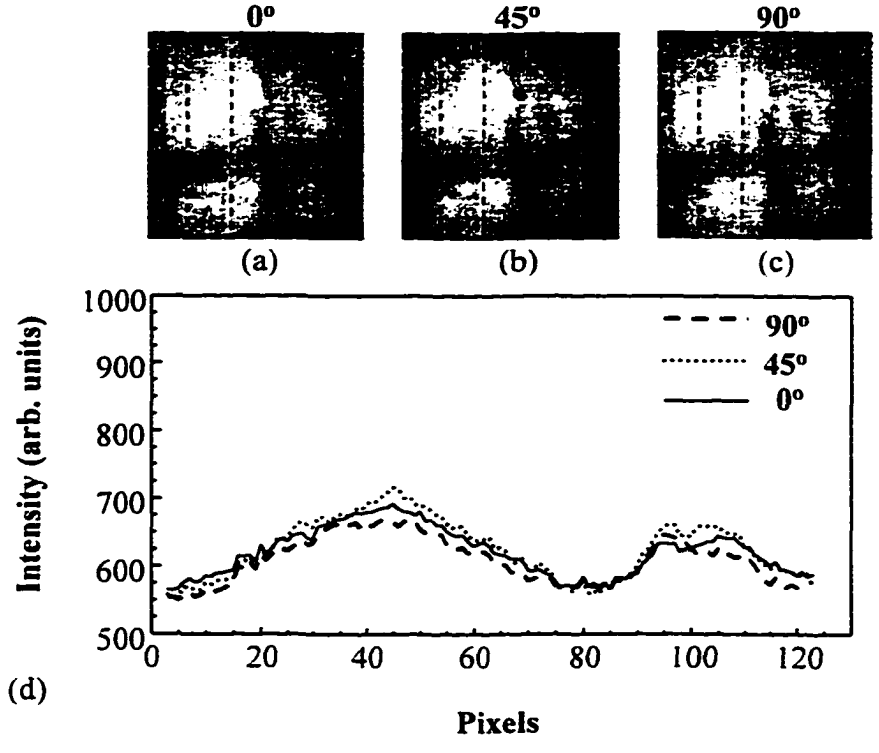

Figure 6.7 (e) Image contrast value found in figure 6.6 (d) and in figure 6.7 (d) as a function of structure orientation.

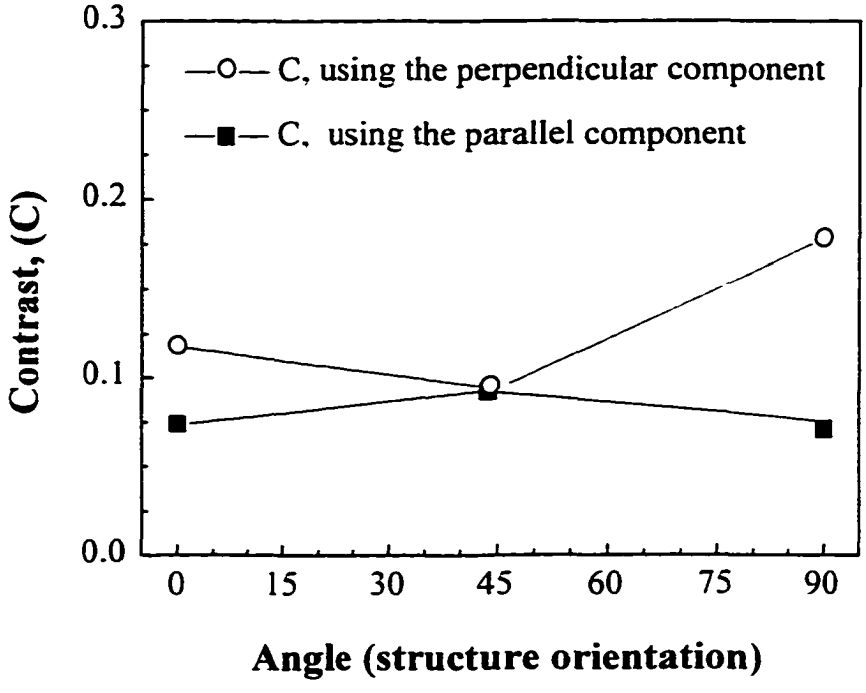

Figure 6.8 Contrast, C and the relative lateral size, W of transillumination images as a function of the thickness of (a) gallinaceous, (b) bovine, and (c) porcine tissue samples. C is represented by triangles and W by circles. Filled circles and triangles pertain to measurements made using 1250 nm light, while open circles and open inverted triangles denote measurements carried out at 1064 nm.

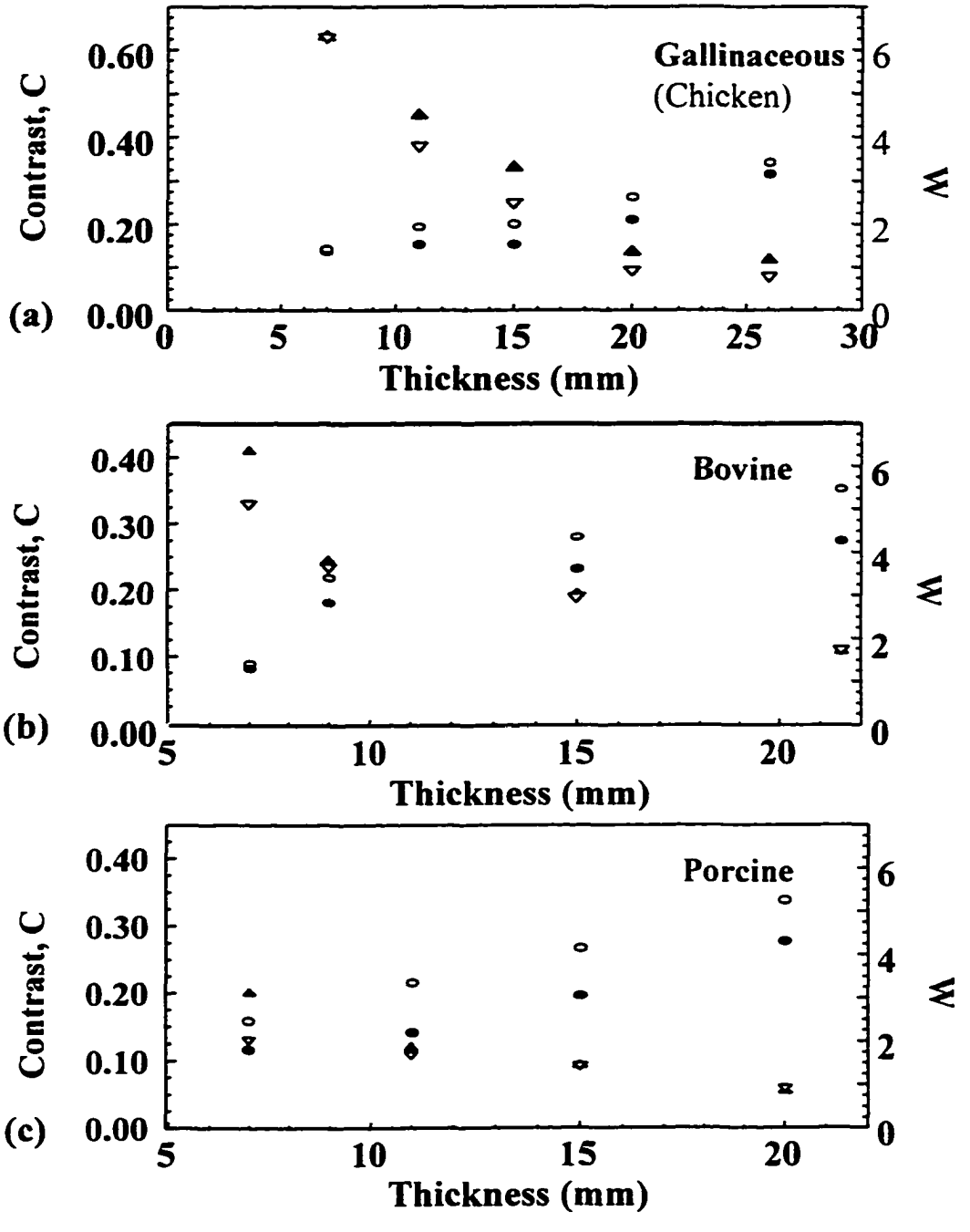

Figures 6.9 Two-dimensional transillumination images of a 1.5 mm black metal rod sandwiched between (a) two 5 mm thick normal human breast tissues, (b) a cancerous and a normal breast tissue each of which is 5 mm thick. (c) Corresponding spatial intensity profiles integrated along a horizontal area (highlighted by white dashed line) of the images. The profile of the image with both normal tissues is shown by the thick line and that containing a cancerous piece by the thin line.

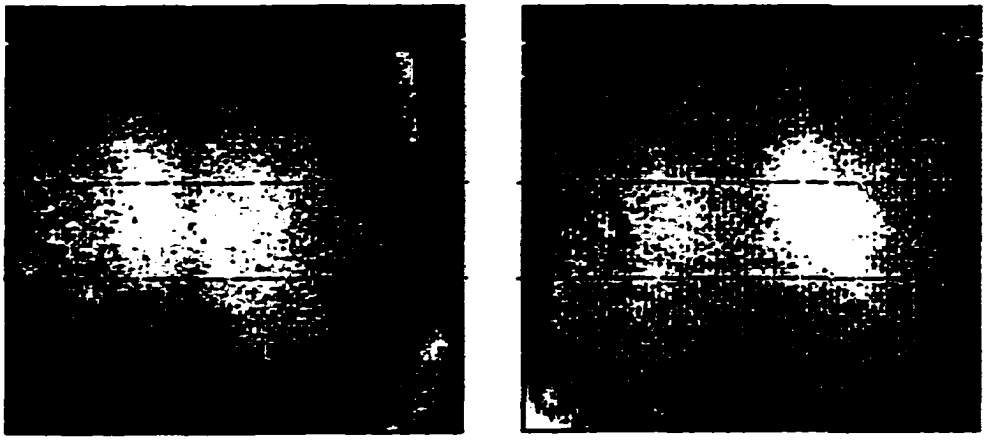

(a) Normal tissue (b) Cancerous tissue

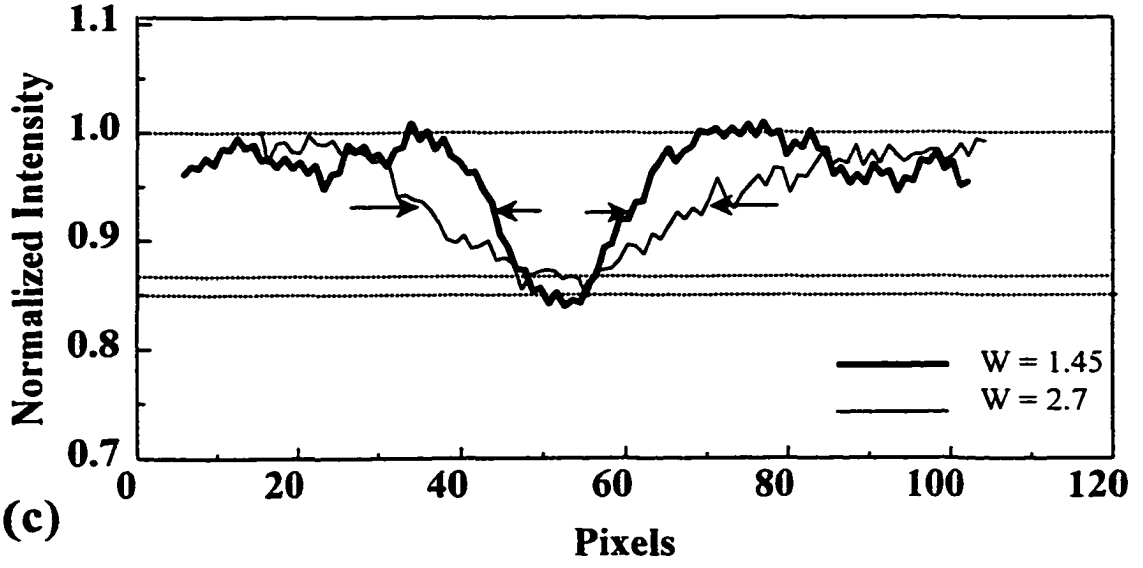

(c)

Figure 6.10 Two-dimensional transillumination images of a 5 mm thick human breast tissue sample comprising fatty and fibrous regions obtained using (a) 1225 nm light, and (b) 1250 nm light from a Cr:forsterite laser. (c) Corresponding spatial intensity profiles integrated over a horizontal area (highlighted by white dashed line) of the images. The lateral dimension of the sample was 35 mm X 14 mm.

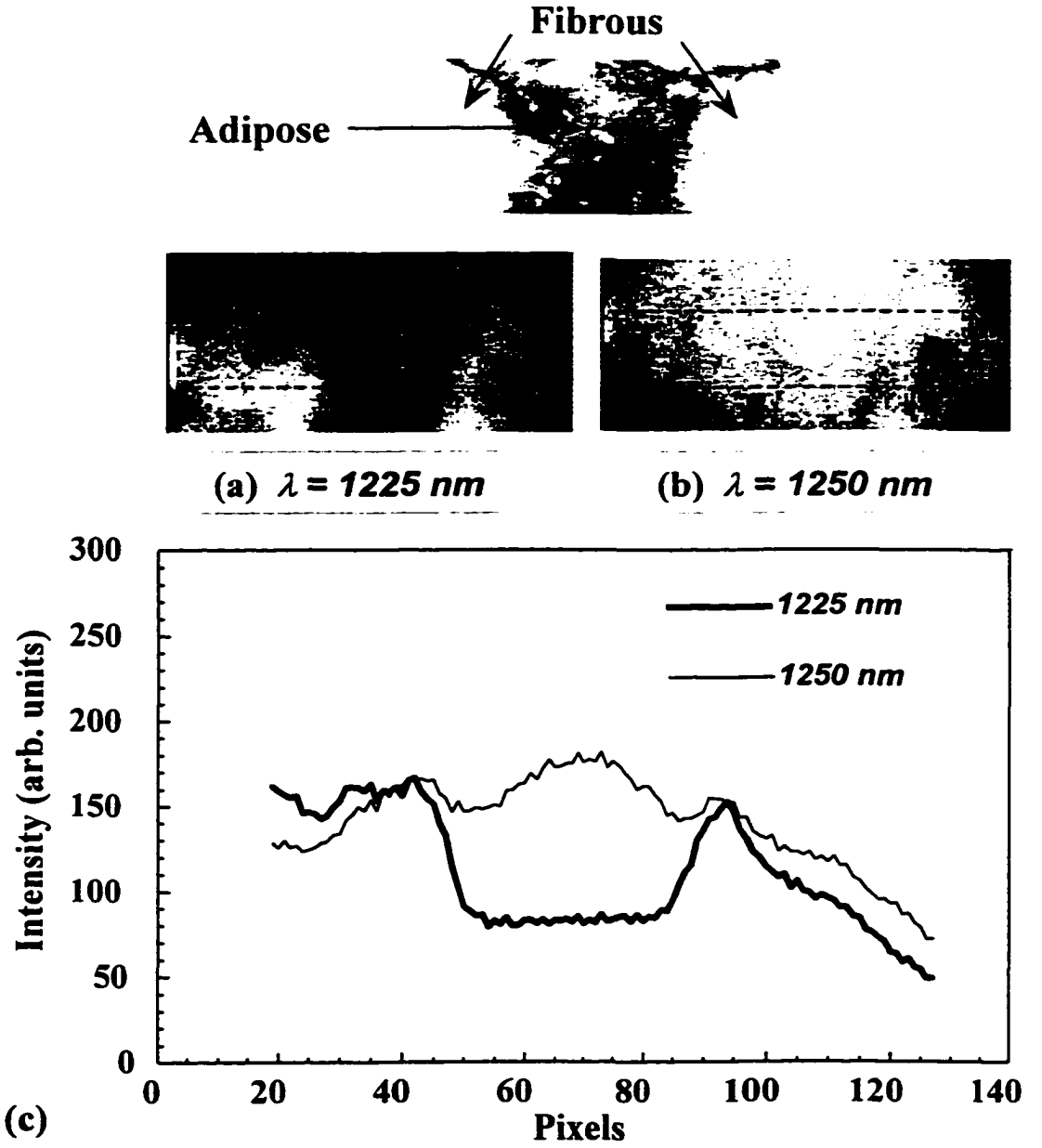

Chapter 7

Two-Dimensional *Time-Sliced* NIR Transillumination Imaging of biological media

7.1 Introduction

Although Fourier space gate and Polarization gate spatial filtering techniques could select ballistic and snake photons in steady state measurements, they cannot remove the diffusive photons scattering along the initial direction of propagation. For thick samples, the probability of diffuse photons scattering parallel to the ballistic or snake photons increases the washing out of the information provided by the undeviated early light. *In order to separate the image bearing photons from the undesirable diffusive ones, one needs to make use of the time domain.* With the technology advancements in pulse lasers and ultrafast detection systems, time resolved optical imaging is becoming a prefer technique among scientist to detect defects or hidden anomalies inside a highly scattering medium.[7.1-7.21]

In principle, it is possible to distinguish the early photons, i.e. ballistic and snake components, from the more diffusive ones, which travel along the axis of propagation- by measuring the time of flight of the transmitted photons. Photons that travel between two points across a medium with the shortest time of flight *must have remained along or closest to the straight line* between the two points, which correspond to the ballistic and snake photons, respectively. The probability of detecting ballistic photons decreases exponentially as e^{-z/l_s} where z is thickness of the medium and l_s is the scattering mean free path assuming that absorption effects are negligible, $l_s << l_a$. Thus, the intensity of light

detected with the shortest time of flight will depend on the absorption properties of the medium contained within a narrow volume element surrounding the straight line. The intensity of the transmitted snake light (I_{snake}) through a piece of tissue arriving at different time intervals Δt have been calculated and defined by F. Liu and co-workers in Refs. 7.5 and 7.6 as:

$$I_{snake}(\Delta t) = \alpha \int_{t_b}^{t_b+\Delta t} I(t)\, dt \qquad (7.1)$$

where $t_b = n\, z/c$ is the ballistic time of the photon travelling straight through a piece of tissue; α, n, z, c are the collection factor, the refractive index of the medium, the thickness of the sample, and c the speed of light in vacuum, respectively. In Liu's works, it was shown that for biological tissues, the snake component decreases much more slowly than the ballistic component as the tissue thickness increases. Hence, it is the snake photons the ones that will survive while going through a thick sample and still carry strong and direct image information about the medium.

Most of the time-resolved imaging experiments performed in the past, by this group and others[7.1-7.6], were one-dimensional (1D) or two-dimensional (2D) *scanning imaging techniques*. The most common of these techniques is described in Fig. 7.1 (a) and (b) where the sample to be scanned is placed between the source and detector. In order to obtain a 1D image, the sample is translated and measurements along one direction are taken. In the same fashion, for 2D images, two directions are scanned and

measured. The basic idea of this technique is integrating the intensity within time window intervals. *The earliest time window interval of the measure profiles across the sample will carry snake photons making it possible to detect any absorption centre within the medium, as can be observed in Fig. 7.1 b, while the later time windows will carry diffusive photons which produce no shadowgram at all.* Although, good results have been obtained in the past, this imaging technique is too lengthy and time consuming. These pioneering works in optical imaging using scanning techniques has led to new ideas for more reliable and faster techniques.

In this chapter, I focus on "*two-dimensional time-sliced NIR optical imaging*" of (a) bones in tissues, and (b) an object hidden inside a 72mm thick human breast sample. By selecting optimal time windows of a transmitted pulse, in particular of the snake photons, improved shadowgram images have been obtained. The results obtained here clearly indicate that the two-dimensional time-sliced imaging approach is more powerful, faster, and direct in obtaining shadowgram images than the conventional scanning shadowgram techniques.

This chapter is organized as follows. Section 7.2 presents the experimental arrangement and samples. The results in section 7.3 illustrate the efficacy of time gating in sorting out image bearing photons, and the feasibility of imaging through thick samples. This section has been divided in two parts. In the first part , two-dimensional time-sliced imaging of turkey bones in tissues were obtained, and in vivo imaging of metacarpal bones were successfully conducted. In the second part, images of an object hidden inside a 72 mm thick human breast tissue sample were obtained and fully analyzed. Finally, section 7.4 presents the conclusion.

7.2 Materials and Methods

7.2.1 Experimental Arrangement

A schematic diagram for the experimental setup for time-sliced imaging used in this work is presented in Fig. 7.2. Ultrashort laser pulses of about 150 fs duration at 800-nm, at an 82 MHz repetition-rate from a self-modelocked Ti:sapphire laser (Spectra Physics Tsunami) were amplified using a regenerative amplifier and a Quantronix Titan multipass power amplifier system for transillumination imaging. The average beam power used in the experiment was approximately 400 mW, reduced from 5W available from the laser system. The repetition rate was 1 kHz. The beam was expanded and the central part of it was selected using an aperture to illuminate the sample. This was done to make the beam smoother by reducing the intensity difference between the center and the edge of the beam at the incidence. An electronic time gate was used to sort out image bearing photons and discriminate against image-blurring scattered light. The time gate was provided by a ultrafast electronic gated imaging camera system (La Vision, Picostart), consisting of a time gated imaging intensifier coupled to the charge coupled device (CCD) camera. The full-width-at-half-maximum duration of the gate could be adjusted to a minimum of 80 ps and the gate position could be varied in steps of 25 ps over a 15 ns range. The transmitted light from the samples was collected by a camera lens and directed to the gated image intensifier. Resulting time-sliced images were recorded by the CCD camera and displayed on a personal computer. The approach selects optimal picosecond-scale time-windows of the transmitted light pulses to form time sliced images of the bones or foreign object hidden inside thick biological media.

In order to measure the image quality, the spreading as well as the contrast of the image (as described in the chapter 6) were monitored here as a function of "*time*".

7.2.2 Samples Characteristics

The samples used in the experiments were: (a) a turkey drum, (b) a chicken wing bones placed inside breast chicken tissues, (c) a chicken thigh bone embedded in tissues from chicken thigh and breast, (d) metacarpal bones of a human palm *in vivo*, and (e) a rod 6.5 mm diameter hidden inside a 72 mm thick human breast sample.

The chicken and turkey samples were compressed and placed between two glass plates in order to keep a uniform thickness. The human breast tissue sample with the rod inside it was placed inside a plexiglass box. The dimensions of the box were 250mm x 250 mm x 72 mm.

(a) The turkey drum sample was compressed using the two glass plates to 60 mm thick. The bone inside the sample was measured after the experiment and was 12 mm in diameter.

(b) The two chicken wing bones were 2.5 –3.5 mm thick with a separation of 7 mm embedded in a 32 mm thick chicken breast tissue.

(c) The chicken thigh bone was 5.5 mm thick and 8.5 mm wide. It was embedded in a 20 mm thick chicken tissue. In order to investigate the potential of this time sliced imaging method to detect fractures in bones, a small 1.5 mm-diameter hole was drilled in the chicken thigh bone.

The animal samples were obtained from a local butcher.

(d) The 72 mm thick human breast tissue sample for part 2 of this work was obtained from an 18 years old female patient following reduction mammoplasty. The breast sample was made available to us by NDRI. The specimen was composed mainly of chunks of fatty tissue, which filled out the dimensions of the plexiglass box described above. A painted black rod, 6.5 mm in diameter, was placed inside the sample, 25 mm away from the exit surface of the light

7.3 Results

The result will be presented in two sections. Section 7.3.1 presents the results of shadowgram images of bones inside animal tissue. In the second part, Section 7.3.2, a sequence of time-sliced images—of the 72 mm thick human breast tissue sample with the hidden rod inside it—are fully analyzed, and some of the images presented.

7.3.1 Transillumination Imaging of Bones

Imaging of turkey and chicken bones inside tissue

Transillumination images of the turkey drum for two different time windows centered at 75 ps and 1200 ps are displayed in Figs. 7.3(a) and 7.3 (b), respectively. For all samples, these time windows were selected relative to the zero-position which was the time of arrival of the light pulse to the detector. The spatial distribution of transmitted light intensity shows the location of the bone clearly (the darker part) when the early-arriving, image-bearing photons are selected by centering the time-gate at 75 ps, Fig. 7.3(a). At a later time-gate position the image deteriorates and the shadow of the bone spreads as more diffuse photons contribute to noise and overwhelm the image-bearing

photons, as is observed in Fig. 7.3(b). Interestingly enough, some structural features of the muscle, such as, the boundary of two layers can be observed in the left upper side of the drum in the images (a) and (b).

The spatial intensity profiles integrated over a horizontal area with a vertical width of 20 pixels are shown in Fig. 7.3(c) to give a measure of the intensity contrast near the bone. The dips in the spatial intensity profiles correspond to the shadow of the bone inside the sample. The full width at half maximum (FWHM) of the dip (shadow), found in the spatial intensity profile at the 75ps-gated image, corresponds to a length of approximately 22 mm. (see Fig. 7.3 (c), thick line). The shadow of the bone for the late time-gated image was totally spread, making the FWHM of the profile unreadable (see Fig. 7.3 (c), thin line). The actual width of the bone was 12 mm. The difference in length between the actual width of the bone and the FWHM of the shadow could be attributed to the high scattering that photons suffer while going through the thick sample. As time passes, the stray impinging light is distorted. By the time it reaches the bone, the initial shape of the beam has already fanned out, which cause the shadow of the bone to be spread more and more as it continues to the exit surface. Only coherent ballistic light, (i.e., travelling a straight path), could produce a perfect shadow equal to the actual width of the bone. (Section 7.3.2 will present a more detail analysis of the spreading of the shadow as a function of time). Furthermore, the intensity contrast which has been define in the prior chapter, e.g., $(I_{max} - I_{min}) / (I_{max} + I_{min})$, was also calculated from the profile obtained for the early light image in Figure 7.3 (a) and was equal to 0.74. (The contrast obtained is the result of light loss in the early time due to the high scattering nature of bone, as compare to the scattering in the soft tissue. For later time slice windows more

scattered photons are detected washing out the image-bearing signal and the intensity dip disappears).

In order to determine if two closely situated thinner bones could be resolved, two-dimensional images of two thin chicken-wing bones inside a 32 mm thick chicken tissue were recorded. The separation of the bones was of about 7mm. Figure 7.4(a) presents one of the images recorded for the time gate positioned at 25 ps where the two bones could be discriminated. The intensity profile of this image is displayed in Fig. 7.4 (b). The profile shows two dips clearly resolving the two thin bones. The contrast obtained for this image was 0.4.

Two dimensional transillumination images of a 1.5 mm diameter hole in a chicken bone (e.g., 8.5 mm wide and 5.5 mm thick) embedded in a 20 mm thick chicken tissue are displayed in Fig. 7.5. The hole was drilled in the bone to show the effectiveness of using time-sliced imaging for detection of bone fractures. The time-sliced transillumination images in Figs. 7.5 (a), (b), and (c) correspond to images taken for gate positions of 0, 50 and 225, respectively. Next to each image, two spatial intensity temporal profiles integrated over a 10 pixel wide area have been plotted: one of the profiles has been chosen to pass through the hole location in the image, while the other pass in its proximity to show the difference in light transmission. In order to calculate the contrast, we have considered I_{max} to be the light going through the position of the hole, while I_{min} was taken to be the light passing next to it. The contrast obtained for the three images were 0.4, 0.08, and 0.00 for the 0, 75, and 225 ps time-gate positions, respectively. The calculated image contrast is higher for early-arriving light than for the late arriving light, as expected, and is easily evident from the spatial intensity profiles

accompanying each image. The most salient feature of the images is the distinct appearance of the hole as a bright circle in the zero-time frame of Fig. 7.5(a). When observing the correspondent profiles for Figure 7.5(a), more intensity transmission is observed in the profile around the spatial position through the hole than the one in its proximity. Although the hole was partially filled with bone marrow, with the hard surface removed, it was more permeable to light. Light through the hole arrived earlier than the rest of the sample giving rise to the early-time image of the hole. At later times, the image became blurred and the profile showing the position of the hole became indistinguishable from the profile in its proximity.

7.3.2 Imaging of a Hidden Object Inside a Large Excised 72-mm Thick Human Breast Tissue Sample

Time-slice shadowgram images of a object inside a thick human breast sample were measured. The object placed inside the breast was a black rod, 6.5 mm in diameter. It was positioned parallel, and 25 mm away from the exit surface, making sure that the axis of propagation of the beam coincides with the position of the rod. In this experiment, the incident 800-nm beam was 5 mm in diameter, with an input power of 300 mW. Fig. 7.7 (a) presents the schematic of the experimental set up.

A spreading of the shadow—in the images of the sample with the object—was observed to be time dependent. In order to analyse this dependence, time-sliced images of the light going through the sample with and without the foreign object were recorded.

Images of the light exiting the sample at various time gate positions provided us with the means to calculate the total intensity per unit image-area (flux) as a function of time. These intensity sampling-values—obtained at different time-gate windows—have been plotted in Figure 7.7 (b) using filled black squares connected by a solid black line. It is interesting to note that the 150-fs probing pulse going through the sample spread to more than 10 nanoseconds, giving a clear indication of the highly scattering properties found in a human breast fatty tissue. In order to calculate the optical parameters, a fit to the experimental data has been performed using the diffusion approximation for slab geometry. This fit has been plotted in Figure 7.7 (b) using a solid thick line. The fitted optical parameter values obtained for l_t and l_a were 1.25 and 377 mm, respectively.

Time-sliced shadow images of the black rod inside the thick sample are presented in Figure 7.8 for times 2, 4 and 9 nanoseconds time-gate position, as marked by the dotted lines in Fig. 7.7 (b). Spatial intensity temporal profiles integrated over a 50 pixel wide area (marked by the two dotted white lines) has been normalized and plotted next to each image. The greyish area on top of the profiles has been drawn to mark the position and actual diameter size of the rod in pixels, for easy reference. The salient features of Figure 7.8 is that the shadow images of the rod obtained using the late-arriving light are not as good as the ones obtained using the early light

The spreading of the shadow was analyzed from images obtained by subtracting the images with the object from the images without the object. The resulting image from each subtraction is called (defined) here the "*bright*" image. The bright image scheme

allows to take care of the noise introduce by our detection system, and give us better appreciation of the kind of distortion the shadow of the rod suffers in the images at different time-gate positions.

Figure 7.9 shows the *"bright"* images obtained for the 2, 4, and 9 nsec images presented in Figure 7.8. The smearing of the black dark region across the *"bright"* images represented the shadow cast by the object at different times. The *"bright"* images presented in Figure 7.9 make the spreading of the shadow of the rod over time more apparent. In the same fashions as before, spatial intensity temporal profiles integrated over a 50 pixel wide area (marked by black dashed box, in the bright images) has been normalized and plotted together (in Fig. 7.9) to observe the spreading of the shadow of the rod diameter size over time. The greyish dotted area drawn on top of the profiles represents the expected *undistorted shadow* cast by the object under no scattering (e.g., ballistic light suffers no scattering). Since only the earliest collinear photons (e.g., ballistic photons) could produce a shadow (*undistorted shadow)* equal to the dimension of the diameter of the rod, the *expected initial spreading of the shadow* was considered to be equal to the diameter of the rod. The dimension of the FWHM(t=0) of the *undistorted shadow* cast by the rod is equal to 23.32-pixels, which correspond to the 6.5-mm rod diameter. The full width at half maximum of the *undistorted shadow* has been labelled $FWHM_o(t=0)$ in Fig. 7.9.

The FWHM of the plotted profiles obtained for t = 2, 4, 9, nsec (in Fig. 7.9) were 3.8, 4.6, and 6.2 $FWHM_o$, respectively. The plotted profiles are time dependent, and

clearly show how the FWHM increases as time increases. The ratio FWHM(t)/FWHM$_o$, give us the number of times the initial shadow of the object has spread, and is called here the *spreading number of the shadow, W(t)*. *W(t)* is unitless, and is a function of time.

The spreading *W* vs. its respective time of acquisition has been plotted in Figure 7.10 using solid squares. The white square at t=0 delay represents the "*initial*" *spreading number of the shadow* W_o=1—e.g., FWHM(t=0) / FWHM$_o$. The *spreading number of the shadow* time dependence, *W(t)*, may be expressed as:

$$W(t) = W_o + b\, t^{1/2}$$

where W_o is the *initial spreading number of the shadow*, and t is the time at which different spreading takes place. b is presumed to be a function of the object position within the sample and the optical parameters of the medium, e.g.,. l_t and l_a. The fitting value for the coefficient b obtained for the shadow spreading as a function of time was 0.0525

In this section, I have only considered the spreading of the shadow as a function of time. A deeper investigation of the shadow spreading as function of position of the object in the sample, optical parameters of the medium, as well as time is without a doubt a worthwhile pursuit.

7.4 Conclusion

The results obtained from these time-resolved transillumination measurements underline the potential of ultrafast optical methods for application in biomedical imaging. The feasibility of using time-sliced imaging for the detection of bones in thick tissues and a small hole (representing a fracture) in a bone embedded in tissue have been demonstrated. Two thin bones in a chicken wing were resolved using the time-slicing technique. The *in vivo* measurement result (of metacarpal bones yielding high contrast two-dimensional images) highly encourages to pursue this optical modality in development of viable alternatives for regular monitoring of bone as in case of osteoporosis, arthritis, rheumatic disorders and other abnormalities. The ability to image a rod 6.5mm embedded in the 72 mm thick excised human breast sample gives a clear indication of the potential time-sliced imaging has in the medical field, as a screening tool for the detection of tumours. The two-dimensional time-sliced imaging approach presented here capture images of the photon spatial distribution in time directly in only few seconds of data accumulation; this is of great importance since it surpasses the imaging acquisition time needed in prior scanning techniques.

It is expected that further improvements in the electronic time-gated imaging system would also enhance the time-slicing imaging approach to more precise and faster measurements. These results underscore the potential of time-sliced optical detection in future biomedical imaging.

7.5 Reference

7.1 K. M. Yoo, B. B. Das, and R. R. Alfano, "Imaging of a translucent object hidden in a highly scattering medium from the early portion of the diffuse component of a transmitted ultrafast laser pulse," *Opt. Lett.*, 17, 958-960, 1992.

7.2 B. B. Das, K. M. Yoo, and R. R. Alfano, "Ultrafast, time-gated imaging in thick tissues: a step toward optical mammography," *Opt. Lett.*, 18, No. 13, 1092-1094, 1993.

7.3 M. A. O'Leary, D. A. Boas, B. Chance, A. G. Yodh, *Phys. Rev. Lett.*, 69, 2658-2661, 1992.

7.4 F. Liu, K. M. Yoo, and R. R. Alfano, "Ultrafast laser-pulse transmission and imaging through biological tissues," Applied Optics, 32(4), 554-558, 1993.

7.5 F. Liu, K. M. Yoo, and R. R. Alfano, "Transmitted photon intensity through biological tissues within various time windows," Opt. Lett., 19(10), 740-743, 1994.

7.6 B. B. Das, Feng Liu, and R. R. Alfano, "Time-resolved fluorescence and photon migration studies in biomedical and model random media," Prog. Phys., 60(2), 227-292, 1997.

7.7 L. Wang, P.P. Ho, G. Liu, G. Zhang, and R.R. Alfano, "Ballistic 2-D imaging through scattering walls using an ultrafast optical Kerr Gate", Science, 253, 769-771, 1991.

7.8 G. Muller and B. Chance Editors, *Medical Optical Tomography*, SPIE, Birmingham, 1993.

7.9 R. R. Alfano Ed., *OSA proceedings on Advances in Optical Imaging and Photon Migration*, 21,1994.

7.10 V. V. Tuchin , Selected papers on Tissue Optics: Applications in Medical Diagnostics and Therapy, (SPIE Milestone Series, Vol. MS102, 1994)

7.11 K. M. Yoo and R. R. Alfano, "Time-resolved coherent and incoherent components of forward light scattering in random media", Opt. Lett., 15, 320-322, 1990.

7.12 J. R. Singer, F. A. Grunbaum, P. Kohn, J. P. Zubelli, Science, 248, 990-993, 1990.

7.13 K. M. Yoo, Q. Xing, and R. R. Alfano, *Opt. Lett.*, 16, 1019-1021, 1991.

7.14 D. Huang, E. A. Swanson, C. P. Lin, J. S. Schuman, W. G. Stinson, W. Chang, M. R. Hee, T. Flotte, K. Gregory, C. A. Puliafito, and J. G. Fujimoto, Science, 254, 1178, 1991.

7.15 B. B. Das, J. Dolne, R. L. Barbour, H. L. Graber, J. Chang, M. Zevallos, F. Liu and R. R. Alfano, *SPIE proceedings*, 1995.

7.16 J. A. Moon, R. Mahon, M. D. Duncan, and Reintjes, *Opt. Lett.*, 18, 1591, 1993.

7.17 L. Wang, A. H. Hielscher, S. L. Jacques, D. V. Stephens, and F. K. Tittel, *Proc. of OSA, Advances in Optical Imaging and Photon Migration*, 21, 288-290, Alfano R R, Ed., Orlando, Florida, 1994.

7.18 S. Anderson-Engels, R. Berg, S. Svanberg, and O. Jarlman, *Opt. Lett.*, 15, 1178-1181, 1990.

7.19 J. C. Hebden, R. A. Kruger, and K. S. Wong, *Appl. Opt.*, 30, 788-794, 1991.

7.20 H. Chen, Y. Chen, D. Dilworth, E. Leith, J. Lopez, and J. Valdmanis, *Opt. Lett.*, 16,487-489, 1991.

7.21 E. N. Leith, C. Chen, H. Chen, Y. Chen, J. Lopez, P. C. Sun, and D. Dilworth, *Opt. Lett.*, 16, 1820-1822, 1991.

7.22 F. Liu, Private Communication.

7.6 Figures

Fig. 7.1 (a) Experimental arrangement diagram commonly used in 1D and 2D scanning imaging.

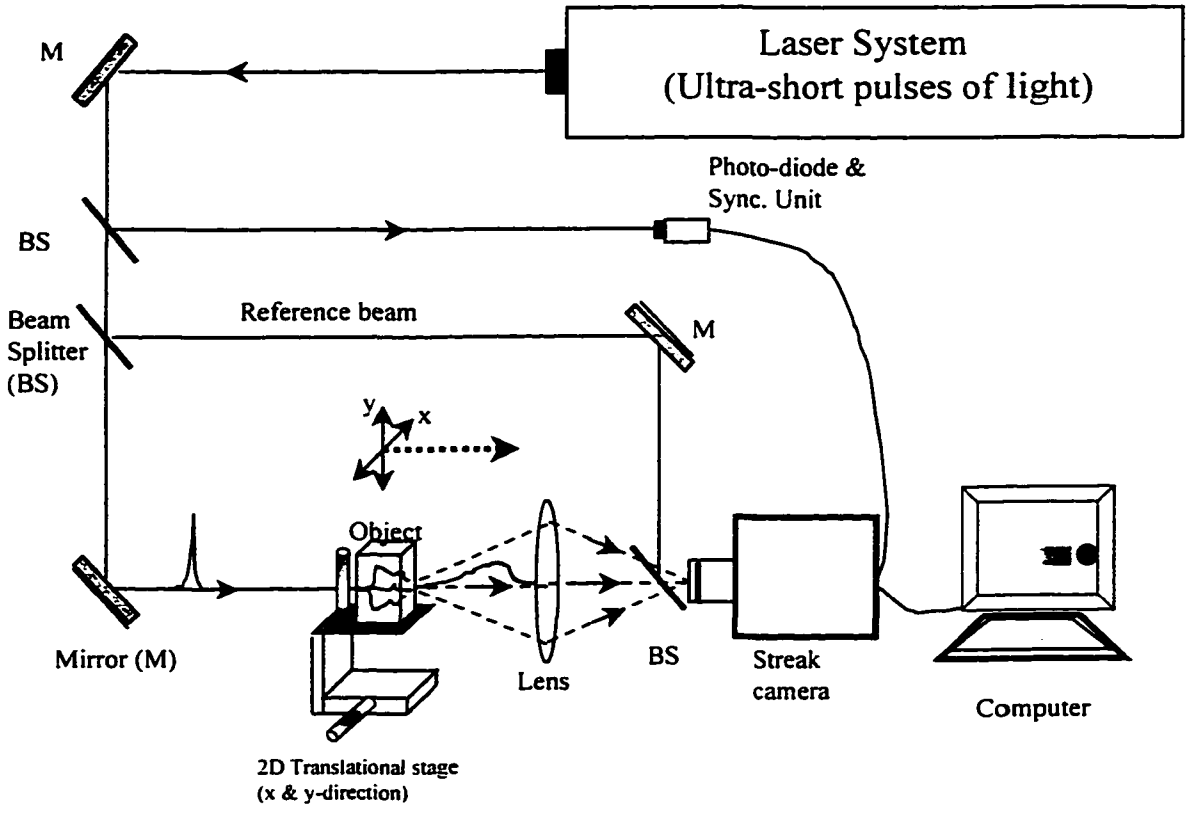

Fig. 7.1 (b) Scanning beam. 1D and 2D-shadowgram approach.

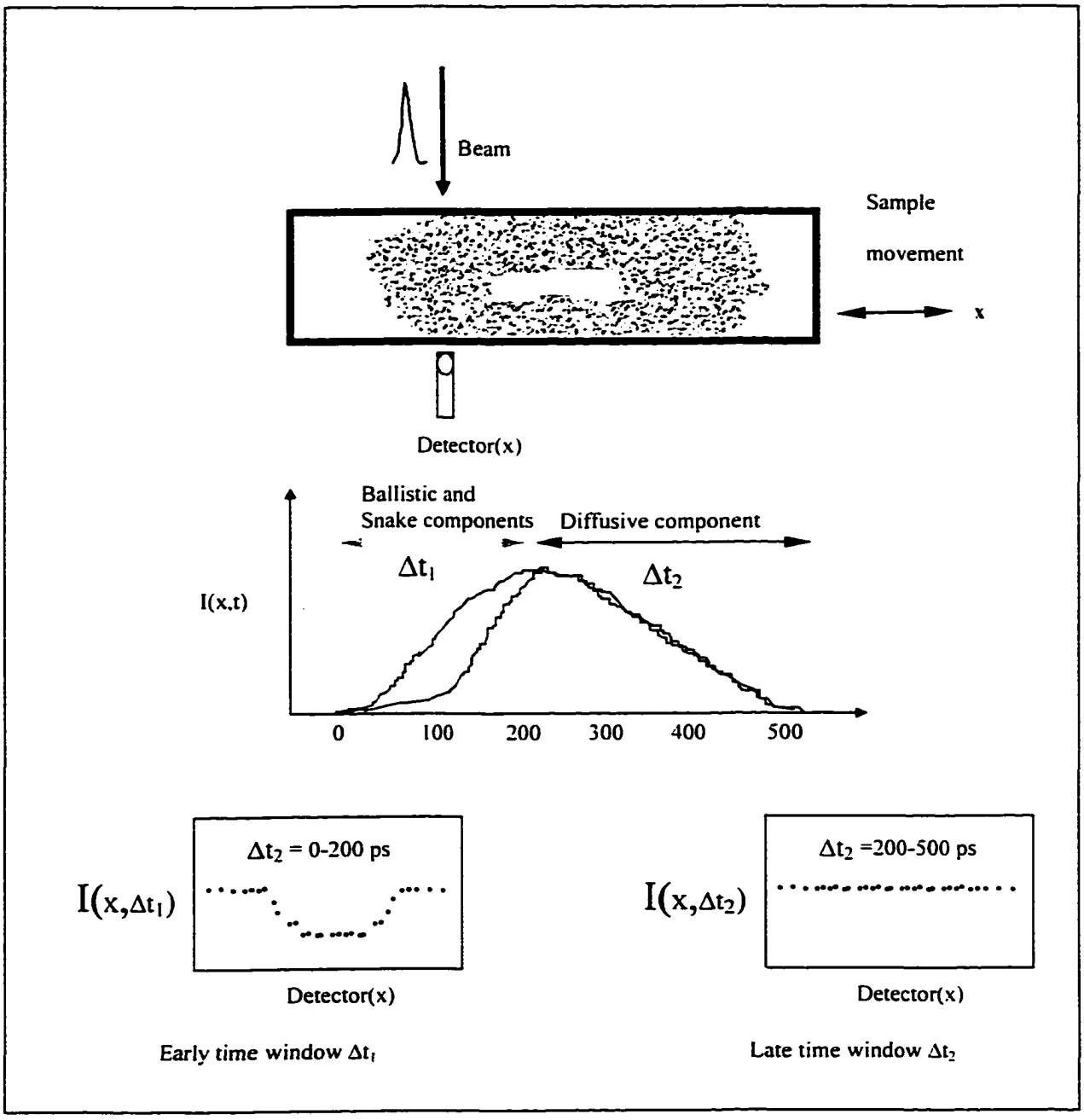

Figure 7.2 Schematic diagram of the experimental arrangement for the two-dimensional *time-sliced* transillumination imaging measurements.

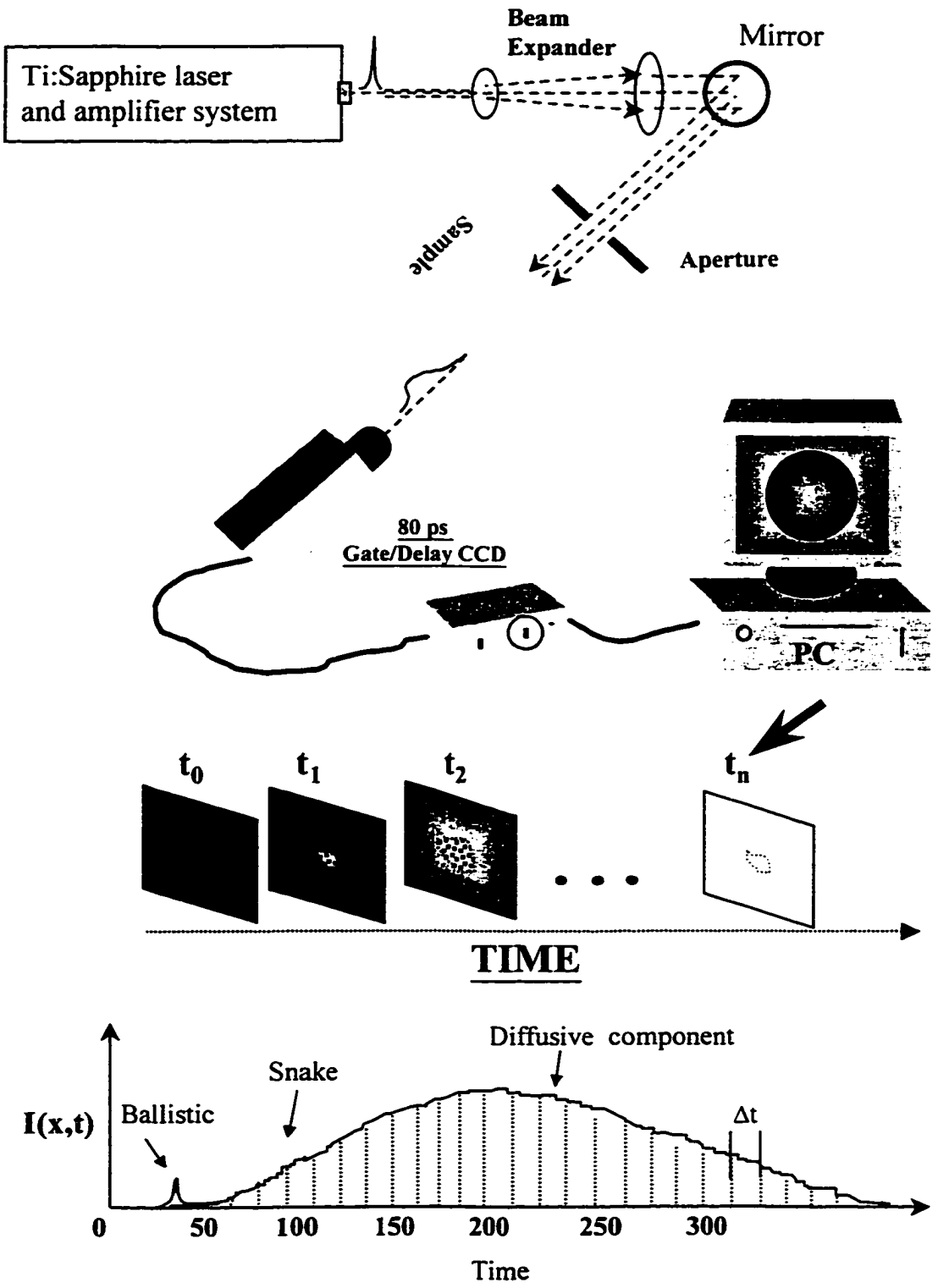

Figure 7.3 Two-dimensional *time-sliced* shadow images of a 60-mm thick turkey drum. The cartoon in the figure is a cross section schematic of the 800-nm laser beam going through the sample. Images (a) and (b) were taken at 75, 1200 ps time-gate position, respectively. The spatial intensity profiles in (c) have been normalized, and were obtained by integrating a cross section of images (a) and (b), as marked by the dotted lines.

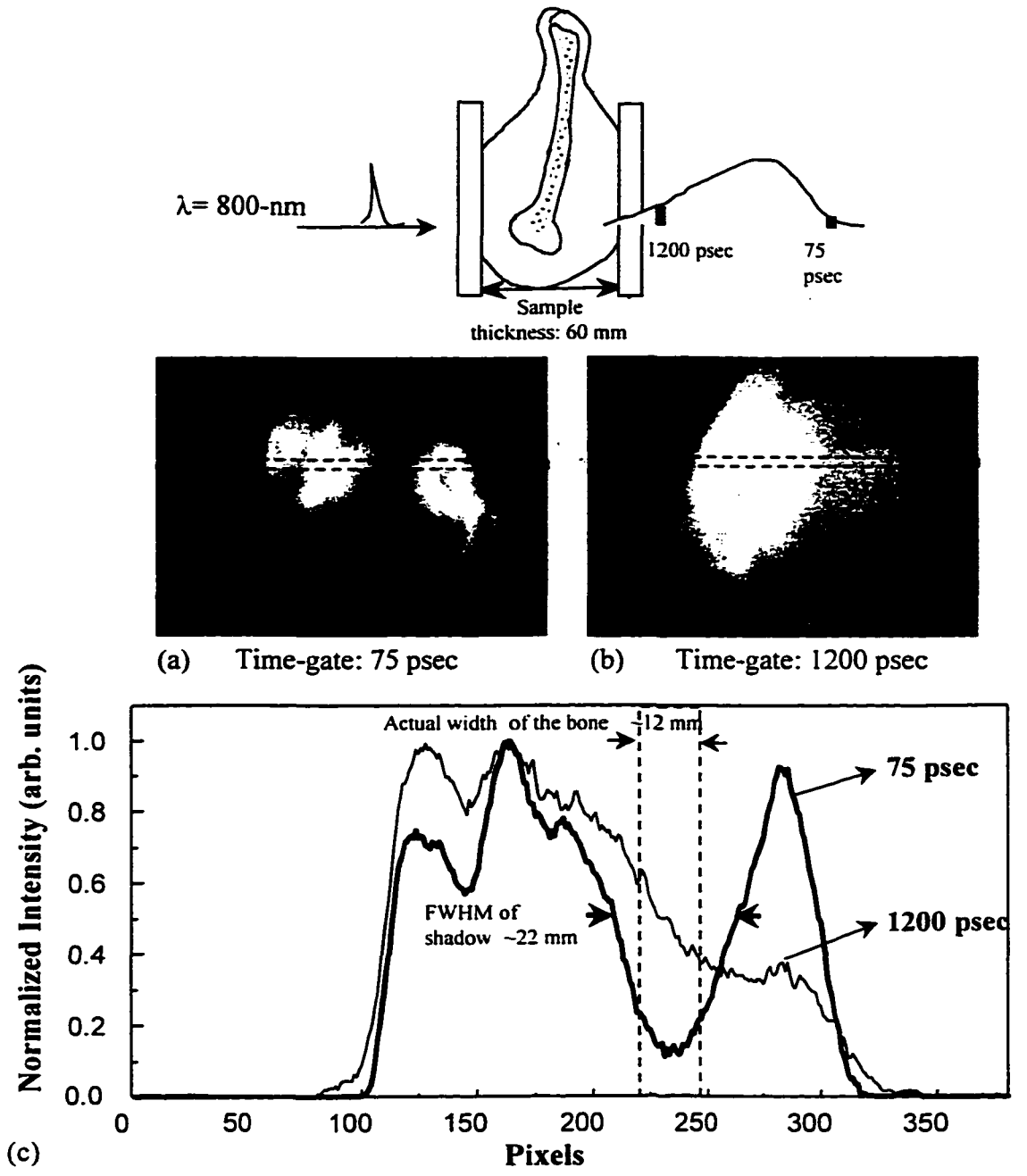

Figure 7.4 Two-dimensional *time-sliced* shadow image of a chicken wing inside chicken tissue. Image (a) was taken at 25 ps time-gate position, using a 800-nm laser beam. (b) Spatial intensity profile obtained from dotted area in image (a)

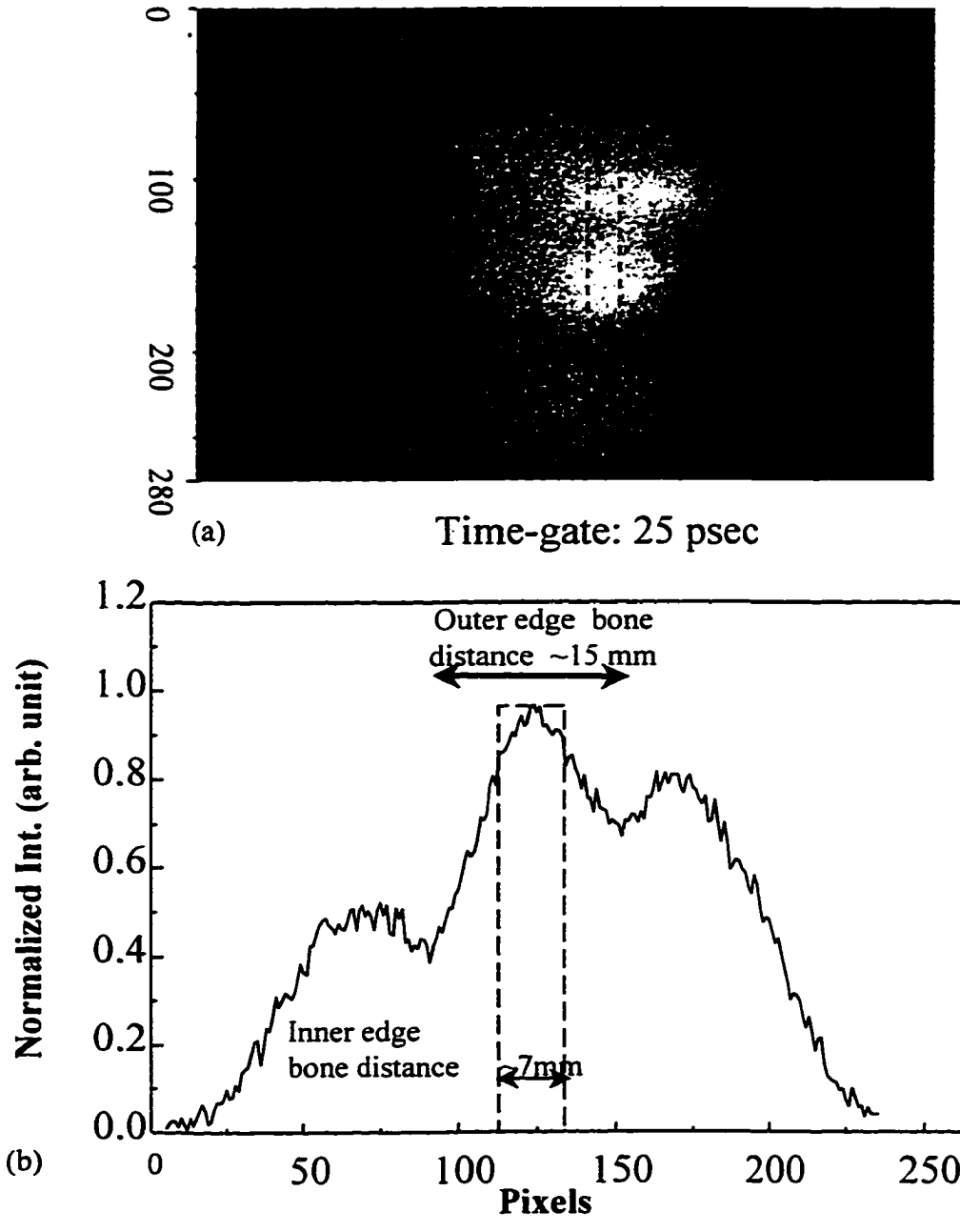

Figure 7.5 Two-dimensional *time-sliced* shadow images of a hole in a chicken wing bone embedded inside chicken tissue, using a 800-nm laser beam. Images (a), (b), and (c) were recorded at 0, 75, 225 ps time-gate position, respectively. Next to each image, respective spatial intensity temporal profiles have been plotted. (see text for explanation)

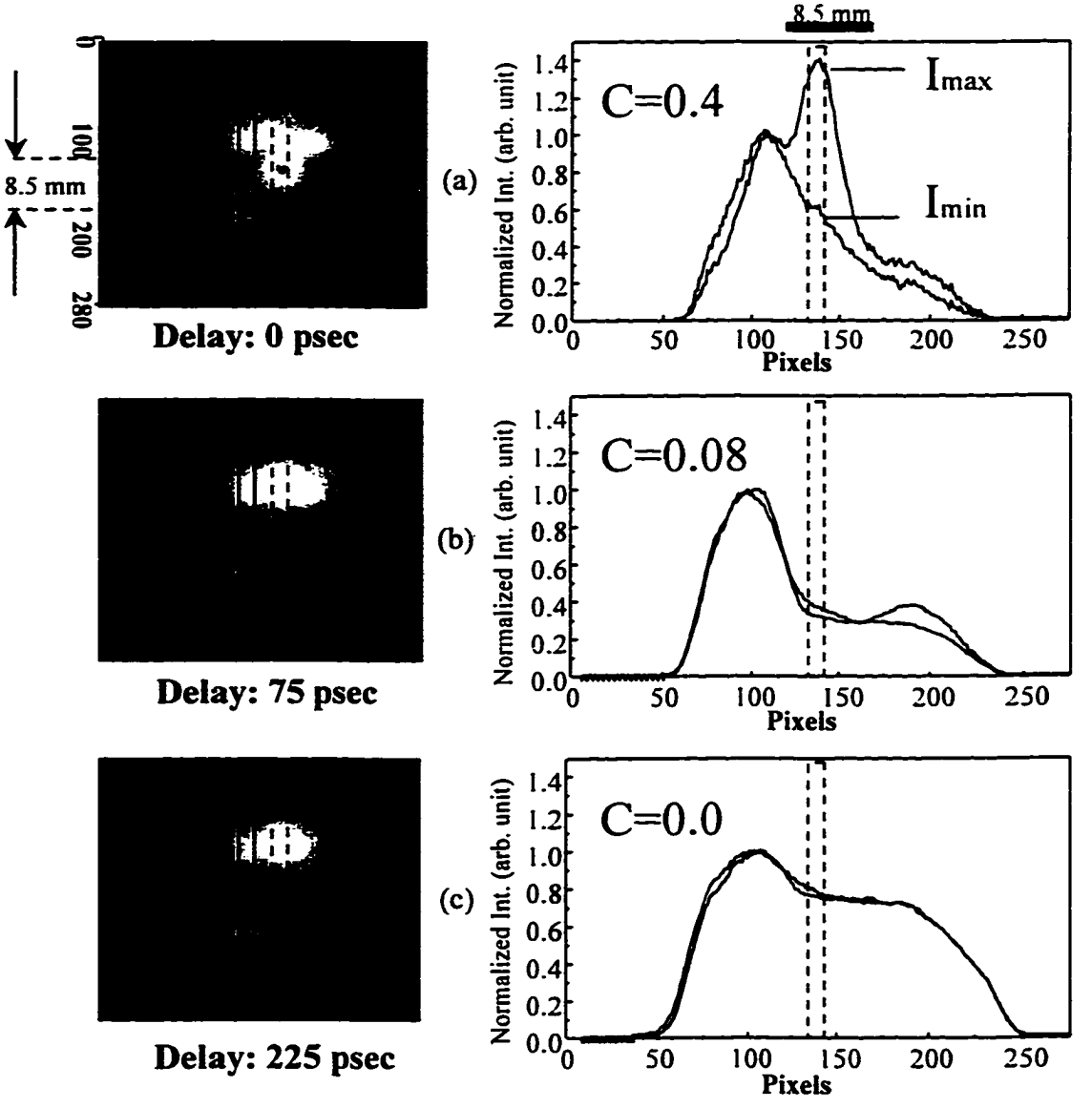

Fig. 7.6 Schematic of the experimental setup to obtain the shadow image of an object hidden inside a 72-mm thick human breast sample, using an electronic time-gated CCD camera.

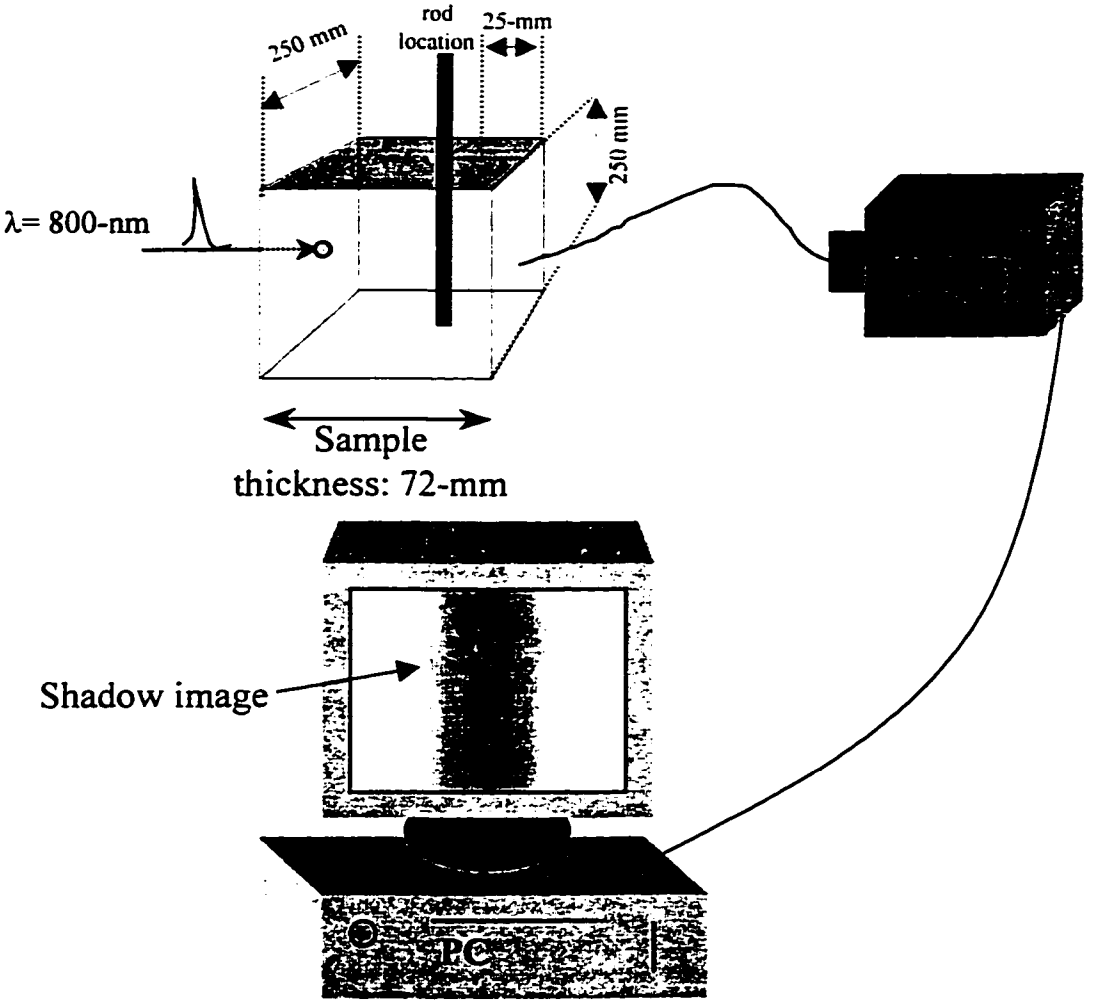

Figure 7.7 Intensity temporal profile of the 800-nm laser light transmitted through a 72-mm thick human breast sample using an electronic time-gated CCD Camera fitted to the Diffusion equation. The experimental data has been plotted using a black squares connected by a solid line. The fit has been plotted using a solid grey line. The fitted optical parameter values obtained for l_t and l_a were 1.25 mm and 377 mm, respectively.

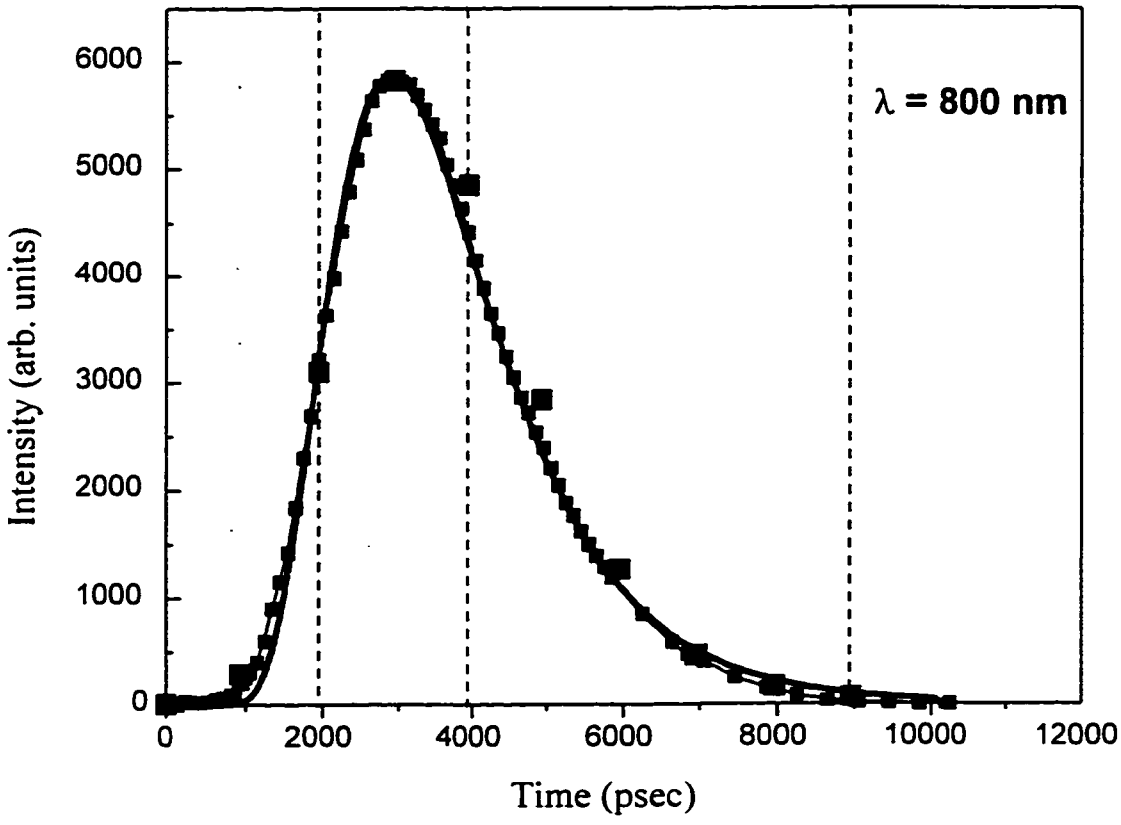

▪ **Experimental Data-1** ■ **Experimental Data-2**

— Diffusion approximation fit to experimental data for a slab geometry

Calculated Parameters:

absorption length, *la = 377 mm*

transport mean free path, *lt = 1.25 mm*

Figure 7.8 Two-dimensional *time-sliced* shadow images of a rod 6.5-mm in diameter embedded in a 72 mm thick human breast tissue sample obtained using 800-nm laser light. Images (a), (b), and (c) were recorded at 2, 4, 9 nsec time-gate position, respectively. (See dashed lines in Fig. 7.7 (b), showing respective location in the temporal profile). Corresponding spatial intensity temporal profiles have been plotted next to each image.

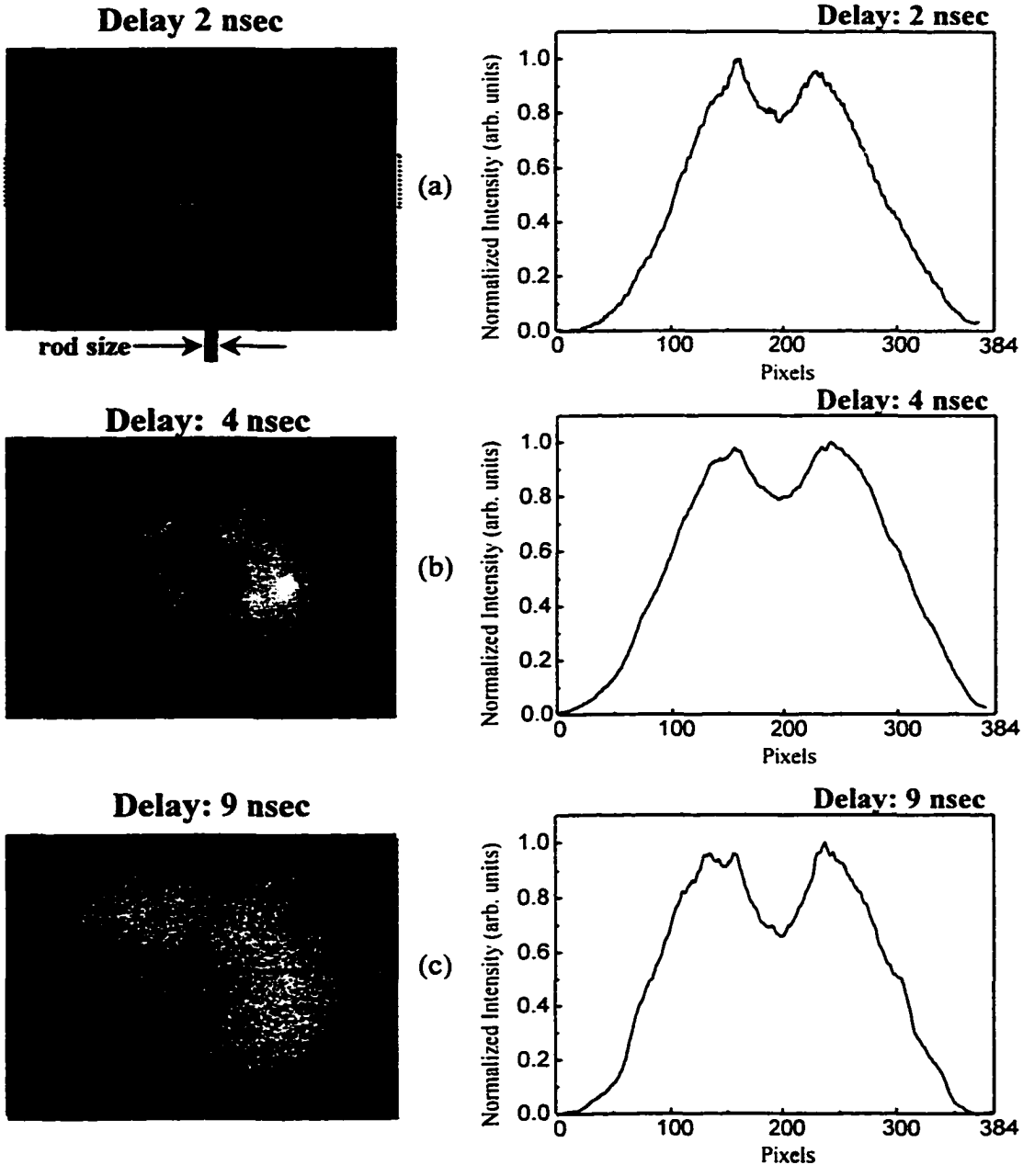

Figure 7.9 "*Bright*" images obtained for images in Fig. 7.8. Each "*Bright*" image is obtained by subtracting the image of the sample recorded with the object inside it form the image of the sample without the object. Spatial intensity temporal profiles obtained from the dashed rectangular region from each image have been plotted below showing the FWHM spreading over time.

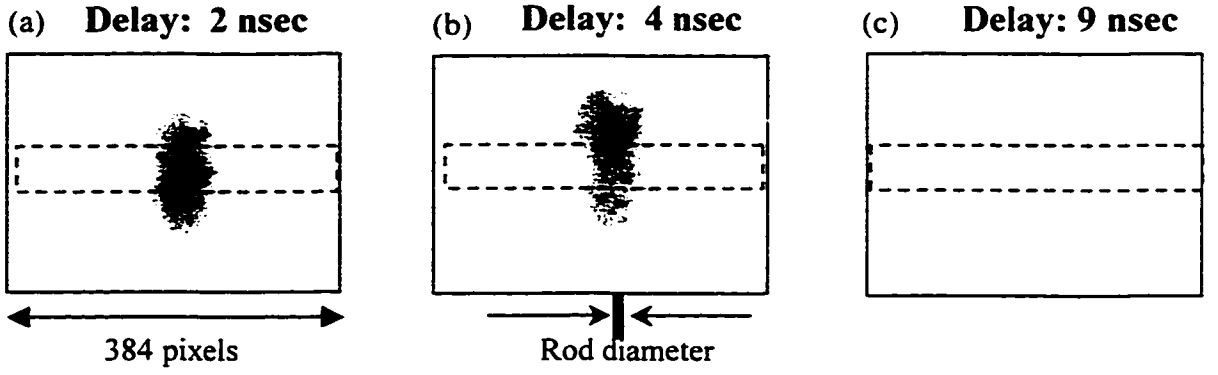

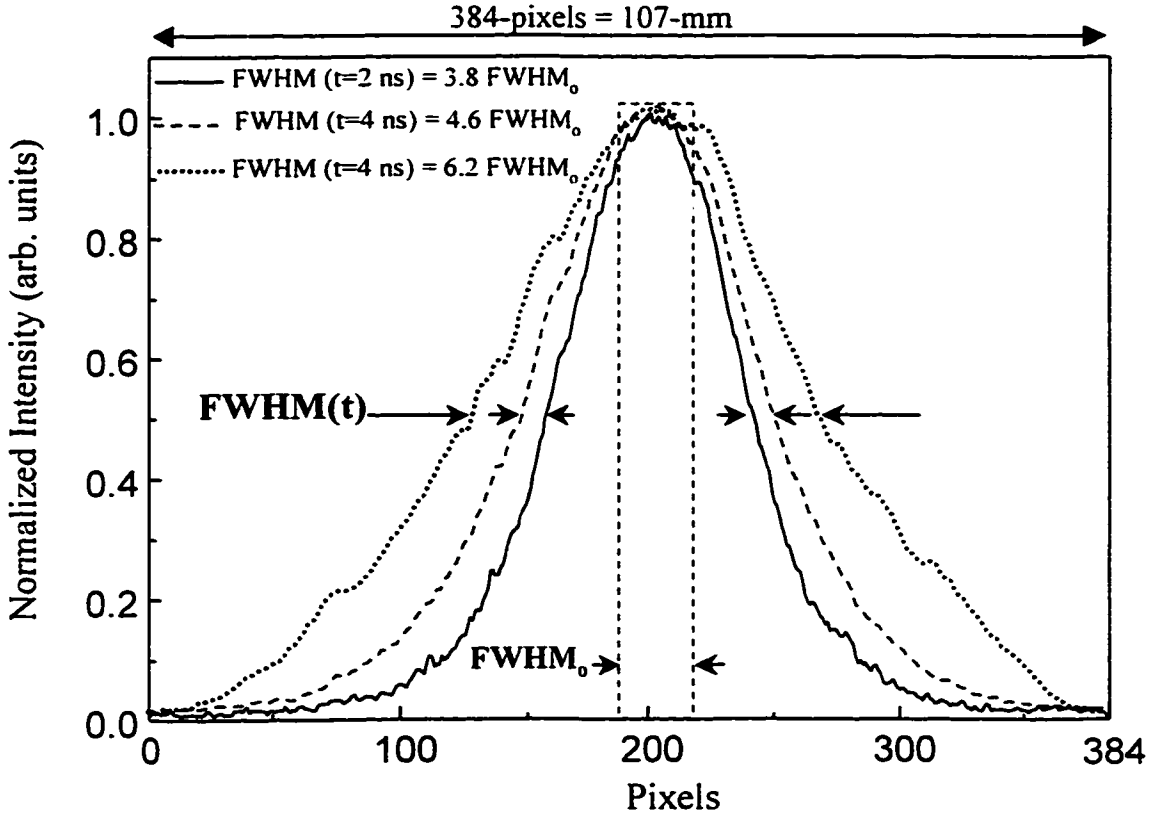

$FWHM_0$ = 23.32-pixels = 6.5-mm (shadow of the diameter of the rod under no scattering)

Figure 7.10 *W(t), Spreading of the shadow Image* of the 6.5-mm diameter rod versus time (time-gate position) were obtained from "*Bright*" images at temporal positions marked with gray squares in Fig. 7.7 (b). The *W(t)* collected values have been plotted using squares, while the solid line represent the fit using the expression $W(t) = Wo + b\,t^{1/2}$. See text for details.

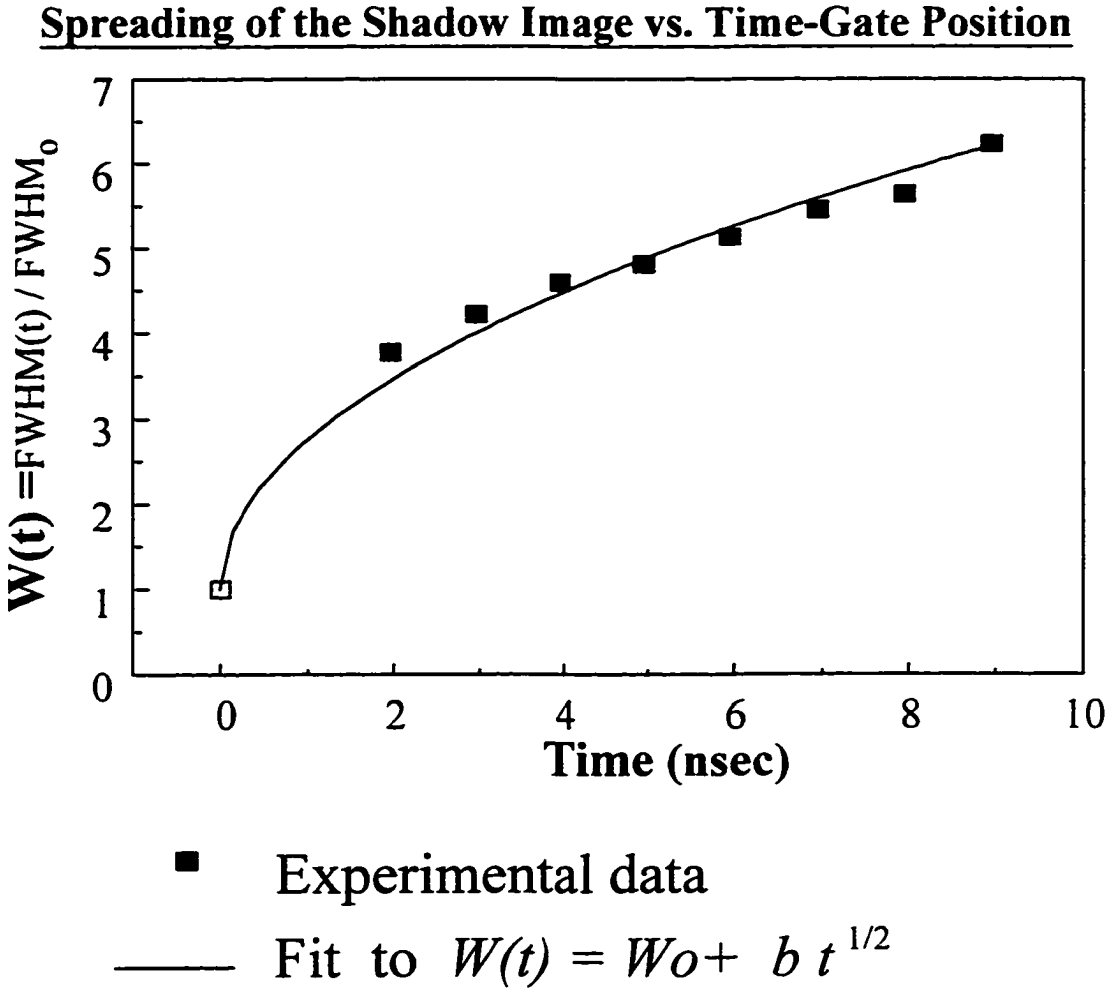

Chapter 8

Two-Dimensional NIR *Laser-Spectroscopic* and *Time-Sliced* Transillumination Optical Imaging of *"in Vitro"* Human Female Breast Tissue Specimens

8.1 Background

Although, the promise of combining the imaging and spectroscopic aspects to develop an optical imaging modality with genuine diagnostic ability has been expounded,[8.1—8.16] there is a paucity of efforts to realize this 'holy grail' for optical mammography in practice. *Insufficient spectroscopic information about the normal and cancer human breast tissues is presumable one of the reasons for this paucity of efforts. Lack of commercially available tunable lasers in the 1000-1300 nm spectra range might have limited the spectroscopic imaging efforts in this important spectral range within the 'therapeutic window.'*

In this chapter, we focus on finding light-tissue signatures that could be used to characterize and distinguish normal and cancer regions of human breast. A combined *laser spectroscopy* and *time-sliced* transillumination optical imaging approach—in the NIR spectral region—is used to characterize breast tissue constituents, by exploiting their intrinsic spectral *"fingerprints"*, as well as the difference in their transit time of transmitted light

A Cr^{4+}-doped Forsterite laser system, tunable over the 1150-1350 nm spectral range, was used for the spectroscopic transillumination imaging study. The results demonstrate that spectroscopic differences may be used to highlight different tissue

constituents. The two-dimensional time-sliced transillumination imaging study was performed using pulses of light (at 800 nm) of 150 fs. and 1kHz repetition rate obtained from a self-mode-locked Ti:sapphire laser and amplifier system. Images of the transmitted pulse of light recorded at different time windows highlighted the different type of tissues, and allowed discrimination of normal and cancer regions in tissues.

8.2 Experimental Methods

NIR two-dimensional laser-spectroscopic transillumination imaging

The key constituents of a normal adult female human breast are glandular tissue. fibrous tissue, adipose tissue, blood vessels. and ducts. Breast lesions include cysts. mastitis, and malignant carcinomas, as well as benign tumors such as, fibrodenomas, lipomas.[8.17] Differences in optical and spectroscopic properties of the normal constituents and lesions of breast tissue are necessary for diagnostic optical imaging of breast lesions. Figure 8.1 shows the optical transmittance spectrum of a 3 mm thick human breast tissue sample in the 1190-1330 nm range. as measured by Marks in Ref. 8.18. The spectrum in Fig. 8.1 was composed of the absorption resonance by adipose tissue at 1203 nm superimposed on a smoothly varying background caused by light scattering. To test if a spectroscopic differences of tissues in a specimen provides any distinguishable signature in the transillumination image, the optical absorption characteristics of adipose tissues around 1203 nm was selected as a *"spectral fingerprint"*. We select this spectral range and this particular adipose absorption resonance since overall light scattering by tissues is weaker in this range as compared to that at shorter wavelengths. The goal is to examine the transillumination image

characteristics as the wavelength of the imaging light is tuned in and out of the adipose optical absorption resonance. The Cr^{4+}-doped Forsterite laser NIR wavelength tunability was advantageous for this spectral range.[8.19]

The experimental arrangement for NIR spectroscopic imaging used the continuous-wave mode-locked output of a Cr^{4+}:Forsterite laser pumped by a Nd:YAG laser. The linearly polarized laser output was tuned from 1225 to 1300 nm using an intracavity birefringent plate. The average beam power was maintained at 35 mW for all the wavelengths by using appropriate neutral density filters. Although, this laser system could deliver ultrashort pulses, we were unable to implement the time-sliced imaging technique due to the lack of commercial ultrafast detectors in the market for this spectral range. A Fourier space gate[8.20] and a polarization gate[8.21] were used to sort out a fraction of image bearing photons and discriminate against image-blurring multiple scattered photons. A 50 mm focal length camera lens collected and collimated the low-spatial-frequency light filtered by the Fourier gate and directed it to the 128x128 pixels sensing element of an InGaAs NIR area camera (Sensors Unlimited SU 128-1.7RT). The experimental arrangement used for NIR spectroscopic imaging is presented in Chapter 6. Fig. 6.1(page 133).

*NIR two-dimensional **time-sliced** transillumination imaging*

The time-sliced two-dimensional transillumination imaging approach used in this work is an extension of the time-gated methods. It uses optimal time-slices at the picosecond-scale of the transmitted light pulse to form images, demonstrating that in specific cases later-arriving light may be as useful in distinguishing between normal and

cancer tissues. The experimental arrangement for time-sliced transillumination imaging is presented in detail in Chapter 7. Fig. 7.2 (page 162).

8.3 Materials

Several human tissue samples were tested and were made available for this work by the National Disease Research Interchange (NDRI) and the Sloan Kattering Hospital under an IRB approval at the City College of New York. Each of the samples was placed between two glass plates and compressed in an attempt to provide uniform thickness.

Measurements taken using the experimental approach described above will be presented for two different breast tissue samples, which demonstrated the most striking results. The first tissue sample was derived from the left breast of a 28-year-old female patient following reduction mammoplasty. The samples dimension was 35x14x5 mm, and it was comprised of adipose tissue in the middle and broad areas of firm fibrous (glandular) tissue on the two sides. The second tissue sample consisted of a cancer placed next to a normal piece of tissue obtained from the same patient. The dimension of the cancer piece was 10x12x5 mm, and the normal piece 10x16x5 mm. Both samples, after compression, have a thickness of 5 mm.

8.4 Spectroscopic and Time-Sliced Imaging Results

a) Adipose and fibrous human breast tissue sample

In the ***laser-spectroscopic imaging approach***, two-dimensional transillumination images of the first tissue sample (see insert in Fig8.2) were recorded using light of several near-infrared wavelengths. The sample consisted of adipose tissue in the middle and

strands of firm fibrous tissue on the two sides as marked in the insert of Fig. 8.2. Images obtained using 1225 nm, 1235 nm, 1255 nm, and 1300 nm light are shown in the left frames of Figs. 8.2(a)-(d), respectively. Corresponding spatial intensity distributions of the images integrated over the same horizontal area as highlighted by the white dashed box in Fig. 8.2(a) are shown in the frames to the right of the respective images

The fatty region in the middle of the specimen appeared much darker and distinct when compared to the fibrous regions on the two sides in the 'resonant image' recorded using light of wavelength 1225 nm. This wavelength is closer to the adipose optical absorption peak at 1203 nm than other wavelengths used in this study. The region appeared as a deep trough in the corresponding spatial intensity distribution. As the wavelength of Cr:forsterite laser output was tuned out of the adipose absorption band the contrast between the fatty and fibrous regions in the images decreased. The depth of the trough in the spatial intensity profile also decreased and the region appeared as a crest in the profiles of the images recorded using light of wavelength 1255 nm or longer. The adipose region appeared brighter than the fibrous regions in the 'nonresonant images' recorded using wavelengths, such as 1300 nm, which are far removed from the 1203-nm resonance. The difference seen is presumably due to nonuniform spatial intensity distribution of the incident beam, and the difference in the light transport characteristics of the tissues. The incident beam had a spatial intensity distribution such that the central region was more intense than the periphery. The adipose tissue was located in the middle of the specimen, and was illuminated by the more intense central part of the beam. If we assume the light transport characteristics of the adipose and the fibrous tissues are comparable, the transillumination image is expected to be brighter around the center

when light is not preferentially absorbed by the adipose tissue. Light transport characteristics of the two types of tissues are expected to be different and may have contributed to the observed behavior. Values of transport coefficients at these wavelengths are not available from literature and can not be extracted from our measurements to make a more quantitative evaluation at this time.

More quantitatively, the change in the contrast between the fibrous and adipose regions of the specimen as a function of wavelength may be described in terms of a wavelength-dependent intensity ratio which we define as,

$$R(\lambda) = I_F(\lambda) / I_A(\lambda), \qquad (8.1)$$

where $I_F(\lambda)$ and $I_A(\lambda)$ are the intensity values at wavelength λ on the spatial profile of the image at locations corresponding to fibrous and adipose tissue regions, respectively. In reference to the spatial profiles in Fig. 8.2, we chose the pixel positions to be 71 for the adipose region which corresponded to the maxima in the 1300 nm profile, and 44 for the fibrous region. The value of $R(\lambda)$ changed from approximately 1.76 for 1225 nm (within the adipose absorption band) to 0.5 for 1300 nm (away from that absorption resonance). The plot of the intensity Ratio as a function of λ can be observed in Fig. 8.3. The inset in Fig. 8.3 shows the values of optical transmittance through a 3-mm thick human breast tissue sample at these wavelengths, as reported by Marks (in Ref. 8.18), see Fig. 8.1. By comparing $R(\lambda)$ and the inset in Fig. 8.3, we could observed $R(\lambda)$ increases when the wavelength used is closer to the absorption resonance peak (1203 nm).

The contrast of the adipose region in the image may be further enhanced if the ratio of/or the difference between a 'resonant image' measured using a wavelength closer to the resonance peak, and a 'nonresonant image' recorded using nonresonant light is

obtained. We illustrate this enhancement in image contrast using the 1235-nm resonant image, and 1300-nm nonresonant image displayed in Figs. 8.2(b) and 8.2 (d), respectively. Spatial intensity distributions integrated over a horizontal region of the 1235 nm and 1300 nm images are shown in Fig. 8.4(a). Figures 8.4(b) and 8.4(c) display the corresponding spatial profiles of the ratio image [*Image*(1235nm)/*Image*(1300nm)] and difference image [*Image*(1235nm) - *Image*(1300nm)]. The images obtained were placed next to the profiles. We next determined the contrast

$$C = (I_{max} - I_{min})/(I_{max} + I_{min}), \qquad (8.2)$$

of the images for comparison. In Eq.(8.2) I_{max} and I_{min} represent the maximum and minimum values of the intensity in the image. We use the integrated intensity values around pixel #71 for adipose region, and pixel #44 for fibrous region for estimating the contrast.

Contrasts of the 1235 nm image, the ratio image, and the difference image thus calculated are 0.09, 0.24, and 0.67, respectively. The contrast of the ratio image is 2.7 times higher, and that of the difference image is 7.4 times higher than that of the 1235 nm image.

The time-sliced imaging approach was performed in the same sample at 800 nm. (See inset at the top) Two-dimensional transillumination images of light propagating through the sample at different times were recorded. Images for the time-gate positioned at 0 and 200 ps are displayed in Fig. 8.5 (a) and 8.5 (b), respectively. The zero position was taken to be the time of arrival of the light pulse through a 5-mm thick glass cell filled with water. The spatial distribution of transmitted light intensity along a horizontal area covering the fibrous-adipose-fibrous (F-A-F) regions in the tissue sample is displayed in

Fig. 8.5 (c). The profile allowed a comparison of the relative magnitude of light intensity transmitted through the normal and the fibrous and adipose tissues at different delay times.

The adipose and the fibrous tissue regions are clearly distinct in both the 0-ps and the 200-ps images. The spatial profile of the 0-ps image displayed by the thick line in Fig. 8.5(c), shows a marked dip indicating much lower light transmission through the fatty (adipose) region. The width of the dip corresponds to the spatial extent of the adipose region.. Interestingly, the situation is completely reversed in the spatial intensity profile of the 200-ps image of Fig. 8.5 (b). The profile displayed by the thin line in Fig. 8.5 (c) exhibits a peak indicative of higher light transmission through the fatty region at later time.

Fig. 8.5 (d) shows a three-dimensional reconstruction of the spatial intensity distribution of the light transmitted through the sample in time. In this figure, twenty profiles were plotted corresponding to integrated intensity areas of images taken 25-ps apart. The wide arrows labeled t_1 and t_8 point to the first and eight profiles taken at 0 and 200 ps time delay, respectively. The color bar on the right-hand side has been placed as a reference to indicate the intensity of the transmitted light, for the time-sliced profiles.

The difference in the spatial intensity distribution of the transmitted light through the fibrous and the adipose human breast tissues at the two different times is attributed to the higher scattering of light by the adipose tissue. Photons transiting through the adipose region scattered more and came out later compared to those transiting through the fibrous regions. *The 0 and 200 ps time slices accentuated this difference and provide*

the observed contrast in the transillumination images, demonstrating the importance of the time-domain imaging approach.

b) Cancerous and normal human breast tissue sample

Following the same procedure as with the first sample, *a second human breast tissue sample* was examined. This sample consisted of a cancer piece placed next to a normal piece obtained from the same patient. In this experiment, the incident beam was further expanded to achieve a plane incident wave of equal spatial intensity distribution by selecting the central region to avoid any misreading.

In the ***spectroscopic imaging approach***, two-dimensional transillumination images of the sample were recorded using 1210 nm, 1225 nm, 1275 nm, and 1300 nm light. The images are presented in Fig. 8.6 (a)-(d), respectively. Corresponding spatial intensity distributions of the images integrated over the same horizontal area as highlighted by the white dashed box in Fig. 8.6(a) are shown in the frames to the right of the respective images.

The cancer region (left-hand side) appeared much brighter than the normal region (right-hand side) in every image of the wavelengths recorded. As the wavelength of Cr:forsterite laser output was tuned from a lower (1210-nm) to a higher (1300-nm) wavelength, the intensity through both regions increased at a different rate, as can be observed in the profiles next to the images. In Fig. 8.6 (e), this increase in intensity as a function of wavelength can be better appreciated. The solid square boxes represent light going through the cancer tissue, while the white filled square boxes represent light going through the normal tissue. The plot values were obtained from the profiles in Figures 8.6

(a)-(d) for pixel positions to be around 80 for the normal region, and around 42 for the cancer region. This plot is a clear indication that deeper penetration of light into the tissue can be achieved using larger wavelengths.

Figure 8.6 (f) shows the intensity ratio $R(\lambda) = I_{Cancer}(\lambda) / I_{Normal}(\lambda)$ as a function of wavelength obtained from Fig. 8.6 (e). The intensity ratio values have been plotted using solid black circles connected by a thin dotted line. The intensity ratio obtained at 1210 nm light was 3.5, seven times higher than the one obtained at 1300 nm light (0.5). Furthermore, the image contrast $C = (I_{cancer}-I_{normal})/(I_{cancer} + I_{normal})]$ was calculated for the 1210, 1225, 1275, and 1300 nm profiles and were 0.55, 0.46, 0.29, and 0.11, respectively. The contrast for the image recorded using the 1210 nm light was five times larger than the one obtained using 1300 nm light.

The differences seen in both regions are attributed to the light transport characteristics of the two types of tissues. In addition, the high intensity rate change increment behavior observed in the normal region, going from darker at 1210-nm to brighter at 1300-nm, is believed to be caused by an unknown percentage of fatty tissue in the sample.

The two-dimensional ***time-sliced transillumination imaging*** *experimental results for the second sample* are presented in Fig. 8.7. Images in Figure 8.7 (a), (b),(c), and (d) correspond to 25, 125, 275, 375 time-gate positions, respectively. The images presented (a) through (d) clearly show the intensity spatial distribution of the transmitted light through the tissue at different time windows, for λ=*800nm*. Profiles plotted next to each

image show the spatial intensity distribution along a horizontal area covering the cancer and normal regions in the tissue sample.

The fact, that light spread more in the normal region than in the cancer region, is more evident if we analyzed the evolution of the pulse in image (a) through (d). The image recorded a 25-ps in Fig 8.7 (a) clearly shows a high transmission through the cancer region, and a minimum amount of light going through the normal region. The spatial intensity profile next to the image gives a more accurate reading of the amount of light going through both regions at this early time window. Approximately 100 hundred counts go through the cancer region and 1 through the normal region, resulting in a contrast of approximately equal to 1, e.g., $C(t=25\ ps) = 1$. At a much later time 325-ps delay in Figure (d), the situation is reversed, and more light goes through the cancer region than the normal region, corresponding to approximately 1 count and 110 counts, respectively, resulting in a negative contrast of -1, e.g., $C(t=325\ ps) = -1$. The negative contrast is due to the fact that the light going through the cancer region is very small as compared to the light going through the normal region. (Notice now, that the contrast time dependent) Fig. 8.7 (e) shows the intensity transmitted through the normal and cancer tissues of similar spatial area for vs. time-gate position. The time dependence intensity ratio of the light transmitted through the cancer and normal tissue $R(t) = I_{Cancer}(\lambda=800nm,t) / I_{Normal}(\lambda=800nm,t)$ using the intensity results obtained in Fig. 8.7 (e) has been plotted in Fig. 8.7 (f) using black circles connected by a thin dotted line. In the same figure, we have plotted the intensity ratio $R(t) = I_{Normal}(\lambda=800nm,t) / I_{Cancer}(\lambda=800nm,t)$ using white filled circles connected by a solid black line. This was done to emphasized the fact that ***different time-windows could help to visualize different tissue***

constituents. The cancer region is more clearly defined by the early-arriving photons, as seen in early time windows. On the other hand, late-arriving photons will better delineate the area of the normal region.

The difference in the spatial intensity distribution of the transmitted light through the cancer and the normal human breast tissues is attributed to the higher scattering of light by the normal tissue over the cancer tissue region. Photons transiting through the normal region scattered more and came out later as compared to those photons transiting through the cancer region. The time-domain very clearly helps to visualize and to separate normal and cancer human breast specimens from each other, by sorting the early light or the late using different time-windows. This without a doubt demonstrates the potential that the time-sliced transillumination imaging approach has in the field of optical mammography for distinguishing cancer lesions from normal tissues.

8.5 Conclusion

Results of the two-dimensional NIR laser-spectroscopic and time-sliced transillumination imaging experiments clearly demonstrate the diagnostic potential of optical imaging. The two-dimensional time-sliced transillumination imaging experiments demonstrate that optical imaging using optimal time slices is a promising method for imaging biomedical media. The incorporation of the time-sliced imaging technique to NIR spectroscopic optical imaging results will add a new dimension to the images obtained at each of the different wavelengths of light. This novel hybrid approach (time/colour) provides a new way for image visualization enhancement. In fact, it has a great potential for highlighting intrinsic differences present in the different human tissue constituents, under key wavelengths and optimal time windows. Both of the methods show selectivity of tissue types based on differences in photon transport and spectroscopic properties.

3D and 2D inverse image reconstruction methods are expected to benefit from the use of spectroscopic *fingerprints* and the *time-slicing* imaging approach. In inverse reconstruction, one uses the scattered light intensity measured around a turbid media with and without the object to reconstruct a spatial map of the interior of the media[8.22]. In practical situations, such as a breast tumor, it is not possible to obtain intensity measurements without the tumor, and approximate schemes will have to be used. Intensity measurements (of molecular components in tissue) at non-resonant wavelengths may substitute for measurements without the object, and while those at a resonant wavelengths may substitute for measurements with the object. The method would then reconstruct a spatial map of the change in absorption due to the object.

Besides the potential benefits these optical techniques could bring to optical mammography and optical tomography fields, it could also be of great help in the analysis and evaluation of histopathology due to disease, where key colors of light instead of staining with a dye could be used to enhance visualization of the disease tissue. (The utilization of dyes to highly tissue structures could add other degree of visualization for imaging breast tissue sample.) Some of the benefits of using this approach are that specific diseases could be differentiated through key colors of light.

In summary, the spectrum of light and the time-domain provides a wealth of opportunities for identification and classification of numerous subtle biological and biochemical changes present in the human body. Since wavelength/time-dependent differences exist between normal and diseased tissues, optical time-sliced spectroscopic imaging may provide simultaneous detection and diagnosis of diseases in the human body.

8.6 References and Notes

8.1 For a brief review of optical imaging and optical biopsy techniques, see R. R. Alfano, S. K. Gayen and A. Katz, "Advances in Mediphotonic Imaging and Biopsy," in "Optics and Imaging in the Information Age," IS&T - The Society for Imaging Science and Technology, Springfield, Virginia, USA, 299 - 304, 1997

8.2 Proceedings of Advances in Laser and Light Spectroscopy to Diagnose Cancer and Other Diseases III: Optical Biopsy, 29-30 January 1996, San Jose, California, edited by R. R. Alfano, SPIE, Volume 2679.

8.3 OSA Trends in Optics and Photonics Series Volume on Advances in Optical Imaging and Photon Migration ('96), edited by R. R. Alfano and J. G. Fujimoto, Optical Society of America, 1996.

8.4 C. H. Liu, B. B. Das, W. L. Sha Glassman, G. Tang, K. Yoo, H. Zhu, D. L. Akins, S. S. Lubicz, J. Cleary, R. Prudente, E. Celmer, A. Caron and R. R. Alfano, J. Photochem. Photobiol. B: Biol. 16, 187, 1992.

8.5 A. Mahadevan and R. Richards-Kortum, J. Biomed. Opt. 1, 31, 1996, and references therein.

8.6 M. S. Feld, R. Manoharan, J. Salenius, J. Orenstein-Carndona, T. J. Romer, J. F. Brennan III, R. R. Dasari, and Y. Wang, "Detection and characterization of human tissue lesions with near infrared Raman spectroscopy," in Advances in Fluorescence Sensing Technology, Vol. II, edited by J. R. Lakowicz, Proc. SPIE 2388, 99, 1995.

8.7 L. Wang, P. P. Ho, C. Liu, G. Zhang, and R. R. Alfano, Science 253, 769, 1991.

8.8 C. Hebden, R. A. Kruger, and K. S. Wong, Appl. Opt. 30, 794, 1991.

8.9 M. R. Hee, J. Izzat, J. M. Jaconson, J. G. Fujimoto, and E. A. Swanson, Opt. Lett. 18, 952, 1993.

8.10 J. Reintjes, M. Bashkansky, M. Duncan, R. Mahon, L. L. Tankerskley, J. A. Moon, C. L. Adler, and J. M. S. Prewitt, Opt. Photon. News, 4(10): 28, 1993.

8.11 R. Berg, S. Anderson-Engels, and S. Svanberg, "Time-resolved transillumination imaging." In Medical Optical Tomography: Functional Imaging and Monitoring, ed. by G. J. Muller et al., SPIE, Bellingham, Washington, 397-424, 1993.

8.12 E. M. Sevick, C. L. Burch, J. K.Frisoli, M. L. Johnson, K. Nowaczyk, H. Szmacinski, and J. R. Lakowicz, "The physical basis of biomedical optical imaging using time-dependent measurements of photon migration in the frequency domain. In Medical Optical Tomography: Functional Imaging and Monitoring, ed. by G. J. Muller et al., SPIE, Bellingham, Washington, 485-512, 1993.

8.13 M. A. O'Leary, D. A. Boas, B. Chance, and A. G. Yodh, Opt. Lett. 20: 426, 1995.

8.14 K. P. Chan, M. Yamada, and H. Inaba, Opt. Lett. 20, 492, 1995.

8.15 D. S. Dilworth, E. N. Leith, and J. L. Lopez, Appl. Opt. 30,1796, 1991.

8.16 S. R. Arridge, "The forward and inverse problems in time-resolved infrared imaging. In Medical Optical Tomography: Functional Imaging and Monitoring, ed. by G. J. Muller, SPIE, Bellingham, Washington, 35-64, 1993.

8.17 S. Thomsen and D. Tatman, "Physiological and pathological factors of human breast disease that can influence optical diagnosis," Ann. N. Y. Acad. Sci. 838, 171, 1998.

8.18 F. A. Marks, SPIE 1641, 227, 1992.

8.19. V. Petricevic, S. K. Gayen, and R. R. Alfano, Appl. Opt. 28, 1609, 1989.

8.20. J. J. Dolne, K. M. Yoo, F. Liu, and R. R. Alfano, Lasers Life Sci. 6, 131, 1994.

8.21. S. G. Demos and R. R. Alfano, Opt. Lett. 21, 161, 1996.

8.22 W. Cai, B. B. Das, F. Liu, M. Zevallos, M. Lax, and R. R. Alfano, Proc. Natl. Acad. Sci. USA 93, 13561, 1996.

8.7 Figures

Fig. 8.1 Transmission spectrum of a normal human breast tissue sample, 3-mm thick. Shadow region shows the wavelengths under study in the NIR spectroscopic studies using a Chromium-doped Forsterite laser system. (After F. A. Marks, SPIE **1641**, 227, 1992).

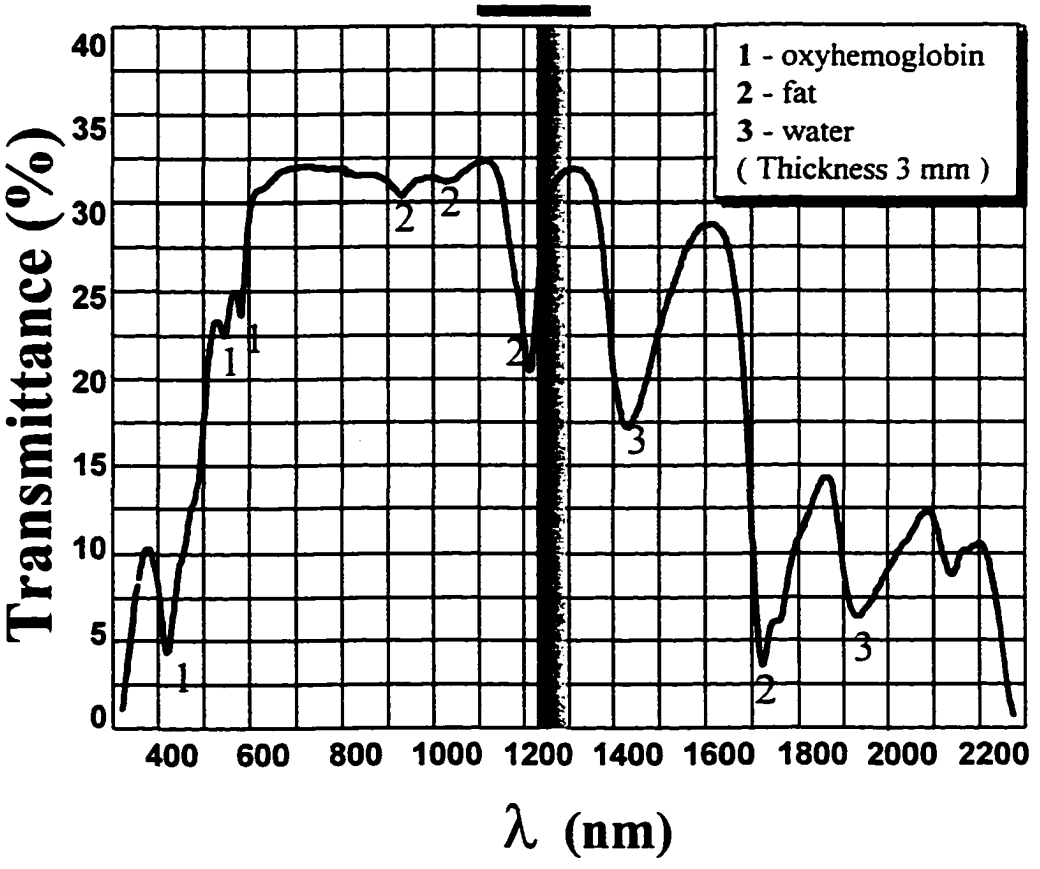

Figure 8.2 Two-dimensional spectroscopic transillumination images of a 5 mm thick human breast tissue sample comprising adipose and fibrous regions obtained using light of wavelength (a) 1225 nm, (b) 1235 nm, (c) 1255 nm, and (d) 1300 nm. Corresponding spatial intensity profiles integrated over the same horizontal area for each image are displayed in the right side of the respective images. The inset at the top is a photograph of the exit surface of the tissue specimen.

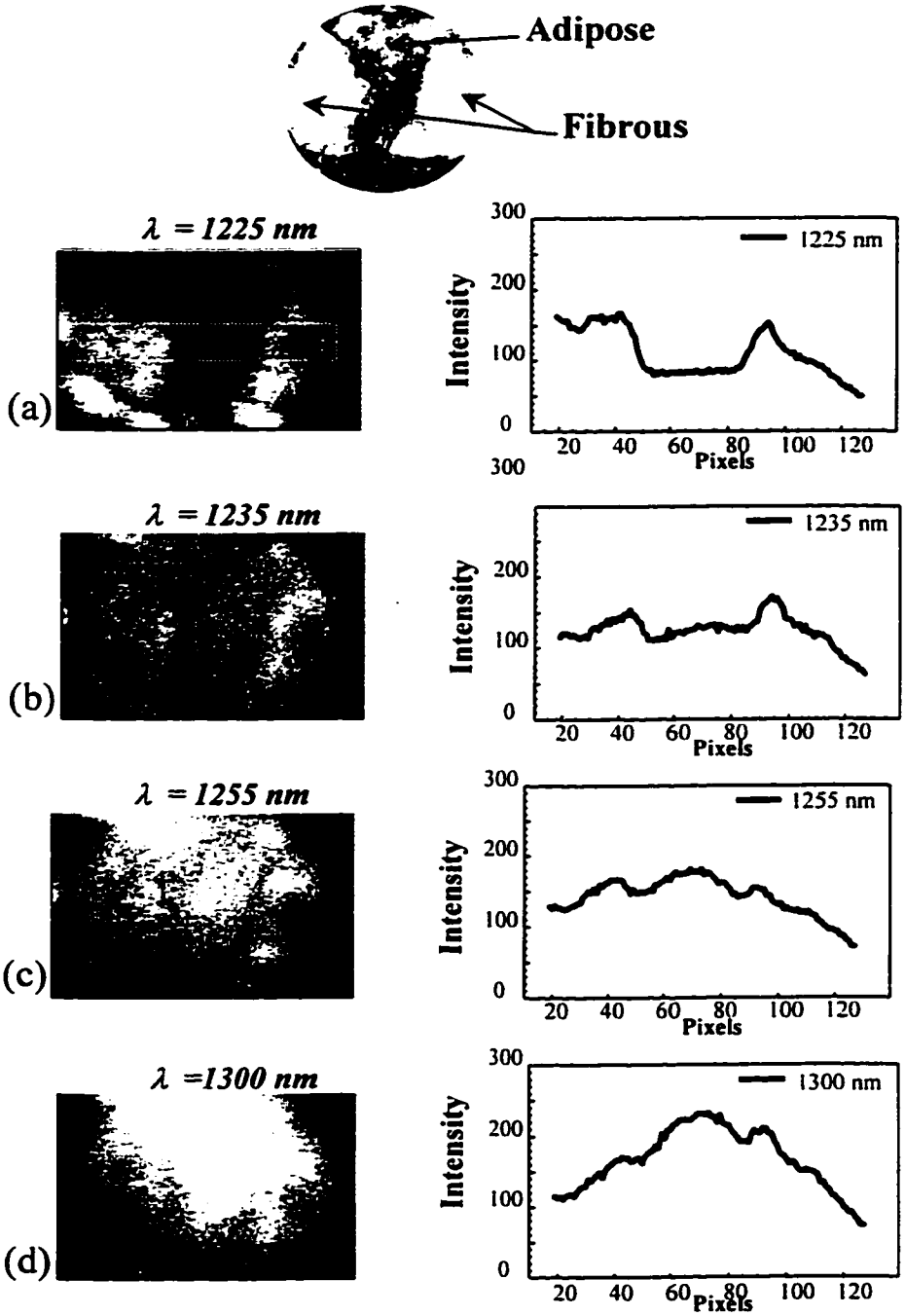

Figure 8.3 Wavelength dependence of intensity ratio of the light going through the adipose (A) and fibrous regions (F), $R(\lambda) = I_A / I_F$. Solid circles represent experimental data and the line is used as a guide for the eye. Inset shows the optical transmission spectrum of a 3-mm thick breast tissue sample over the 1200-1300 nm range (after Ref. 8.18)

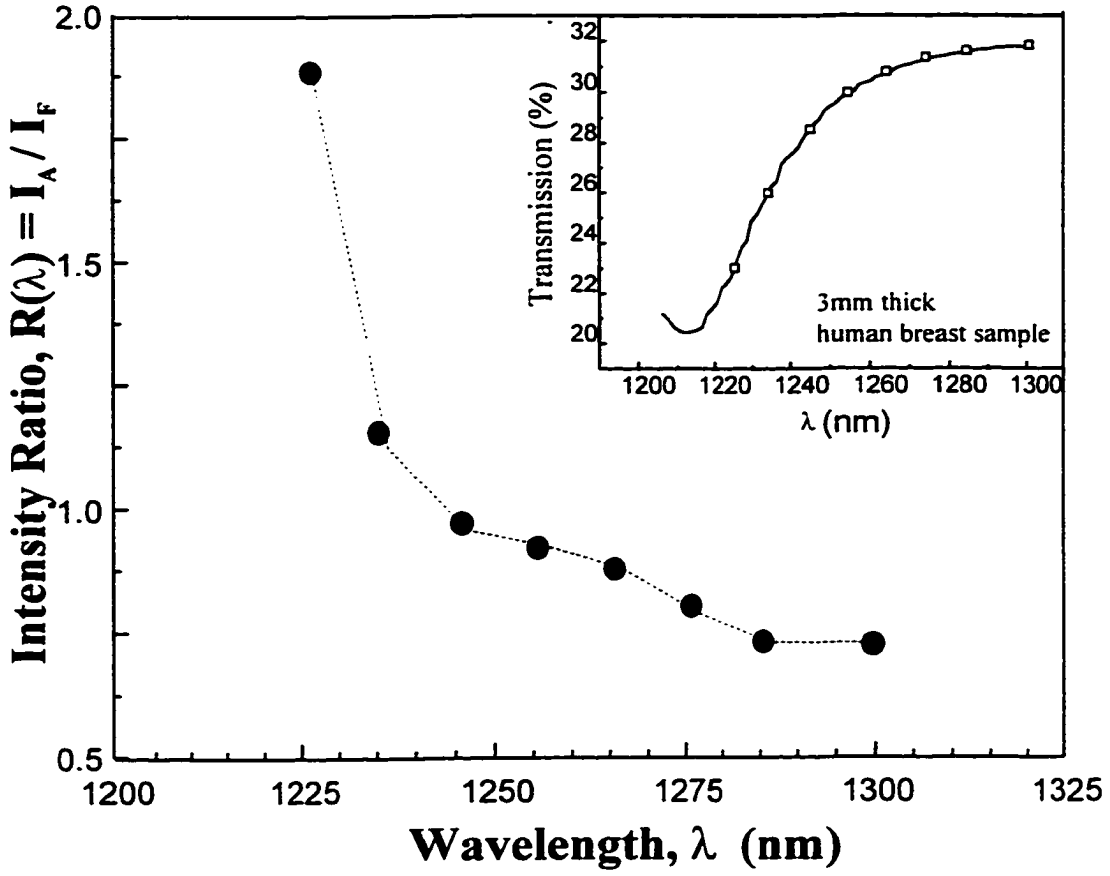

Figure 8.4 Spatial intensity profile—integrated over the same horizontal area as displayed in Fig.8.2—of (a) the resonant image. *Image*(1235 nm), and the nonresonant image, *Image*(1300 nm); (b) the ratio image. *Image*(1235nm)/*Image*(1300nm); and (c) the difference image, *Image*(1235nm) - *Image*(1300nm).

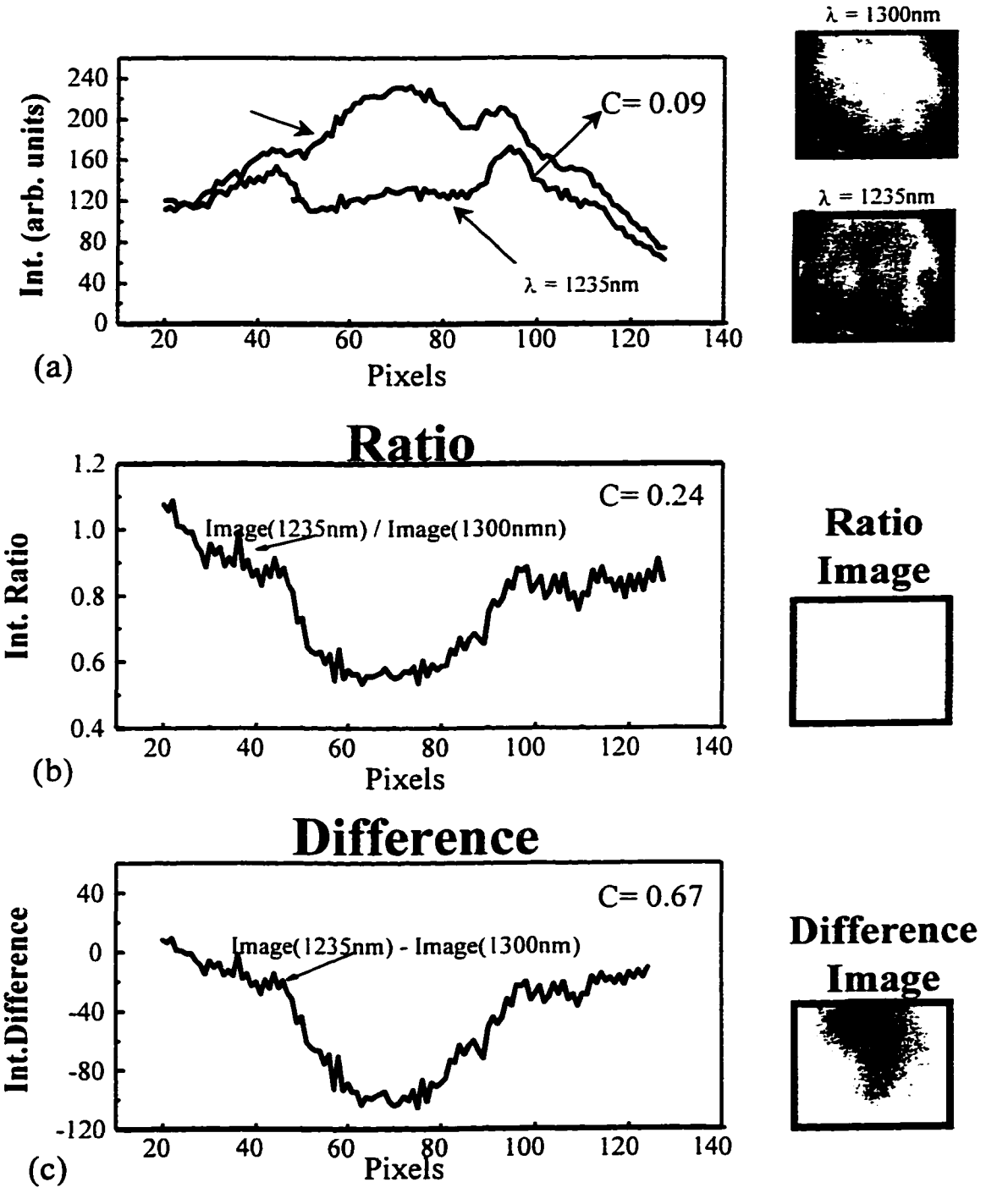

Figure 8.5 Time-sliced transillumination image of the first human breast tissue sample for gate delays of (a) 0-ps and (b)-200 ps. (c) Intensity spatial profiles of the (0)-ps (thick line) and the 200-ps (thin line). (d) Three-dimensional reconstruction of the pulse transmitted through the tissue. See text for details. The inset at the top is a photograph of the exit surface of the tissue specimen.

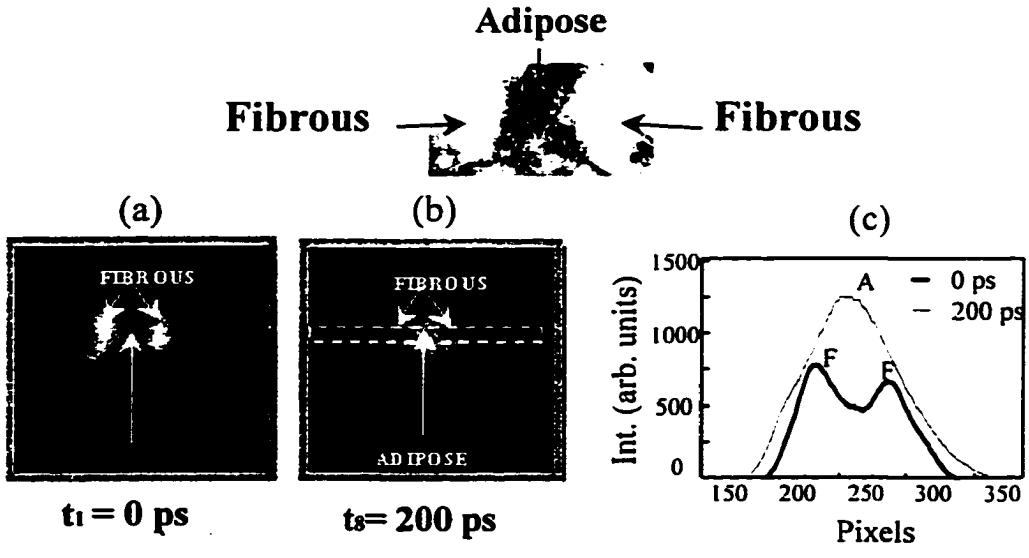

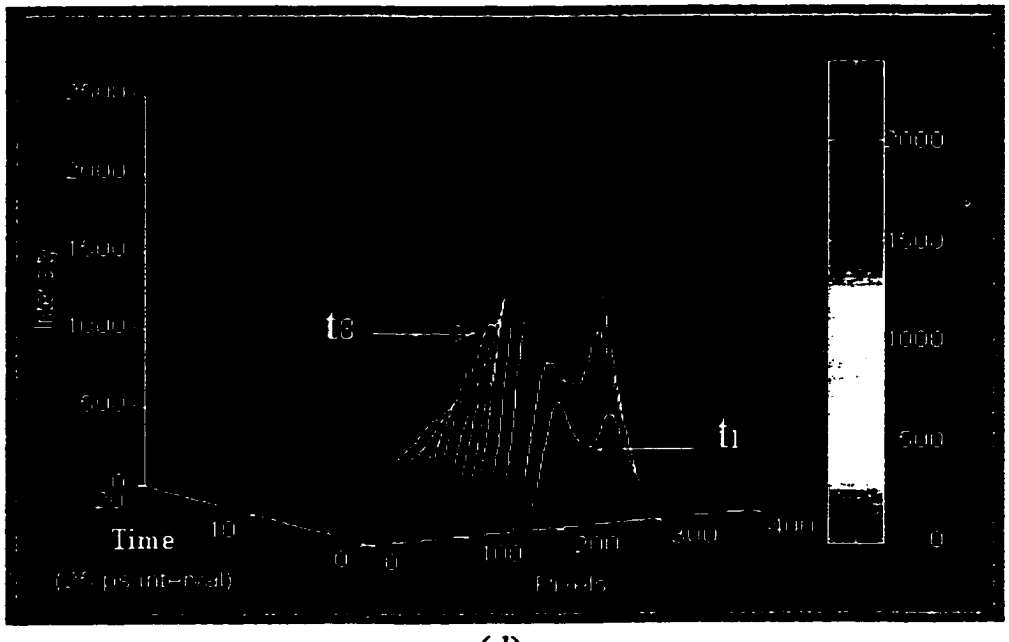

(d)

Figure 8.6 Two-dimensional NIR spectroscopic transillumination images of cancer and normal human breast tissue specimens. 5 mm thick, obtained using light of wavelength (a) 1210 nm, (b) 1225 nm, (c) 1275 nm, (d) 1300 nm. Corresponding spatial intensity profiles integrated over the same horizontal area for all the images are displayed in the frames to the right of the respective images. The cartoon at the top is just to indicate the size and the positions of the sample regions.

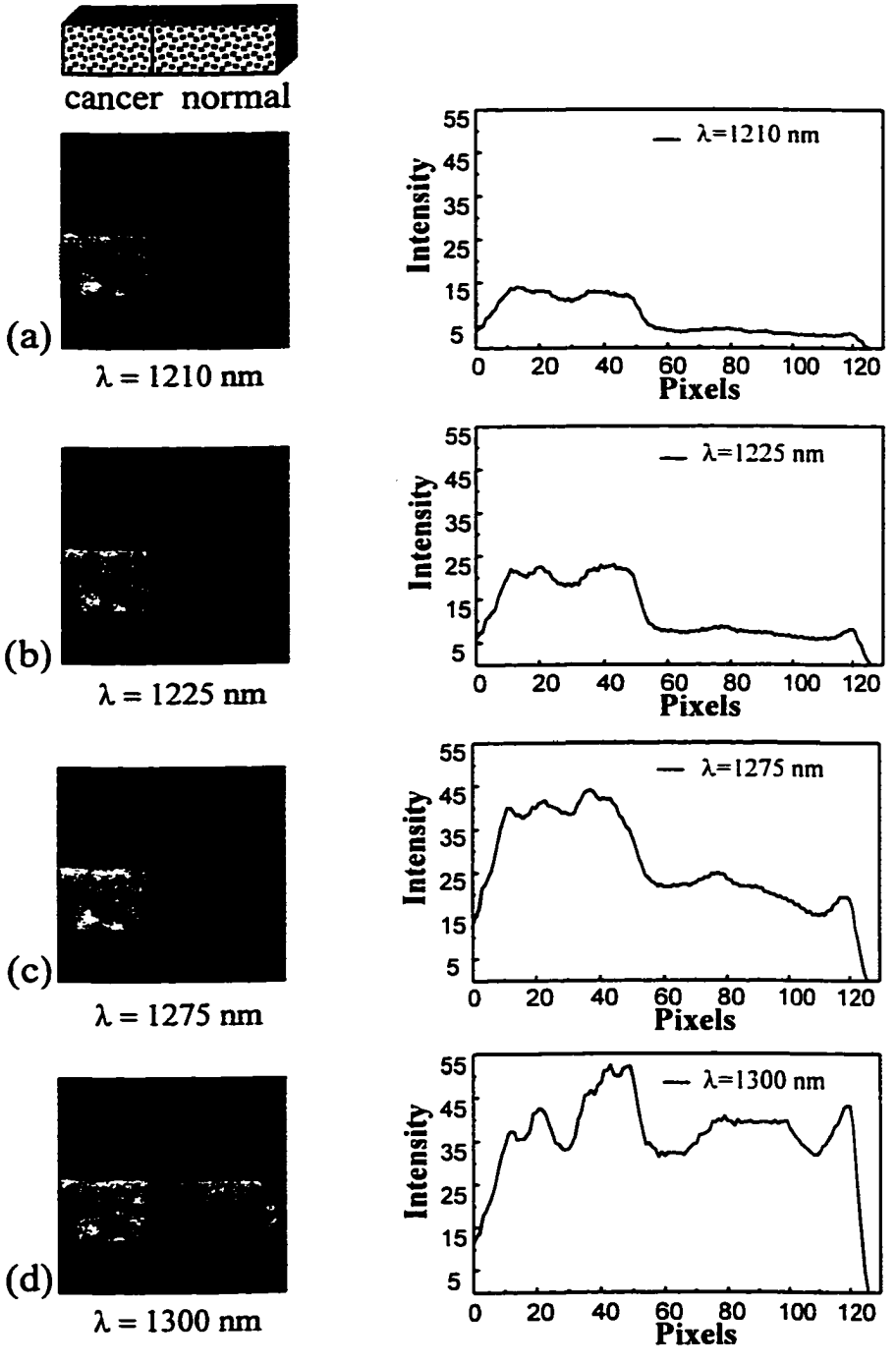

Figure 8.6 (e) Intensity transmitted through the normal and cancerous regions vs. wavelength. Spatial intensity profiles of the light going through the cancerous and normal region has been plotted using black and white squares. respectively. Figure 8.7 (f) presents the wavelength dependence on intensity ratio. Solid circles represent experimental data and the line is used as a guide for the eye.

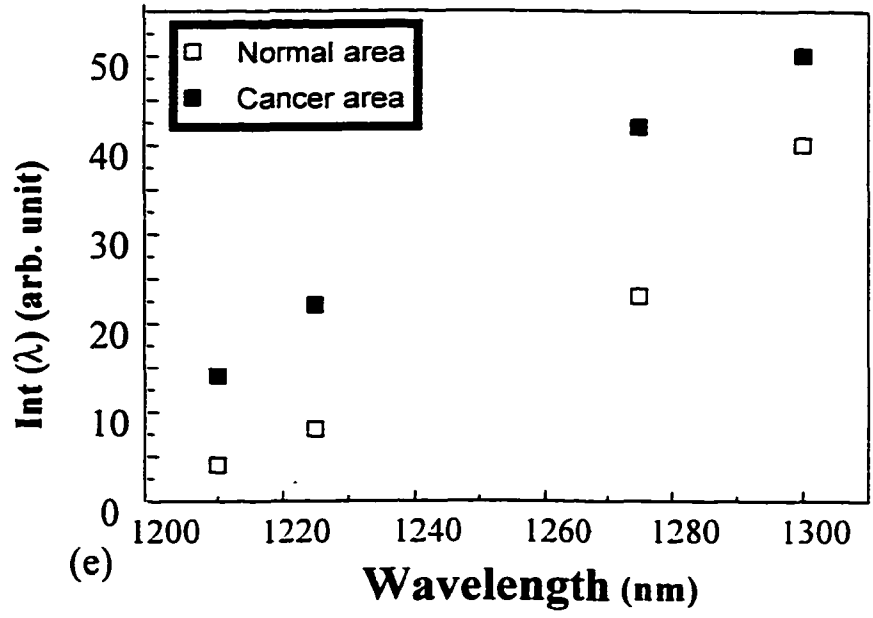

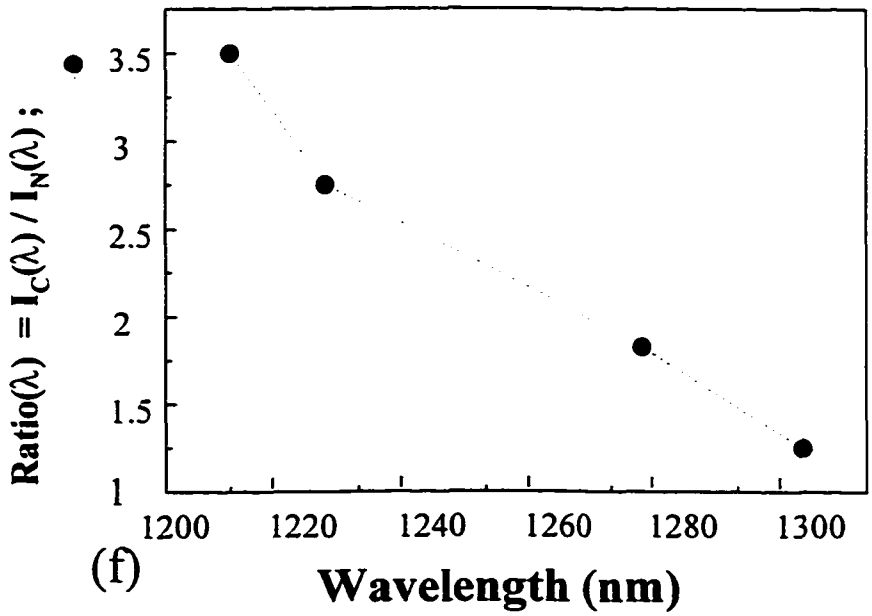

Figure 8.7 Time-sliced transillumination image of the second sample in the text for gate delays of (a) 25-ps, (b) 125-ps, (c) 275-ps, and (d) 375-ps. Intensity spatial profiles of the light transmitted through the sample have been plotted next to each image. The cartoon at the top is just to indicate the size and the positions of the sample regions.

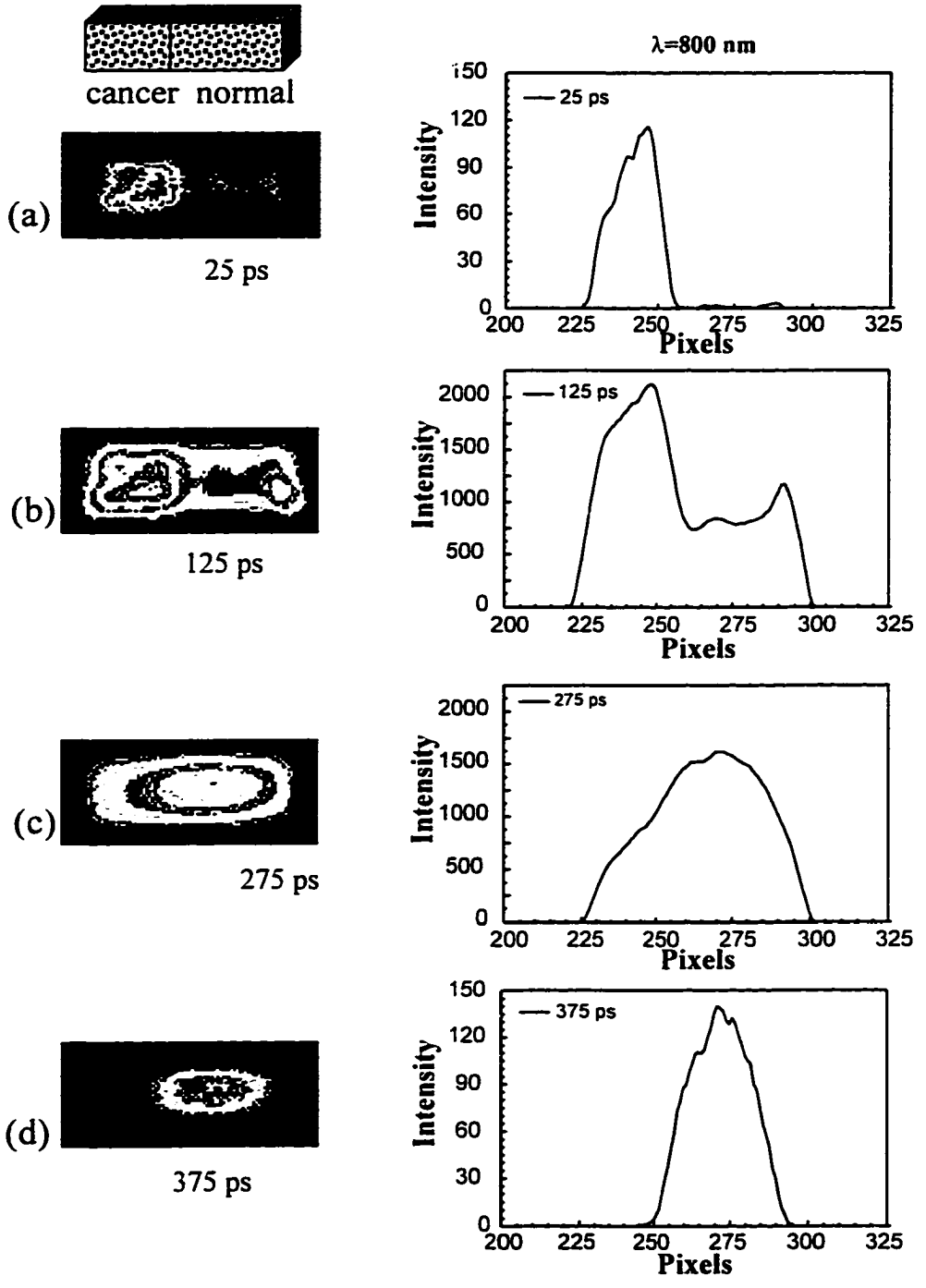

Figure 8.7 (e) presents the intensity transmitted through both samples vs. time-gate position. See text for details. Figure 8.7 (f) presents the wavelength dependence of intensity ratio in Fig. 8.7 (e). See text for explanation.

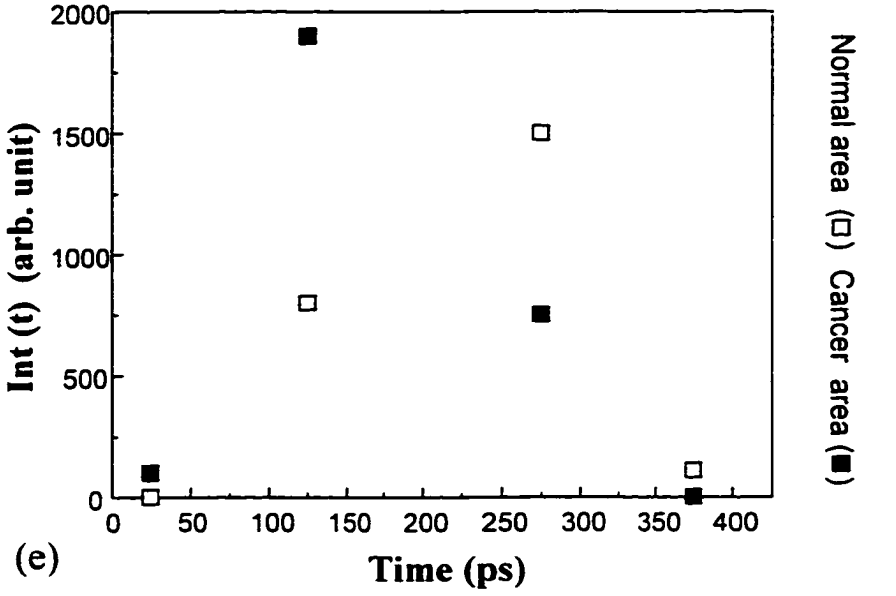

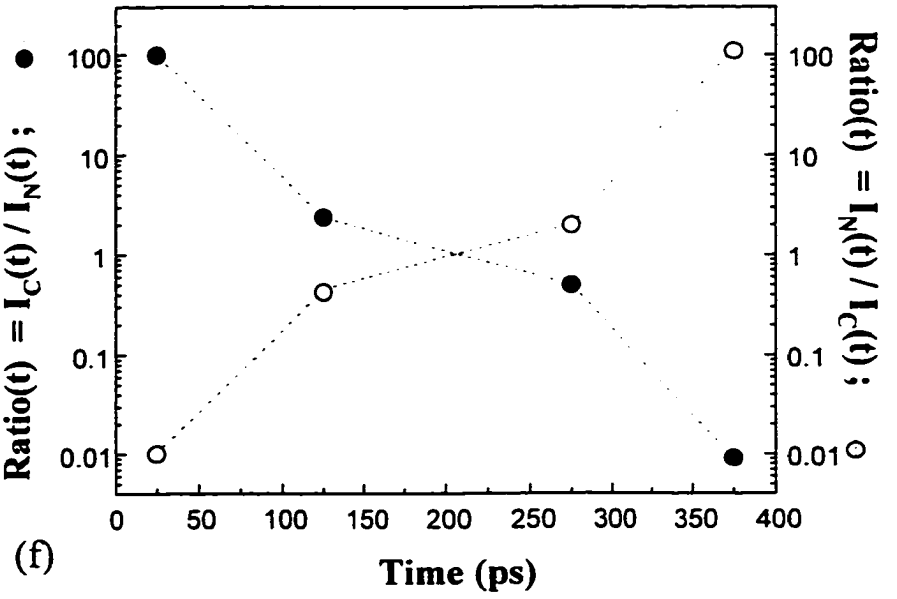

Chapter 9

Summary

In the first part of this thesis we have theoretically and experimentally investigated the propagation of light through various types of highly scattering anisotropic media. This was achieved via steady state and ultrafast detection schemes, with the aim to develop a better understanding of photon migration and light-tissue interaction.

The second part of the research is aimed to improve the image quality and involved near-infrared transillumination imaging, by implementing detection schemes based on spatial, polarization, and time gated light sorting techniques, while paying special attention to the spectroscopic information obtained through the selection of an optimum wavelength. This was accomplished using state of the art two-dimensional CW and time-resolved light detection imaging systems.

The main findings in this thesis are in Chapters 3 through 8 and are summarized as follows:

In Chapter 3, ultrashort pulses of light propagating in highly scattering media were measured. We found that the intensity temporal profiles of scattered pulses measured at fixed spatial positions inside the medium depend on the angle of arrival of photons at a point. We observed that light retains a strong angular dependence for distances as far as 20 l_t. This is a clear indication that well-defined photon paths are preserved in the launching direction and that photon direction (momentum) is maintained

even in the early diffusive regime. The angular information of photons travelling through a fixed spatial position may provide an additional parameter. which could help scientist to predict photon transport with higher accuracy.

In order to describe the degree of anisotropy in photon distribution due to the source directionality, two new equations were introduced. These equations describe the angular anisotropy at a point and the angular-spatial anisotropy between two points. Here, it was found that there is a higher degree of anisotropy in the early time of propagation that is where photons experience less scattering events.

In Chapter 4, we demonstrated that the NED model provides a better description of the temporal and spatial evolution of scattered light than the DA does. We ascertained this by comparing the accuracy of the DA and the NED equations in predicting light propagation in a highly forward-scattering medium against measured scattered light temporal profiles acquired for the pre-diffusive and diffusive regime. Appreciable differences between the NED and DA were observed for photon number density for distances as large as 15 l_t. For distance beyond 20 l_t (in the well diffuse regime) the NED and DA predict comparable results. The NED approach may be considered as a possible alternative to the DA in future optical imaging algorithms.

In Chapter 5, we found that the structures of the samples play an important role in light propagation. In particular, we found that the orientation of fibers in the sample structure with respect to the polarization direction of the incident beam influences on the

parallel and perpendicular components of the transmitted scattered light. The found difference on the transmitted intensity temporal profiles along and across the fibers of a tissue sample suggests the existence of different diffusion coefficients for a medium with definite internal fibrous or tubular structure (such as tissues). The observed existence of preferred orientation of tissue fibers for higher transmission of light is a useful information for optimizing the performance of a transillumination imaging system.

In Chapter 6, two-dimensional NIR transillumination images of an object hidden inside different biological media were obtained by implementing a Fourier gate in tandem with a polarization gate to improve the image quality. The image quality of shadowgrams obtained using a 1250-nm and 1064-nm light was compared. A salient observation of this work is that the near-infrared light around 1250 nm enables deeper penetration and provides higher image contrast than that obtained using 1064 nm or shorter-wavelength light. A combination of lower scattering and higher absorption (due to water content in the sample) accounts for the better image quality obtained using 1250-nm light.

The polarization gate and the Fourier gate were both found to be effective in sorting out some of the image-bearing photons. The polarization gate is simple and easy to implement. Its efficacy for transillumination imaging is limited to sample thicknesses for which the polarization of the transmitted light is not completely randomized by scattering events within the tissue. In our experimental arrangement, this limit was approximately 10 mm for human breast tissues, and 16 mm for bovine brisket tissues.

The Fourier gate, in principle, may be effective in discriminating against multiple-scattered photons for samples of any thickness. However, its effectiveness is more evident for thicker samples. It cannot discriminate against on-line scattered photons. As the thickness of the turbid sample increases, the relative magnitude of image-bearing photons decreases and that of the on-line scattered photon increases, making the signal-to-noise ratio poorer. When combined with a time gate both the polarization gate and the Fourier gate may provide much stronger discrimination against multiple-scattered light.

In Chapter 7 we make use of the transit time of fly to select the early arriving photons to improve the image quality. Two-dimensional time-sliced NIR transillumination images of bones and foreign objects hidden inside thick biological media were recorded at different time windows. Better quality images were acquired by sorting the early arriving photons through the use of an 80ps time-gate. The feasibility of using time-sliced imaging for the detection of bones in thick tissues and bone fractures has been shown, and highly encourages us to pursue this optical modality in development of viable alternatives for regular monitoring of bone as in case of osteoporosis, arthritis, rheumatic disorders and other abnormalities. The ability of imaging a rod 6.5mm embedded in the 72 mm thick excised human breast sample gives a clear indication of the potential time-sliced imaging has in the medical field, as an screening tool for the detection of tumours.

The results obtained from these time-resolved transillumination measurements underline the potential of ultrafast optical methods for application in biomedical imaging. It is expected that further improvements in the electronic time-gated imaging system

would also enhance the time-slicing imaging approach to more precise and faster measurements.

Finally in Chapter 8, we combine the time-sliced and the laser-spectroscopy and transillumination optical imaging approach to characterize breast tissue constituents in the near infrared spectral band.

In the NIR laser-spectroscopy approach, we were able to obtained images that had marked contrast between adipose and fibrous tissues, and between cancer and normal tissues, by tuning the Cr:forsterite laser output into an absorption band of fatty human breast tissue.

In the two-dimensional time-sliced transillumination approach, we found that different time windows can highly different tissue constituents, based on the sample absorption and scattering properties. In particular we found that early light images can highlight some type of cancer tissues, and that late light images show better the highly scattering tissues such as fat.

Results of the two-dimensional NIR laser-spectroscopic and time-sliced transillumination imaging experiments clearly demonstrate the diagnostic potential of ultrafast optical imaging. The incorporation of the time-sliced imaging technique to NIR spectroscopic optical imaging results add a new dimension to the images obtained at each of the different wavelengths of light. This novel hybrid approach (time/color) provides a new way for image visualization enhancement, which has a great potential for highlighting intrinsic differences present in the different human tissue constituents, under key wavelengths and optimal time windows.

In summary, the spectrum of light and the time-domain provides a wealth of opportunities for identification and classification of numerous subtle biological and biochemical changes present in the human body. With presence of wavelength/time-dependent differences between normal and diseased tissues. Optical time-sliced spectroscopic imaging may provide for simultaneous detection and diagnosis of diseases in the human body.

Certainly, the wide spectrum of light offers a vast amount of possibilities for the detection and monitoring of diseases, which are being and would be discovered to the pace of the emerging technology.

Chapter 10

Future Research Directions

The research work conducted in this thesis needs to be continued. A clear and better understanding of light propagation in highly scattering media, and light-tissue interaction are key requirements to the successful development and introduction of optical imaging in the medical field.

More experiments of light propagating through highly scattering media need to be performed in order to understand how time-sliced shadowgrams of an object hidden inside a highly scattering medium gets distorted as a function of the optical parameters of the medium, position of the object, as well as time. A theory that could predict the distortion of the shadow image would be extremely helpful to aid mathematical algorithms for 3D and 2D inverse image reconstruction.

Experiments using different light source geometries are highly encouraging since during the investigation performed on shadowgrams we were able to observe that expanded plane waves and convergent light sources could improve the quality of the image depending on the position of the object inside the medium.

The results obtained on NIR time-sliced shadowgram imaging on thick human breast samples highly suggest experiments in vivo as the next course of action. A

multiple wavelength approach is recommended in the time-sliced imaging technique. where key wavelengths of light could highlight the different tissue constituents.

Fingerprint wavelengths of light that could highlight different tissue constituents and more importantly particular types of cancer are yet to be found for 2D and 3D imaging.

Inverse-image reconstruction methods for 3D is the next step and is expected to benefit particularly from the use of spectroscopic *fingerprints* and *time-sliced* imaging.

10.1 List of Publications and Presentations Related to this Thesis.

Publications

M. E. Zevallos, S. K. Gayen, B. B. Das, M. Alrubaiee, and R. R. Alfano, "Time-sliced transillumination Imaging of bones", to be published in IEEE Journal of Selected Topics in Quantum Electronics, 1999.

S. K. Gayen, M. E. Zevallos, M. Alrubaiee, and R. R. Alfano, Near-infrared laser spectroscopic imaging: a step towards diagnostic optical imaging of human tissues, to be published in Lasers in Life Sciences, 1999.

S. K. Gayen, M. E. Zevallos, M. Alrubaiee, J. M. Evans, and R. R. Alfano, Two-dimensional near-infrared transillumination imaging of biological medical media using a chromium-doped forsterite laser, Applied Optics Letters, Sept 15 1998.

M. E. Zevallos, A. Ya Polishchuk, B. B. Das, F. Liu, and R. R. Alfano, Time-Resolved Scattering Measurements from Scattering Media Fitted to Non-Euclidean and Conventional Diffusion Model, Phys. Rev. E, 57, 6, 1998.

S. K. Gayen, M. E. Zevallos, B. B. Das, and R. R. Alfano, Time-sliced transillumination Imaging of normal and cancer breast tissues, to be presented in OSA trends in Optics and Photonics on Advances in Optical Imaging and Photon Migration on March 10, 1998.

S. K. Gayen, L. Wang, M. E. Zevallos, and R. R. Alfano, Near-infrared transillumination imaging with the use of a chromium-doped forsterite laser, OSA Technical Digest Series, Vol. 11, 150-151 (1997)

M. E. Zevallos, F. Liu, and R. R. Alfano, Time-resolved pulse propagation in tissue tubular structure, OSA Technical Digest Series, Vol. 11, 148-149, 1997.

M. E. Zevallos, F. Liu, B. B. Das, A. Ya. Polishchuk, and R. R. Alfano, Angular Dependence of The Intensity Temporal Profiles of Scattered Pulses in Diffusive Regime, OSA trends in Optics and Photonics on advances in Optical Imaging and Photon Migration, R. R. Alfano, and James G. Fujimoto, eds., Vol. II, 21-24, 1996.

A. Ya Polishchuk, M. E. Zevallos, Feng Liu, and R. R. Alfano, Generalization of Fermat's principle for photons in random media: The least mean square curvature of paths and photon diffusion on the velocity sphere, Phys. Rev. E, 53, 5523 (1996)

A. Ya Polishchuk, Jean Dole, Feng Liu, M. E. Zevallos, B. B. Das, and R. R. Alfano, Fermat Photons: Paths Propagation and Imaging in Turbid Media, OSA trends in Optics and Photonics on Advances in Optical Imaging and Photon Migration, R. R. Alfano, and James G. Fujimoto, Eds., Vol. II, 14-17, 1996.

W. Cai, B. B. Das, F. Liu, M. E. Zevallos, M. Lax, and R. R. Alfano, Time Resolved Diffusion Tomographic Image Reconstruction in Highly Scattering Turbid Media, Proc. Natl. Acad. Sci. USA, Vol. 93, 13561-13564, Nov. 1996.

W. Cai, B. B. Das, F. Liu, M. E. Zevallos, M. Lax, and R. R. Alfano, Time Resolved Diffusion Tomographic Image Reconstruction in Highly Scattering Turbid Media, OSA trends in Optics and Photonics on Advances in Optical Imaging and Photon Migration, R. R. Alfano, and James G. Fujimoto, Eds., Vol. II, 269-275, 1996.

B. B. Das, J. Dolne, R. L. Barbour, H. L. Graber, J. Chang, M. E. Zevallos, F. Liu, and R. R. Alfano, Analysis of Time-Resolved Data For Tomographical Image Reconstruction of Opaque Phantoms and Finite Absorbers in Diffusive Media, SPIE Vol. 2389, 16-28, 1995.

Presentations

M. E. Zevallos, S. K. Gayen, and R. R. Alfano, Imaging of bones inside tissues using electronic gate, Presented in the1998 OSA Annual Meeting/ILS-XIV, held on October 4-9 in Baltimore, Maryland.

S. K. Gayen, M. E. Zevallos, and R. R. Alfano, Time-sliced and spectroscopic near-infrared imaging of normal and cancer human breast tissues, Presented in the1998 OSA Annual Meeting/ILS-XIV, held on October 4-9 in Baltimore, Maryland.

M. E. Zevallos, S. K. Gayen, and R. R. Alfano, Two-dimensional transillumination imaging of tissues
using 1250-nm light from a tunable chromium-doped forsterite laser, presented at the CLEO'98 conference held on May 3-8, 1998 at the Moscone Center in San Francisco California

S. K. Gayen, M. E. Zevallos, M. Alrubaiee, J. M. Evans, and R. R. Alfano, Time-sliced two-dimensional near-infrared imaging of normal and malignant human breast tissues, presented at the CLEO'98 conference held on May 3-8, 1998 at the Moscone Center in San Francisco California

M. E. Zevallos, S. K. Gayen, M. Alrubaiee, J. M. Evans, and R. R. Alfano, Near-Infrared Imaging Through Biological Tissues Using a Cr^{4+}:Forsterite Laser and a Nd:Yag Laser, presented at the NASA URC Technical Conference '98 held Feb. 21-26, 1998 at Huntsville, AL

M. E. Zevallos, S. K. Gayen, M. Alrubaiee, J. M. Evans, and R. R. Alfano, Near-Infrared Imaging with the use of a Cr^{4+}:Forsterite Laser, presented at the NASA Minority

University Space Interdisciplinary Network (MU-SPIN) Seventh Annual Users Conference, held on Oct 8-10, 1997 New York, NY

M. E. Zevallos, F. Liu, and R. R. Alfano, Time-resolved pulse propagation in tissue tubular structure, presented at the CIEO'97 conference, held on Baltimore, Maryland.

M. E. Zevallos, F. Liu, B. B. Das, A. Ya Polishchuk, and R. R. Alfano, Angular Dependence of The Intensity Temporal Profiles of Scattered Pulses in Diffusive Regime, presented at the CIEO'96 conference, held on Orlando, Florida.

Appendix A

In this appendix, some of the computer programs used in this thesis will be presented. The programs were provided by Dr. Feng Liu and Dr. A. Ya Polishchuck.

A.1 Program to Average the Intensity Temporal Profiles Obtained at a Fixed Spatial Point Over Angles of Arrival. (Equation 4.5 in chapter 4)

```
# AVERAGE INTENSITY (INTENSITY TEMPORAL PROFILES INTEGRATED OVER ANGLES)
#ifndef lint
#static char sccsid[] = "@(#)scsubr.r 1.6.1.2 95/12/05";
#endif
#
      implicit double precision (a-h,o-z)
      character*12 name1,name2,name3
      real*8 pi,z(30,2500),yout(2500),zout(2500),fac(30),tt
      integer ny(30,2500), ncount(30),iflag
      pi=3.141592654
      nmin=2500
      print *, " number of file , max 30 files, and mode of operation"
      read *, np,iflag
      do i=1,np {
      write(6,*)"the ",i,"file"
      print*, "read in file name, and corresponding angle in degree"
      print*, "From small angle to large angle"
      read*, name1,fac(i)
      open(3,file=name1)
      do ii=1,2500 {
      read(3,*,end=222)ny(i,ii),z(i,ii)
      }
222   ncount(i)=ii-1
      print*,ncount(i)
      close(3)
      if(nmin .gt. ncount(i)){nmin=ncount(i)
      }
      }
      do i=1,nmin {
      z(np+1,i)=z(np,i) #assign I(180) to be same as largest angle
      }
      fac(np+1)=180.
      do ii=1,np+1 {
      tt=sin(fac(ii)*pi/180.)
      print*,fac(ii),tt
}
      print*, "read in averaged file name"
      read*, name2
      open(3,file=name2)
```

```
      dc i=1,nmin {
      zout(i)=0.
      if (iflag .eq. 1) {
      do ii=1,np {
      zout(i)=zout(i)+(z(ii+1,i)*sin(fac(ii+1)*pi/180.)-z(ii,i)*sin(fac
(ii)*pi/180.))*(fac(ii+1)-fac(ii))/360.*pi
      yout(i)=yout(i)+(z(ii+1,i)*sin(fac(ii+1)*pi/90.)+z(ii,i)*sin(fac(
ii)*pi/90.))*(fac(ii+1)-fac(ii))/720.*pi
      }
      }
      else if (iflag .eq. 2) {
      do ii=1,np {
      zout(i)=zout(i)+(z(ii+1,i)+z(ii,i))*sin((fac(ii)+fac(ii+1))/360.*
pi)*(fac(ii+1)-fac(ii))/360.*pi
      yout(i)=yout(i)+(z(ii+1,i)+z(ii,i))*sin((fac(ii)+fac(ii+1))/180.*
pi)*(fac(ii+1)-fac(ii))/720.*pi
      }
      }
      ratio=yout(i)/zout(i)
      write(3,111)ny(1,i),zout(i),yout(i),ratio
      }
      close(3)
111   format(I4,1x,3e15.5)
      stop
      end
```

A.2 Programs to Fit the Angular-Integrated Intensity Temporal Profile to the Non-Euclidean and Conventional Difusion Models, in Chapter 4.

```
!<arch>
fitayp.r        853179788   7534  70    100400  2022
#ifndef lint
#static char sccsid[] = "@(#)fitayp.r 1.4 97/01/13";
#endif
#     program fitayp.r
#     for point source diffusion eq. fit
#     must be linked with taurosv.f
#     and payp.r,ayppro.f
#     ALL UNIT IN PS, MM
#
#
      subroutine fcn(npar, g,f,x,iflag)
      implicit double precision ( a-h, o-z)
      character * 12 anam, outfile,comfle
      character * 72 jj1,jj2
      real*8  y(2500), z(2500), sd(3),w(2500), x(6), c(2500)
      go to (10,60,60,60,120) iflag
 10   print *, "enter infile"
      read  *, anam
      open(1,file=anam)
      print *, "enter outfile"
```

```
      read *, outfile
      open(8,file=outfile)
#     print *,"enter comfle for diff. out put"
#     read *,comfle
#     open(4,file=comfle)
      print *, "index"
      read*, dex
      print*, "sd locations x, y, z (mm)"
      read*, sd(1),sd(2),sd(3)
      print*,"read in start time to do fitting (ps)"
      read*,ttsta
      ymax=0.
      yto=0.
#     read(1,*)jj1,jj2
#     read(1,*)ttjj1,tttj2
      do i=1,2500 {
      read (1,*,end=222)w(i),y(i)    #, c(i)
      if (y(i).gt.ymax)ymax=y(i)
      if (y(i).lt.0)y(i)=.0
      }
222   n=i-1
      nn=n-1
      close(1)
      do m=1,nn {
      yto=yto+(y(m)+y(m+1))*(w(m+1)-w(m))/2.
      }
#     write(6,*)"area=",yto
60    f=0.0
      zmax=0.
      zto=0.
      do i=1,n {

      call fayp(x(1),x(2),dex,sd,w(i),z(i), wwjunk) #wwjunk diffusion
      if(z(i).gt.zmax) {zmax=z(i)
      }
      if(z(i).lt.0) z(i)=.0
}
      do i=1,n {
      z(i)=z(i)/zmax*ymax*x(3)       #equal total intensity
      if (w(i) .ge.ttsta) {
#     f=f+(z(i)-y(i))*(z(i)-y(i))/sqrt(y(i)*y(i))
      f=f+(z(i)-y(i))*(z(i)-y(i))
      }
}
      f=f/ymax/ymax
      if (iflag.ne.3) return
120   #     print *,x(1),x(2),wd
      write(8,*)"%lt=",x(1)
      write(8,*)"%la=",x(2)
      write(8,*)"%thickness=",sd(1),sd(2),sd(3),"norm factor=",x(3)
      write(8,*)"%fcn=",f,"theory max=",zmax
      write(8,*)"%exp. max=",ymax,"time-fit-exp"
      do m=1,nn {
      zto=zto+(z(m)+z(m+1))*(w(m+1)-w(m))/2.
      }
      rat=yto/zto
      write(8,*)"%total count exp.=",yto
```

```
      write(8,*)"%total count thec=", ztc,"ratio=exp/thec",rat
      write(8,*)"ndata=["
      do i=1,n {
#     com=-z(i)-y(i)     #exp-fitting
      write(8,111)w(i), z(i),y(i)
#     write(4,*)w(i), com
}
111   format(1x,1e15.5,1x,1e15.5,1x,1e15.5)
      write(8,*)"];"
      #print *, "chi** =",xx
      end
payp.r          853179846   7534  70    100400  541
#ifndef lint
#static char sccsid[] = "@(#)payp.r 1.3 95/07/03";
#endif
#     ===============
#     must linked with ayppro.f subroutine.
      subroutine fayp(alt,ala,dex,sd,t,ff,ffd)
      implicit double precision ( a-h, o-z)
      real*8  sd(3),x(3)

      #data preparation
      tau=t*0.3/dex/alt
      x(1)=sd(1)/alt
      x(2)=sd(2)/alt
      x(3)=sd(3)/alt
      ff=f(tau,x)
       ff=ff*exp(-t*0.3/dex/ala)/alt**3*0.3/dex #unit /mm**2ps
       ffd=fd(tau,x)/alt**3*0.3/dex*exp(-t*0.3/dex/ala) #diffusion
#     ff=ff/alt**3*0.3/dex #unit /mm**2ps
#     ffd=fd(tau,x)/alt**3*0.3/dex  #diffusion

      end

ayppro.f        799714809   7534  70    100640  1609
c
c      tau= tc/lt
c      x=x/lt

       double precision function btt (tau)
       implicit double precision (a-h,o-z)
       expmtau = dexp (-tau)
       expmtau3=expmtau**3.d0
       btt=2.d0/3.d0*tau
       btt=btt-(1.d0-expmtau) + 1.d0/9.d0 * (1.d0-expmtau3)
       btt=btt/2.d0
       return
       end

       double precision function bll (tau)
       implicit double precision (a-h,o-z)
       expmtau = dexp (-tau)
       expmtau3=expmtau**3.d0
       bll = 1.d0-expmtau
       bll = bll -1.d0/3.d0*(1.d0-expmtau3)-(1.d0-expmtau)**2.d0
       bll=bll/2.d0
       return
```

```
      end

      double precision function a(tau)
      implicit double precision (a-h,o-z)
      expmtau = dexp (-tau)
      a=1-expmtau
      return
      end

      double precision function f(tau,x)
      implicit double precision (a-h,o-z)
      dimension x(3)
      pi=3.1415926d0
      coeff=1.d0/8.d0/pi**1.5
      bt = btt (tau)
      bl = bll (tau)+bt
      detb=bl * bt*bt
      coeff1=coeff/dsqrt(detb)
      e1=(x(1)-a(tau))**2.d0/4.d0/bl
      e2=x(2)**2.d0/4.d0/bt
      e3=x(3)**2.d0/4.d0/bt
      es=e1+e2+e3
      expt= dexp(-es)
      f=coeff1*expt
c     log scale
c      f= -es + dlog(coeff1)
      return
      end


      double precision function fd(tau,x)
      implicit double precision (a-h,o-z)
      dimension x(3)
      pi=3.1415926d0
      coeff=1.d0/8.d0/pi**1.5
      b=1.d0/3.d0*tau
      coeff1=coeff/dsqrt(b*b*b)
      r2=x(1)**2.d0+x(2)**2.d0+x(3)**2.d0
      expt=dexp(-r2/4.d0/b)
      fd=coeff1*expt
      return
      end
```

```
fayd            818096531   7534  70    100640  99
3
2.001,0.0002,2.01,2.00
2.e+2,5.e+1,4.e+2,1.e+2
1.,.05,1.1,.9
xlt10a
jxa10.m
1.334
20., 0.,0.
40.
```

```
#ifndef lint
#static char sccsid[] = "@(#)aypmain.r 1.1 95/06/18";
#endif
#      program lpnt3n.r
       implicit double precision (a-h,o-z)
       real*8 cj(5000),txx(1000), sd(3),cd(5000),cc(4),cdd(4)
       character*10 name3
       print*,"  transport mean free path tmfp (mm) ? "
       read*, tmfp
       print*,"absorption lenth (mm)"
       read*,ale
       print*, " detection loaction, x,y,z (mm)"
       read*, sd(1), sd(2), sd(3)
       print*, "index of material"
       read*, dex
       print*, " output file name "
       read*,name3
open(3,file=name3)
       print*, "read in starting time  (ps)~ ballistic time "
       read*,tstart
       print*, "read in step time  (ps) and nuber of terms"
       read*,step,nterm

cjmax=0.
cdmax=0.
cto=0.
do iii=1,nterm {
tx=step*float(iii)
       if(tx .gt.tstart) {
call fayp(tmfp,ale,dex,sd,tx,cj(iii),cd(iii))
txx(iii)=tx
#cto=cto+cj(iii)
       if(cj(iii).gt.cjmax) {cjmax=cj(iii)
       tmax=txx(iii)
}
       if(cd(iii).gt.cdmax) {cdmax=cd(iii)
       tdmax=txx(iii)
}
}
}
#        find FWHM
         iold=-20
ii=0
         do j=1,nterm {
         jj=j+1
         bbb=cj(j)-cjmax/2.
         bbb1=cj(jj)-cjmax/2.
         if (bbb*bbb1 <= 0.) {
         if (iold == j-1 ) {
         continue }
         else {
         ii=ii+1
         cc(ii)=(txx(j)+txx(jj))/2
         iold=j
}
}
```

```
}
#       end FWHM
#       find FWHM
ii=0
        iold=-20
        do j=1,nterm {
        jj=j+1
        bbb=cd(j)-cdmax/2.
        bbb1=cd(jj)-cdmax/2.
        if (bbb*bbb1 <= 0.) {
        if (iold == j-1 ) {
        continue }
        else {
        ii=ii+1
        cdd(ii)=(txx(j)+txx(jj))/2
        iold=j
}
}
}
#       end FWHM
write(3,*)"%distance=",sd(1),sd(2),sd(3)
write(3,*)"%index=",dex, "%amax=",cjmax
      write(3,*) "%max time&fwhms", tmax,cc(1),cc(2)
write(3,*)"%ls=",tmfp,"la=",ale,"scaling=",sca
      write(3,112)"%dmax=",cdmax, "time&fwhms",tdmax,cdd(1),cdd(2)
112   format(a10, 1e10.5, a12,3f10.4)
write(3,*) "data=["
nn=int(tstart/step)
do iii=nn+1,nterm {
#compute total intensity
time=txx(iii)     #ps
cjun=cj(iii)/cjmax
cdjun=cd(iii)/cdmax
      write(3,111)time,cj(iii),cjun,cd(iii),cdjun
}
111   format(5e16.6)
write(3,*) "];"
      stop
      end
```

Bibliography

Chapter 1

S. Webb, The Physics of Medical Imaging: Medical Science Series. (Institute of Physics (IOP) Publishing Ltd., 1988).

M. Cutler, "Transillumination as an aid in the diagnosis of breast lesions: with special reference to its value in cases of bleeding nipples," Surg. Gyncol. Obstet., 48, 721-729. 1929.

Z. H. Cho, J. P. Jones and M. Singh, Foundations of Medical Imaging (Wiley, New York. 1993).

R. R. Alfano, S. G. Demos, and S. K. Gayen, "Advances of Optical Imaging of Biomedical Media," Annals of the New York Academy of sciences, 820, 248-271 1997.

L. Wang, P. P. Ho, C. Liu, G. Zhang, and R. R. Alfano, "Ballistic 2-D imaging through scattering walls using an Ultrafast Optical Kerr Gate," Science 253, 769-771, 1991.

K. M. Yoo, and R. R. Alfano, "Time resolved coherent and incoherent components of forward light scattering in random media," Opt. Lett., 15, 320-322, 1990.

Koichi Furutsu, and Yukio Yamada, "Diffusion approximation for a dissipative random medium and the applications," Phys. Review E, 50, 3634-3641, 1994.

B. B. Das, J. Dolne, R. L. Barbour, H. L. Grabber, J. Chang, M. E. Zevallos, F. Liu, and R. R. Alfano, "Analysis of Time-Resolved Data For Tomographical Image Reconstruction Of Opaque Phantoms And Finite Absorbers In Diffusive Media," Proc. SPIE, 2389, 16-28, 1995.

L. Wang, P. P. Ho, X. Liang, H. Dai, and R. R. Alfano, "Fourier-Kerr imaging in thick turbid media," Opt. Lett., 18, 241-243, 1993.

L. Wang, P. P. Ho, C. Liu, G. Zhang, and R. R. Alfano, "Ballistic 2-D imaging through scattering wall using an ultrafast Kerr gate," Science 253, 769-771, 1991.

D. Huang, J. Wang, C. P. Lin, C. A. Puliafito, and J. G. Fujimoto, "Micro-resolution ranging of cornea anterior chamber by optical reflectometry," Las. Sur. Med., 11 419-425, 1991.

K. M. Yoo, Y. Takiguchi and R. R. Alfano, "Dynamic Effect of Weak Localization on the Light Scattering from Random Media Using Ultrafast Laser Technology," Appl. Opt., 28, 2343-2349, 1989.

S. L. Jacques, "Time Resolved Propagation of Ultrashort Laser Pulses within Turbid Tissues," Appl. Opt., 28, 2223-2229, 1989.

J. Fishkin, E. Gratton, M. J. vande Ven, and W. W. Mantulin, "Diffusion of Intensity Modulated Near-Infrared Light in Turbid Media," Time-Resolved Spectroscopy and Imaging of Tissues, B. Chance, Editor, Proc., SPIE, 1431, 122-135,1991.

M. S. Paterson, B. C. Chance, and B. C. Wilson, "Time resolved reflectance and transmittance for the non-invasive measurements of tissue optical properties," App. Optics, 28, 2331-2336, 1989.

S. J. Madsen, M. S. Patterson, B. C. Wilson, Y. D. Park, J. D. Moulton, S. L. Jacques, M. D. Anderson, and Y. Hefetz. "Time-resolved diffuse reflectance and transmittance studies in tissue simulating phantoms: a comparison between theory and experiment," Time-Resolved Spectroscopy and Imaging of Tissues, B. C. Chance, Editor, Proc. SPIE, 1431, 42-52, 1991.

S. R. Arridge, P. van der Zee, M. Cope, and D. T. Delpy, "Reconstruction methods for infrared absorption imaging," Time-Resolved Spectroscopy and Imaging of Tissues, B. C. Chance, Editor, Proc. SPIE, 1431, 204-217, 1991.

P. M. Morse and H. Feshback, Methods of theoretical Physics, McGraw-Hill, New York, Part 1, p. 865, 1993.

A. Ya. Polishchuk, S. Gutman, M. Lax, and R. R. Alfano, "Photon-density modes beyond the diffusion approximation: scalar wave-diffusion equation," J. Opt. Soc. Am. A., 14, 230-234, 1997.

J. Kaltenbach, M. Kashke, and C. Zeiss, "Frequency and Time Domain Modelling of Light Transport in Random Media," Medical Optical Tomography, 64-86, 1996.

V. G. Peters, D. R. Wyman, M. S. Patterson, and G. L. Frank, "Optical properties of normal and diseased human breast tissues in the visible and near infrared," Phys. Med. Biol. 35, 1317-1334, 1990.

H. Key, E. R. Davics, P. C. Jackson, and P.N. T. Wells, "Optical attenuation characteristics of breast tissues at visible and near-infrared wavelengths," Phys. Med. Biol. 6, 579-590, 1991.

P. French, "The light fantastic," New Scientist magazine, 25-29, 11 march, 1995.

Chapter 2

Lord Rayleigh, Scientific Papers I, (Cambridge University Press, 1899), Phil. Mag. 41,107; p. 96, 1871.

G. Mie, Ann. Physik, 25. 377. 1908.

H. C. Van de Hulst. Light Scattering by Small Particles. (Dover Publications Inc., New York, 1981)

Distances between sphere to ensure independent scattering is estimated to be bigger than 3 times the radio of the sphere. See Ref. 2.4 p. 5.

A. Schuster, Astrophys. J., 21, 1, 1905.

K. Schwarzschild, Sitz.ber. Preuss. Akad. Wiss. Berlin, 1183, 1914.

Frederich Kottler, The elements of radiative transfer. Progress in Optics Vol. III, part I, edited by E. Wolf, University of Rochester, NY, USA, 1964.

B. Davison and J. B. Sykes, Neutron Transport Theory, (Oxford University Press, London, 1957).

S. Glasstone and M. C. Edlund, The Elements of Nuclear Reactor Theory, (D. van Nostrand Co., Princeton NJ, 1952).

K. M. Case and P. F. Zweifel, Linear Transport Theory, (Addison-Wesley, MA, 1967).

A. Ishimaru, Wave propagation and scattering random media, (Academic Press, New York, 1978).

B. B. Das, Feng Liu, and R. R. Alfano, "Time-resolved fluorescence and photon migration studies in biomedical and model random media," Rep. Prog. Phys., 60, p. 227-292, 1997.

S. Chandrasekhar, Radiative Transfer, (Dover Publications Inc., New York, 1960).

J. Fishkin, E. Gratton, M. J. vande Ven, and W. W. Mantulin, "Diffusion of Intensity Modulated Near-Infrared Light in Turbid Media", Time Resolved Spectroscopy and Imaging of Tissues, B. Chance, Editor, Proc. SPIE, 1431, p. 122-135, 1991.

M. S. Patterson, B. Chance, and B. C. Wilson, "Time resolved reflectance and transmittance for the non-invasive measurement of tissue optical properties", Appl. Optics, 28, p. 2331-2336, 1989.

S. J. Madsen, M. S. Patterson, B. C. Wilson, Y. D. Park, J. D Moulton, S. L. Jacques, M. D. Anderson, and Y. Hefez, "Time-resolved diffusive reflectance and transillumination and transmittance studies in tissue simulating phantoms: a comparison between theory and experiment," Time Resolved Spectroscopy and Imaging of Tissues, B. Chance, Editor, Proc. SPIE, 1431, p. 42-51, 1991.

S. R. Arridge, P. van der Zee, M. Cope, and D. T. Delpy, "Reconstruction methods for infrared absorption imaging," Time Resolved Spectroscopy and Imaging of Tissues, B. Chance, Editor, Proc. SPIE, 1431, p. 204-217, 1991.

R. Aronson, "Subcritical problems in spherical geometry", Nuclear Science and Engineering 86, 436 (1984).

J. Kaltenback, and M. Kashke, "Frequency and time-domain modeling of light transport in random media", Medical Optical Tomography, 65-86, 1994

K. M. Case and P. F. Zweifel, in Linear Transport Theory (Addison-Wesley, MA, 1967).

V. Kourganoff, Basic methods in transfer problems, radiative equilibrium and neutron diffusion, (Dover Publications Inc., New York, 1963)

A. Eddington, The Internal Constitutions of the Stars, (Dover Publications Inc., New York, 1926)

Leming Wang, Ph.D. Thesis, The City Univesity of NY, 1995.

K. M. Yoo, F. Liu, and R. R. Alfano, Phys. Rev. Lett., 64, 2647, 1990.

F. Liu, K. M. Yoo, and R. R. Alfano, "Early arriving transmitted photon intensity through tissues," edited by R. Alfano, OSA Proc. on Advances in Optical Imaging and Photon Migration, OSA, vol. 21, p. 170, 1994.

E. P. Zege, A. P. Ivanov, and I. L. Katsev, Image Transfer through a Scattering Medium, (Springer -Verlag, Heidelberg, 1991).

A. Ya Polishchuk, and R. R. Alfano, "Non-Euclidean diffusion and "Fermat" photons in turbid media," SPIE Proc., in Optical tomography, Photon Migration, and spectroscopy of Tissue and Model Media: Theory, Human Studies, and Instrumentations, SPIE Vol. 2389, 1995.

A. Ya Polishchuk, and R. R. Alfano, "Photon diffusion on the velocity sphere," Opt. Lett. 21, 916,-918, 1996.

A. Ya Polishchuk, M. E. Zealous, F. Liu, and R. R. Alfano, "Generalization of Fermat's principle for photons in random media: The least mean square curvature of paths and photon diffusion on the velocity sphere," Phys. Rev. E, 53, 5523, 1996.

M. E. Zevallos, A. Ya Polishchuk, F. Liu, B. B. Das and R. R. Alfano, "Time-resolved scattering measurements from scattering media fitted to Non-Euclidean and Conventional Diffusion model," Phys. Rev. E, 56, No 6, 1998.

R. R. Alfano, S. G. Demos, and S. K. Gayen, "Advances in Optical imaging of Biomedical Media, on Imaging Brain Structure and Function," Annals of the New York Academy of Sciences, 820, 248-271, 1997.

S. G. Demos and R. R. Alfano, "Temporal gating in highly scattering media by the degree of optical polarization," Opt. Lett., 21, 161-163, 1996.

H. Horinaka, K. Hashimoto, K. Wada, and Y. Cho, "Extraction of quasi-straightforward-propagating photons from diffused light transmitting through a scattering medium by polarization modulation," Opt. Lett., 20, 1501-1503, 1995.

J. C. Hebden, S. R. Arridge, D. T. Delpy, "Optical imaging in medicine: I. Experimental Techniques," Phys. Med. Biol., 42, 825-840, 1997.

B. B. Das, K. M. Yoo, and R. R. Alfano, "Ultrafast time-gated imaging in thick tissues: A step toward optical mammography,". Opt. Lett., 18,1002-1004, 1993.

J. C. Hebden, R. A. Kruger, and K. S. Wong, "Time resolved imaging through a highly scattering medium," Appl. Opt., 30, 788-794, 1991.

K. M. Yoo, Q. Xing, and R. R. Alfano, "Imaging objects hidden in highly scattering media using femtosecond second-harmonic generation cross-correlation time gating," Opt. Lett., 16, 1019-1021, 1991.

M. R. Hee, J. A. Izzat, J. M. Jacobson, J. G. Fujimoto, and E. A. Swanson, "Femtosecond transillumination optical coherence tomography," Opt. Lett., 18, 950-952, 1993.

Chapter 3

M. A. O'Leary, D. A. Boas, B. Chance, and A. G. Yodh, "Experimental images of heterogeneous turbid media by frequency-domain diffusing-photon tomography", Opt. Lett., 20.426-428, 1995

B. Chance, K. Kang, L. He, J. Weng, and E. Sevick, "Highly sensitive object location in tissue model with linear in-phase and anti-phase multi-element optical arrays in one and two dimensions", Proc. Natl. Acad. Sci., USA., 90, 3423-3427, 1993.

M. Miwa, Y. Ueda and B. Chance, "Development of time resolved spectroscopy system for quantitative non-invasive tissue measurement", SPIE, 2389, 142-149, 1995.

P. Liu, K. M. Yoo, and R. R. Alfano, "Should the photon flux or the photon density be used to described the temporal profiles of scattered ultrashort laser pulses in ransom media?", Opt. Lett., 18, 432-434, 1993.

Chapter 4

P. M. Morse, and H. Feshbach, Methods of Theoretical Physics, (McGraw-Hill Book Co., Part 1, 865, 1953).

A. Ya. Polishchuk, S. Gutman, M. Lax, and R. R. Alfano, J. Opt. Soc. Am. A, 14, 230, 1997.

K. M. Yoo, Feng Liu, and R. R. Alfano, Phys. Rev. Lett., 64, 2647, 1990.

K. M. Yoo, Feng Liu, and R. R. Alfano, SPIE Proceedings on Time-Resolved Laser Spectroscopy in Biochemistry II, 1204, 492, 1990.

A. Ya Polishchuk and R.R. Alfano, Optics Letters, 21, 916, 1996.

A. Ya. Polishchuk, M. E. Zevallos, F. Liu, and R. R. Alfano, Phys. Rev. E, 53, 5523, 1996.

K. M. Yoo, B. B. Das, F. Liu, and R. R. Alfano, Medical Optical Tomography, SPIE, IS11, 425, 1993.

F. Liu, K. M. Yoo, and R. R. Alfano, OSA Proceedings on Advances in Optical Imaging and Photon Migration, R. R. Alfano (ed.), 21, 170, 1994.

Samuel Glasstone and Milton C. Edlund, The Elements of Nuclear Reactor Theory, (D. Van Nostrand Company, Inc., New York, 174-180, 1952).

Enrico Fermi, Nuclear Physics, Course Notes Compiled by Jay Orear, A. H. Rosenfeld, and R. A. Schluter, (The University of Chicago Press, Chicago, 187-189, 1950.

A. Ya Polishchuk, "A solution to the non-Euclidean diffusion equation for photon migration in random media," unpublished, records on IUSL Department at CCNY.

G.H. Watson, S. L. McCall, P. A. Fleury, and K. B. Lyons, Phys. Rev. B, 41, 10947, 1990.

A. Ishimaru, Wave Propagation and Scattering in Random Media, (Academic Press, New York, 1978).

John Gowar, Optical Communication Systems, (Second Edition, Prentice Hall, New York, 34-36 and 337-338, 1994).

Leo Levi, Applied Optics, (John Wiley & Sons, Inc., New York, 2, 231-233, 1996).
John R. Taylor, Scattering Theory: the quantum theory of nonrelativistic collisions, (John Wiley & Sons, Inc., New York, 44-51, 1972)

M. E. Zevallos, F. Liu, B. B. Das, A. Ya Polischuck, and R. R. Alfano, OSA Trends in Optics and Photonics on Advances in Optical Imaging and Photon Migration, R. R. Alfano and James G. Fujimoto, eds., Vol. II, 21-24, 1996.

Chapter 5

S. L. Jacques, "Origins of tissue optical properties in the UVA, visible, and NIR regions," in *Advances in Optical Imaging and Photon Migration*, R. R. Alfano and J. G. Fujimoto, eds., Vol. 2, OSA Trend in Optics and Photonics (Optical Society of America, Washington D. C., 1996), pp. 364-371.

Y. C. Fung , Biomechanics: Mechanical Properties of Living Tisssues, Second Edition, (Springer-Verlag, New York, 1993).

The organizational hierarchy of skeletal muscle, From Gray's Anatomy, 35th British edn. (1973), edited by Warwick and Williams

J. F. de Boer, T. E. Milner, M. J. C. van Gemert, J. S. Nelson, "Two-dimensional birefringence imaging in biological tissue by polarization-sensitive optical coherence tomography," Opt. Lett., 22, 934-936, 1997.

Chapter 6

S. K. Gayen and R. R. Alfano, Emerging optical biomedical imaging techniques, Opt. Phot. News 7 (3), 17-22,1996.

B. E. A. Saleh and M. C. Teich, *Fundamentals of Photonics*, John Wiley and Sons, Inc., New York, 136-139, 1991.

J. J. Dolne, K. M. Yoo, F. Liu, and R. R. Alfano, "IR Fourier space gate and absorption imaging through random media," Lasers Life Sci., 6, 131-141, 1994.

H. Horinaka, K. Hashimoto, K. Wada, and Y. Cho, "Extraction of quasi-straightforward-propagating photons from diffused light transmitting through a scattering medium by polarization modulation," Opt. Lett. 20, 1501-1503, 1995.

S. G. Demos and R. R. Alfano "Temporal gating in highly scattering media by the degree of optical polarization," Opt. Lett. 2, 161-163 (1996).

T. Troy, D. Page, and E. Sevick-Muraca, "Optical properties of normal and diseased breast tissues: prognosis for mammography," J. Biomed. Opt., 1, 342-355, 1996.

W. Cheong, S. A. Prahl, and A. J. Welch, "A review of the optical properties of biological tissues," IEEE J. Quantum Electron., 26, 2166-2185, 1990.

S. Gayen, M. E. Zevallos, M. Alrubaiee, J. M. Evans, and R. R. Alfano, "Two-dimensional near-infrared transillumination imaging of biomedical media with a chromium-doped forsterite laser" Appl. Opt. Vol., 37, No. 32, 1998.

S. L. Jacques, "Origins of tissue optical properties in the UVA, visible, and NIR regions," in OSA TOPS on *Advances in Optical Imaging and Photon Migration 1996*, Vol. 2, R. R. Alfano and J. G. Fujimoto (eds.), Optical Society of America, Washington D. C., 364-371, 1996.

J. A. Moon, P. R. Battle, M. Bashkansky, R. Mahon, M. D. Duncan, and J. Reintjes, "Achievable spatial resolution of time-resolved transillumination imaging systems which use multiply scattered light," Phys. Rev. E ., 53, 1142-1155, 1996.

F. A. Marks, "Optical determination of the hemoglobin oxygenation state of breast biopsies and human breast cancer xenografts in nude mice," SPIE, 1641, 227-237, 1992.

K. M. Yoo, Z. W. Zang, S. A. Ahmed, and R. R. Alfano, "Imaging objects hidden in scattering media using fluorescence-absorption techniques," Opt. Lett., 16, 1252-1254, 1991.

V. Petricevic, S. K. Gayen, and R. R. Alfano, "Near infrared tunable operation of chromium-doped Forsterite Laser", Appl. Opt., 28, 1609-1611, 1989.

E. Bouma, G. J. Tearney, I. P. Bilinsky, B. Golubovic, and J. Fujimoto, "Self-phase-modulated Kerr-lens-modelocked Cr:forsterite laser source for optical coherence tomography," Opt. Lett., 21, 1839-1841, 1996.

S. G. Demos and R. R. Alfano, "Optical polarization imaging," Appl. Opt., 36,150-155, 1997.

J. F. de Boer, T. E. Milner, M. J. C. van Gemert, J. S. Nelson, "Two-dimensional birefringence imaging in biological tissue by polarization-sensitive optical coherence tomography," Opt. Lett., 22, 934-936,1997.

Chapter 7

K. M. Yoo, B. B. Das, and R. R. Alfano, "Imaging of a translucent object hidden in a highly scattering medium from the early portion of the diffuse component of a transmitted ultrafast laser pulse," *Opt. Lett.*, 17, 958-960, 1992.

B. B. Das, K. M. Yoo, and R. R. Alfano, "Ultrafast, time-gated imaging in thick tissues: a step toward optical mammography," *Opt. Lett.*, 18, No. 13, 1092-1094, 1993.

M. A. O'Leary, D. A. Boas, B. Chance, A. G. Yodh, *Phys. Rev. Lett.*, 69, 2658-2661, 1992.

F. Liu, K. M. Yoo, and R. R. Alfano, "Ultrafast laser-pulse transmission and imaging through biological tissues," Applied Optics, 32(4), 554-558, 1993.

F. Liu, K. M. Yoo, and R. R. Alfano, "Transmitted photon intensity through biological tissues within various time windows," Opt. Lett., 19(10), 740-743, 1994.

B. B. Das, Feng Liu, and R. R. Alfano, "Time-resolved fluorescence and photon migration studies in biomedical and model random media," Prog. Phys., 60(2), 227-292, 1997.

L. Wang, P.P. Ho, G. Liu, G. Zhang, and R.R. Alfano, "Ballistic 2-D imaging through scattering walls using an ultrafast optical Kerr Gate", Science, 253, 769-771, 1991.

G. Muller and B. Chance Editors, *Medical Optical Tomography*, SPIE, Birmingham, 1993.

R. R. Alfano Ed., *OSA proceedings on Advances in Optical Imaging and Photon Migration*, 21,1994.

V. V. Tuchin , Selected papers on Tissue Optics: Applications in Medical Diagnostics and Therapy, (SPIE Milestone Series, Vol. MS102, 1994)

K. M. Yoo and R. R. Alfano, "Time-resolved coherent and incoherent components of forward light scattering in random media", Opt. Lett., 15, 320-322, 1990.

J. R. Singer, F. A. Grunbaum, P. Kohn, J. P. Zubelli, Science, 248, 990-993, 1990.

K. M. Yoo, Q. Xing, and R. R. Alfano, *Opt. Lett.*, 16, 1019-1021, 1991.

D. Huang, E. A. Swanson, C. P. Lin, J. S. Schuman, W. G. Stinson, W. Chang, M. R. Hee, T. Flotte, K. Gregory, C. A. Puliafito, and J. G. Fujimoto, Science, 254, 1178, 1991.

B. B. Das, J. Dolne, R. L. Barbour, H. L. Graber, J. Chang, M. Zevallos, F. Liu and R. R. Alfano, *SPIE proceedings*, 1995.

J. A. Moon, R. Mahon, M. D. Duncan, and Reintjes, *Opt. Lett.*, 18, 1591, 1993.

L. Wang, A. H. Hielscher, S. L. Jacques, D. V. Stephens, and F. K. Tittel, *Proc. of OSA, Advances in Optical Imaging and Photon Migration*, 21, 288-290, Alfano R R, Ed., Orlando, Florida, 1994.

S. Anderson-Engels, R. Berg, S. Svanberg, and O. Jarlman, *Opt. Lett.*, 15, 1178-1181, 1990.

J. C. Hebden, R. A. Kruger, and K. S. Wong, *Appl. Opt.*, 30, 788-794, 1991.

H. Chen, Y. Chen, D. Dilworth, E. Leith, J. Lopez, and J. Valdmanis, *Opt. Lett.*, 16,487-489, 1991.

E. N. Leith, C. Chen, H. Chen, Y. Chen, J. Lopez, P. C. Sun, and D. Dilworth, *Opt. Lett.*, 16, 1820-1822, 1991.

Chapter 8

R. R. Alfano, S. K. Gayen and A. Katz, "Advances in Mediphotonic Imaging and Biopsy," in "Optics and Imaging in the Information Age," IS&T - The Society for Imaging Science and Technology, Springfield, Virginia, USA, 299 - 304, 1997

Proceedings of Advances in Laser and Light Spectroscopy to Diagnose Cancer and Other Diseases III: Optical Biopsy, 29-30 January 1996, San Jose, California, edited by R. R. Alfano, SPIE, Volume 2679.

OSA Trends in Optics and Photonics Series Volume on Advances in Optical Imaging and Photon Migration ('96), edited by R. R. Alfano and J. G. Fujimoto, Optical Society of America, 1996.

C. H. Liu, B. B. Das, W. L. Sha Glassman, G. Tang, K. Yoo, H. Zhu, D. L. Akins, S. S. Lubicz, J. Cleary, R. Prudente, E. Celmer, A. Caron and R. R. Alfano, J. Photochem. Photobiol. B: Biol. 16, 187, 1992.

A. Mahadevan and R. Richards-Kortum, J. Biomed. Opt. 1, 31, 1996, and references therein.

M. S. Feld, R. Manoharan, J. Salenius, J. Orenstein-Carndona, T. J. Romer, J. F. Brennan III, R. R. Dasari, and Y. Wang, "Detection and characterization of human tissue lesions with near infrared Raman spectroscopy," in Advances in Fluorescence Sensing Technology, Vol. II, edited by J. R. Lakowicz, Proc. SPIE 2388, 99, 1995.

L. Wang, P. P. Ho, C. Liu, G. Zhang, and R. R. Alfano, Science 253, 769, 1991.

C. Hebden, R. A. Kruger, and K. S. Wong, Appl. Opt. 30, 794, 1991.

M. R. Hee, J. Izzat, J. M. Jaconson, J. G. Fujimoto, and E. A. Swanson, Opt. Lett. 18, 952, 1993.

J. Reintjes, M. Bashkansky, M. Duncan, R. Mahon, L. L. Tankerskley, J. A. Moon, C. L. Adler, and J. M. S. Prewitt, Opt. Photon. News, 4(10): 28, 1993.

R. Berg, S. Anderson-Engels, and S. Svanberg, "Time-resolved transillumination imaging." In Medical Optical Tomography: Functional Imaging and Monitoring, ed. by G. J. Muller et al., SPIE, Bellingham, Washington, 397-424, 1993.

E. M. Sevick, C. L. Burch, J. K.Frisoli, M. L. Johnson, K. Nowaczyk, H. Szmacinski, and J. R. Lakowicz, "The physical basis of biomedical optical imaging using time-dependent measurements of photon migration in the frequency domain. In Medical Optical Tomography: Functional Imaging and Monitoring, ed. by G. J. Muller et al., SPIE, Bellingham, Washington, 485-512, 1993.

M. A. O'Leary, D. A. Boas, B. Chance, and A. G. Yodh, Opt. Lett. 20: 426, 1995.

K. P. Chan, M. Yamada, and H. Inaba, Opt. Lett. 20, 492, 1995.

D. S. Dilworth, E. N. Leith, and J. L. Lopez, Appl. Opt. 30,1796, 1991.

S. R. Arridge, "The forward and inverse problems in time-resolved infrared imaging. In Medical Optical Tomography: Functional Imaging and Monitoring, ed. by G. J. Muller, SPIE, Bellingham, Washington, 35-64, 1993.

S. Thomsen and D. Tatman, "Physiological and pathological factors of human breast disease that can influence optical diagnosis," Ann. N. Y. Acad. Sci. 838, 171, 1998.

F. A. Marks, SPIE 1641, 227, 1992.

V. Petricevic, S. K. Gayen, and R. R. Alfano, Appl. Opt. 28, 1609, 1989.

J. J. Dolne, K. M. Yoo, F. Liu, and R. R. Alfano, Lasers Life Sci. 6, 131, 1994.

S. G. Demos and R. R. Alfano, Opt. Lett. 21, 161, 1996.

W. Cai, B. B. Das, F. Liu, M. Zevallos, M. Lax, and R. R. Alfano, Proc. Natl. Acad. Sci. USA 93, 13561, 1996.

IMAGE EVALUATION
TEST TARGET (QA-3)

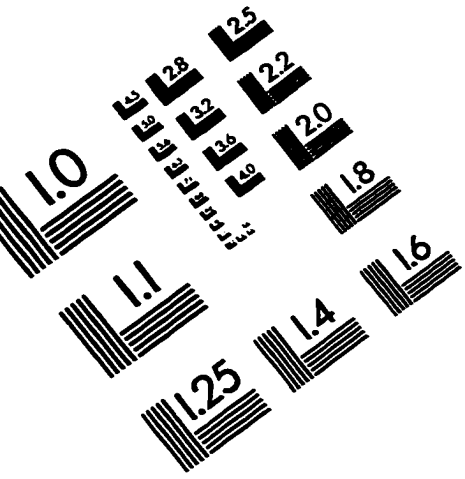

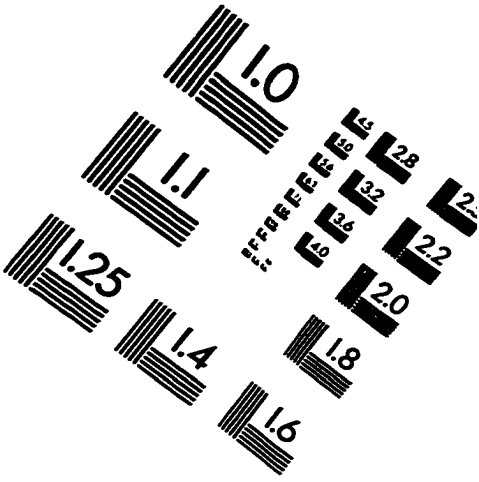

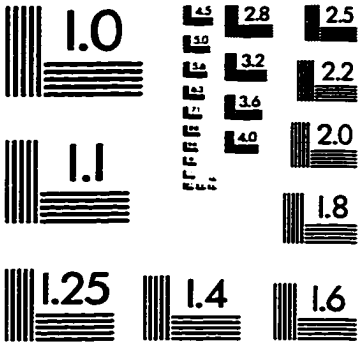

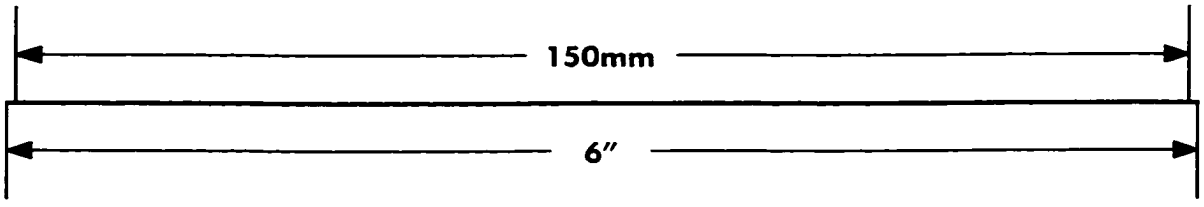

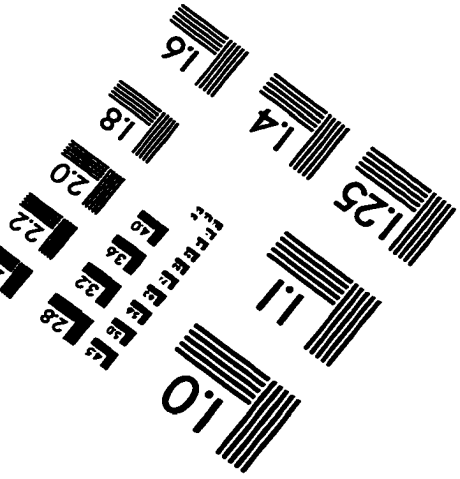

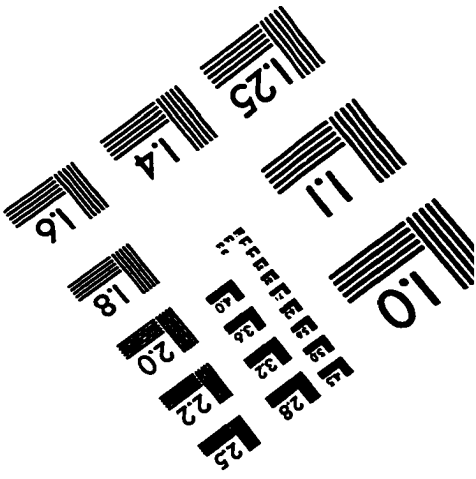

APPLIED IMAGE, Inc
1653 East Main Street
Rochester, NY 14609 USA
Phone: 716/482-0300
Fax: 716/288-5989